1-1-2011

Durability performance of frp strenghtened concrete beams and columns exposed to hygrothermal environment

Abulgasem Mohamed Elarbi
Wayne State University,

DURABILITY PERFORMANCE OF FRP STRENGHTENED CONCRETE BEAMS AND COLUMNS EXPOSED TO HYGROTHERMAL ENVIRONMENT

by

ABULGASEM MOHAMED ELARBI

DISSERTATION

Submitted to the Graduate School

of Wayne State University,

Detroit, Michigan

in partial fulfillment of the requirements

for the degree of

DOCTOR OF PHILOSOPHY

2011

MAJOR: CIVIL ENGINEERING

Approved by:

_____

Advisor Date

_____

_____

_____

_____

DEDICATION

To my Mother's soul,

my brother Salem's soul

I was wishing you attend this day, but the destiny is stronger than us.

"To Allah we belong and to Him we shall return"

Also,

To: my father,

my wife,

my sons: Mohamed, Muhab, Moneib,

my daughter Jana,

my brothers and sisters

ACKNOWLEDGMENTS

I would like to express my grateful thanks to ALLAH for all his bounties, particularly health, knowledge and patience.

Then; I wish to thank the following people for their help:

Dr. Hwai-Chung Wu, my committee chair, academic advisor and mentor during my study at Wayne State University. I would like to extend my deepest gratitude for his continuous help, advice, interest, guidance, and patience. He provided valuable time and knowledge of the subject making this dissertation successful. It has been a great pleasure working with Dr.Wu over the past four years.

Dr. Usmen Mumtaz, my committee member, for his assistance during my PhD study at Wayne State University.

Dr. Gongkang Fu, my committee member, for the help he provided during my study.

Dr. Emmanual Ayorinde, my committee member.

Dr. Carol Miller, Civil and Environmental Engineering Department Chair. I would like to extend special thanks to Dr. Miller for providing help and support with this research by providing the funding for some of the materials.

Many thanks to **Fyfe Company** and **Sika Company** for donating FRP materials.

Furthermore, thanks are extended to all the staff members of the Civil and Environmental Engineering Department at Wayne State University.

TABLE OF CONTENTS

LIST OF TABLES

LIST OF FIGURES

CHAPTER 1 INTRODUCTION

1.1 General Review

Concrete structures may deteriorate with time due to external environmental conditions. One of these environmental conditions is hot weather. Hot weather can be defined as any period of high temperature during which special precautions need to be taken. The effects of temperature, wind, and air humidity, can all have a negative impact on the performance of concrete. The most important factors are temperature and humidity. These two environmental factors can have serious effects on hardened concrete, often times these effects are not immediately evident and develop years later making determination of responsibility difficult and repair expensive.

Many development projects being executed in hot-climate countries involve construction of reinforced concrete structures in hot weather. As a sample of these hot-climate places, table 1.1 shows the extreme maximum temperatures and the highest relative humidities in some cities in Libya during the years from 1971-2006. The maximum temperature during this period of time was recorded 54^{o}C while the highest relative humidity (RH) was 100%.

Effects of temperature are usually referred to as “thermal” effects, whereas those of moisture are often referred to as “hygroscopic” effects. The combined effects of temperature and moisture are described as “hygrothermal” effects [1].

Deteriorated structures should be repaired to ensure proper functioning and to extend their service life. Structures without damage may also need to be strengthened because of design or construction errors, or to accommodate changes in use or increased loads. As a result, various strengthening techniques have been developed. Traditional strengthening and retrofitting

techniques that use steel and cementitious materials do not always provide the most appropriate solutions.

The bonding of thin fiber-reinforced plastics (FRP) composites on the surface of concrete members has emerged as an effective method to increase both the strength and stiffness of concrete members [2,3,4,5]. Fiber reinforced polymer (FRP) composites have been extensively investigated for strengthening, due to its superior performance [6]. To understand the performance of composite materials under mechanical loading, extensive researches have been carried out and studies have been made during the past four decades [7]. Analytical models have been developed and experimental results have been reported to explain various failure phenomena of Fiber Reinforced Polymer (FRP) composites. Although a large volume of literature is available on performance of composite materials under mechanical loads, there appears to be less work reported on the long term effect of temperature and moisture on the composite materials. Available researches on the effects of hygrothermal aging on the durability of composite materials mostly focus on aerospace applications [7].

External bonding with Fiber Reinforced Polymer composites (FRPs) is increasingly considered as a viable means of strengthening, retrofitting, and repairing existing reinforced concrete structures. In appropriate situations, FRP materials can offer significant advantages over more traditional techniques of adding new or replacing lost load carrying capacity. FRPs do not suffer from corrosion as do steel plates, allowing the possibility of extended service lives or perhaps limiting required maintenance. Their high strength and stiffness to weight ratios mean that a smaller weight of FRP needs to be applied as compared to steel plates bonding. Such light weight reduces transportation costs, significantly eases installation, even in tight spaces, and can

eliminate the need for scaffolding. The low weight also means that FRPs add only a negligible weight to the structure's dead load. These advantages make FRPs a preferred repair option when significant additional weight could cause failure. Additionally, FRPs are typically applied in thin strips or sheets, resulting in very little change in the structural profile, an important feature for structures that require a tight clearance for vehicles or machinery [8,9,10].

There is a pressing need for this type of technology to be used in infrastructures [7], since many infrastructures have been deteriorating due to aging, overuse, or negligence. Several outstanding problems with FRP materials are premature debonding failure between concrete and the FRP, and the effect of environmental conditions on the durability performance of FRP strengthening materials [10]. Therefore, this study will focus on the bonding between the FRP materials and concrete subject to hygrothermal conditioning and how temperature and humidity influence the properties of FRP materials. Consequently, the long-term structural performance of FRP bonded beams/columns can be better designed under natural hygrothermal environments.

Table 1.1:Extreme maximum temperature and relative humidity in some cities in Libya 1971 - 2006

LIBYAN NATIONAL METEORLOGICAL CENTER CLIMITOLOGICAL DEPARTMENT												
GHADAMES	JAN	FEB	MAR	APR	MAY	JUN	JUL	AU	SEP	OCT	NOV	DEC
EXTREME MAX. TEMPERUTURE ^{o}C	31.8	34.4	39.0	45.7	45.3	54.2	48.4	47.2	45.2	41.2	38.0	33.0
HIGHEST RELATIVE HUMIDITY %	100	100	100	99	97	87	92	90	95	100	100	100
TRIPOLI AIRPORT	JAN	FEB	MAR	APR	MAY	JUN	JUL	AU	SEP	OCT	NOV	DEC
EXTREME MAX. TEMPERUTURE ^{o}C	32.0	35.4	37.8	43.0	46.7	48.4	48.0	49.1	46.2	44.5	39.0	32.1
HIGHEST RELATIVE HUMIDITY %	100	100	100	100	100	100	10	100	100	100	100	100
SEBHA	JAN	FEB	MAR	APR	MAY	JUN	JUL	AU	SEP	OCT	NOV	DEC
EXTREME MAX. TEMPERUTURE ^{o}C	30.0	36.5	40.0	43.8	46.5	47.6	46.5	47.0	45.4	42.2	37.5	35.0
HIGHEST RELATIVE HUMIDITY %	100	100	99	100	93	80	75	81	91	100	100	100
GHAT	JAN	FEB	MAR	APR	MAY	JUN	JUL	AU	SEP	OCT	NOV	DEC
EXTREME MAX. TEMPERUTURE ^{o}C	31.2	36.0	39.0	43.0	44.5	45.8	45.8	44.6	43.6	41.8	47.0	36.0
HIGHEST RELATIVE HUMIDITY %	100	94	97	93	87	96	57	83	77	95	92	100

1.2 Material Properties

Ageing infrastructure worldwide has attracted the interest of many researchers and organizations to look for alternative materials and techniques to restore the deficient structures. Structure materials can be divided into four basic categories: metals, polymers, ceramics, and composites. Advanced composites have received great attention as materials of choice for a variety of applications in repair and strengthening projects due to their superior properties. An advanced composite is primarily made with two constituents-the fibers and the binding matrix which holds together both materials [11].

Properties of composite materials are dependent on manufacturing and fabrication processes as well as the nature of the constituent materials. The strength properties of composite materials do not differ so much from conventional materials except anisotropy, i.e. the properties have directional characteristics. Moreover, the list of candidate materials of both reinforcement (fibers and matrices) used for composites is extensive and the range of properties can be selected for optimum result [11,12].

1.2.1 Fibers

There are mostly three types of fiber reinforcement that are used in civil structures, namely glass, aramid, and carbon fibers, as shown in Figure 1.1. The physical and mechanical properties vary not only between fiber types but also within the same fiber type. Stress strain diagrams of different unidirectional FRPs are shown in Figure 1.2. Carbon is the stiffest, while glass and aramid have a longer elongation at failure. All fibers have a linear elastic behavior up to failure [11,12,13,14].

Figure 1.1: Common glass and carbon fibers and FRPs used in structural engineering [16]

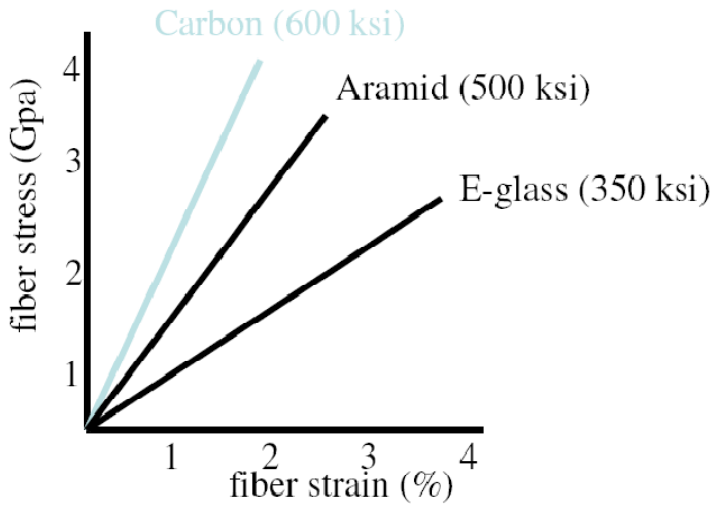

Figure 1.2: Stress-strain curves of various fiber types [16]

Glass fiber: Glass FRPs have been widely used in various commercial products such as piping, tanks, boats, and sporting goods. Glass is by far the most widely used fiber, because of the combination of low cost, corrosion resistance, and in many cases efficient manufacturing potential. It has relatively low stiffness, high elongation, moderate strength and weight, and generally lower cost relative to other fibers. It has been used extensively where corrosion resistance is important, such as in chemical works and in marine applications.

Glass fibers are classified into three types: E-glass, S-glass, and alkali resistant AR-glass fibers. E-glass or electrical grade, is a glass with calcium alumina-borosilicate compositions and

has a maximum alkali content of 2.0%. E-glass is the best for general-purpose structural applications. It also has good heat and electricity resistance. E-glass fibers are disadvantageous in having low alkali resistance. S-glass, or strength grade, which has a magnesium alumina-silicate composition, is a special glass with a higher tensile strength and modulus with a good heat resistance. In comparison to E-glass, S-glass has a better resistance to acids such as H_2SO_4, HCL and HNO_3, but it is still not resistant to alkali solutions [5,6,10].

To prevent glass fiber from being eroded by the high alkalinity in cement, a considerable amount of zircon is added to produce alkali resistant glass, AR-glass. AR-glass has mechanical properties similar to E-glass [5,6].

Aramid fibers: Aramid fibers are strong synthetic fibers and mainly used in aerospace and military applications. They are commonly used in ballistic rated body armor fabric and as an asbestos substitute. The name is a shortened form of "aromatic polyamide". They are fibers in which the chain molecules are highly oriented along the fiber axis, so the strength of the chemical bond can be exploited. The aramid fibers were first introduced in 1971 [6,11]. The structure of organic aramid fibers is anisotropic and gives higher strength and modulus in the fiber longitudinal direction. Aramid is resistant to fatigue, both static and dynamics, and it responds elastically in tension but exhibits non-linear and ductile behavior under compression [11,12]. Applications of aramid fibers in civil engineering structures includes ropes, cables, curtain walls, floors and ceilings, pipes and pre-stressing tendons [5,11]. However, aramid fibers are sensitive to high heat and moisture [11].

Carbon fibers: Carbon fibers are very durable and perform very well under fatigue loading in hot moist environments [1,11]. Carbon fiber has been described as a fiber containing at least 90% carbon obtained by the controlled pyrolysis of appropriate precursor fibers. The existence of

carbon fiber was dated back in 1879 when Edison took out a patent for the manufacture of carbon filaments suitable for use in electric lamps [13]. However, it was in the early 1960s when a successful commercial production was started, to meet the demands of the aerospace industry.

Especially for military aircraft, high performance and lightweight materials became of paramount importance [11]. In recent decades, carbon fibers have found wide applications in the commercial aircraft, recreational, industrial, structures, and transportation markets. Carbon fibers are used in composites with a lightweight matrix material. Carbon fiber composites are ideally suited to applications where strength, stiffness, lower weight, and outstanding fatigue characteristics are critical requirements. Carbon FRP (CFRP) sheets and strips are being used to strengthen concrete structures such as beams, columns, slabs, piles, and decks [5,6,11,13,15]. They also can be used in the occasion where high temperature, chemical inertness and high damping are important [11,15] .

1.2.2 Matrices

Fibers by themselves have limited use in engineering application since they cannot transmit loads from one to another; therefore, the matrix material plays an important role in the overall function of the composite. When the matrix binds the fibers together, it enables transfer of loads to the fibers and protects them against environmental attack and damage due to handling.

The matrix for structural composite materials can either be of thermosetting type or of thermoplastic type, with the first being more common. Polyester, Vinyl-ester, and Epoxy are the most commonly used polymeric matrix materials used with high performance reinforcing fibers. They are all thermosetting polymers with good processability and chemical resistance. Epoxies are more expensive than polyesters and vinyl-esters, but have in general better mechanical

properties and outstanding durability [5,6,11,16]. Thermoset polymers, including epoxy, are cured by chemical reactions, and the cure is a one-time irreversible process. Thermoplastics, on the other hand, can be melted repeatedly by heating. Table 1.2 shows some typical properties of polyester, vinyl-ester, and epoxy matrices.

Table 1.2: Typical properties for polyester, vinyl-ester and epoxy matrices [16]

Fiber	Elastic Modulus (GPa)	Tensile Strength (MPa)	Ultimate Tensile Strain (%)
Polyester	2.1-4.1	20-100	1.0-6.5
Vinyl-ester	3.2	80-90	4.0-5.0
Epoxy	2.5-4.1	55-130	1.5-9.0

1.2.3 Composites

A composite is a product made with two materials or more in which one of them is called the reinforcing phase, is in the form of fibers, sheets, or particles, and is embedded in the other material called the matrix phase (figure 1.3). The reinforcing material and the matrix material can be metal, ceramic, or polymer. Typically, reinforcing materials are strong with low densities while the matrix is usually a ductile, or tough, material. If the composite is designed and fabricated correctly, it combines the strength of the reinforcement with the toughness of the matrix to achieve a combination of desirable properties not available in any single conventional material. The downside is that such composites are often more expensive than conventional materials [16,83].

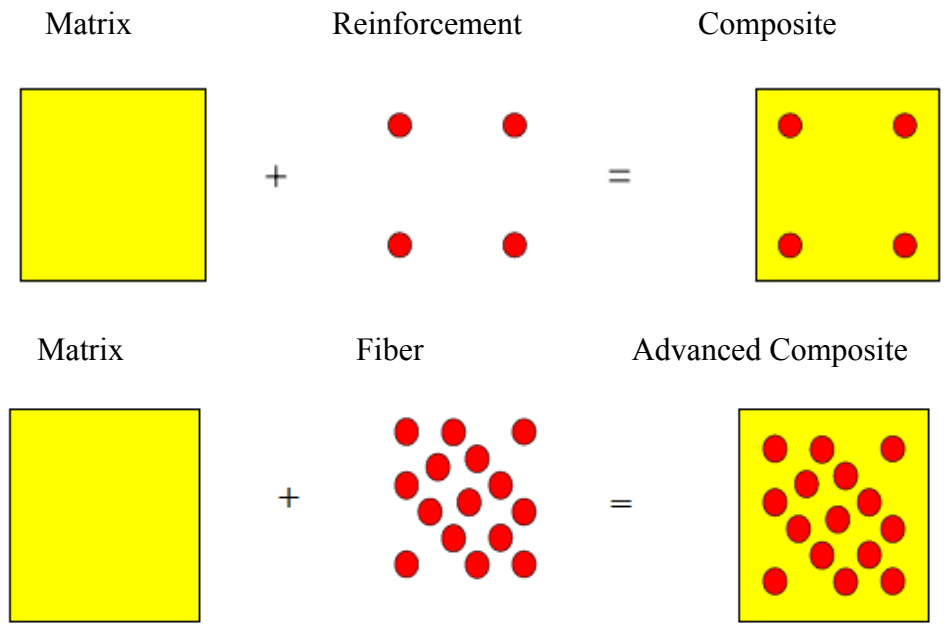

Figure 1.3: Composite materials [16]

1.2.4 Adhesive

Adhesive is a compound that adheres or bonds two items together. The term adhesion refers to the attraction between substances when they are brought into contact, whereby work must be applied in order to separate them. Furthermore, adhesives in the general term used for substance capable of holding materials together by surface attachment include, cement, glue, paste, etc. The majority common structural adhesive is epoxy adhesive (matrix resin). Epoxy resins are a group of polymers with extremely different chemical, thermal and mechanical properties. The properties of epoxy adhesives mainly depend on the hardener used. The rate of hardening of a thermosetting adhesive such as epoxy is strongly dependent on temperature. The reaction is slow in cold to moderate temperatures and faster in warm temperatures [5,6,11].

1.3 Applications of FRP Composites

The selection of FRP composite materials depends on the performance and intended use of the product. The composites designer can tailor the performance of the end product with proper selection of materials. It is important for the end-user to understand the application

environment, load performance, and durability requirements of the product, and convey this information to the composites industry professionals.

Fiber reinforced polymer (FRP) composites or advanced composite materials are very attractive for use in civil engineering applications due to their high strength-to-weight and stiffness-to-weight ratios, corrosion resistance, light weight, and potentially high durability. Their application is of most importance in the renewal of constructed facilities such as buildings, bridges, pipelines, etc. Recently, their use has increased in the rehabilitation of concrete structures, mainly due to their tailorable performance characteristics, ease of application and low life cycle costs [12,82].The application of FRP is divided roughly into two categories. The first category consists of rebar and grid type FRP (fiber reinforced polymer reinforcement) that are used in place of steel reinforcement. The second is fiber composite sheets that are used to repair and strengthen concrete or steel members. In both cases, FRP offers unique properties that steel reinforcements do not have, such as corrosion resistance, light weight, high strength, and non-magnetism. These properties help to give concrete structures new and better performance and make them easier to build [14].

1.4 FRPs Strengthening Systems

FRPs (or advanced fiber composites) have been successfully utilized over a long time by the aerospace and aircraft industries. Composites are currently gaining a rapid momentum in finding their way into civil engineering structural applications. The earliest reported application with plate bonding is from South Africa in the end of 1960s where a concrete beam in an office building was strengthened with steel plates [17]. Since then numerous strengthening applications have been reported, both with steel plates and in the last decade with various FRP systems. As compared with steel plates, FRP systems have more advantages. In addition to their resistance to

corrosion which allowing the possibility of extended service lives or perhaps limited required maintenance, FRP laminates and fabric come in great lengths, which can be cut to suitable sizes in the field. Also, the light weight of FRP provides considerable cost savings in terms of labor: a worker can handle the FRP material, whereas a crane would be required for its steel equivalent.

Structures designed by civil engineers are intended to have a long lifespan, and during that time there are numerous reasons make the structure may require strengthening or repair [8]. The most significant of these reasons includes:

- Environmental Exposure – Civil structures are exposed to changing environmental conditions throughout their lifetime. These factors can cause materials degradation over time or impart significant damage during one extreme event. The impacts of environmental degradation will be especially felt in cases where regular maintenance is not performed.
- Changing Usage – It is not uncommon for civil structures to outlive the purpose for which they were originally designed. Changes in tenancy or use may place different or large load demands on the structure
- Changing Design Standards – Even if the use of the structure is not significantly changed, the standards the structure must meet may change over time.
- Errors in Design or Construction - Civil structures may even require strengthening before they are ever use due to errors in initial design or construction.

Now many types of strengthening can be accomplished with FRPs [11,13]. FRP strengthening can be applied to mitigate several failure modes. For flexural strengthening of beams, slabs, or girders, FRP plates can be applied to the tensile face of the concrete [11,13]. Shear and torsion strengthening can be accomplished by placing FRP on the sides of beams [11]. Columns are typically strengthened by wrapping the FRP around the column in the hoop

direction, thus increasing the confinement of the concrete core [11,13]. This can be accomplished with wet lay-up or prefabricated cylindrical jackets.

1.4.1 Advantages Using FRPs in Civil Engineering

For years, civil engineers have been in search for alternatives to steel and alloys to combat the high costs of repair and maintenance of structures damaged by corrosion and heavy use. Since the 1940s, composite materials, formed by the combination of two or more distinct materials in a microscopic scale, have gained increasing popularity in the engineering field. Fiber reinforced polymer (FRP) has proven efficient and economical for the development and repair of new and deteriorating structures in civil engineering.

The unique properties of FRPs result in many advantage, including: handling and transportations, durability and maintenance, thin strip layers, time of construction, pre-stressing possibilities, and cost [11,18].

Handling and transportations: The composite materials used for strengthening are very light and easy to handle. In addition, no need for overlap plating is necessary. Also compared to traditional concrete overlays or shotcrete, much less material has to be transported to the job sites when FRPs strengthening are used [14].

Durability and maintenance: carbon fiber composite have especially good durability, long term fatigue properties, and they do not require maintenance over time.

Thin strip layers: FRPs are typically applied in thin strips, resulting in very little change in the structure profile, an important feature on bridges or other structures that require clearance for vehicles or machinery [12,13].

Time of construction: Time is always a critical factor in the construction industry. If construction time can be reduced, money can be saved. FRP strengthening can often be done during short

periods without closing the traffic or evacuate the buildings and the hardening of the bonding agents takes a short time (few hours).

Pre-stressing possibilities: During the last few years, products have been introduced to the market that FRP sheets can be pre-stressed in combination with bonding [13]. This gives high utilization of the strengthening product, at the same time reducing existing cracks, and increasing the yield load of existing steel reinforcement.

Cost: The total cost of a strengthening work with composites compared to traditional methods is often lower, even though the material costs are higher. This is because the FRPs materials have high strength and stiffness to weight ratio mean that a smaller weight of FRP needs to be applied. This low weight reduces transportation and installation costs [11].

1.4.2 Disadvantages Using FRPs in Civil Engineering

Despite their numerous advantages FRPs are not without drawbacks [11]. Unidirectional FRP materials are characterized by linear elastic behavior up to failure (see Fig. 1.2); this lack of yielding can result in less ductile structures unless this behavior is specifically considered at the design stage. These materials are very susceptible to damage from impact, fire, or vandalism, and as such need to be protected. Though FRPs do not exhibit corrosion, they are not immune to environmental impacts and do suffer degradation due to long term exposure to moisture and temperature. This disadvantage is of particular importance because there is currently little long-term information on the durability of composites in exposed hygrothermal environments. This research intends to fill the gap.

1.5 Objectives

The present investigation intends to study the effects of changing hygrothermal conditioning cycles (by changing either relative humidity while temperature is kept constant, or

by changing temperature while relative humidity is maintained constant) on the durability performance of FRP strengthened concrete beams and columns. The study will include the long term influence of moisture, high temperature, and combined hygrothermal conditions on the mechanical properties of FRPs composites and the bonding behavior between concrete and FRPs. The long term effect of the deteriorated composites on the structural behavior of bonded concrete beams and columns when subjected to realistic environmental conditions will be studied by analytical and finite element modeling. This research will also investigate the fracture behavior between concrete and external FRP strips under various hygrothermal conditions. The overall objectives are:

- Developing a durability test method of the bondline between the concrete and its FRP strengthening material at various temperature and humidity levels to evaluate long term performance of FRP bonded concrete beams and columns.
- Evaluating the cycling influence of temperature, moisture, and their combined effects (hygrothermal) on short and long term mechanical properties of the FRP composites.
- Investigating the effects of combined environmental loading and mechanical loading on the long-term mechanical properties of the FRP composites and the effect of deteriorated composites on the structural behavior of FRP bonded concrete beams and columns when subjected to realistic environmental conditions using finite element method.

CHAPTER 2 LITERATURE REVIEW

2.1 Durability Performance of Existing FRP Strengthened Structures

Installation of FRP plates includes two possibilities: pre-cured and cured-in-place laminates (manual lay-up). For the latter, a surface primer is often applied first to the concrete surface to fill up micro-cavities. After the primer is cured, a layer of putty is applied to level uneven spots and fill surface cavities. The recommended resin is then mixed and applied to the concrete surface in a thin uniform layer using a roller. A fiber sheet (pre-impregnated or dry) is cut to the desired length and width and pressed to the concrete using a "bubble roller". This act eliminates the entrapped air between the fibers and resin and ensures the full impregnation of the FRP sheet by the resin [19,20]. Attention should be paid to the alignment of the fiber orientation when installing the FRP sheet since a poor orientation of the fibers generally reduced the strength of the FRP [21]. While Pre-cured FRP systems consist of a wide variety of composite shapes manufactured in the system supplier's facility and shipped to the job site. Typically an adhesive is used to bond the pre-cured sheets or plates to the concrete surface or inserted into slots cut into the substrate. The system manufacturer must specify the adhesive used to bond the pre-cured system to the concrete surface [22].

Application of FRPs composites in civil/infrastructure engineering are diverse, including internal reinforcement, structural elements, and externally bonded reinforcement. The most popular forms of FRP internal reinforcement are smooth and deformed bars, prestressing tendons, and pre-cured and cured-in place laminates [19]. The externally reinforcement FRPs composites have been used to improve the performance of the structures include contract-critical applications, such as lateral confinements, of RC columns using hoop FRP wraps to increase both strength and ductility capacity, and contract-critical applications, such as flexural and shear

strengthening by bonding FRPs in various configurations to the exterior face of beams, columns and slabs [12].

Performance of FRP bonded structures is highly affected by the bond characteristics and the long-term performance is very sensitive to the process in which the material is stored, handled, installed, and cured. Surface FRP reinforcement requires a high level of process control. Performance of fiber reinforced polymer (FRP) composites in repair and retrofit of concrete structures depends on a great extent on the substrate condition to which they are bonded [23]. The bond between FRP and concrete is an important factor affecting the performance of the strengthening system. The effect of the surface roughness has been studied by several investigators [24]. Before applying the FRP system, the levelness of the concrete surface should be ensured. Previous research has indicated that concrete surface roughness is a key factor that can affect bond characteristics of epoxy with concrete [19]. Concrete surface is usually sandblasted prior to the installation of the FRP strengthening/repair system to remove dust, laitance, and other loose materials. Too smooth a surface may result in poor bonding. Too rough a surface will require the addition of putty filler under the epoxy. An optimal level of roughness will result in maximum bond strength while reducing the additional cost and effort of emplacing putty filler [19]. Low spots should be filled with the appropriate epoxy and high spots should be ground flat. If the FRP follows the contour of the irregular concrete surface, the curvature of the laminate may initiates pull-out forces [19].

Chajes et al. (1996) also studied the influence of surface preparation on the overall bond strength, and showed that the interfacial bond strength is increased using mechanical abrading. Sand blasting and chipping have also been considered as the most effective methods of surface preparation to increase the bond strength [24].

2.2 Environmental Factors on Composite Materials

Excellent mechanical properties have promoted the use of FRPs for structural applications [34]. In particular, repair and upgrade using FRP bonded sheets and laminates have gained acceptability in the United States construction market. They have been used to retrofit parking garages, marine and industrial structures [24,25].

Carbon fiber reinforced polymer (CFRP) materials have higher stiffness and enhanced durability characteristics compared to other fiber composites and have been frequently used for applications in concrete [26]. Some difficulties still exist during the field applications, which are related to ambient temperature, relative humidity, or combined factors. All the said factors affect the short-term and long-term bonding between the concrete structure and the FRP material to various degrees [15].

Recently, glass fiber reinforced polymers (GFRP) are being increasingly used in construction applications because of a number of advantages of glass fibers, such as relatively low costs and large elongations (3-4.5%) [27,28,29]. Pultruded GFRP is suitable for construction applications because it is possible to form long parts in various cross sections at relatively low cost.

Haque et al. (1991) [30] have shown that the degradation of GFRP in strength at temperatures below 100 degrees Celsius (212 degrees Fahrenheit) is negligible, and that moisture degradation is less severe than temperature degradation. Other researchers have supported this with experiments showing that carbon/epoxy composites at 50 degrees Celsius (106 degrees Fahrenheit) and at 95 percent relative humidity show almost no degradation in mechanical properties (Birger et al. 1989) [31].

In 2003, Mavalar et al. [26] studied the short-term effects of temperature, moisture, and chloride content on the CFRP adhesion using pull-off tests. As a result of their study, they found that the bond strength decreased significantly at high temperatures and humidities. A maximum allowable humidity of 85% RH for adhesive seems appropriate. They found that 35^{o}C (or 95^{o}F) and 95% relative humidity can reduce the bond strength to just above the minimum ACI 440 proposed requirement of 1.38MPa (200psi), but below the Navy's requirement of 2.07MPa (300psi). Tests on dollies bonded to mortar cubes indicated that, in several cases, bond strength would decrease significantly at high temperatures and RH. Out of 216 tests were done, 35 did not meet the Navy's requirement, and 15 would not meet the ACI 440 requirement. Most of these failures also occurred at a high temperature (38^{o}C or 100^{o}F) and RH (95%) [15].

2.2.1 Thermal Effect on FRP Composite

During the past several years, a relatively large body of research has been directed toward better understanding of the behavior of civil infrastructures employing Fiber Reinforced Polymer (FRP) composites, and for development of design guidelines. Nevertheless, these studies have generally ignored or marginally evaluated the reaction of structural systems using FRP to the environments, most importantly temperature changes, to which civil engineering structures is subjected [27,32]. Using an extensive array of instruments and field as well as laboratory tests, the short-term and long-term performances of four types of FRP composite bridge decks were recently evaluated [11]. The coefficient of thermal expansion and the level of temperature gradient were found to be higher than those of standard reinforced concrete decks [7]. Lack of attention to detailing and thermal characteristics of individual components as well as the entire FRP deck system can lead to build up of large thermal stresses, which can result in unexpected deformations and damage. To ensure satisfactory performance, thermal behavior and the

resulting thermal stresses need to be incorporated into design and detailing of panel-girder connections, field joints, and face sheet-core connection in sandwich type panels [33].

Temperature variation can effect composite behavior as a result of thermal expansion mismatch (for instance between the fiber and matrix or between the plies of different orientation); the level of residual stress will depend on temperature variations [34].

Extensive research works have been carried out on the behavior of FRP reinforced concrete elements subject to various types of mechanical loads; however much less attention has been given to the behavior of these elements under thermal loading.

Masmoudi et al. [35] have presented the results of an experimental investigation on the effect of the ratio of concrete cover thickness to FRP bar diameter (c/d_b) on the strain distributions in the concrete and the FRP bars, using concrete cylindrical specimens reinforced with a glass FRP bar and subjected to thermal loading from -30 to +80^{o}C. The experimental results show that the transverse coefficient of thermal expansion of the glass FRP bars tested in their study is found to be equal $33x10^{-6}$ mm/mm/^{o} C, on average, the ratio between the transverse and longitudinal coefficients of thermal expansion of these FRP bars is equal to 4. Also, the cracks induced by high temperature start to develop on the surface of concrete cylinders at a temperature varying between +50 and +60^{o}C for specimens having a ratio of concrete cover thickness to bar diameter c/d_b less than or equal to 1.5. A ratio of concrete cover thickness to glass fiber reinforced polymers (GFRP) bar diameter c/db greater than or equal to 2.0 is sufficient to avoid cracking of concrete under high temperature up to +80^{o}C. The results obtained from their analytical model of study were in good agreement with the experimental results, particularly for negative temperature variation. However, for positive temperature variations, the model does not represent the actual thermal behavior of the concrete cylinders concentrically

reinforced with FRP bar. The difference at high temperature variations was due to the concrete cracking which was not considered in the linear-elastic analytical model. Also; they found that the ratio of concrete cover thickness to GFRP bar diameter c/d_b greater than or equal 1.9 seems to be sufficient to avoid cracking of concrete under high temperature up to +80^{o}C for these material tested. Moreover; the thermal expansion behavior of glass FRP bars can be considered linear for the temperature range of -30 – 80^{o}C. In general; Table 2.1 shows the typical coefficient of thermal expansion of reinforcing bars.

Table 2.1: Typical coefficient of thermal expansion for reinforcing bars [16]

Direction	CTE, x 10^{-6}/C			
	Steel	GFRP	CFRP	AFRP
Longitudinal, α_L	11.7	6.0 to 10	-9 to 0.0	-6.0 to -2.0
Transverse, α_L	11.7	21.0 to 23.0	74.0 to 104.0	60.0 to 80.0

Tadeu *et al*. [36] performed several double-lap shear tests on concrete specimens externally bonded with steel plates. The authors noted a significant reduction of the failure load by increasing the temperature and reported failures in the adhesive for temperatures higher than 30 ºC. This is very likely due to the fact that the adhesive used had a low *Tg*.

Di Tommaso et al. [37] investigated the influence of temperature in three point bending tests at temperatures ranging from -100°C up to 40°C. Relative to the failure load at room temperature, decreasing failure loads were found both for increasing and decreasing temperatures (Figure 2.1). Furthermore, different types of failure were found depending on the applied temperature. For high temperature (40°C), cohesive failure of the adhesive was found (figure 2.2a). For moderate temperatures failure of the concrete was found near the interface with the adhesive (figure 2.2b), while for very low temperatures (-100°C) delamination within the CFRP

was found (figure 2.2c). The first two types of failure were similar to those observed in the double-lap shear tests.

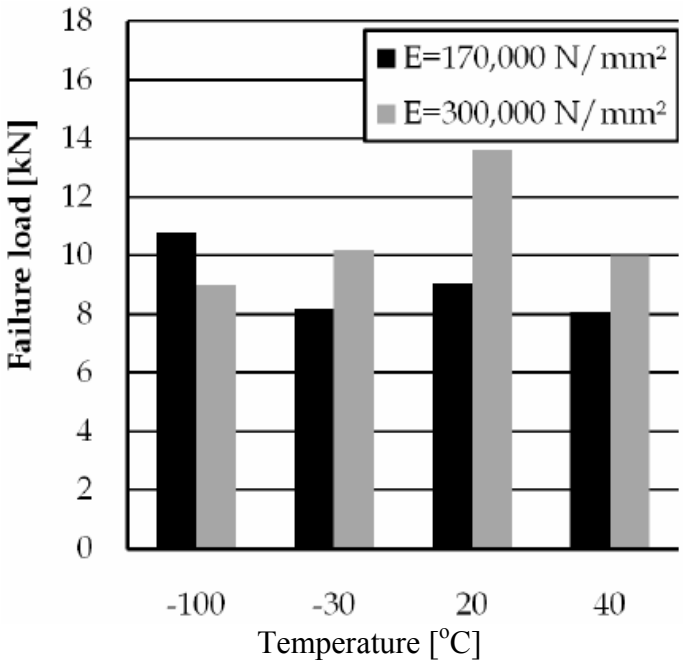

Figure 2.1: Temperature-failure load relation of flexural tests by Di Tommaso et al. [37]

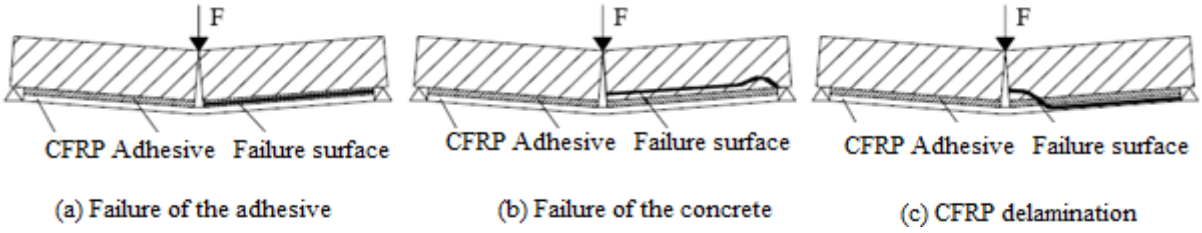

Figure 2.2: Failure of the three point bending tests at different temperatures [37]

In 2006 the influence of temperature on small scale three point bending tests was investigated by *Klamer et al*. [38]. In these tests, an increasing failure load was found with increasing temperatures, until around the glass transition temperature of the adhesive (62°C) (Figure 4.3). For higher temperatures, a decreasing failure load was found due to the changed type of failure. Failure changed above the glass transition temperature from failure in the

concrete near the interface with the adhesive to failure exactly in the interface in between the concrete and the adhesive.

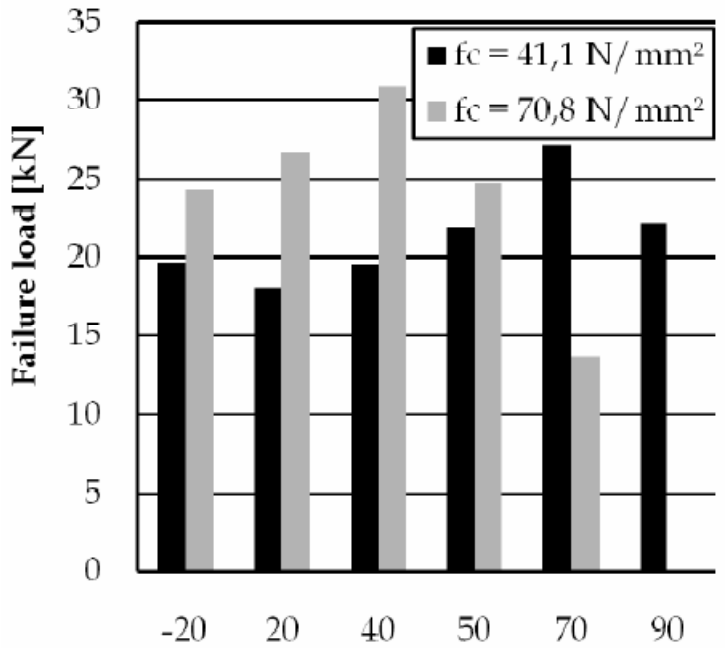

Figure 2.3: Temperature-Failure load relation of flexural tests [38]

2.2.2 Moisture Effect on FRP Composite

Externally bonded fiber reinforced polymers (FRP) composite materials have been successfully used for strengthening/repairing concrete structures. Numerous experimental studies on bond durability show that moisture plays an important role in the durability of the bond between fiber-reinforced polymer (FRP) and concrete [39,40]. The durability of FRP bonded concrete structure in moist environments is largely controlled by the rate at which water and the deleterious ions that use water as a carrier move through the system. The knowledge of moisture transport in the FRP bonded concrete structures is very important since the bond interface between concrete substrate and adhesive layer is susceptible to damage due to the presence of

moisture. Therefore, a fundamental understanding of the moisture transport in the FRP-adhesive-concrete system is needed to quantify the effect of moisture on bond performance [41,42].

Many research studies have been conducted to model the moisture diffusion in porous materials, composite, and polymer [41]. However, very few works have focused on the moisture transportation in multilayered structures containing FRP composites, polymer adhesive, and concrete [43].

Ouyang et al. [41] modeled moisture transportation in the FRP strengthened concrete specimens by using relative humidity as a global variable. They derived a moisture diffusion governing equation for a multilayered composite. Based on their experimental and numerical results, they concluded that moisture accumulated at the interface mainly came from the bond free area close to the FRP and the sides of the concrete specimen. A highly uneven moisture distribution along the adhesive thickness was found, especially in the case of a relatively short period of exposure. Also, they concluded that the higher environmental relative humidity (RH) increased not only the interface region relative humidity (IRRH) at the given exposure time, but also the wetting speed.

In 2002, Nishizaki *et al*. [44] carried out a study on the long-term deterioration of GFRP composites in a water and moisture environment. The main findings of their study are cracks emerged on the surface of the GFRP specimens and the weight of the specimens decreased during the deterioration test which may be attributed to the surface treatment oil for the glass-fiber cloth being dissolved away. The bending strengths of the GFRP specimens dropped compared to the initial bending strength values. Specimens immersed in 60^{o}C exhibited faster weight-reduction rates and greater declines in bending strength compared to the specimens conditioned at atmosphere at 60^{o}C or an immersion in 40^{o}C. They proposed that these

differences were due to debonding between the glass fiber and the matrix resin that occurred in the immersion at the 60^{o}C condition.

2.2.3 Hygrothermal Effect on FRP Composite

The effect of a hygrothermal environment on the performance of composites has been the subject of numerous investigations. In polymer-matrix composites, the effects of a hygrothermal environment are primarily observed in the matrix properties. Composites strength is closely related to the strength and orientations of the fibers. Nevertheless, matrix properties have a fundamental effect on damage resistance and durability. Matrix properties are a deciding factor with respect to the location and nature of damage initiation, damage growth, and subsequent damage progression. For most composite structures, initial damage occurs in the matrix material as transverse tensile failure or shear failure depending on geometry and loading [45].

Experimental and numerical studies on the effects of hygrothermal conditions on the flexural and interlaminar strength and the defect growth in composites have been reported [46]. In 2002, Patel and Case [47] studied the durability of hygrothermally aged graphite/epoxy woven composite under combined hygrothermal conditions. The hygrothermal aging consisted of cyclical temperature and moisture variations which were meant to simulate mission conditions for an advanced subsonic aircraft. Durability studies were carried out on the aged material system in the form of fatigue and residual strength testing under humid and elevated temperature environments. Damage mechanisms and failure modes were determined through fatigue testing, residual strength testing, and nondestructive evaluation. The experimental design of the study was established for the purpose of determining the effects of temperature and moisture (individually and alternatively) on the residual strength and durability of the aged material

system. The durability was measured by their fatigue life and damage progression. The temperature and moisture conditions used were as follows:

1. Room temperature (to provide baseline behavior).
2. Elevated temperature (120 °C, engine operating condition).
3. Wet (saturated and then tested at 85% RH at 30 °C, storage condition).
4. Hygrothermal cycling—alternation between temperature and humidity conditions during fatigue.

As a result of their experimental testing, they found that the initial and residual tensile properties of the aged material were virtually unaffected by the imposed aging (as compared to unaged material testing results), except when at elevated temperature. At elevated temperature, both the dynamic and static stiffness and residual strength were noticeably lower than those of room temperature.

2.3 Finite Element Modeling

Finite element method is a powerful alternative approach to solving the governing equations of structural problems. This method consists of envisioning the structure to be composed of discrete parts (i.e. finite elements), which are then assembled in such a way as to represent the distortion of the structure under the specified loads. Each element has an assumed displacement field, and part of the skill of applying the method is in selecting appropriate elements of the correct size and distributions (The FE "mesh"). FEM is useful because that an analytical solution is only available for a simple structure subject to a simple loading.

2.3.1 Finite Element Modeling of FRP Laminate

Thin sheet constructions, known as laminates, are an important class of composite. They are made by stacking together, usually, unidirectional layers (also called plies or laminate) in

predetermined directions and thicknesses to give the desired stiffness and strength properties. Such constructions are frequently encountered. The skins of aero plane wings and tails, the hull sides and decking of ships, the sides and bottom of water tanks are typically examples. Even cylindrical components, such as filament wound tanks, can be treated as laminates, provided the radius-to–thickness ratio is sufficiently large (say>50). Laminates typically consist of between 4 and 40 plies, and each ply is around 0.125mm thick if it is carbon or glass fiber/epoxy. Typical lay-ups (the arrangement of fiber orientations) are cross-ply, angle ply and quasi-isotropic. When making a laminate one must decide on the order in which the plies are placed through the thickness (known as the stacking sequence). This has an important influence on the flexural performance of the laminate. There is an established convention for denoting both the lay-up and stacking sequence of a laminate. Thus, a cross-ply laminate which has ply fiber orientations in the sequence 0^o,90^o,0^o from the upper to the lower surface, would be denoted $(0/90^o)_s$. the suffix 'S' means that the stacking sequence is symmetric about the mid –thickness of the laminate. Laminates denoted by $(0/45/90^o)_s$ and $(45/90/0^o)_s$ have the same lay-up but different stacking sequences [13].

For a laminated construction interface shears are referred to as interlaminar shear stresses; they can give rise to interlaminar failure, or delamination. A three-point flexure test on a short beam (span-to-depth=5) is a common way to determine the interlaminar shear strength of unidirectional composites [1,13].

2.3.2 Finite Element Modeling of Composite

The finite element method was initially developed for isotropic materials. One obvious difference between isotropic material and composites is the fibrous nature of the composites. The fiber direction has to be specified in the input to the finite element package. Most composite

structures are made by laying up plies of material with the fibers having different directions in each ply. A laminate composite material differs from an isotropic in two ways: it is a layered material built up from stacked plies of material, and, in addition each ply is not isotropic but has directional properties with a higher stiffness in the directions of the fibers, which can change from ply to ply. Composites should mean a combined plate of laminate and other materials such as lightweight core. In most lay-ups the thickness is small compared with the other dimensions of the material so that it forms a plate type structure, and this is used to simplify the description. It is assumed that the strains through the thickness of the plate vary linearly in the local through-thickness (z) direction. Since the material properties vary from layer to layer, the stress variation through the thickness of the composite is much more complicated than that of the strains. In general there will be discontinues changes of stress from ply to ply. This means that a simple material stiffness cannot be used for a laminated material. Instead laminate theory is employed. The stresses are integrated through the thickness of the plate. The average values of the stress give the in-plane loads N and the linear variation gives the couples M. The end loads and moments are shown in Figure (2.4). Using the elasticity properties of each ply, rotated to the propitiateiber directions, the end loads and moments can be related to the mid-plane strains ε^o and curvatures κ to give the laminate stiffness properties as

$$\begin{bmatrix} N \\ M \end{bmatrix} = \begin{bmatrix} A & B \\ B & D \end{bmatrix} \begin{bmatrix} \varepsilon^o \\ k \end{bmatrix}$$

Where A are in-plane stiffness propitiates, D are the bending stiffness propitiates, and B is the coupling that arises between the bending and membrane actions.

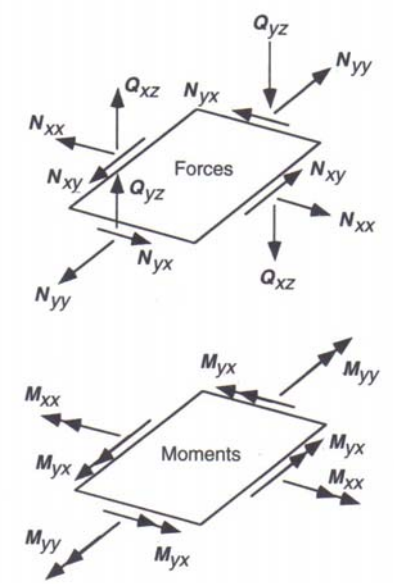

Figure 2.4: Mid-plane forces and moments [13]

2.3.3 Finite Element Modeling of FRP Strengthened Beams/Columns

Use of fiber reinforced plastic (FRP) composites for strengthening of beams and columns in RC structures has attracted great attention in recent decades [48]. However, less attention has been paid to strengthening RC connections with FRP laminates.

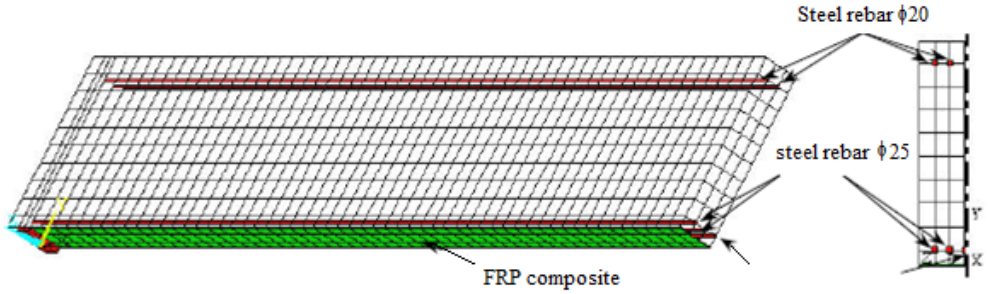

Figure 2.5: Finite element model of the reinforced concrete beam strengthened with FRP laminate [49]

A finite element (FE) model has been proposed by Mostofinejad et al. [48] for the non-linear analysis of RC joints covered with FRP overlays. The model consists of the effects of anchorage slip and anchorage extension of the steel reinforcement in the connection zone. To validate this FE model, some available experimental works were simulated by the model and

also non-linearly analyzed using ANSYS. The results showed that the model can predict the experimental works with good accuracy. At the end and as a case study, a base joint specimen was strengthened with FRP laminates in 7 different cases and all the beam specimens were analyzed using the aforementioned FE modeling. The results showed that good ductility and strength enhancement could be achieved by employing correctly configured FRP laminates.

In 2004 Supaviriyakit et al. [22] presented a non-linear finite element analysis of reinforced concrete beam strengthened with externally bonded FRP plates. The finite element modeling of FRP-strengthened beams was demonstrated. Concrete and reinforcing bars were modeled together as 8-node isoparametric 2D RC element. The FRP plate was modeled as 8-node isoparametric 2D elastic element. The glue was modeled as a perfectly compatibable element by directly connecting the nodes of the FRP with those of the concrete since there is no failure at the glue layer. The key to the analysis was the correct material models of concrete, steel and FRP. Cracks and steel bars were modeled as smeared over the entire element. Stress-strain properties of cracked concrete consist of tensile stress model normal to crack, compressive stress model parallel to crack and shear stress model tangential to crack. Stress-strain property of steel reinforcement is assumed to be elastic-hardening to account for the bond between concrete and steel bars. FRP is modeled as elastic-brittle material. From the analysis, it was found that FEM can predict the load-displacement relation, ultimate load and failure mode of the beam correctly. It can also capture the cracking process for both shear-flexural peeling and end peeling modes similar to the experimental observations [22].

In 2006, Kishi et al. [50] developed a numerical analysis method by using a three-dimensional elasto-plastic finite element method to simulate the load-carrying capacity of FRP bonded RC beams, which failed in the FRP sheet peel off mode. The discrete crack approach was

employed to consider geometrical discontinuities such as opening of cracks, slipping of rebar, and debonding of the FRP sheet.

Comparisons between analytical and experimental results confirm that the proposed numerical analysis method is appropriate for estimating the load-carrying capacity and failure behavior of RC beams flexurally reinforced with a FRP sheet. In their study, One quarter of each RC beam was three dimensionally modeled for numerical analysis with respect to the two symmetrical axes. Figure 2.6 shows the mesh geometry of one beam as an example. In this model, axial rebar and FRP sheet were modeled using eight-node solid elements and concrete was modeled using eight-node and/or six-node solid elements. Stirrups were modeled using embedded reinforcement elements (DIANA 2000) assuming a perfect bond between the stirrup and concrete. In this study, to limit the stress concentration occurring in the concrete elements around the loading and the supporting points, elastic steel plates 50-75-20 mm in dimension were introduced into the numerical analysis and were modeled using eight-node solid elements.

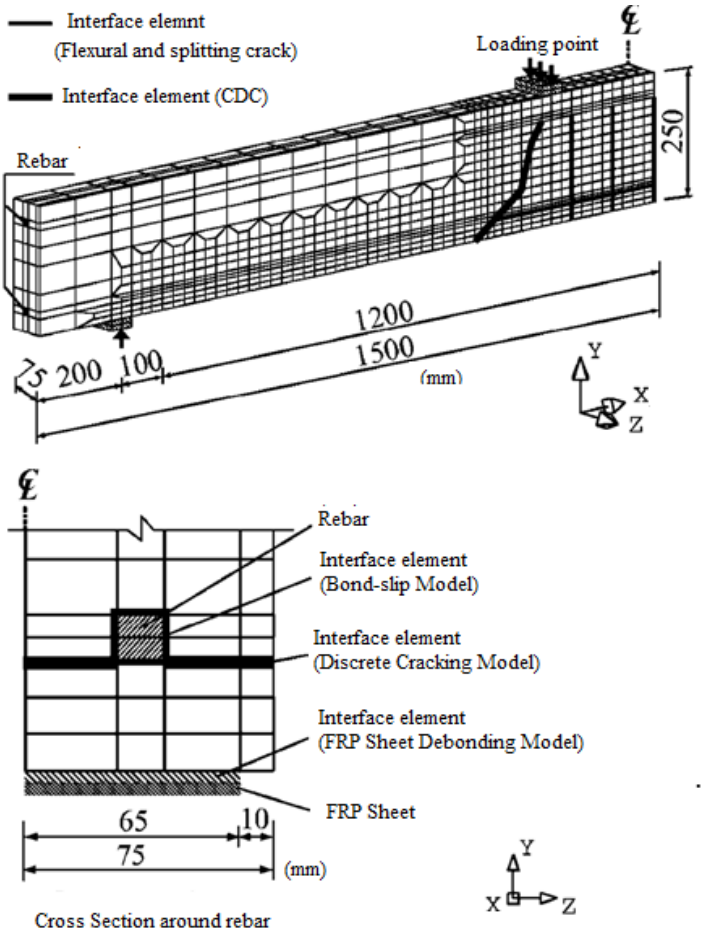

Figure 2.6: Finite element analysis model for the beam [50]

In 2007 Lu at al. [51] discussed the intermediate crack (IC) debonding in FRP-strengthened RC beams using FE Analysis and Strength Model. In their paper, they first presents a finite-element (FE) model based on the smeared crack approach for concrete for the numerical simulation of the IC debonding process. Lu's finite-element model included two novel features: (1) the interfacial behavior within the major flexural crack zone is differentiated from that outside this zone and (2) the effect of local slip concentrations near a flexural crack is captured using a dual local debonding criterion. As a result of their study they found that the FE model was shown to be accurate through comparisons with the results of 42 beam tests. The paper also presented an accurate and simplified strength model based on interfacial shear stress distributions

from finite-element analyses. The new strength model was shown to be accurate through comparisons with the test results of 77 beams, including the 42 beams used in verifying the FE model, and was suitable for direct use in design.

In 2008, a numerical analysis using an incremental nonlinear displacement-controlled 3D finite-element "FE" model was developed by Kotynia et al. [52] to investigate the flexural and CFRP/concrete interfacial responses of the tested beams. The finite-element model accounts for the orthotropic behavior of the CFRP laminates. An appropriate bond-slip model was adopted to characterize the behavior of the CFRP/concrete interface. Comparisons between the FE predictions and experimental results show very good agreements in terms of the load-deflection and load-strain relationships, ultimate capacities, and failure modes of the beams [53].

A 3D displacement-controlled nonlinear finite-element analysis of the FRP-strengthened beams of the above experimental investigation was carried out using the finite-element package (ADINA 2004a). Interface elements between the CFRP and concrete that accommodate a nonlinear bond stress-slip law were used to simulate the interface. The formulations for the concrete, steel, and FRP of this software package were employed in their analysis. To represent the concrete, eight-node 3D brick elements with three degrees of freedom at each node and eight integration points per element were used. The steel reinforcement was modeled using two-node truss elements with three translational degrees of freedom at each node. Four-node thin membrane elements, with three translational degrees of freedom at each node, were used for the CFRP sheets and laminates. The nodes of the CFRP elements were connected to those of the concrete elements through interface elements. These elements were aligned in the direction of the fiber, i.e., in the longitudinal beam direction in the case of bottom CFRP laminates and in the vertical direction of the beam for the case of spaced L-shaped laminates or continuous U-shaped

sheets with the fiber orientation being perpendicular to the beam direction. When using continuous U-shaped sheets with the fiber orientation parallel to the beam direction, the interface elements are aligned in both the directions. The constitutive relationship for the interface elements was based on the above bond-slip model. Due to the geometrical and loading symmetries, only one-quarter of each beam was analyzed. The total element sizes of the concrete were selected to be 50 mm^3, except for the part of the concrete beam between the longitudinal tensile steel bars and the CFRP laminates, the element sizes were taken as small as 12.5 mm^3 to allow for finer meshing at the FRP/concrete interface. [53]. The results showed that the finite element model predicted the ultimate load carrying capacities of the various FRP strengthened beams with an average numerical to experimental ratio and standard deviation of 0.998 and 0.0276 respectively. As far as the CFRP strains at the ultimate loads were concerned, the average numerical-to-experimental ratio and its corresponding standard deviation were 1.096 and 0.147, respectively. For all of the specimens, the finite-element analysis was capable of predicting the experimentally observed CFRP debonding mode of failure intermediate crack debonding.

2.4 Conclusion

Although the influence of temperature, moisture, and temperature and moisture combined (i.e. hygrothermal) on concrete and FRP composite have been studied in several researches, it appears that the research on durability of FRP strengthened beams and columns so far doesn't correlate with long term performance of FRP strengthened concrete beams and columns subjected to both hygrothermal environmental and mechanical loading. Also, all the previous durability studies mainly focused on the FRP material level. On the other hand, most of the existing FE studies focused on the short-term performance of FRP bonded concrete structures.

Very few studies have investigated the influence of hygrothermal environments and mechanical loading on the long-term durability performance of bonded concrete structures. The target environments must be able to represent natural weathering conditions. The long-term performance of FRP composite materials should be obtained through laboratory testing in various simulated environments. Such degradation rates of the FRP materials and the bond properties should be used in the analytical and FE modeling for the predictions of long term performance. Results of the laboratory tests shall be correlated with results of are obtained from finite element modeling and analytical solutions.

The goal of this study is to construct a comprehensive framework including durability experiments and modeling (both analytical and numerical based). This framework is able to assist in rational designs of FRP bonded concrete structures subjected to hygrothermal environments and mechanical loading, and warrant a satisfactory long term performance.

CHAPTER 3 EXPERIMENTAL PROGRAM

3.1 Concrete Material Properties

All concrete specimens, beams and cylinders, were made of Type I Portland cement, 1/2" Limestone, 3/8″ P-Stone course aggregate, and 2NS-Sand as shown in Figure 3.1.

a) Lime-stone coarse aggregate

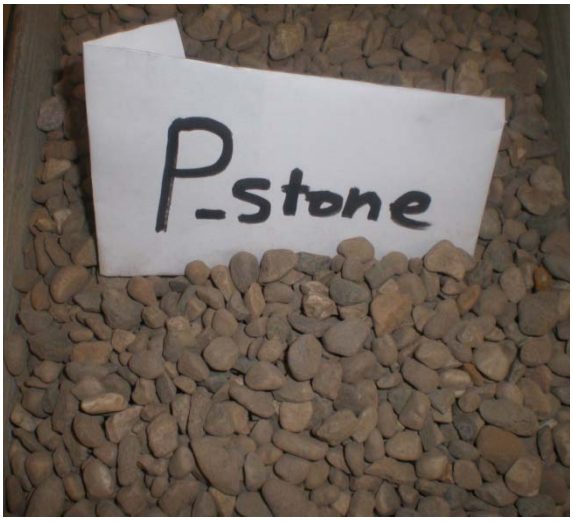

b) P-stone coarse aggregate

c) 2NS-sand fine aggregate

Figure 3.1: Concrete aggregate materials

3.1.1 Sieve Analysis Test

Sieve analysis, commonly known as the "gradation test" is a basic essential test for both fine and course aggregate. The sieve analysis determines the gradation (the distribution of aggregate particles, by size, within a given sample) in order to determine compliance with design, production control requirements, and verification specifications. The gradation data can be used to calculate relationships between various aggregate or aggregate blends, to check compliance with such blends, and to predict trends during production by plotting gradation curves graphically and compared with the specifications.

In general, the sieve analysis test can be done by following these procedures: weigh a certain weight of a dry sample, a set of sieves should be arranged in order (the top sieve has the largest screen openings and the screen opening sizes decrease with each sieve down to the bottom sieve which has the smallest opening size screen for the type of material specified), the sample is put in the upper sieve, and then shaken by mechanical means for a period of time (about 10 minutes). After shaking the material through the nested sieves, the material retained on each of the sieves is weighed using one of two methods.

The cumulative method requires that each sieve beginning at the top be placed in a previously weighed pan (known as the tare weight) and be weighed. Then the next sieve's contents are added to the pan, and the total is weighed. This is repeated until all sieves and the bottom pan have been added and weighed.

The second method requires the contents of each sieve and the bottom pan to be weighed individually. Either method is satisfactory to use and should result in the same answer. The amount passing the sieve is then calculated.

In this research, sieve analysis test has been done for both fine and course aggregates by using the second method according to ASTM C33-08 [67], and ASTM E11-08 [68] standard limitation. Figure 3.2 shows a mechanical testing sieve shaker.

Figure 3.2: Testing sieve mechanical shaker (model # B)

a) Sieve analysis for fine aggregate "2NS-sand"

The total weight of the sample was 500g, and the test result is shown in Table 3.1.

Table 3.1: Sieve analysis results for fine aggregate"2NS-sand"

Sieve size (mm)	Weight of remaining (g)	Wt. of remaining Cumulative (g)	Remaining %	Passing %	ASTM Standard limitation C33-08, %
2.36	96.0	96.0	19.4	80.6	80-100
1.18	75.1	171.1	34.6	65.4	50-85
600 µm	95.8	266.9	53.9	46.1	25-60
300 µm	158.5	425.4	86.0	14.0	5-30
150 µm	62.2	487.6	98.54	1.46	0-10
Pan	7.2	494.8	100	0.00	

Based on the above data, the sieve analysis for this sand sample of fine aggregate "2NS-sand" is within the ASTM standard limitation. Therefore, this sand had been used in the concrete mix for all this research work. Figure 3.3 shows the curve test result.

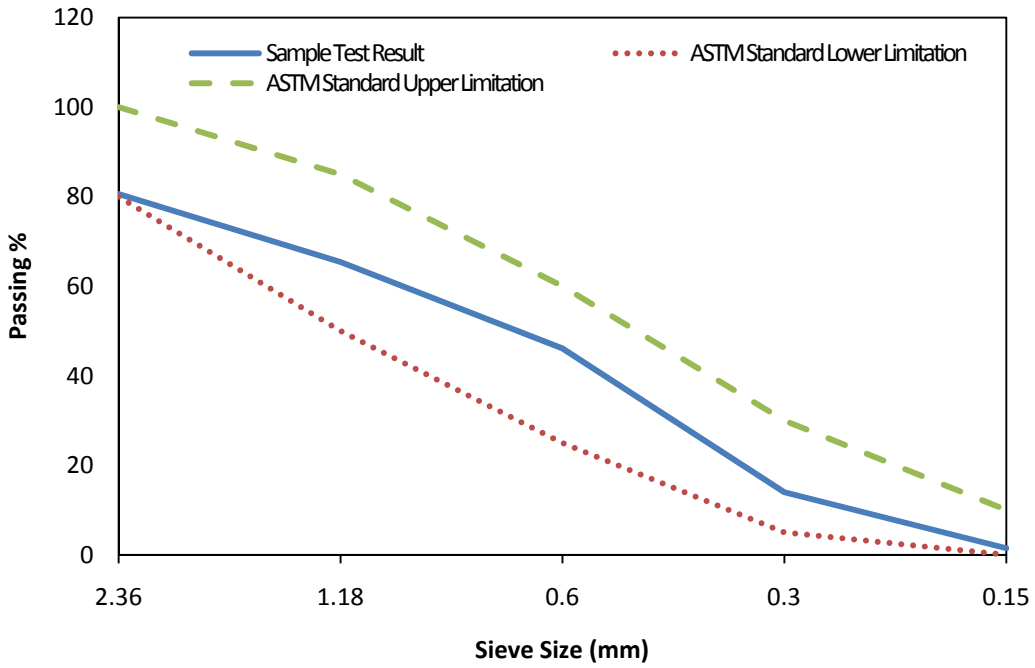

Figure 3.3: Sieve analysis test curve for fine aggregate "2NS-sand"

b) Sieve analysis for Course aggregate

Several samples of course aggregates had been acquired, tested, and compared with the ASTM standard limitation. Also, hybrid mixing of the two types of aggregates at different ratios were performed till an optimum ratio was found, which gave a gradation curve conformed to the ASTM standard (C33-08). The results are shown in Tables (3.2, 3.3, and 3.4) and Figures (3.4, 3.5, and 3.6).

Table 3.2: Sieve analysis for the course aggregate "P-stone" sample weight =3000g.

Sieve size (mm)	Weight of remaining (g)	Wt. of remaining Cumulative (g)	Remaining %	Passing %	ASTM Standard limitation C33-08 %
19	0.0	0.0	0.0	100.0	100.
12.5	0.0	0.0	0.0	100.0	90-100
9.5	242.3	242.3	8.08	91.92	40-70
4.75	2501.8	2744.1	91.47	8.53	0-15
2.36	202.4	2946.5	98.21	1.79	0-5
Pan	53.5	3000.0	100.0	0.0	

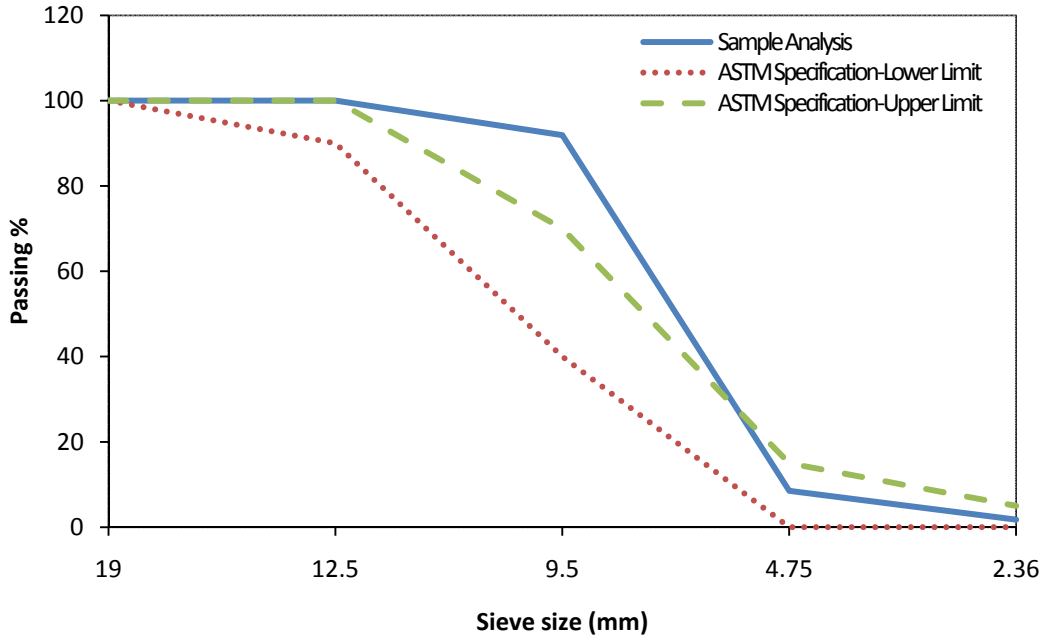

Figure 3.4: Sieve analysis test curve for coarse aggregate "P-Stone"

According to the above test results, this aggregate sample is out of specification due to excessive passing ratio of sieve 9.5mm size.

Table3.3: Sieve analysis for the course aggregate crushed stone "Lime-Stone" Sample weight =3000g.

Sieve size (mm)	Weight of remaining (g)	Wt. of remaining Cumulative (g)	Remaining %	Passing %	ASTM Standard limitation C33-08 %
19	0.0	0.0	0.0	100.0	100
12.5	66.4	66.4	2.21	97.79	90-100
9.5	2110.0	2176.4	72.56	27.44	40-70
4.75	803.1	2979.5	99.34	0.66	0-15
2.36	6.1	2985.6	99.54	0.46	0-5
Pan	13.8	2999.4	100.0	0.0	

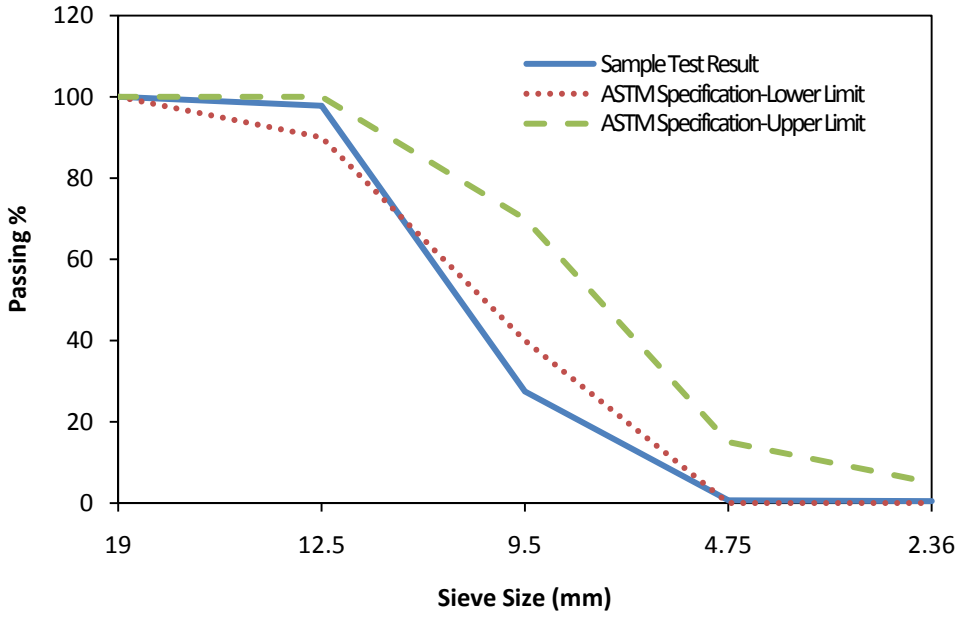

Figure 3.5: Sieve analysis test curve for coarse aggregate "Lime-Stone

Table 3.3 and figure 3.5 show that the sieve analysis test results of that sample is out of specification as well due to a low passing ratio of sieve 9.5mm size. Therefore, those two course aggregate samples had been mixed together by using trial and error method. Several trials had been done until an optimum ratio was found. The resulting curve fit within the ASTM standard limits. The optimum ratio of the P-stone sample to the lime stone sample was 1:1. Table 3.4 and figure 3.6 show the sieve analysis results of the hybrid sample.

Table 3.4: Sieve analysis test results for the mixing sample, sample weight =3000g.

Sieve size (mm)	Weight of remaining (g)	Wt. of remaining Cumulative (g)	Remaining %	Passing %	ASTM Standard limitation C33-08 %
19	0.0	0.0	0.0	100.0	100
12.5	137.95	137.95	4.60	95.4	90-100
9.5	985.55	1123.5	37.46	62.54	40-70
4.75	1733.9	2857.4	95.28	4.72	0-15
2.36	106.7	2964.1	98.84	1.16	0-5
Pan	34.8	2998.9	100.0	0.0	

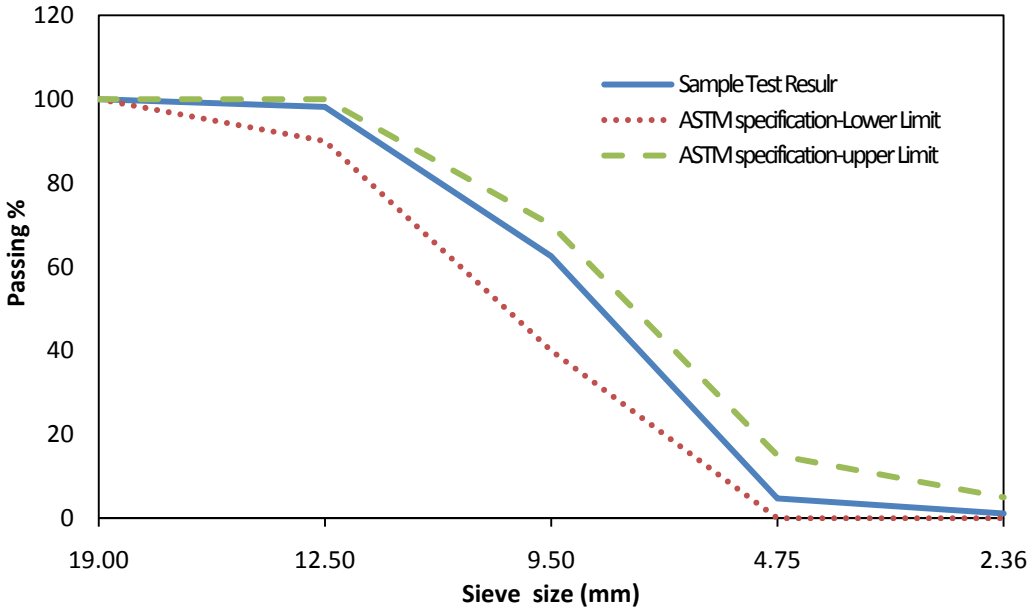

Figure 3.6: Sieve analysis for course aggregate "hybrid sample"

From Table 3.4 and Figure 3.6, the above mixed sample is appropriate per the ASTM standard. Therefore, the 1:1 ratio is used throughout this study.

3.1.2 Concrete Mix Design

A medium degree of workability was chosen, the water cement ratio (w/c) was assumed as equal to 0.53, ρ_c=3.12, ρ_a=2.6, and ρ_w=1.0, where ρ_c, ρ_a, and ρ_w are the specific gravities of cement, aggregate, and water respectively. The density of water =1000 kg/m^3.

From Table 3.5, the aggregate to cement ratio, A/C, could be found by interpolation.

Table 3.5: Aggregate cement ratio (by weight) for irregular aggregate [85]

Degree of Workability																
W/C %	Very low				Low				Medium				High			
	1	2	3	4	1	2	3	4	1	2	3	4	1	2	3	4
0.35	3.7	3.7	3.5	3.0	3.0	3.0	3.0	2.7	2.6	2.6	2.7	2.4	2.4	2.5	2.5	2.2
0.40	4.8	4.7	4.7	4.0	3.9	3.9	3.8	3.5	3.3	3.4	3.5	3.2	3.1	3.2	3.2	2.9
0.45	6.0	5.8	6.7	5.0	4.8	4.8	4.6	4.3	4.0	4.1	4.2	3.9	x	3.9	3.9	3.5
0.50	7.2	6.8	6.5	5.9	5.5	5.5	5.4	5.0	4.6	**4.8**	4.8	4.5	x	4.4	4.4	4.1
0.55	8.3	7.8	7.3	6.7	6.2	6.2	6.0	5.7	x	**5.4**	5.4	5.1	x	4.8	4.9	4.7
0.60	9.4	8.6	8.0	7.4	6.8	6.9	6.7	6.2	x	6.0	6.0	5.6	x	x	5.4	5.2
0.65	-	-	-	8.0	7.4	7.5	7.3	6.8	x	x	6.4	6.1	x	x	5.8	5.6
0.70	-	-	-	-	8.0	8.0	7.7	7.4	x	x	6.8	6.6	x	x	6.2	6.1
0.75					-	-	-	7.9	x	x	7.2	7.0	x	x	6.2	6.5
0.80					-	-	-	-	x	x	7.5	7.4	x	x	x	7.0
0.85									x	x	7.8	7.8	x	x	x	7.4
0.90									x	x	x	8.1	x	x	x	7.7
0.95									x	x	x	-	x	x	x	8.0
1.00													x	x	x	x

- Indicates that the mix was outside the range tested.
x Indicates that the mix would segregate.
These proportions are based on specific gravities of approximately 2.5 for the course aggregate and 2.6 for the fine aggregate.

$$\frac{0.5}{4.8} = \frac{0.55}{5.4} = \frac{0.53}{x}$$

So, x =5.16, where x represents the aggregate to cement ratio, A/C.

From the sieve analysis results, the maximum size of coarse aggregate was found to be 12.5mm.

The concrete mix design equation is given by:

$$\frac{W}{1000\rho_w} + \frac{A}{1000\rho_a} + \frac{C}{1000\rho_c} = 1.0 \tag{3.1}$$

Where:

W, A, C, represent water, aggregate, and cement respectively.

$$W = C \times W/C \tag{3.2}$$

$$A = C \times A/C \tag{3.3}$$

By Substituting of *W* and *A* into equation (3.1) we get

$$\frac{C \times W/C}{1000\rho_w} + \frac{C \times A/C}{1000\rho_a} + \frac{C}{1000\rho_c} = 1.0 \quad (3.4)$$

By substituting of W/C and A/C into the previous equation we find that

$$\frac{0.53C}{1000} + \frac{5.16C}{2600} + \frac{C}{3120} = 1.0$$

Then; C= 353kg/m^3

By substituting C into equations (3.2) and (3.3) we can find the weight of water and aggregate per cubic meter.

W= 353×0.53 = 187.0 kg/m^3

A= 353×5.16 =1820 kg/m^3

The weight of the aggregate A represents the weight of both fine and coarse aggregate.

To find the ratio of fine aggregate to coarse aggregate, Table 3.6 was utilized. Since the maximum size of the coarse aggregate is 12.5mm, the coarse/fine aggregate ratio, x, is given by

$$\frac{19.05 - 9.52}{2 - 1.5} = \frac{19.05 - 12.5}{2 - x}$$

$$x = 1.65 \Rightarrow Fine/Coarse = 1:1.65$$

Therefore; the weight of coarse aggregate per m^3 is

$$1820 \times \frac{1.65}{2.65} \cong 1133.5\ kg/m^3$$

And the weight of fine aggregate per m^3 is

$$1820 \times \frac{1}{2.65} \cong 687 kg/m^3$$

Also the coarse aggregate was divided to two parts to include P-stone and Lime-stone with equal weight according to the sieve analysis results. Therefore,

P-stone = $1133.5 \times 0.5 = 566.75\ kg/m^3$

and Lime-stone =$1133.5 \times 0.5 = 566.75 kg/m^3$ too.

Table 3.6: Coarse/Fine aggregate ratio for various sand zones [86]

Maximum size of coarse aggregate		coarse/fine aggregate ratio for sand zone			
mm	*in*	1	2	3	4*
9.52	3/8	1	$1\,1/2$	2	3
19.05	¾	$1\,1/2$	2	3	31/2
38.1	$1\,1/2$	2	3	31/2	-

*The suitability of the mix for use in reinforced concrete should be ascertained by test.

As a result of the sieve analysis and concrete mix design, the mix proportions of the concrete that was used in this research work are listed in Table 3.7.

Table 3.7: Mix compositions of concrete

Concrete material	Quantity (Kg/m^3)
Cement	353
Crushed Lime-Stone (coarse aggregate)	566.75
P-Stone (coarse aggregate)	566.75
2-NS Sand (fine aggregate)	687.0
Water	187.0

3.1.3 Concrete Mixing Procedures

A 6 cubic foot heavy duty concrete mixer was used to produce concrete, as shown in Figure 3.7. All concrete compositions were measured by weight by using a digital balance Figure 3.8. All dry constituents were mixed for one minute before water was added and mixed for three more minutes to provide a homogeneous concrete mix. The composition ratio of the overall concrete mix was 1: 3.2: 1.95: 0.53 (cement: coarse aggregate: fine aggregate: water) respectively.

Figure 3.7: Heavy duty concrete mixer

Figure 3.8: Digital balance (model# SL3000)

External vibrators were used to gain a dense concrete (see figure 3.9). All the specimens were casted from the same batch, and cured for 28-days in a water tank. A digital Temperature-Humidity scale was used to record the temperature and relative humidity in the laboratory during mixing and casting times.

a) Concrete external vibrator was used for column specimens (model # AP-910-A)

b) Concrete external vibrator was used for beam specimens

Figure 3.9: Concrete external vibrators

3.1.4 Concrete Slump Test

The concrete slump test is an empirical test that is used for the measurement of the fresh property of concrete such as consistency and workability.

Although, the water/cement ratio and all other properties were constant for entire concrete batches, the slump test had been taken place for most patches to confirm the quality control of the mixes. The test has been done per ASTM C143-08 “Standard Test Method for Slump of Hydraulic-Cement Concrete” [69]. Figure 3.10 shows the slump test for one batch The procedures which had been followed to find the slump value were as follows: a standard concrete slump test cone with 305 mm ((12″) high, the base 203mm (8″) diameter, and 102mm (4″) diameter at the top. The cone was placed on a smooth surface plate, the small diameter at the top, and the container was filled with fresh concrete in three layers. Each layer was tamped 25 times with a standard 16 mm (5/8″) diameter steel rod before add the next layer. The final top surface of concrete was struck off by means of a screeding and rolling motion of the tamping rod (see figure 3.10 a). The cone was firmly held by foot-rests against its base during the operation. After the filling, the cone was slowly lifted and put it upside down and then measure the slump value (see figure 3.10 b)

a) Slump test cone filled out by concrete

b) measure the slump value

Figure 3.10: Concrete slump test

3.2 FRP Material properties

Carbon fiber, Glass fiber, and Epoxy materials had been provided from two different sources, SIKA Company and FYFE Company. Either carbon or glass FRPs sheets were prepared according to the manufacturer's recommendations and used for strengthening the concrete specimens. The same epoxy was used as a matrix and bonding agent to the concrete.

3.2.1 Sika Material Properties

Sikadur 300 high-modulus and high strength resin was used as a bonding material between concrete and fiber surfaces. Sikadur 300 consists of two components, "A" and "B" that are mixed together. The mixing ratio of component A to component B is 100 to 34.5 by weight. The properties of Sikadur 300 are shown in Table 3.8.

Table 3.8: Sikadur300 epoxy mechanical properties (Sika manual)

Mechanical Properties, 14 days cure at 73°F (23°C) and 50% R.H.		
Property	ASTM Method	Typical Test Value
Tensile Strength[1]	D-638	8,000 psi (55 MPa)
Tensile Modulus	D-638	$2.5x10^6$ psi (1,724 MPa)
Elongation Percent	D-638	3.0%
Flexural Strength	D-790	11,500 psi (79 MPa)
Flexural Modulus	D-790	$5x10^5$ psi (3,450 MPa)

[1] Testing temperature 70 °F (21°C)

SikaWrap Hex 113 Bi-directional ($0^o/90^o$) carbon fiber fabric has been used as strengthening material figure 3.11a. Such dry fabric is typically field laminated using epoxy materials to form a carbon fiber reinforced polymer (CFRP) that is then used to strengthen structural elements. Table 3.9 shows the properties of this material.

Selected specimens have also been strengthened by using SikaWrap Hex 100G glass fiber sheets, figure 3.11b. SikaWrap 100G glass fiber is a unidirectional E-glass fiber fabric. Material is field laminated using epoxy materials to form a glass fiber reinforced polymer (GFRP) used to strengthen structural elements. The properties of this material are shown in Table (3.9)

a) SikaWrap Hex 113C bi-directional carbon fiber fabric

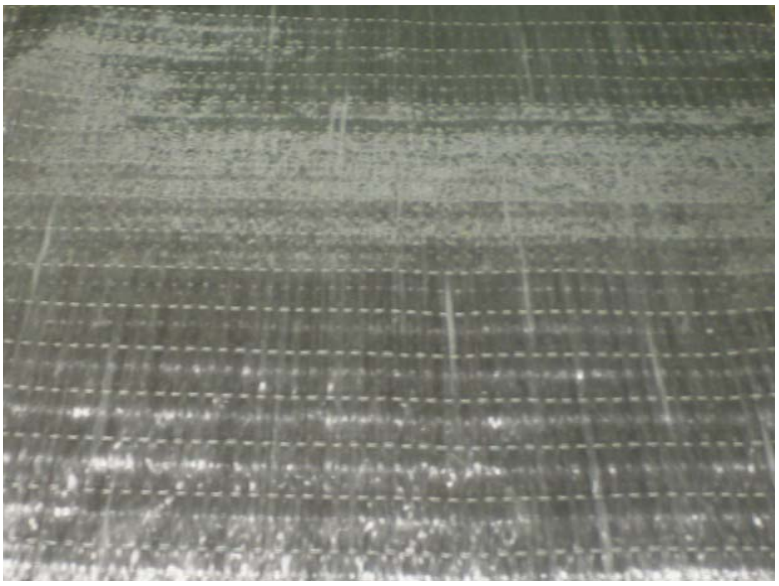

b) SikaWrap Hex 100G uni-directional glass fiber fabric

Figure 3.11: Carbon and glass fiber sheets of Sika

Table 3.9: SikaWrap Hex 113C carbon fiber fabric and Sika Wrap Hex 100G E-glass fiber fabric properties

Typical Data	SikaWrap Hex 113C Carbon Fiber	SikaWrap Hex 100G E-glass Fiber
Color	Black	White
Primary fiber direction	$0^o/90^o$ (bi-directional)	0^o (unidirectional)
Weight per square yard	5.7 oz. (196 g/m^2)	27 oz. (913 g/m^2)
Fiber Properties		
Tensile Strength	$5x10^5$ psi (3450 MPa)	$3.3x10^5$ psi (22,76 MPa)
Tensile Modulus	$33.4x10^6$ psi (230000MPa)	$10.5x10^6$ psi (72,413 MPa)
Elongation	1.5%	4%
Density	0.065 Ibs./in^3 (1.8 g/cc)	0.092 Ibs/in^3 (2.54 g/cc)
Normal Thickness	-	0.014 in (0.359 mm)
Cured Laminate Properties Design Values*		
Tensile Strength	66000 psi (456MPa)	77,100 psi (531MPa)
Tensile modulus	$6.0x10^6$psi (41,400MPa)	$3.4x10^6$ psi (23,607 MPa)
Elongation at breaks	1.2%	2.12%
Thickness	0.01 in (0.25 mm)	0.04 in (1.016 mm)

*Cured laminate properties with Sikadur Hex 300 Epoxy. Properties after standard post cure [70^o-75^oF (21^o-24^oC)-5 days, 48 hours at 140^oF(60^oC)

3.2.2 Fyfe Material Properties

Tyfo S epoxy is a two-component epoxy matrix material for bonding applications. It is a high elongation material which gives optimum properties as a matrix for the fiber-wrap system. It provides a long working time for application, with no offensive odor. The two components of Tyfo S epoxy A and B are mixed together by ratio A: B is 100 : 34.5 by weight, or 100 parts of component A to 42 parts of component B by volume. Table 3.10 shows the properties of this epoxy material.

Table 3.10: Tyfo S saturant epoxy mechanical properties (Fyfe manual)

Curing Schedule 72 hours post cure at 140°F (60°C).		
Property	ASTM Method	Typical Test Value
Tg	D-4065	180°F (82°C)
Tensile Strength[1]	D-638	10,500 psi (72.4 MPa)
Tensile Modulus	D-638	461,000 psi (3.18 GPa)
Elongation Percent	D-638	5.0%
Flexural Strength	D-790	17,900 psi (123.4 MPa)
Flexural Modulus	D-790	452,000 psi (3.12 GPa)

[1] Testing temperature 70 °F (21°C)

Tyfo SCH-41 composite sheet has been used. Tyfo SCH-41 composite is comprised of Tyfo S Epoxy and Tyfo SCH-41 reinforcing fabric. Tyfo SCH-41 is unidirectional carbon fabric with glass cross fiber for added strength and fabric stability during installation. The carbon material is orientated in the 0° direction. Figure (3.12a). The typical dry fiber and composite gross laminate design properties are shown in table 3.11.

Tyfo SHE-51A composite (figure 3.12b), has been used to strengthen selected specimens. Tyfo SHE-51A composite is comprised of Tyfo S Epoxy and Tyfo SHE-51A glass fabric.

Tyfo SHE-51A is a custom weave, unidirectional glass fabric used in the Tyfo fibrwrap system. The glass material is orientated in the 0° direction with additional yellow glass cross

fiber at 90^{o}. Table 3.11 shows the typical dry fiber and composite gross laminate design properties.

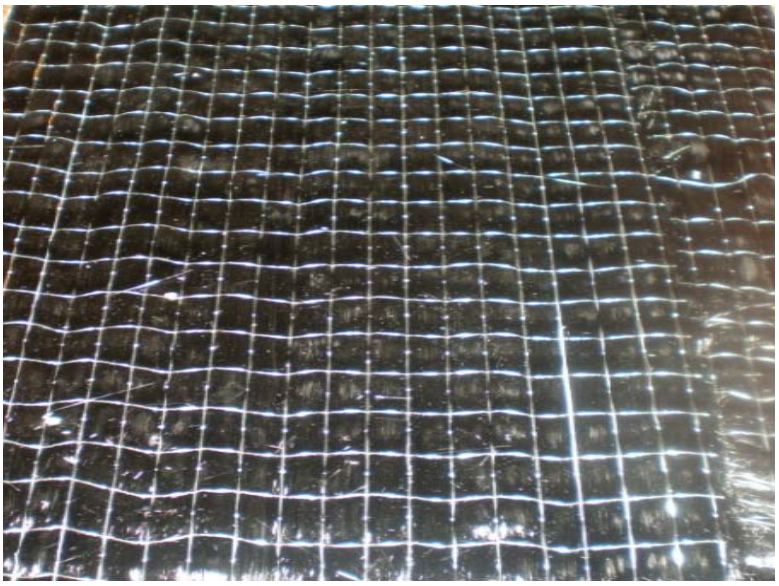

a) Tyfo SCH-41 Composite uni-directional carbon fiber

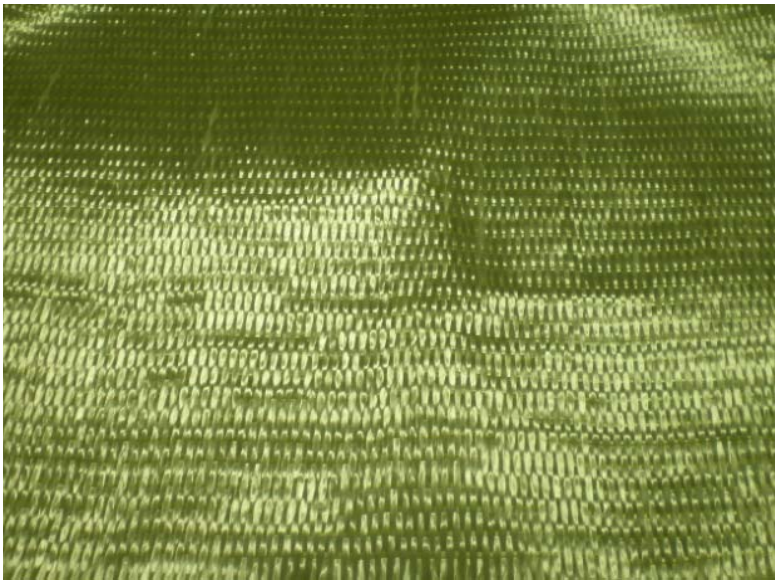

b) Tyfo SEH-51A Composite uni-directional glass fiber

Figure 3.12: Carbon and glass fiber sheets of Fyfe

Table 3.11: Tyfo SCH-41 Carbon fabric and Tyfo SEH-51A glass fabric properties

Typical Data	SCH-41 Carbon Fabric	SCH-51A Glass Fabric
Color	Black	White
Primary fiber direction	0^o (unidirectional)	0^o (unidirectional)
Weight per square yard	19 oz. (644 g/m^2)	27 oz. (915 g/m^2)
Fiber Properties		
Tensile Strength	550,000 psi (3.79 GPa)	470,000psi (3.24GPa)
Tensile Modulus	33.4x10^6 psi (230 GPa)	10.5x10^6psi (72.4GPa)
Elongation	1.7%	4.5%
Density	0.063 lbs./in^3 (1.74 g/cm^3)	0.092 lbs./in^3. (2.55 g/cc)
Cured "Composite" Laminate Properties Design Values*		
Tensile Strength	121,000 psi (834 MPa)	66,720 psi (460 MPa)
Tensile modulus	11.9x10^6 psi (82 GPa)	3.03x10^6 psi (20.9 GPa)
Elongation at breaks	0.85%	1.76%
Thickness	0.04 in (1.0 mm)	0.046 in. (1.18 mm)

3.3 Description of Test Specimens

16″,4.3″,4.1″ (length, width, and height) respectively, rectangular beam molds, (see figure 3.13a) has been used for beam specimens, and 4″ diameter with 8″ height cylindrical molds were used to produce column specimens (figure 3.13b). The dimensions of the beam molds were selected according to the ASTM standard C293-8 [70] for flexural strength concrete using simple beam with center-point loading, whereas the effective span length was three times of the beam depth and the distance from the center of the support to the beam edge was 2″ each side. The cylindrical column molds has been used according to ASTM C39-08 [71] for compressive strength of cylindrical specimen. Plastic molds were used with height equals two times of the diameter Figure 3.13b.

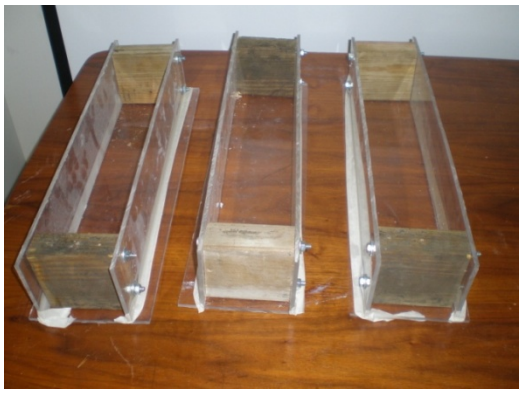

a) Rectangular beam molds

b) Cylindrical molds

Figure 3.13: Rectangular beam and cylindrical molds

In addition, 13″ length, 1.3″wide, and 0.6″ thick, rectangular molds have been used to cast epoxy beam specimens. These molds constructed are consistent with ASTM D790-07 [72] standard test methods for flexural properties of unreinforced and reinforced plastics and electrical materials; the effective length of these specimens was sixteen times of the thickness, Figure (3.14).

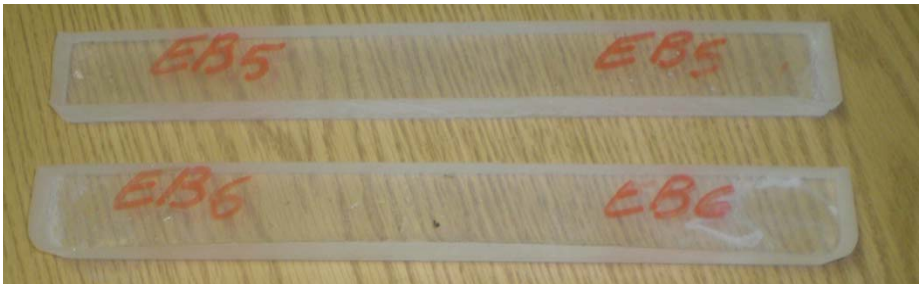

Figure 3.14: Epoxy beam specimens

3.4 Surface Preparation

The surface to receive the composites should be free from fins, sharp edges, and protrusions that may cause voids behind the installed surfaces. Existing uneven target surfaces shall be filled with epoxy filler or other materials approved by the engineer.

In this research, to ensure a good and strong bond between concrete and FRP sheets, the bottom surface of the concrete beams and the entire perimeter of the concrete cylinders were prepared by following these steps.

- After the samples were removed from water, sprayed the target surfaces with foaming cleaner to dissolve any residual oil that might be stuck on the surface due to the oiling of the molds, and left them dry for 15 minutes.
- Cleaned the surface using a wire brush, (see figure 3.15)
- Cleaned the target surface with water and brush to ensure free of any dirt and debris materials.
- Vacuumed the surface by using a vacuum cleaner.
- All specimens were allowed to dry for 48 hours before applying the epoxy adhesive.

Figure 3.15: Concrete surface cleaning

3.5 Bonding of FRP Sheet Procedures

After confirming that the concrete surface was completely dry, two components (A and B) of Sika or Fyfe epoxy were mixed thoroughly for 5 minutes in the ratio of 100: 34.5 by

weight. A mechanical drill equipped with a mixer beater was used to mix the two parts of the epoxy at low speed (400-600 rpm) until the mix became homogeneous, figure 3.16. The mixing time was typically 5 minutes.

Figure 3.16: Mixing of epoxy components

The mixed epoxy was applied on the concrete surface, and also on the surface of a FRP sheet by using a roller and paint brush, (see figure 3.17). A saturated FRP sheet was installed over the concrete surface by starting at one end and moving along the length to the other end for the beams and around the perimeter for cylinders until completed (figure 3.18). For cylinder specimens, figure 3.19, the overlap length was 6 ″ (150mm). Enough pressure was applied by hand during installation to press out the excessive epoxy and trapped air pockets. When a second layer of FRP sheet was needed, the same process was repeated. All strengthened specimens were cured for 14 days in the laboratory at room temperature and humidity (77^{o}F and 25%) respectively.

Figure 3.17: Applying epoxy on beam concrete surface

Figure 3.18: Carbon fiber strengthening for cylindrical column

3.6 Environmental Conditioning

Temperature and humidity play an important role in the process and strengthening of the existing concrete structures using FRP sheets and laminates. It is an external factor that guides the efficiency of the process to a high extent. The strength of the bond between the FRP laminates and concrete depends on the adhesive that bonds them together and thus the adhesive forms the medium through which force gets transferred from the concrete to FRP laminates that acts as reinforcement in the system. The most used adhesive for bonding is epoxy. The efficient working of this epoxy depends on the temperature at which the repair or strengthening has taken place. It is recommended that temperature shall be between 10^{o}C and 30^{o}C at which the epoxy is applied [56].

3.6.1 Temperature

The influence of temperature on concrete structures strengthened with externally bonded FRP was a most important part of this research. In addition to room temperature, specimens have been exposed to two different temperatures 100^{o}C and 180^{o}C. Two furnaces with a maximum heat power range of 400^{o}C, (figure 3.19), and two environmental chambers with a maximum temperature of 200^{o}C, (see figure 3.20), have been used for this purpose.

Figure 3.19: Laboratory furnaces (,model #21-350)

3.6.2 Relative Humidity

Relative humidity is another factor that was investigated in this research. Two levels of relative humidity have been carried out for this experimental work. These relative humidities were 0.0% and 100%. The two furnaces were used for all samples conditioned at 0% humidity, whereas the two environmental chambers for used for the 100% humidity tests.

Figure 3.20: Temperature/Humidity environmental chambers

3.7 Age Accelerating

The performances of the FRP-to-concrete bond are crucial in bond critical FRP strengthening applications such as flexural or shear strengthening of RC beams. Such bond characteristics and long-term durability need to be carefully assessed so that the long-term performance of the bonded structures could be guaranteed for the entire service life [61].

To evaluate the durability performance of the bondline between the concrete and its FRP strengthening materials, the environment factors that have been considered in this test program are number of thermal cycles, cycle length, exposure time, and media type including various degrees of humidity and dry air.

In this study, flexural strength and compression strength tests were carried out to evaluate the deterioration after 0, 40, 100, 250, 625 cycles. The cycle period was another challenging issue to determine how long a period of cycle is suitable to carry out the durability test. Since there is no guidance on the influence of cycle period, it was decided to first investigate the effect of cycle period (2 hs vs. 4 hs) on the damage of the specimen. Furthermore, seleced specimens were exposed to a constant temperature at 25^{o}C to examine the influence of the cycling effect. The temperature and humidity regime cycles for 2 hrs, 4 hrs, and continue cycle (no cycle period) for both 100^{o}C and 180^{o}C of temperatures are shown in figures (3.21 to 3.23).

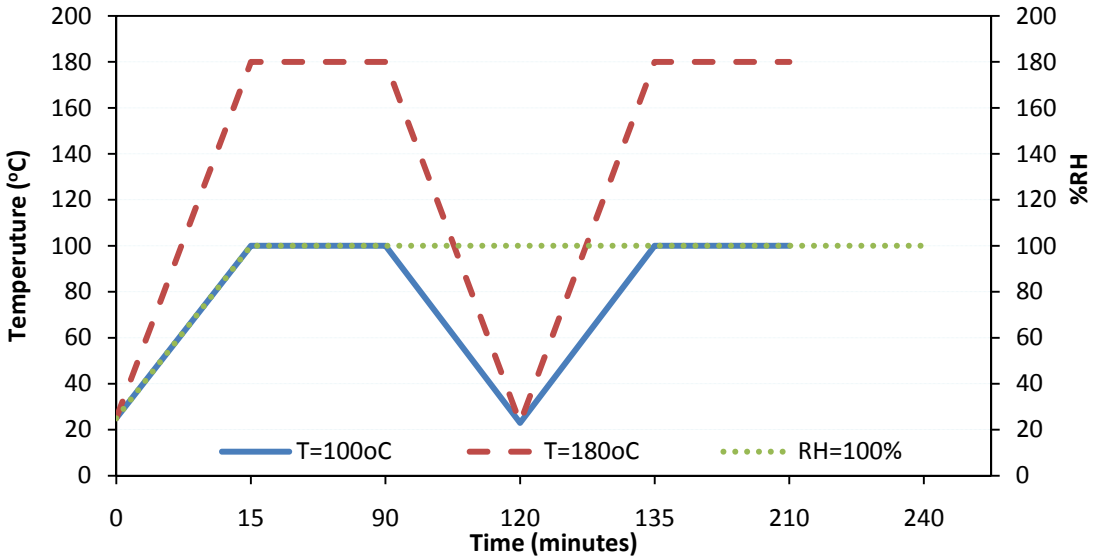

Figure 3.21: Temperature and humidity regime cycles (2 hrs-cycles)

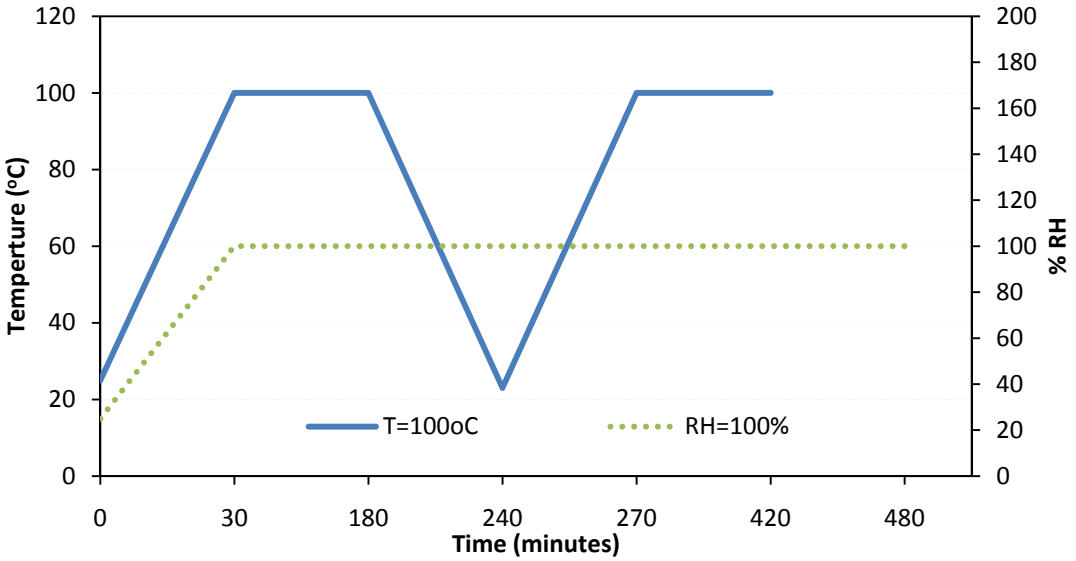

Figure 3.22: Temperature and humidity regime cycles (4 hrs-cycles)

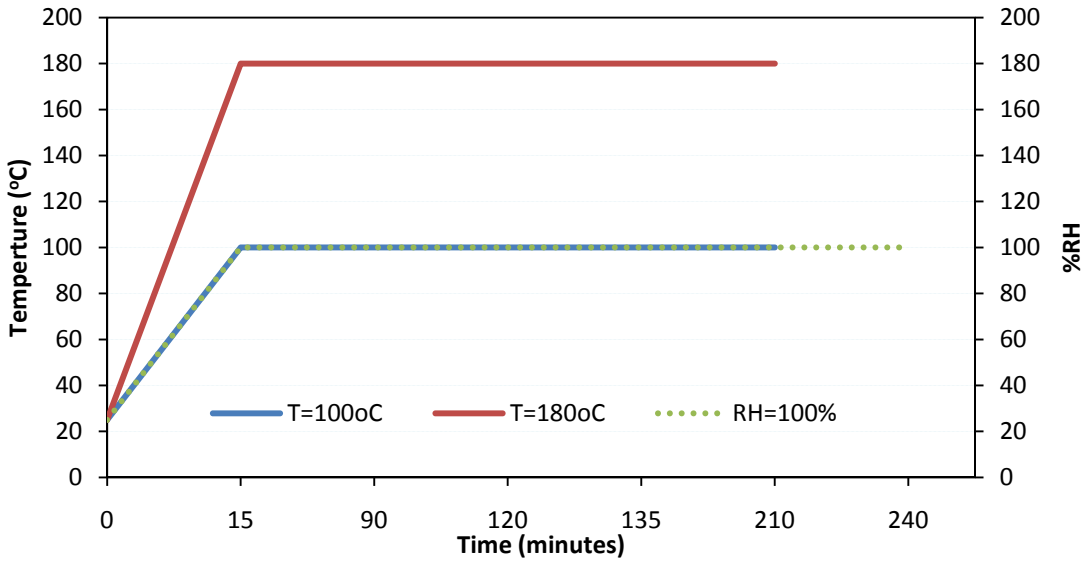

Figure 3.23: Temperature regime cycles (no cycles)

3.8 Mechanical Test Procedures

Two different mechanical tests have been carried out in this experimental program, i.e. flexural strength test and compressive strength test. All plain concrete beams, FRP strengthened beams, and plain epoxy beams have been subjected to flexural strength testing. While all concrete strengthened or unstrengthened columns were subjected to compressive strength testing.

3.8.1 Flexural Strength Test Procedures

The 16″x4.3″x4.1″ concrete beams were simply supported over a 12 ″ span and loaded at the middle of the span according to ASTM C293 [70]. The load was applied monotonically under displacement control at a constant rate of 0.003 mm/sec. The load and displacement data were recorded every 0.8 sec up to the test specimen failure.

13″x1.3″x0.6″ epoxy beams have also been tested. The supporting span was 9.6″. Displacement control mode was used and the rate of crosshead motion was 0.1066 mm/sec calculated by using the following equation [72].

$$R = ZL^2/6d \tag{3.5}$$

Where:

R = rate of crosshead motion, mm [in]/min.

L= support span, mm [in].

d= depth of beam, mm [in], and

Z= rate of straining of outer fiber, mm/mm/min [in/in/min]. Z equal to 0.01

Figure 3.24 shows the MTS-810 testing machine which was used for all flexural strength tests. All tests were done at laboratory temperature and humidity (77^{o}F and 25%) respectively.

Figure 3.24: MTS-810 material test system

3.8.2 Compressive Strength Test Procedure

Existing concrete columns under pure compressive loads can be strengthened by externally-bonded FRP wraps by wrapping the columns in the circumferential direction. When the column is subjected to axial load, it shortens longitudinally but dilates (expands) laterally. This dilation causes tensile stress to develop in the FRP wrap, and this tensile stress confines the concrete and places it in a state of triaxial (3-dimensional) stresses. The result of this stress condition is that both the load capacity and deformation capability of the concrete in the column are significantly improved, leading to stronger and more ductile structural members.

In this research, cylindrical samples of 4″ diameter and 8″ height were loaded axially according to ASTM (C39-2008) [70] until failure (see figure. 3.25). A high–capacity MTS-290 testing machine was used. The machine was operated under displacement control at a rate of 0.01mm/sec. The test had been done at laboratory temperature and humidity (77^{o}F and 25%) respectively.

Figure 3.25: MTS -290 material test system

CHAPTER 4 ANALYTICAL MODELING

4.1 Introduction

Concrete structures usually have a very long life; it is quite common that the load demands on the structure changes with time. The structures may have to carry larger loads at a later date or to be reinforced to meet new standards when they become in effect. In some cases, a structure needs to be repaired due to an accident. Another reason can be that errors have been made during the design or construction stage; such errors usually require strengthening to the structure before it can be used.

There are many different methods can be used to strengthen existing concrete structures such as enlargement of cross section, external pre-stressing. As already discussed, another alternative strengthening method to improve a structure's load-bearing capacity is to attach FRP sheets of fabric or fiber composite to the structure.

In the last decade, the effect of external application of fiber-reinforced polymers (FRP) to concrete beams and columns on improving their performance has been investigated both theoretically and experimentally.

The majority of the FRP strengthened structures are for the improvements of flexural capacity. Strengthening for shear, axial, and torsion loads is also needed. This chapter is devoted to state-of-the-art analysis concerning FRP sheets. The focus was placed on design for flexural and compressive capacity.

4.2 Non-strengthened Concrete Members

Both flexural and compressive strength capacity of plain concrete members has been discussed in ACI 318R-05 [58]. These analysis procedures are further discussed in the following sections

4.2.1 Flexural Strength of Non-Strengthened Concrete Beams

Plain concrete members are designed to be proportioned for adequate strength using factored loads and forces. When the design strength is exceeded, the section should be enlarged or the specified strength of the concrete should be increased, or both.

Design of cross sections subject to flexure shall be based on ACI 318R-5

$$\varphi M_n \geq M_u \tag{4.1}$$

if tension controls

$$M_n = 5\sqrt{f_c'}\, S_m \tag{4.2}$$

and if compression controls

$$M_n = 0.85 fc'\, S_m \tag{4.3}$$

Where:

M_n is the nominal moment capacity

M_u is the ultimate moment capacity

φ is the strength reduction factor = 0.9 for flexural members.

fc' represents concrete compressive strength

S_m represents the corresponding elastic section modulus and equals

$$S_m = \frac{bh^2}{6}$$

b and h represent the section width and depth respectively

The modulus rupture of concrete f_r can be defined as given

$$f_r = 7.5\sqrt{f_c'} \tag{4.4}$$

$$M_{cr} = \frac{f_r I_g}{y_t} \tag{4.5}$$

Where:

f_r the modulus rupture of concrete, psi

$f_c^{'}$ is the specified compressive strength of concrete, psi

M_{cr} is the cracking moment, *in.-lb*

I_g is the moment of inertia of gross concrete section about centroidal axis, neglecting reinforcement, in^4. For rectangular sections $I_g = bh^3/12$.

y_t represents the distance from centroidal axis of gross section, neglecting reinforcement, to tension face, in., for rectangular sections y_t =h/2

In the case of center concentrated load on the mid span of the rectangular simply supported beam

$$P_{cr} = \frac{4M_{cr}}{L_c} \tag{4.6}$$

Where:

P_{cr} is the cracking load, *lb*

L_c represents the clear span, measured center-to-center of supports, in

4.2.2 Compressive Strength Of Non-Strengthened Concrete Columns

A column is a vertical structural member which supports axial compression loads, with or without bending moments. The cross-sectional dimensions of a column are generally considerably less than its height. Columns support loads from floors and roofs and transmit these loads to the foundations.

Concrete columns are normally reinforced with steel bars and can be classified into two types, tied or spiral columns. Tied column is a concrete column reinforced with longitudinal bars and horizontal ties. Tied columns may be square, rectangular, L-shaped, circular, or any other required shape. Occasionally, when high strength and/or high ductility are required, the

longitudinal bars are placed in a circular, and the discrete ties replaced by a bar bent into a helix or spiral in this case the column is called a spiral column. [75].

In the ACI 318R-05[58], sections 10.3.6.1 and 10.3.6.2, the maximum load on the column has been specified for both cases, tied and spiral columns by multiplied the maximum nominal load ($P_{n(max)}$) by a reduction factor that is 0.8 for tied columns and 0.85 for spiral columns.

Therefore; for tied columns

$$\emptyset P_{n,(\max)} = 0.80\emptyset[0.85f_c^{'}(A_{\mathrm{g}} - A_{st}) + f_y(A_{st})] \tag{4.7}$$

and for spiral columns

$$\emptyset P_{n,(\max)} = 0.85\emptyset[0.85f_c^{'}(A_{\mathrm{g}} - A_{st}) + f_y(A_{st})] \tag{4.8}$$

$P_{n(\max)}$ is the maximum allowable value of $P_n\, lb$

A_{g} gross area of concrete section, in^2

A_{st} total area of non-prestressed longitudinal reinforcement, (bars or steel shapes), in^2

f_y specified yield strength of reinforcement, psi

$\emptyset$ is the strength reduction factor.

When the area of steel is neglected, The maximum load (failure load) can be found by multiplying the concrete compressive strength times the gross area of the concrete section.

$$P_{(\max)} = f_c^{'}(A_{\mathrm{g}}) \tag{4.9}$$

4.3 Flexural Strength of Epoxy Beams

This section covers the flexural strength of simply supported rectangular epoxy beams subjected to a center point concentrated load.

The maximum flexural stress may be obtained as given:

$$\sigma_f = \frac{3PL}{2bd^2} \tag{4.10}$$

Where:

σ_f = stress in the outer fibers at midpoint. MPa (psi),

P= load at s given point. N (lbf).

L= support span, mm (in).

b= width of the beam, mm (in)

d= beam depth, mm [in].

The flexural strain can be obtained as follows:

$$\varepsilon_f = \frac{6Dd}{L^2} \tag{4.11}$$

ε_f is the strain in the outer surface, mm/mm [in/in]

D represents the maximum deflection of the center of the beam, mm (in).

4.4 Design Flexural Strength of FRP Strengthened Beams

The use of Fiber-reinforced polymer (FRP) materials for flexural strengthening of both reinforced and non-reinforced concrete structures started in the late 1970s. Since then FRP strengthening was established as an efficient and economical technique for repair and rehabilitation of deteriorating concrete structures. To understand the complex behavior and possible failure mechanisms of FRP composite structures, extensive experimental investigations were carried out by different researchers. Several failure modes were observed during these tests. These failure modes were classified into two types by Thomsen (2004) [73]. Type one includes modes exhibiting composite action up to failure of the strengthened beam, which could be due to concrete crushing, FRP rupture, or lack of shear resistance. Type two, on the other hand, consists of failure due to loss of composite action. In this case either debonding between the FRP

laminate and concrete surface is observed, or end peeling takes effect, where the concrete cover in the region near the supports peels off.

The ACI 440.2R-02 guidelines [74] for flexural strengthening with FRP composites recognized this fact and introduced a bond reduction factor k_m for the FRP strength. This factor equals the effective FRP stress at failure divided by the original FRP strength. The development of the proposed values for the bond reduction factor k_m was based mainly on experimental investigations. Due to the high cost of experimental research, the proposed factor accounts only for a limited number of parameters, and don't take into account the deterioration of the bond strength at the interface level.

There exists a need to conduct an analytical investigation, where an evaluation of the parameters affecting the debonding failure is carefully examined.

In the flexural strengthening of reinforced concrete beams with externally applied fiber-reinforced polymer FRP sheets or strips, it is essential to understand the effects that the FRP reinforcement has on the beam failure mode, especially for the development of rational design equations under ultimate loading conditions.

Bonding FRP reinforcement to the tension face of a concrete flexural member with fibers oriented along the length of the member will provide an increase in flexural strength. Increases in overall flexural strength from 10 to 160% have been documented (Meier and Kaiser 1991; Ritchie et al. 1991; Sharif et al. 1994). When taking into account ductility and serviceability limits, however, increases of 5 to 40% are more reasonable [6].

4.4.1 Assumptions

The following assumptions and possible failures are made in calculating the flexural resistance of a section strengthened with an externally applied FRP system:

- The strains in the reinforcement and concrete are directly proportional to the distance from the neutral axis, that is, a plane section before loading remains plane after loading.
- There is no relative slip between external FRP reinforcement and the concrete.
- The shear deformation within the adhesive layer is neglected since the adhesive layer is very thin with slight variations in its thickness.
- The maximum usable compressive strain in the concrete is 0.003.
- The tensile strength of concrete is neglected.
- The FRP reinforcement has a linear elastic stress-strain relationship to failure.
- Crushing of the concrete in compression before yielding of the reinforcing steel.
- Yielding of the steel in tension followed by rupture of the FRP laminate.
- Yielding of the steel in tension followed by concrete crushing.
- Shear/tension delamination of the concrete cover (cover delamination.
- Debonding of the FRP from the concrete substrate (FRP debonding).

Concrete crushing is assumed to occur if the compressive strain in the concrete reaches its maximum usable strain ($\varepsilon_c = \varepsilon_{cu} = 0.003$). Rupture of the FRP laminate is assumed to occur if the strain in the FRP reaches its design rupture strain ($\varepsilon_f = \varepsilon_{fu}$) before the concrete reaches its maximum usable strain.

4.4.2 Failure Modes

Following are the general failure modes that may occur in FRP bending stiffened structure:

1. Crushing of the concrete in the compression zone before rupture of the FRP strengthening laminate or yielding of the reinforcing steel. This type of failure is of brittle nature.

2. Yielding of steel in tension before concrete crushing or rupture of FRP strengthening laminate yield (Ductile failure).

3. The steel reinforcement in the compression zone of doubly reinforced section is yielded (Relatively ductile failure).

4. Rupture of the FRP strengthening laminate. This represents the most brittle failure. In this case the FRP fails before the steel yields with the strain in the concrete below its ultimate strain. Therefore, the FRP stress is set to the effective FRP failure strength, $f_{fe} = k_m f_{fu}$. Since the concrete has not reached the ultimate compressive strain which is 0.003, the Whitney stress block parameters should technically not be used.

5. Anchorage failure (delamination) in the bond zone of the laminate (Often ductile failure).

6. Peeling or shear/tension failure of concrete substrate at the laminate's cut off zone (Brittle failure). Figure 4.1 shows the varieties of failure modes.

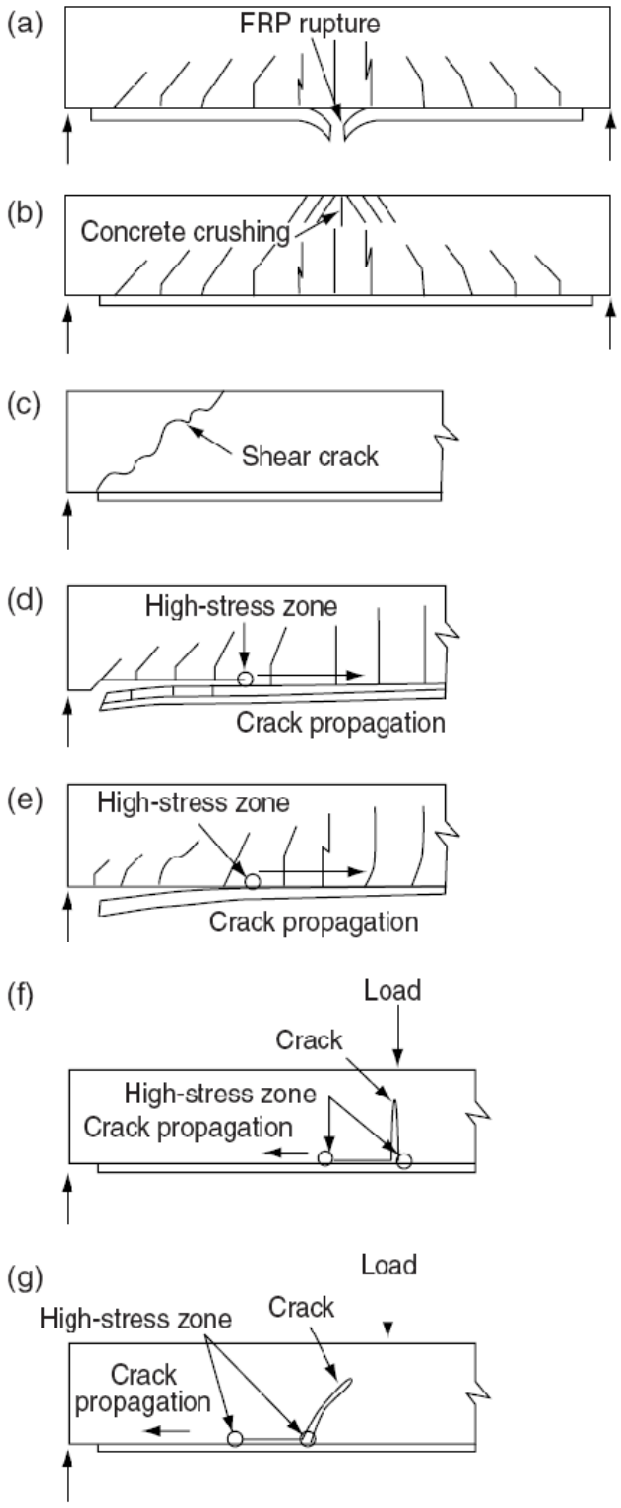

Figure 4.1: Failure modes of flexural strengthened beams [6],

To avoid detachment failure at the interface surface, Figure (4.1-d-4.1g), the ACI guide limits the strain permitted in the FRP strengthening system to ensure that any of these failures will not occur. The bond reduction factor k_m has been introduced by ACI 440.2R-02. k_m is a reduction factor of FRP ultimate strength due to debonding failure. In order to prevent debonding of the FRP laminate, a limitation is placed on the strain level developed in the laminate. The following equations give the expression for the bond-dependent coefficient k_m which is a function of the stiffness and thickness of the FRP system.

For $nE_f t_f \leq 1{,}000{,}000\ Ib/in$

$$k_m = \left\{\frac{1}{60\varepsilon_{fu}}\left(1 - \frac{nE_f t_f}{2{,}000{,}000}\right)\right\} \leq 0.90 \tag{4.12}$$

For $nE_f t_f > 1{,}000{,}000\ Ib/in$

$$k_m = \left\{\frac{1}{60\varepsilon_{fu}}\left(\frac{500{,}000}{nE_f t_f}\right)\right\} \leq 0.90 \tag{4.13}$$

Or:

For $nE_f t_f \leq 180{,}000\ N/mm$

$$k_m = \left\{\frac{1}{60\varepsilon_{fu}}\left(1 - \frac{nE_f t_f}{360{,}000}\right)\right\} \leq 0.90 \tag{4.14}$$

For $nE_f t_f > 180{,}000\ N/mm$

$$k_m = \left\{\frac{1}{60\varepsilon_{fu}}\left(\frac{90{,}000}{nE_f t_f}\right)\right\} \leq 0.90 \tag{4.15}$$

Where: n represents the number of layers or plies for FRP strips or sheets or fabrics.

E_f is the longitudinal modulus of the fiber in the strengthening direction in the case of sheets or fabrics. Where t_f is the thickness of the fibers in a single sheet of fabric.

A new specifications for bond reduction factor has been developed by ACI440.2R according to the FRP strain level at which debonding may occur, ε_{fd} is evaluated as follow comment on how this is different than equations (4.12 to 44.15) [82]

$$\varepsilon_{fd} = 0.083\sqrt{\frac{f_c'}{nE_f t_f}} \leq 0.9\varepsilon_{fu} \text{ ----------}US \tag{4.16}$$

$$\varepsilon_{fd} = 0.41\sqrt{\frac{f_c'}{nE_f t_f}} \leq 0.9\varepsilon_{fu} \text{ ----------}SI \tag{4.17}$$

In case failure is governed by debonding, the effective FRP stress, f_{fe}, is equal

$$f_{fe} = E_f \varepsilon_{fd} \tag{4.18}$$

To prevent debonding, the k_m factor may be multiplied by the rupture strain of the FRP laminate to reach a strain limitation to prevent debonding. According to the ACI 440.2R-02 guide (Eqns 4.12-4.13), since k_m must be less than 0.9, the strain in the FRP is never allowed to reach the ultimate rupture strain in the ACI 440.2R-02 design procedures. Therefore, theoretically, the FRP rupture can never occur. As a result, throughout design calculations, only two modes of failure are assumed to occur. The first mode of failure might be a compressive failure of concrete and the second one is the failure of FRP strengthening material [6]. Each scenario of these two failures contains two types of failure modes. In other words, for the design purpose, there are four potential flexural failure modes for externally strengthened reinforced concrete flexural members as follows:

- Concrete crushing after steel yields;
- Concrete crushing before steel yielding.
- Steel yielding followed by FRP rupture
- Debonding of the FRP Strengthening at the FRP/Concrete interface.

It is not always clear at the outset of a design or analysis which of the above failure modes will govern. Thus, an assumption must be made and the responsible failure mode must be checked and confirmed. If the assumption is incorrect, a different failure mode must be considered and the analysis is repeated.

In this research, all concrete beams have been executed without steel reinforcement (plane concrete) and it is assumed that the bond surface between concrete and FRP strengthening sheets is strong enough, so, the last failure mode, FRP debonding, will not occur. Moreover, the strength of FRP in tension more than of concrete thus, the concrete crushing will occur before FRP rupture.

Concrete compression failure may occur either after or before the internal steel has yielded with the FRP strengthening intact and still attached. This is the failure mode of an over reinforced strengthened concrete beam. In this case, the effective strain in the FRP at failure is obtained from the assumed linear variation of the strain through the depth of the section as shown in figure 4.2. Therefore, the effective strain in the FRP is given by the following equation.

$$\varepsilon_{fe} = \varepsilon_{cu}\frac{h-c}{c} - \varepsilon_{bi} \tag{4.19}$$

Where: ε_{fe} represents the effective strain in the FRP at ultimate failure of the member.

ε_{cu} is the ultimate compressive strain in the concrete equals 0.003.

h is the depth that represented by distance to the centroid of the FRP material

c represents the depth of the neutral axis.

ε_{bi} represents and the existing tensile strain in the concrete substrate at the location of the FRP strengthening system, ε_{bi} equals

$$\varepsilon_{bi} = \frac{m_1(h-kd_1)}{(I_{cr})_1 E_c} \tag{4.20}$$

Where: m_1 is represents the service load moment in the beam at the time the FRP is attached, k_1 is the ratio of the depth of the neutral axis to the effective depth of the section under surface load, and $(I_{cr})_1$ represents the cracked (transformed) second moment of area.

The effective strain of the FRP at failure ε_{fe} can be defined by this equation:

$$\varepsilon_{fe}=k_m\varepsilon_{fu} \tag{4.21}$$

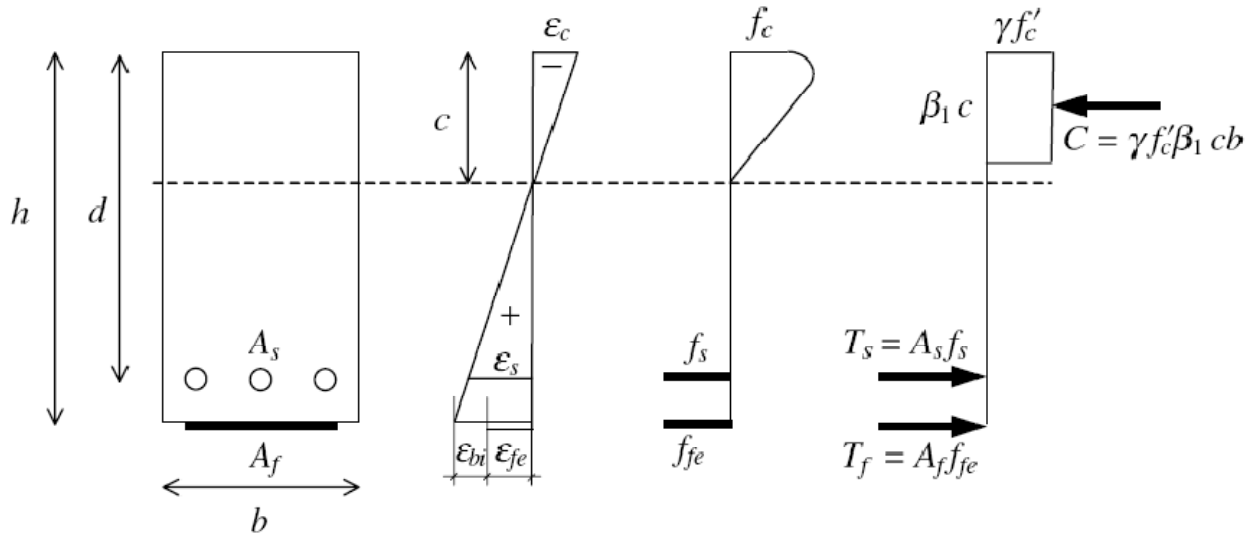

Figure 4.2: Strain, stresses, and force resultants in strengthened section at the ultimate state [6]

The effective stressf_{fe} is linearly related to the effective strain and given by equation (4.22).

$$f_{fe} = E_f\varepsilon_{fe} \tag{4.22}$$

The strain in the reinforcement steel can be found as follows:

$$\varepsilon_s = (\varepsilon_{fe} + \varepsilon_{bi})\frac{d-c}{h-c} \tag{4.23}$$

Where: d is the depth from extreme compression fiber to the centeroid of the steel reinforcement.

The stress of steel reinforcement f_s must be less than or equal the yield stress f_y and is equal:

$$f_s = E_f\varepsilon_s \leq f_y \tag{4.24}$$

From Whitney block, (Figure 4.2), we can calculate the depth of neutral axis *c* by taking the summation of compression and tension forces in the *x*-direction.

$$\sum F_x = 0 \Rightarrow T_s + T_f - C = 0 \tag{4.25}$$

Then;

$$A_s f_{s+} A_f f_{fe} - \gamma f_c' \beta_1 c b = 0$$

So;

$$c = \frac{A_s f_{s+} A_f f_{fe}}{\gamma f_c' \beta_1 b} \tag{4.27}$$

Where f_s is the tensile stress of steel reinforcement at failure, A_s the area of tensile steel, d is the depth from extreme compression fiber to the centroid of steel reinforcement, β_1 the depth ratio of an equivalent rectangular stress block, A_f is the area of FRP strip or sheet, b the width of the section, while γ represents the intensity of an equivalent rectangular stress block (usually= 0.85)

Therefore,

The nominal moment capacity of the section can be obtained by the following equation

$$M_{n=} A_s f_s \left(d - \frac{\beta_1 c}{2}\right) + \psi A_f f_{fe} \left(h - \frac{\beta_1 c}{2}\right) \tag{4.28}$$

Where ψ represents an extra reduction of FRP

The modes of failure can be classified as follows:

Mode1a) concrete crushing after steel yields: this mode of failure occur when the steel reinforcement yields before the concrete reach the maximum strain which is assumed a constant for all concrete and equals 0.003. Under this mode of failure, the stress in the tension reinforcement steel f_s equals the yielding stress of the reinforcement steel $f_{y..}$ Therefore;

$$T_s = A_s f_y \tag{4.29}$$

$$T_f = A_f f_{fe=} A_f E_f \varepsilon_{fe} = A_f E_f \left(\varepsilon_{cu} \frac{h-c}{c} - \varepsilon_{bi}\right) \tag{4.30}$$

And, the compression force, *C* is

$$C = 0.85 f_c' \beta_1 c b \tag{4.31}$$

So; by substituting in the equation of equilibrium in x-direction, equation (4.25) we get

$$(0.85 f_c' \beta_1 b) c^2 - A_s f_y - A_f E_f [\varepsilon_{cu} - (h - c) - \varepsilon_{bi} c] = 0 \tag{4.32}$$

Equation (4.32) can be written in the form

$$(0.85 f_c' \beta_1 b) c^2 + \left[-A_s f_y + A_f E_f (\varepsilon_{bi} + \varepsilon_{bi})\right] c - (A_f E_f \varepsilon_{cu} h) = 0 \tag{4.33}$$

The above equation is a polynomial equation of the second degree "quadratic equation". The general solution form is

$$Ac^2 + Bc + C = 0$$

Where: $A = 0.85 f_c' \beta_1 b$

$B = -A_s f_y + A_f E_f (\varepsilon_{bi} + \varepsilon_{bi})$

$C = -(A_f E_f \varepsilon_{cu} h)$

By solving the above equation, the value of *c* can be gotten.

Once we find the value of *c*, the strains in the steel and FRP should be checked.

$$\varepsilon_s = \varepsilon_{cu} \frac{d-c}{c} \geq \varepsilon_{sy} \tag{4.34}$$

$$\varepsilon_{fe} = \varepsilon_{cu} \frac{h-c}{c} - \varepsilon_{bi} \leq k_m \varepsilon_{fu} \tag{4.35}$$

If the above two equations are satisfied, the steel stress and FRP stress are taken as

$$f_s = f_y \tag{4.36}$$

And;

$$f_{fe} = E_f \varepsilon_{fe} \tag{4.37}$$

$$M_n = A_s f_y \left(d - \frac{\beta_1 c}{2}\right) + \psi A_f f_{fe} \left(h - \frac{\beta_1 c}{2}\right) \tag{4.38}$$

The ultimate moment capacity

$$M_u = \emptyset M_n \tag{4.39}$$

The reduction factor $\emptyset$ =0.7+0.2$(\varepsilon_{s-}\varepsilon_{sy})/(0.005-\varepsilon_{sy})$ and depends on the value of the strain in the steel at the time of concrete crushing failure (ACI 440.2R-2).

Mode1b) concrete crushing before steel yields: this mode of failure concrete reaches the maximum strain of 0.003 before the steel reinforcement reach the yield strain, and the strain of the FRP below its effective rupture strain. Therefore the, the tension and compression forces will be as follow:

$$T_s = A_s f_s = A_s E_s \varepsilon_s = A_s E_s \varepsilon_{cu} \frac{d-c}{c} \tag{4.40}$$

$$T_f = A_f f_{fe=} A_f E_f \varepsilon_{fe} = A_f E_f \left(\varepsilon_{cu} \frac{h-c}{c} - \varepsilon_{bi}\right) \tag{4.41}$$

And, the compression force, $C = 0.85 f_c' \beta_1 cb$

By substituting in the equilibrium equation we get

$$(0.85 f_c' \beta_1 b)c^2 - A_s E_s \varepsilon_{cu}(d-c) - A_f E_f [\varepsilon_{cu}(h-c) - \varepsilon_{bi} c] = 0 \tag{4.42}$$

Also, the above equation is the quadratic equation on the form

$$Ac^2 + Bc + C = 0 \tag{4.43}$$

Where:

$$A = 0.85 f_c' \beta_1 b \tag{4.44}$$

$$B = A_s E_s \varepsilon_{cu} + A_f E_f (\varepsilon_{cu} + \varepsilon_{bi}) \tag{4.45}$$

and

$$C = -(A_s E_s \varepsilon_{cu} d + A_f E_f \varepsilon_{cu} h) \tag{4.46}$$

by obtaining the value of *c*, the steel strain and FRP strain should be checked

$$\varepsilon_s = \varepsilon_{cu} \frac{d-c}{c} \leq \varepsilon_{sy} \tag{4.47}$$

$$\varepsilon_{fe} = \varepsilon_{cu} \frac{h-c}{c} - \varepsilon_{bi} \leq k_m \varepsilon_{fu} \tag{4.48}$$

If the strain in steel less than the yielding strain, $\varepsilon_s \leq \varepsilon_{sy}$and the maximum effective tensile strain in the FRP strengthening system less than the ultimate strain of FRP multiplied in the bond-dependent coefficient k_m , $\varepsilon_{fe} \leq k_m \varepsilon_{fu}$, then the stress in the steel reinforcement is

$$f_s = E_f \varepsilon_s \tag{4.49}$$

And the stress in FRP strengthening system is

$$f_{fe} = E_f \varepsilon_{fe} \tag{4.50}$$

Consequently, the nominal moment capacity can be found

$$M_{n=} A_s f_s \left(d - \frac{\beta_1 c}{2}\right) + \psi_f A_f f_{fe} \left(h - \frac{\beta_1 c}{2}\right) \tag{4.51}$$

Whereas the ultimate moment capacityM_u equals

$$M_{u=} \emptyset M_n$$

Since the steel has not yielded at the time of concrete crushing failure, ∅=0.7

Then; 0.7 did not apply to the second term???

$$M_{u=} 0.7 A_s f_s \left(d - \frac{\beta_1 c}{2}\right) + \psi_f A_f f_{fe} \left(h - \frac{\beta_1 c}{2}\right) \tag{4.52}$$

Mode 2a) The other mode of failure may occur when the FRP fails after steel yields. In this mode of failure the steel reaches the yield strength then the FRP fails but the strain of the concrete is still below the ultimate strain of 0.003. In this situation of failure, the effective strain of FRP strengthening system,$\varepsilon_{fe} = k_m \varepsilon_{fu}$, and the stress in steel reinforcement equals the yielding stress, $f_s = f_y$. Since the concrete has not reached its ultimate compressive strain, the Whitney stress block parameters should technically not be used and the stress block parameters, β_1, γ should be obtained as follow (ACI 440.2R-02):

$$\beta_1 = 2 - \frac{4[(\varepsilon_c/\varepsilon_c') - \tan^{-1}(\varepsilon_c/\varepsilon_c')]}{(\varepsilon_c/\varepsilon_c') \ln[1 + (\varepsilon_c/\varepsilon_c')^2]} \tag{4.53}$$

$$\gamma = \frac{0.9\ln[1+(\varepsilon_c/\varepsilon_c')^2]}{\beta_1(\varepsilon_c/\varepsilon_c')} \tag{4.54}$$

Where:

$$\varepsilon_c' = \frac{1.71 f_c'}{E_c} \tag{4.55}$$

Therefore, to find the depth of the neutral axis *c,* the equilibrium equation should be applied as follows

$$T_s = A_s f_y \tag{4.56}$$

$$T_f = A_f f_{fe=} A_f k_m f_{fu} \tag{4.57}$$

And, the compression force,

$$C = 0.85 f_c' \beta_1 c b \tag{4.58}$$

So, the summation of forces in *x*-direction is equal

$$(0.85 f_c' \beta_1 b)c - A_s f_y - k_m f_{fu} = 0 \tag{4.59}$$

The depth of neutral axis can be found from the following equation

$$c = \frac{A_s f_y + A_f k_m f_{fu}}{0.85 f_c' \beta_1 b} \tag{4.60}$$

The strains of the steel and concrete must then be checked:

$$\varepsilon_s = \left(\varepsilon_{fu} + \varepsilon_{bi}\right)\frac{d-c}{h-c} \geq \varepsilon_{sy} \tag{4.61}$$

$$\varepsilon_c = \left(\varepsilon_{fe} + \varepsilon_{bi}\right)\frac{c}{h-c} \leq \varepsilon_{cu} \tag{4.62}$$

When the above conditions are satisfied, the stress of the steel equals the yield strength, $f_s = f_y$, and the effective stress in the FRP sheet is given by the following equation

$$f_{fe} = E_f \varepsilon_{fe} = k_m f_{fu} \tag{4.63}$$

And the nominal moment capacity is given as

$$M_{n=}A_s f_y\left(d-\frac{\beta_1 c}{2}\right)+\psi_f A_f f_{fe}\left(h-\frac{\beta_1 c}{2}\right) \tag{4.64}$$

The ultimate moment capacity equals

$$M_{u=}\emptyset M_n \tag{4.65}$$

Where: $\emptyset$ =0.7+0.2$(\varepsilon_{s-}\varepsilon_{sy})/(0.005-\varepsilon_{sy})$

Mode 2b) Other mode of failure may take place when the FRP fails before the steel yields. This mode of failure occurs when the effective strain of the FRP reaches the maximum effective value (ultimate stress multiplied by bond coefficient, $f_{fe}=k_m f_{fu}$). In the meantime, the steel doesn't yield and the strain of the concrete is still below the ultimate strain. This mode of failure is undesirable (explain why!) and we must avoid that to happen. Since the concrete doesn't reach the ultimate strain, theoretically, Whitney stress block should not be applied.

$$T_s=A_s f_s=A_s E_s\varepsilon_s=A_s E_s(\varepsilon_{fe}+\varepsilon_{bi})\frac{d-c}{h-c} \tag{4.66}$$

$$T_f=A_f f_{fe=}A_f k_m f_{fu}=A_f E_f\varepsilon_{fe} \tag{4.67}$$

$$C=0.85f_c'\beta_1 cb \tag{4.68}$$

By applying the equation of equilibrium $T_s+T_f-C=0$ we find;

$$(0.85f_c'\beta_1 b)c(h-c)-A_s E_s\left(\varepsilon_{fe}+\varepsilon_{bi}\right)(d-c)-A_f E_f\varepsilon_{fe}(h-c)=0 \tag{4.69}$$

The above equation can be written in the form

$$Ac^2+Bc+C=0$$

Where:

$$A=0.85f_c'\beta_1 b$$

$$B=-[0.85f_c'\beta_1 bh+A_s E_s\left(\varepsilon_{fe}+\varepsilon_{bi}\right)+A_f E_f\varepsilon_{fe}]$$

$$C=A_s E_s\left(\varepsilon_{fe}+\varepsilon_{bi}\right)d+A_f E_f\varepsilon_{fe}h$$

Therefore;

$$\varepsilon_s = \left(\varepsilon_{fe} + \varepsilon_{bi}\right)\frac{d-c}{h-c} \leq \varepsilon_{sy} \tag{4.70}$$

And; $$\varepsilon_c = \left(\varepsilon_{fe} + \varepsilon_{bi}\right)\frac{c}{h-c} \leq \varepsilon_{cu} \tag{4.71}$$

If the above two conditions (4.67) and (4.68) are satisfied, then the steel stress is taken as

$$f_s = E_f \varepsilon_s \tag{4.72}$$

$$f_{fe} = E_f \varepsilon_{fe} = k_m f_{fu} \tag{4.73}$$

The nominal moment capacity can be found in this form

$$M_{n=} A_s f_s \left(d - \frac{\beta_1 c}{2}\right) + \psi_f A_f f_{fe} \left(h - \frac{\beta_1 c}{2}\right) \tag{4.74}$$

And the ultimate moment capacity equals

$$M_{u=} \emptyset M_n \tag{4.75}$$

Since the steel has not yielded at the time of FRP failure, then $\emptyset$ =0.7 [6].

In this research, there is no steel reinforcement and the concrete crushing failure is assumed to occur before the FRP failure. As shown in Figure 4.3, the equilibrium of forces in x-direction results is

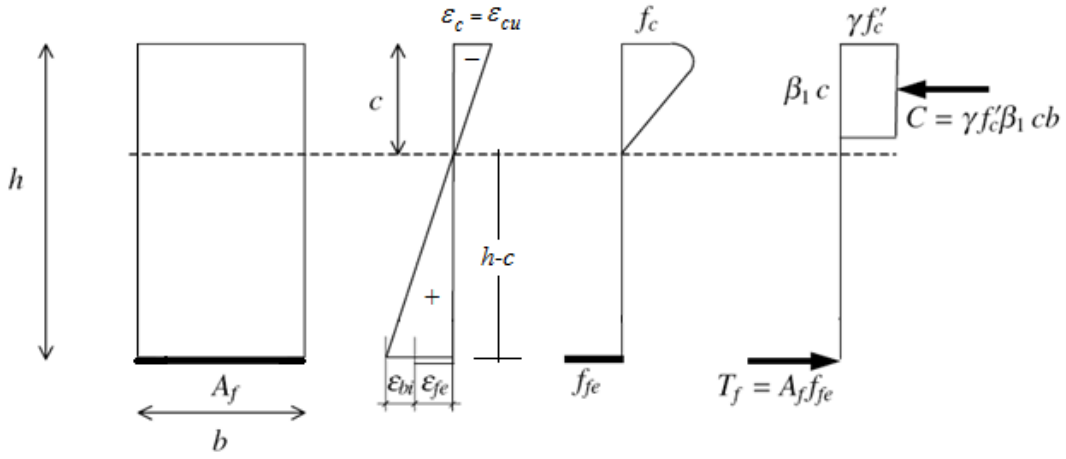

Figure 4.3: Strain, stresses, and force resultants in strengthened section at the ultimate state (no steel reinforcement)

$$\varepsilon_c = \varepsilon_{cu} = 0.003 \tag{4.76}$$

$$T_f = C \tag{4.77}$$

Where:

$$C = 0.85 f_c' \beta_1 c b \tag{4.78}$$

$$T_f = A_f f_{fe} = E_f \varepsilon_{fe} \tag{4.79}$$

By substituting equations (4.78) and (4.79) into equation (4.77) we find that

$$0.85 f_c' \beta_1 c b + E_f \varepsilon_{fe} = 0 \tag{4.80}$$

The effective strain of the FRP at the time of concrete crushing is given as

$$\varepsilon_{fe} = \frac{h-c}{c} \varepsilon_{cu} \tag{4.81}$$

By substituting equation (4.81) into equation (4.80) and solving, we find c, therefore the nominal moment capacity is

$$M_{n=} \psi_f A_f f_{fe} \left(h - \frac{\beta_1 c}{2} \right) \tag{4.82}$$

The ultimate moment capacity can be obtained from Equation (4.75).

4.5 Compressive Strength of FRP Strengthened Columns

FRP confinement can be used to increase the strength and the lateral displacement capacity of concrete structural members such as columns, walls, and beams.

Reinforced concrete structural members such as columns and beams can be confined with FRP systems to increase their axial load-carrying capacity. Axial strengthening is most suitable for circular non-slender (i.e., short) reinforced concrete columns. Combined axial and flexural strengthening of short eccentrically loaded reinforced concrete columns will increase their axial and flexural capacity. An axial load-bending moment (*P–M*) strength interaction diagram can be constructed for an FRP-strengthened reinforced concrete column in a fashion similar to that of a non-strengthened column.

Axial strengthening is obtained by applying the FRP system oriented such that its principal fiber direction is in the circumferential (or hoop) direction of the member, perpendicular to its longitudinal axis. In addition to providing axial strengthening, hoop FRP reinforcement provides shear strengthening to the member, since it is oriented perpendicular to the member axis. When strengthening for only a single mode is intended, it is incumbent on the designer to determine the effects of the strengthening on the other modes and to ensure that the member has sufficient capacity in the other modes to resist the higher applied loads.

When the FRP hoop reinforcement is added to the exterior of the column, the apparent compressive strength of the concrete is increased. This apparent increase in the concrete strength is due to the confining effect of the FRP, which encircles and wraps the column completely (and thus is often referred to as a jacket). This increased concrete strength, known as the confined compressive strength and denoted as f'_{cc} occurs only after the concrete in the column has begun to crack and hence dilate. This typically occurs after the internal transverse reinforcing steel has yielded. By preventing the cracked concrete from displacing radially, the FRP serves to confine the concrete and allow it to carry additional compressive stress (and hence compressive load) [6,83].

The confining pressure provided by the FRP jacket is uniform around the circumference of the column when the column is circular. A free-body diagram of a half of the cross section of a thin-walled pressure vessel is shown in Figure (4.4). The relationship between the geometric parameters of the column and the thin-walled FRP wrap (diameter, D, and thickness, t), the circumferential (hoop) stress, f_θ, and the radial stress due to the internal pressure, f_r, is found from equilibrium as

$$f_r = \frac{2 f_\theta t}{D} \tag{4.83}$$

$$f_\theta = E_{f\theta}\varepsilon_{f\theta} \tag{4.84}$$

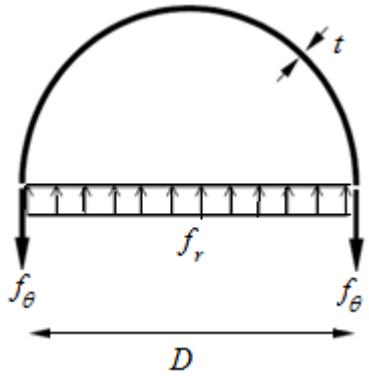

Figure 4.4: Free-body diagram of a thin-walled pressure vessel in the cross-sectional plane [6]

The cross-sectional reinforcement ratio is defined as

$$\rho_f = \frac{A_f}{A_c} = \frac{\pi D n t_f}{\pi D^2/4} = \frac{4nt_f}{D} \tag{4.85}$$

Then;

$$f_r = \frac{\rho_f E_{f\theta}\varepsilon_{f\theta}}{2} \tag{4.86}$$

FRP axial strengthening of circular columns can be achieved using either continuous or intermittent coverage. Since the axial load is constant along the full height of the column, the FRP wrap must cover the full height of the column; however, it can be spaced intermittently, in either intermittent or spiral hoop form. It has been shown that the confining effect is reduced when intermittent hoops are used and that the confining effect depends on the spacing of the hoops (Saadatmanesh et al., 1994; Nanni and Bradford, 1995). Equations to estimate the confinement effectiveness of intermittent hoop strips can be found in Saadatmanesh et al. (1994) and Mander et al. (1988). Consider to include these equations in your thesis! It is important to note that the ACI 440.2R-02 equations presented below apply only to continuous FRP wraps.

The theoretical concentric (nominal) axial load capacity of an FRP strengthened non-slender non- prestressed normal-weight concrete column internally reinforced steel reinforcement is given as

$$P_0 = 0.85\psi_f f'_{cc}\left(A_g - A_{st}\right) + f_y A_{st} \tag{4.87}$$

Where: A_g is the gross area of the concrete, A_{st} the area of the internal longitudinal steel, and f_y the yield stress of the internal longitudinal steel. Except for the addition of the FRP partial strength reduction factor, ψ_f, and the use of the confined concrete compressive strength, f'_{cc} , instead of the conventional concrete compressive strength f'_c, this equation is the same as that used for conventional concrete columns.

For an FRP-strengthened non-slender non-prestressed normal weight concrete column reinforced internally with spiral steel, the maximum nominal axial load capacity is given as

$$P_{n(\max)} = 0.85[0.85\psi_f f'_{cc}\left(A_g - A_{st}\right) + f_y A_{st}] \tag{4.88}$$

The maximum nominal axial capacity of an FRP-strengthened non-slender non-prestressed normal-weight concrete column reinforced internally with tied steel reinforcement is given as

$$P_{n(\max)} = 0.80[0.85\psi_f f'_{cc}\left(A_g - A_{st}\right) + f_y A_{st}] \tag{4.89}$$

According to ACI 440.2R-02, the confined compressive strength, f'_{cc} is to be taken as

$$f'_{cc} = f'_c\left(2.25\sqrt{1 + 7.9\frac{f_l}{f'_c}} - 2\frac{f_l}{f'_c} - 1.25\right) \tag{4.90}$$

f'_{cc} is a confined concrete compressive strength, function of the unconfined concrete strength f'_c, and the confining pressure provided by the FRP wrap, denoted by ACI 440.2R-02 as f_l and given as:

$$f_l = \frac{k_a \rho_f E_f \varepsilon_{fe}}{2} \tag{4.91}$$

Where:

$$\varepsilon_{fe} = 0.004 < 0.75 f_{fu} \tag{4.92}$$

In the case when steel reinforcement is not used, the term which is related to steel should be neglected. Therefore, the maximum nominal axial load capacity will be in the form of:

$$P_{n(\max)} = 0.85\psi_f f'_{cc}(A_g) \tag{4.92}$$

CHAPTER 5 NUMERICAL MODELING

5.1 Introduction

Since the early years of the mathematical modeling of problems in continuum and mechanics, the numerical analysis have concluded that the exact solution to some of the controlling differential equations hardly ever exists, and even if it did, it is frequently hard to accustom for common use. Analytical approaches like series expansions asymptotic integration have been used in solving some problems, but they still fall short of general applicability [81].

Recently, numerical analysis has become the essential tool for design and research problems.

Analytical solution can be found for certain simplified situations. For problems concerning complex materials properties and boundary conditions, numerical methods are typically used, that give approximate and suitable solutions. In the numerical methods, the solution more commonly capitulates approximate values of unidentified quantities only at a separate number of points in the structure. The way of choosing only a certain number of discrete points in the body structure can be described as “discretization”. One of the ways of discetizing a body or a structure is to split it into an equivalent system of small bodies or structures. These bodies are then assembled to represent the solution for the original body, and inside this combination, the bodies are assumed to be connected to each other at separate points called nodes.

Many numerical methods had been developed before the electronic computers being. The best well know methods are the finite difference method, residual methods for instance, the method of least squares and variational methods such as the Rayleigh-Ritz method, in which approximate functions are assumed for the unknown functions to be determined. Both these

methods take linear combination of approximating functions which makes a given function stationary. But the major difference between these two methods is that assumed approximating functions, in the finite element methods are not defined over the entire solution domain, but only in the small domain (element) and mainly at the nodes, and they are not necessary to satisfy boundary conditions, but it has to satisfy the continuity condition at the nodes. In the Ritz method, functions are defined over the whole domain, therefore, it can be used only for domains of relatively simple geometric shapes, while in finite element method the same constraint exists but for the elements only, since element of simple shape can be collected to present complex geometries [82].

5.2 Finite Element Method

Finite element method came into the sight of numerical analysis about seven decades ago; it has been developed in 1943 by R. Courant. Finite element method started as an extension to the matrix methods and their applications to trusses and frames of directly connected members by matching the nodal displacements and with no consideration for the inter-element continuity. Since that time, finite element method has expended beyond proportions to the extent of covering more fields than structural mechanics such as heat flow, fluid flow, seepage of water, and others.

The formulation of finite element method was mainly based on two principles. The first is the principle of minimum potential energy, which is concerned with satisfying the continuity conditions within the structure and the kinematic boundary conditions, but no requirements that the equilibrium of stress and boundary conditions be satisfied (displacement or stiffness model); the second is a principle of minimum complementary energy which is concerned with the stress

fields that satisfy the conditions of equilibrium, but not necessarily the requirements of compatibility (stress or flexibility model).

In 1943 R. Courant, benefited of the Ritz method of numerical analysis and minimization of variational calculus to obtain approximate solutions to vibration problems.

Afterward, M. J. Turner, R. W. Clough, H. C. Martin, and L. J. Topp published their paper. The paper focused on the "stiffness and deflection of complex structures"; then by the early of 70s, the use of FE analysis was very limited, partially due to the high cost of mainframe computers. Such mainframes were generally owned only by the aeronautics, automotive, defense, and nuclear industries. With the development of personal computers, the finite element analysis came into existence as one the most powerful tools to be used in the analysis of engineering problems , and since the rapid decline in the cost and the extraordinary increase in computing power, FEA has been developed to an unbelievable accuracy. Today with more development and improvement that happened on computer technology, supercomputers are now able to produce accurate results for all types of parameters.

Finite element analysis includes a computer model of a material or structure that is stressed and analyzed for specific results. It is used for both new product design and existing product improvement.

In general, two types of analysis are used in finite element to model any type of structure, 2-D modeling, and 3-D modeling. Although 2-D modeling has advantage of simplicity and allows the analysis to be run on a normal-speed computer, it tends to yield less accurate results. 3-D modeling, however, produces more accurate results while sacrificing the ability to run on all but the fastest computers effectively. Within each of these modeling systems, the users can insert many functions which may make the system conduct linear or non-linear analysis. Linear

systems are less complex and generally do not need to take plastic deformation in the consideration. While non-linear systems do account for plastic deformation.

FEA uses a complex system of points called nodes which make a grid called a mesh. This mesh is programmed to contain the material and structural properties which define how the structure will react to certain loading conditions. Nodes are assigned at a certain density throughout the material depending on the predictable stress levels of a particular area. Sections which will receive large amounts of stress typically have a higher node density than those which experience little or no stress. Points of interest may consist of fracture point of previously tested material, fillets, corners, complex detail, and high stress areas. The mesh acts like a spider web in that from each node, there extends a mesh element to each of the adjacent nodes. This web of vectors is what carries the material properties to the object, creating many elements.

One of the important applications of FEM is the analysis of crack propagation problems. Basics of the present form of the linear elastic fracture mechanics (LEFM) came to the existence practically in marine laboratories during the First World War. Since then, LEFM has been productively applied to a variety of classical crack and defect problems, but remained relatively limited to simple geometries and loading conditions.

Rapidly, development of the finite element method has changed the extent of application of LEFM. FEM practically had no limitation in solving complex geometries and loading conditions, and soon it was extended to nonlinear materials and large deformation problems. Application of FEM into linear elastic fracture mechanics and its extension to elastic plastic fracture mechanics (EPFM) has now extended to almost all crack problems. Parametric studies and experimental observations have even resulted in the introduction of new design codes for containing a stable crack. However, the essence of analyses remained almost unchanged: LEFM

basic concepts combined with classical continuum based FEM techniques through smeared or discrete crack models. After that, a major breakthrough seemed to be developing in the basic idea of part of unity and in the form of the eXtended Finite Element Method (X-FEM or XFEM) [78].

5.3 Extended Finite Element Method

The Extended Finite Element Method (XFEM) is a method used to model strong and weak discontinuities independent of the finite element mesh by using the partition of unity finite element method [81].

The first attempt to develop the extended finite element method could be dated back to 1999 when Belytschko and Black (1999) presented a minimal re-meshing finite element method for crack growth. The concept has been built by adding discontinuous enrichment functions to the finite element approximation to account for the being there of the crack. The method allowed the crack to be arbitrarily allied within the mesh, in spite it required re-meshing for harshly curved cracks.

In 1999, *Moës et al.* improved the method and called it the extended finite element method (XFEM). This improvement allowed for independent representation of the whole crack from the mesh, based on the construction of the enriched approximation from the interaction of the crack geometry with the mesh.

In 1999, Dolbow has achieved a major step during his PhD thesis at Northwestern University which was titled “Extended finite element method with discontinuous enrichment for applied mechanics”. As a result of his work a solution of two dimensional elasticity and Mindlin–Reissner plates by using both a jump function and the asymptotic near tip fields using XFEM. Also, in 2000, Dolbow *et al.* 2000 have presented a system to model arbitrary

discontinuities in the finite element framework by locally enriching a displacement based approximation through a partition of unity method.

Furthermore, in 2000, Sukumar et al. extended the XFEM for three-dimensional crack modeling and addressed geometric matters connected with the representation of the crack and the enrichment of the finite element approximation.

Another topic has been studied by Daux *et al.* (2000) as extensions to the original XFEM. They focused on the modeling of random branched and intersecting cracks with multiple branches, multiple holes and cracks originating from holes.

Level set methods gradually grew to represent the crack location, including the location of crack tips. In 2001, Stolarska *et al.* introduced a way of coupling the level set method (LSM) with XFEM to model crack growth. By the year of 2001, Belytschko *et al.* presented a technique for modeling arbitrary discontinuities in the function and its derivatives in finite elements. The discontinuous approximation was constructed in terms of a signed distance function, so level sets could be used to update the location of the discontinuities. Also, another effort has been done by Sukumar *et al.* (2001) who described modeling holes and inclusions by level sets in the extended finite element method.

Meanwhile, in 2002, Moës *et al*, and Gravouil *et al* discussed the mechanical model and level set update for non-planar three dimensional crack growth, based on a Hamilton–Jacobi equation to update the level sets with a velocity extension approach to preserve the old crack surface [78].

Lately, the extended finite element method (X-FEM) has come out as a powerful numerical procedure for the analysis of crack problems. It has been widely acknowledged that the method eases crack growth modeling under the assumptions of linear elastic fracture

mechanics (LEFM). Since the introduction of the method about a decade ago, many new extensions and applications have shown up in the scientific literature, with substantially many contributions on X-FEM in recent years.

In the extended finite element method, additional functions, commonly referred to as enrichment functions, can be added to the displacement approximation as long as the partition of unity is satisfied, $\sum N_I(x) = 1$, whereas $N_I(x)$ represent the finite element shape functions. The XFEM uses these enrichment functions as a tool to introduce a non-smooth behavior of field variables, for instance, stress across the interface between different materials or displacement across cracks. Generally, the enrichment functions presented into the displacement approximation are only described in excess of a small number of elements relative to the total size of the domain. Extra degrees of freedom are presented in all elements where the discontinuity is exist, and depending on the type of function selected, probably some adjacent elements identified as combination elements.

Comparing to the standard finite element method, the X-FEM offers significant benefits in the numerical modeling of crack propagation. In the traditional concept of the FEM, the existence of a crack is modeled by requiring the crack to follow element edges. On the contrary, the crack geometry in the X-FEM does not need to be aligned with the element edges that provide flexibility and versatility in modeling. The method is based on the enrichment of the finite element model with extra degrees of freedom (DOFs) which are tied to the nodes of the elements discussed by the crack [79]. In this manner, the discontinuity is included in the numerical model with no modifying the discretization, as the mesh is generated without taking into account the being there of the crack. Therefore, only a single mesh is needed for any crack length and orientation. As well, nodes around the crack tip are

enriched with DOFs associated with functions that copy the asymptotic LEFM fields. This enables the modeling of the crack discontinuity within the crack-tip element and substantially increases the accuracy in the calculation of the stress intensity factors (SIFs).

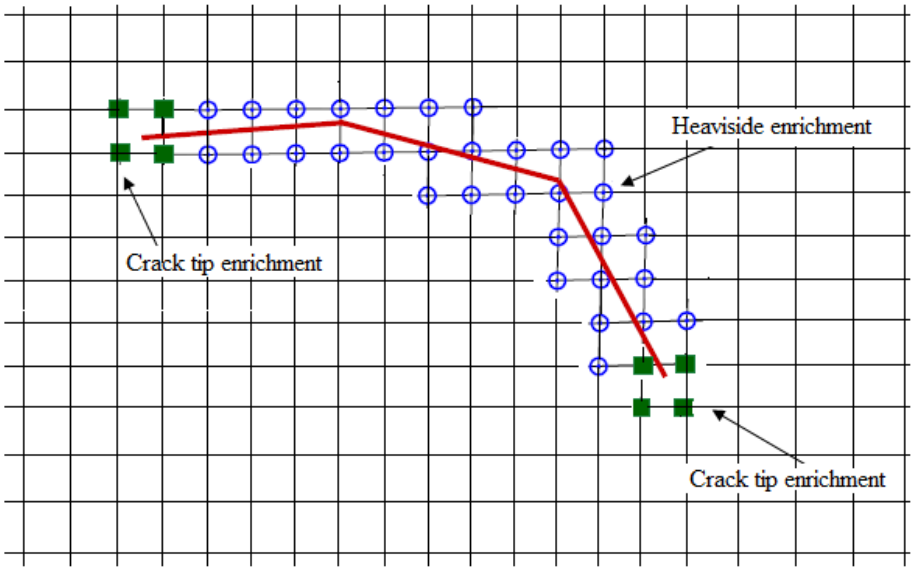

Figure 5.1: The nodes enriched with the Heaviside and crack tip enrichment functions.

As shown in figure 5.1, the circled nodes are the nodes enriched with two additional DOFs (total of four DOFs per node), whereas the nodes marked with a square are enriched by eight more DOFs (total of ten DOFs per node). Elements that contain at least one enriched node are known as enriched elements. Nodes with two additional DOFs (one for each coordinate direction) have shape functions that multiply the Heaviside function H(x) (function of unit magnitude whose sign changes across the crack, H(x) = ±1), whereas H(x) equals positive above the crack, and is negative below the crack. Actually, this function introduces the discontinuity across the crack faces. Nodes with eight additional DOFs are enriched in the two Cartesian directions with four crack tip functions $F_\alpha(x)$ [18].

$$[F_\alpha(r,\theta), \alpha = 1-4] = \left[\sqrt{r}\sin\frac{\theta}{2}, \sqrt{r}\cos\frac{\theta}{2}, \sqrt{r}\sin\frac{\theta}{2}\sin\theta, \sqrt{r}\cos\frac{\theta}{2}\sin\theta\right] \quad (5.1)$$

Where: r,θ represent local polar co-ordinates defined at the crack tip. The displacement approximation for crack modeling in the extended finite element method can be written in the form

$$u_{xfem}(x) = \sum_{i\epsilon I} N_i(x)u_i + \sum_{i\epsilon j} N_i(x)H(x)a_i + \sum_{i\epsilon k}\left[N_i(x)\sum_{\alpha=1}^{4} F_\alpha(x)b_{i\alpha}\right] \quad (5.2)$$

Where: I represents the set of all nodes in the mesh, $N_i(x)$ is the nodal shape function and u_i is the standard DOF of node i (u_i represents the nodal displacement for non-enriched nodes only). j and k contain the nodes enriched with Heaviside function $H(x)$ or crack-tip functions $F_\alpha(x)$, respectively, and a_i, $b_{i\alpha}$ are the corresponding DOFs. In case there is no enrichment, then the above equation reduces to the classical finite element approximation

$$u_{fe}(x) = P_i N_i(x)u_i \quad (5.3)$$

The additional functions are used in the displacement approximation are typically called enrichment functions and the approximation is written as

$$u^h(x) = \sum_I N_I(x)\left[u_I + \sum_j v^j(x)a_I{}^j\right] \quad (5.4)$$

Where: u_I represents the classical finite element degrees of freedom, $v(x)$ is the j^{th} enrichment function, and $a_I{}^j$ is the enriched degrees of freedom corresponding to the j^{th} enrichment function at the I^{th} node. The enriched degrees of freedom defined by Eq. (5.1) generally do not have a physical meaning and instead can be considered as a calibration of the enrichment functions which result in the correct displacement approximation.

Equation (5.4) does not satisfy the interpolation property, $u_I=u^h(x_I)$ because of the enriched degrees of freedom, instead additional calculations are required in order to calculate the physical displacement by utilizing equation (5.4). The interpolation property is important in practice in applying boundary or contact conditions. Therefore, it is a common

practice to shift the enrichment function to the shape:

$$\Upsilon_I^J(x) = v^J(x) - v_I^J(x) \tag{5.5}$$

Where: $v_I^J(x)$ is the value of the J^{th} enrichment function at the I^{th} node. As the shifted enrichment function now takes a value of zero at all nodes, the solution of the resulting system of equations satisfies $u_I=u^h(x_I)$ and the enriched degrees of freedom can be used for additional actions such as interpolation and post-processing. Here, the shifted enrichment functions are referred to with upper case characters, and the unshifted enrichment functions are referred to with lower case font. The shifted displacement approximation is in the form

$$u^h(x) = \sum_I N_I(x)\left[u_I + \sum_j \Upsilon_I^J(x) a_I{}^j\right] \tag{5.6}$$

Where: $\boldsymbol{\Upsilon_I^J(x)}$ represents the J^{th} shifted enrichment function at the I^{th} node.

5.4 Finite Element Simulation by Using ABAQUS- CAE Software

ABAQUS/CAE is a complete ABAQUS environment that provides a simple, consistent interface for creating, submitting, monitoring, and evaluating results from ABAQUS/Standard and ABAQUS/Explicit simulations. ABAQUS/CAE is divided into modules, where each module defines a logical aspect of the modeling process; for example, defining the geometry, defining material properties, and generating a mesh. As one moves from module to module, you can build the model from which ABAQUS/CAE generates an input file that you submit to the ABAQUS/Standard or ABAQUS/Explicit analysis product. The analysis product performs the analysis, sends information to ABAQUS/CAE to allow you to monitor the progress of the job, and generates an output database. At a minimum the analysis model consists of the following information:

- Discretized geometry.
- Element section properties.

- Material data.
- Loads and boundary conditions.
- Analysis type.
- Output requests.

In this research, ABAQUS/CAE 6.9 release has been utilized to implement the scope of work. Compared with other computer softwares, one of the major advantages of this software is the flexibility of implementing, revising, analyzing the model, and getting results. But the more important function of this release of ABAQUS/CAE 6.9 is that it allows a crack to grow up with or without specifying the locations of the crack initiation.

5.4.1 Concrete Beam Simulation

For non-linear finite element analysis, ABAQUS-CAE software was used to model the behavior of plain concrete. The modeling space was chosen 2D planar and the type was deformable, (figure 5.2).

Figure 5.2: 2D planar concrete beam model

The element has been considered as an elastic-isotropic material. The material behaviors have been selected to be “Maxps Damage”, and the properties are shown in table 5.1.

Table 5.1: Concrete material properties

Young's Modulus	$4.23x10^6$ psi
Compressive Strength	5502psi
Poisson's ratio	0.18
Density	0.0867 lb/in^3

The element has been meshed by size of 0.2 and for the mesh control the element shape was considered a quad-dominated structured. Figure (5.3)

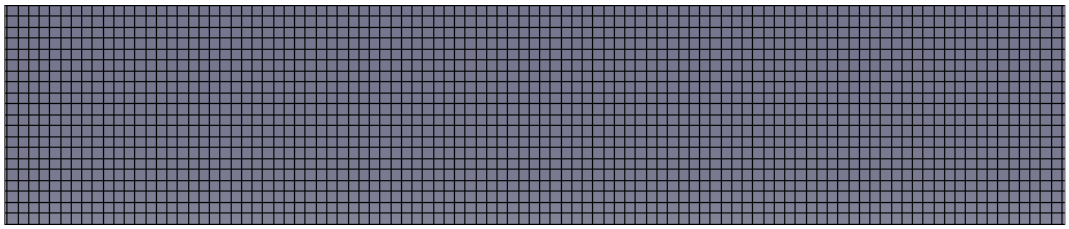

Figure 5.3: Mesh of the 2D planar concrete beam model

The load has been used as a static concentrated dead load and the type of boundary conditions was selected displacement/rotation, one support was considered as a pin and the other roller, figure (5.4).

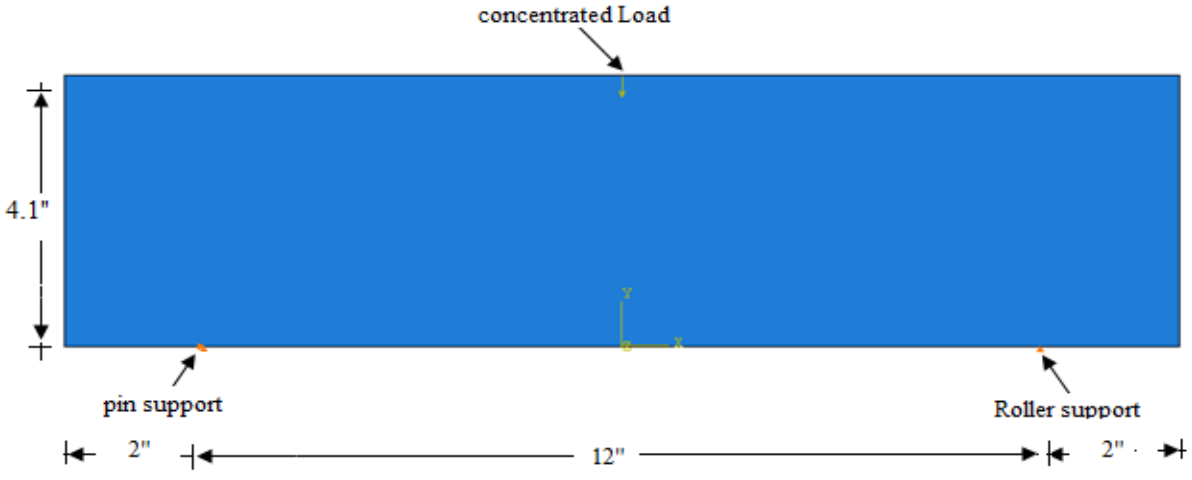

Figure 5.4: Load and boundary conditions of concrete beam model

5.4.2 Concrete Column Simulation

ABAQUS-CAE software was used to model the behavior of concrete column. The modeling space was chosen 3D and the type was deformable (see figure 5.5).

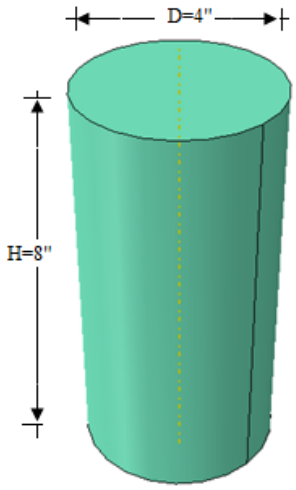

Figure 5.5: 3D Concrete column model

Similar to the concrete beam model, the element has been considered as an elastic-isotropic material. The material behaviors have been selected “Maxps Damage”, and the properties are listed in Table 4.1.

The element has been meshed by size of 0.1 and for the mesh control the element shape was considered “Hex” while the element shape technique has been chosen “sweep” and the element type was “3D stress”. The fine mesh of the concrete column is shown in figure 5.6.

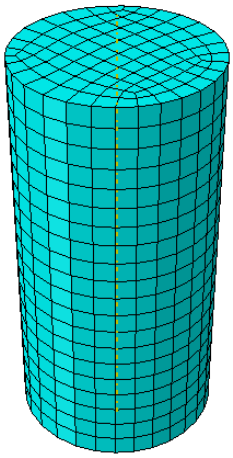

Figure 5.6: Mesh of 3D concrete column model

The type of load has been used as a static pressure on the upper surface and the type of boundary conditions at the bottom surface was selected displacement/rotation, figure (5.7).

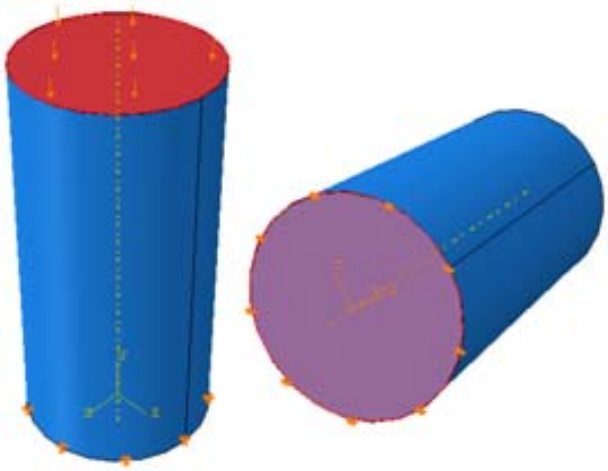

Figure 5.7: Load and boundary conditions of 3D concrete column model

5.4.3 Simulation of Epoxy Beams

The strength of epoxy materials plays an important role in the bonding between concrete and FRP strengthening materials because it is used as an interface adhesive. To compare the experimental investigation, 2D-deformable Epoxy beams have been modeled with a thickness (width) of 1.3″, figure (5.8). The objective is to simulate the flexural behavior of the epoxy

specimens, which have been prepared as already discussed in Chapter three (sections 3.3, 3.8.1) and tested under different conditions.

Figure 5.8: 2D planar Epoxy beam model

The properties of each epoxy materials were provided by the manufacturers, as listed in Tables 3.8 and 3.10 in Chapter three.

The beam model has been meshed by a size of .05, as shown in Figure (5.9). A quad-dominated structured was selected of the mesh control, the element type has been chosen as plane strain.

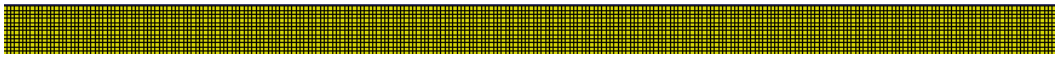

Figure 5.9: Epoxy beam meshing

Concerning the load and boundary conditions, same steps and procedures was followed here. The load was applied by a static concentrated load at the center of the span, while the beam was simply supported. The type of boundary conditions was chosen to be displacement/rotation; one end was supported by a pin (u_1 and u_2=0), and the other by a roller (u_2=0). Both the end supports were located at a distance of 1.7″ from the edge with a clear supported length of 9.6″ as shown in Figure 5.10.

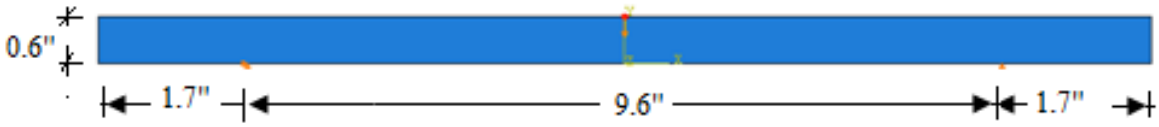

Figure 5.10: Load and boundary conditions of Epoxy beam model

5.4.4 FRP Strengthened Beam Simulation

Numerical analysis is performed using the ABAQUS-CAE extended finite element program to predict the flexural deflection and failure of rectangular concrete beam

strengthened by a fiber reinforced plastics sheet applied at the bottom of the beam.

Two-dimensional planar extended finite element model was developed to examine the structural behavior of the strengthened beam. The modeling space was chosen 2-D planar and divided into two parts. The first part represented the rectangular concrete beam model where all geometries and properties have been considered previously same as the un-strengthened concrete beam model, (Figure 5.2). The second part was for the FRP Strengthening Sheet. The modeling space has been chosen 2-D planner and deformable was selected as a type of model (Figure 5.11).

Figure 5.11: FRP strengthening sheet model

The material properties of the FRP sheets depend on the type of fibers and resin of the composite. The meshing seed was chosen edge by size 0.1 and the mesh controls selected Quad dominated, while the mesh technique has been considered as structured and the element type was plane strain. (Figure 5.12).

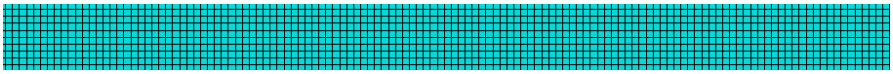

Figure 5.12: Mesh of FRP strengthening sheet

The damage evaluation has been selected to be the same as in the un-strengthened concrete beam simulation.

To connect the two parts, the type of constraint that has been used was “Tie” and a surface-to-surface contact was assumed. The concrete beam was designated as the master surface and the FRP was the slave surface (see figures 5.13 and 5.14).

Figure 5.13: Contact surfaces between concrete beam and FRP strengthening sheet

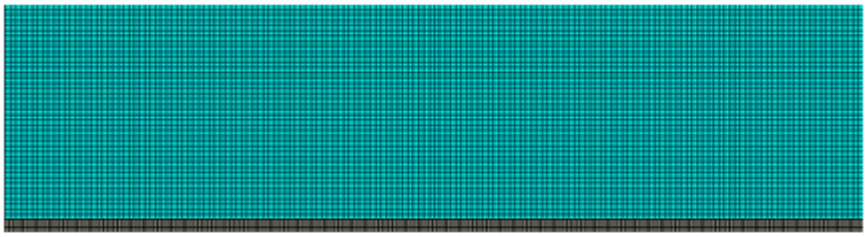

Figure 5.14: Mesh of FRP strengthened beam model

The load was applied as a static concentrated load and the type of boundary conditions has been selected “displacement/rotation”. One support was considered as a pin and the other a roller, (see figure 5.15)

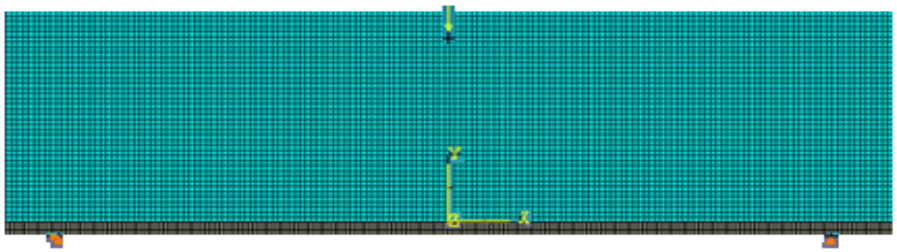

Figure 5.15: Load and boundary conditions of FRP strengthened beam model

5.4.5 FRP Strengthened Column Simulation

Likewise with some differences of the procedures which have been followed to simulate the FRP strengthened concrete beam, the FRP strengthened column has been treated. A 3D nonlinear extended finite-element analysis of the FRP-strengthened column was carried out using the ABAQUS/CAE release 6.9. Interface elements between the FRP and concrete have been utilized. The model was divided into two parts. While the first part represented the 3-D cylindrical concrete column with a dimension of 8″ in height and 4″ in diameter, the second part dealt with the FRP jacket. The same steps and procedures that were used to simulate the plain concrete column have been followed to implement the first part of this simulation. Figure (5.16)

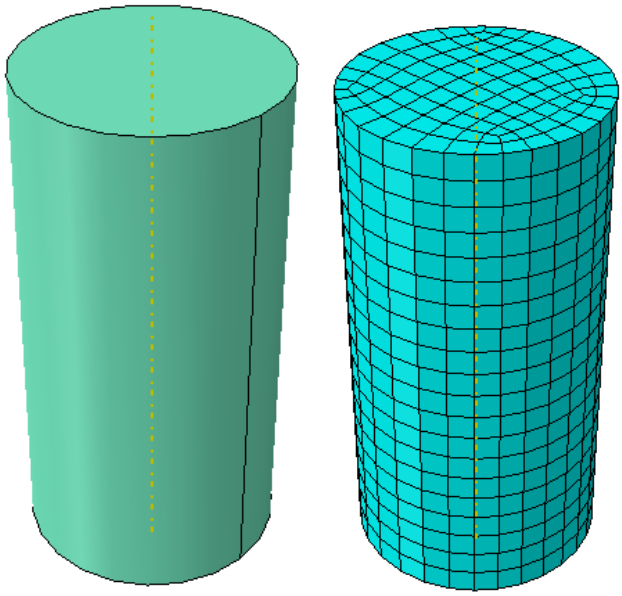

Figure 5.16: Concrete column model

The second part of this simulation involved the FRP Strengthening Sheet. The modeling space has been chosen 3-D and deformable was selected as a type of model figure (5.17).

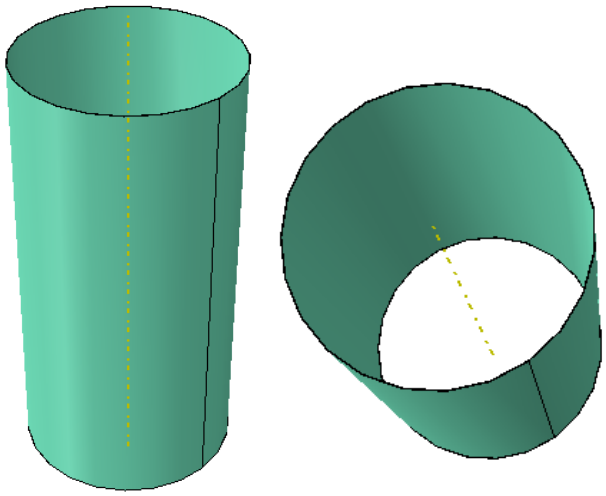

Figure 5.17: FRP strengthening jacket

The material properties of the FRP depend on the type of the fiber and the resin used. The mesh seed was chosen edge by size 0.1 and the mesh controls selected Quad dominated, while the mesh technique has been considered as structured and the element type was 3-D stress. (Figure 5.18).

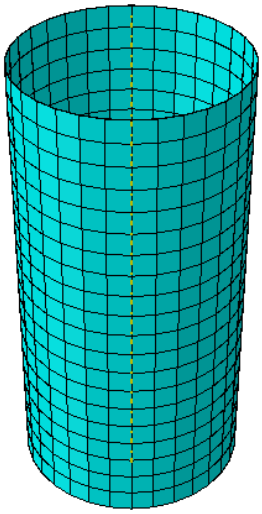

Figure 5.18: Mesh of FRP strengthening jacket Model

The damage evaluation has been selected to be the same as those for the un-strengthened concrete column simulation.

To connect the two parts, a tie constraint connection was used. Therefore, a surface-to-surface contact was established. The concrete was chosen as the master surface and the FRP was taken as the slave surface (Figure 5.19).

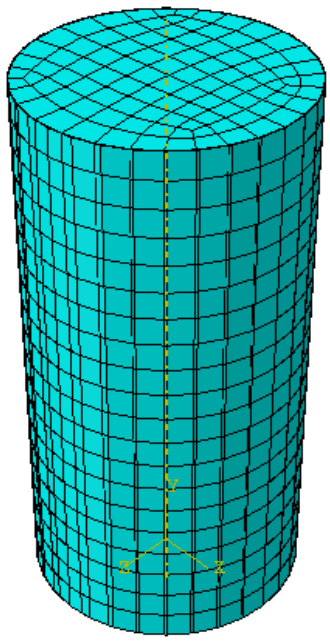

Figure 5.19: Contact surfaces between concrete column and FRP strengthening sheet

The load has been selected as a static pressure on the upper surface the model and the type of boundary conditions at the bottom surface was chosen displacement/rotation (Figure 5.20).

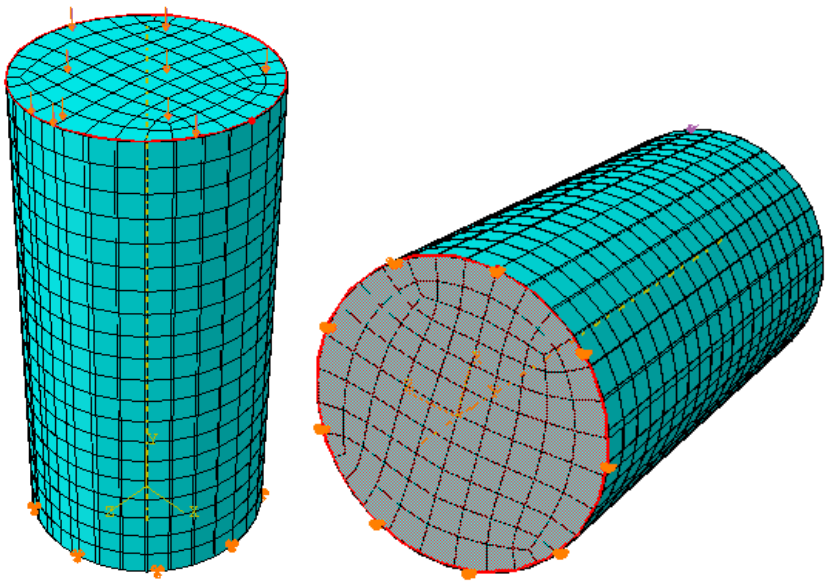

Figure 5.20: Load and boundary conditions of FRP strengthened Column model

CHAPTER 6 EXPERIMENTAL RESULTS AND DISCUSSIONS

6.1 Introduction

In total, 255 concrete specimens were constructed, cured, and tested under various environmental conditions with and without FRP strengthening materials. 135 specimens were rectangular concrete beams, and 120 specimens were cylindrical concrete column specimens. Each of these two groups has been divided into two different and separate sets. While the first set was concrete specimens without FRP strengthening materials, the second one had strengthened with different types and sources of FRP and epoxy materials. In addition, within each one of these two sets, there were subsets that were subjected to different environmental conditions.

In addition, 69 epoxy beam specimens were casted, cured, and experimentally tested under center point flexural load after have been yielded to different environmental conditions.

Concrete mix was designed for a nominal compressive strength of 5502 psi (38MPa). The control specimens were tested at the age of 28 days. All concrete specimens were taken out from the molds at the second day of casting and placed into water basin for curing.

6.2 Experimental Results and Discussions for Unstrengthened Concrete Specimens

To make this study comprehensive, the influence of temperature (T), relative humidity (RH), number of cycles (Cy), and the cycle period (Cp) on the compressive and flexural strength of concrete were of significant interest in this research. 28 plain concrete beams, (Figure 6.1) and 12 cylindrical plain concrete column specimens, (Figure 6.2) were implemented and tested after subjected to diverse environmental conditions. Prior to environmental conditioning, all specimens were cured for 28 days in water.

Figure 6.1: Concrete beam specimens

Figure 6.2: Cylindrical concrete column specimens

6.2.1 Experimental Results for Unstrengthened Concrete Beams

Three plain concrete beams B2, B21, B67 have been utilized as the control beam. These beams were tested for flexural strength using three-point loading according to ASTM C293-08 after 28 days in water. To verify the quality control of the concrete mix design, casting, and

curing, these specimens were selected from three different batches of concrete specimens which were prepared at different time. As shown in table 6.1, the average maximum flexural load of these three specimens was 3061.6 *lbs*. The type of failure of these three beams was flexural failure, where the vertical crack originated at the mid-span, then propagates vertically to the top of the beam, Figure 6.3.

Figure 6.3: flexural failure of control concrete beam B2

The relationship curves between flexural load and deflection of these specimens are shown in figure 6.4. The deflection reading represents the crosshead displacement of the MTS machine.

Table 6.1: Flexural strength test results of control beam specimens

Beam no.	Max. deflection^{+} (in)	Max. load (lbs)	Mean* (lbs)	Max. flexural strength (psi)	Stiffness (lbs/in)	Failure mode
B2	0.0243	2876.3	3061.6	808.2	98623	Flexural
B21	0.0265	3264.5		911.6	108112	Flexural
B67	0.0278	3044.1		856.2	101303	Flexural

*mean of the max. flexural load in *lbs*

$^{+}$ mid-span deflection at the maximum load

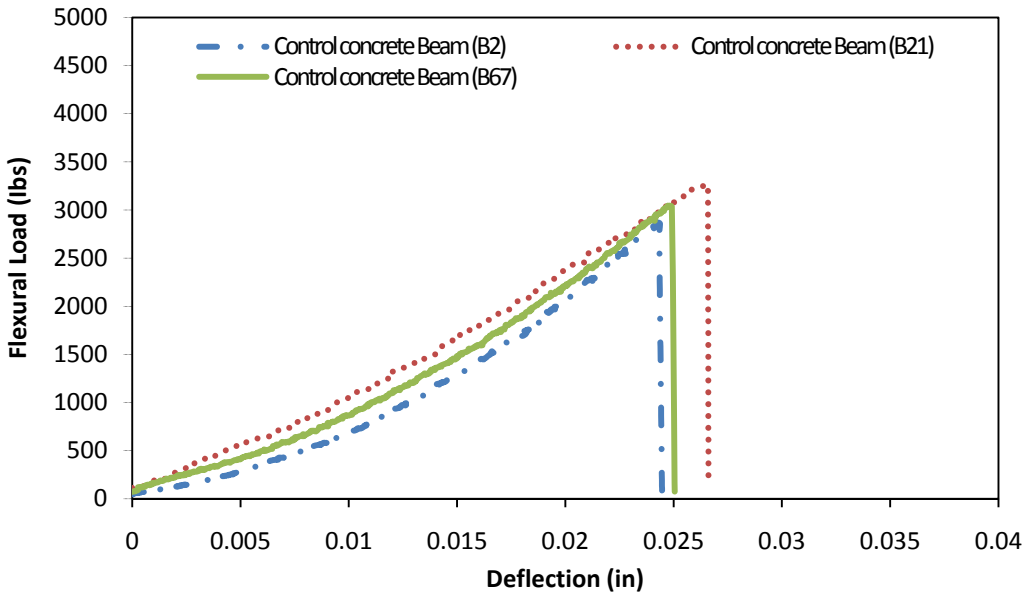

Figure 6.4: Control-concrete beams, flexural load-max. deflection results

To study the effect of temperature and relative humidity on concrete flexural strength, ten plain concrete beams have been subjected to 100^{o}C temperature and different relative humidities, number of cycles, and cycle periods as shown in table 6.2. Figure 6.5 shows the center point deflection-flexural load curves.

Table 6.2: Flexural strength test results of concrete beam specimens conditioned at 100^{o}C

Beam no.	Temp. ^{o}C	RH %	Cy	CP (*Hr*)	Max. load *Ibs*	Mean* lbs	Flex. strength (*psi*)	**Difference** - %	Failure mode
B62	100	0.0	100	2	4555.4	4335.9	1280.1	41.6	Flexural
B63					4116.4		1156.7		Flexural
B68			625		3453.9	3788.9	970.5	23.8	Flexural
B69					4123.9		1158.8		Flexural
B64		100	100	2	3744.3	4022.5	1052.1	31.4	Flexural
B65					4300.7		1208.5		Flexural
B82			250		4305.4	4348.5	1209.8	42.0	Flexural
B83					4391.4		1234.0		Flexural
B70			625		3643.1	3858.7	1023.7		Flexural
B71					4076.3		1145.4	26.0	Flexural

*mean of the max. flexural load in *lbs*

Figure 6.5: Concrete beam subjected to flexural load test

All the above ten specimens failed due to flexural crack at the center of the beam, Figure 6.6 shows the mode of failure for one of these beams.

Figure 6.6: Flexural failure of concrete beam-100^{o}C

The above results showed that the flexural strength of concrete beams increased due to subjecting to 100^{o}C of temperature, the magnitudes of flexural strength increases varied with the

number of cycles. The strength was the highest after 250 cycles, comparing to 100 cycles, then the strength was reduced after 625 cycles. The relative humidity shows small changing between 0% and 100% of humidity. Figure 6.7 shows the flexural load and deflection curves. For clearance, only one curve from each group was plotted.

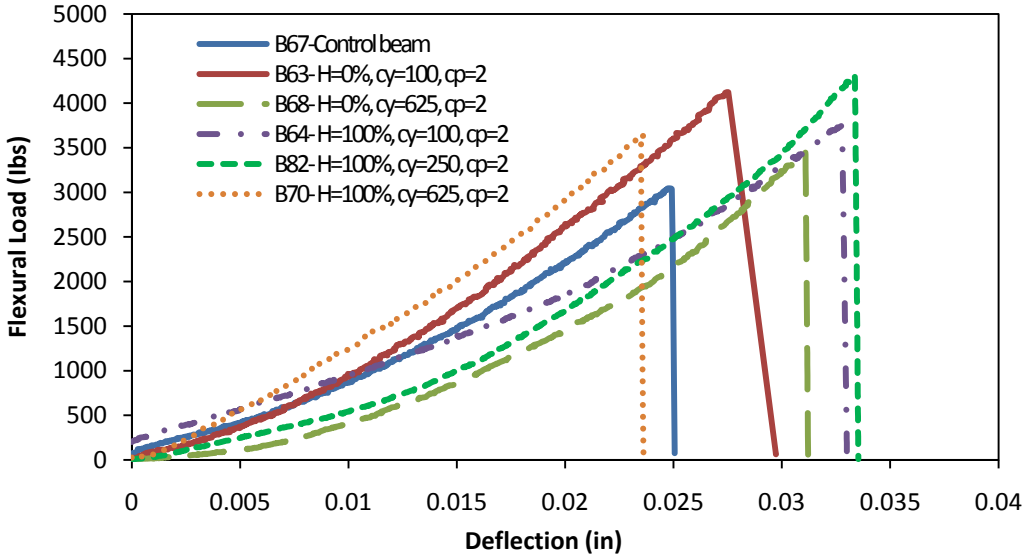

Figure 6.7: Concrete beams, flexural load - deflection results - 100°C

Another 16 plain concrete beam specimens have been exposed to 180°C of temperature and various relative humidities, number of cycles, and cycle periods. As shown in table 6.3 and figure 6.8, the flexural strength at 180°C decreased if compared to 100°C of temperature. The relative humidity showed some influence on the flexural strength of the specimens at 180°C. The flexural strengths of the samples conditioned at 100% relative humidity were less than those results of 0% relative humidity at the same numbers of cycle. On the other hand, the effect of cycle period (2 hours vs. constant temperature at 180°C) became insignificant. The mode of failure for all these 16 specimens was flexural failure where, the flexural crack appeared at the center of the specimens then it propagated through the specimen's height. Figure 6.9 explains the mode of failure of one of these specimens.

Table 6.3: Flexural strength test results of concrete beam specimens 180°C

Beam no.	Temp. °C	RH %	Cy	CP[1] (Hr)	Max. load *lbs*	Mean *lbs*	Flex. strength (*psi*)	Difference[-] %	Failure mode
B76	180	0	100	0	3535.3	3501.8	93.4	14.4	Flexural
B77					3468.2		974.6		Flexural
B78			625		3222.1	3172.2	905.4	3.6	Flexural
B79					3122.2		877.3		Flexural
B72			100	2	3361.6	3606.7	944.6	17.8	Flexural
B73					3851.7		1082.3		Flexural
B74			625		3187.5	3089.7	895.7	0.918	Flexural
B75					2991.9		840.7		Flexural
B84		100	100	0	2381.4	2504.9	669.2	-18.2	Flexural
B85					2628.4		738.6		Flexural
B86			625		2654.9	2454.7	746.0	-19.8	Flexural
B87					2254.5		633.5		Flexural
B80			100	2	3464.5	3254.6	973.5	6.3	Flexural
B81					3044.7		855.6		Flexural
B88			625		2479.6	2463.3	696.8		Flexural
B89					2447.0		687.6	-19.5	Flexural

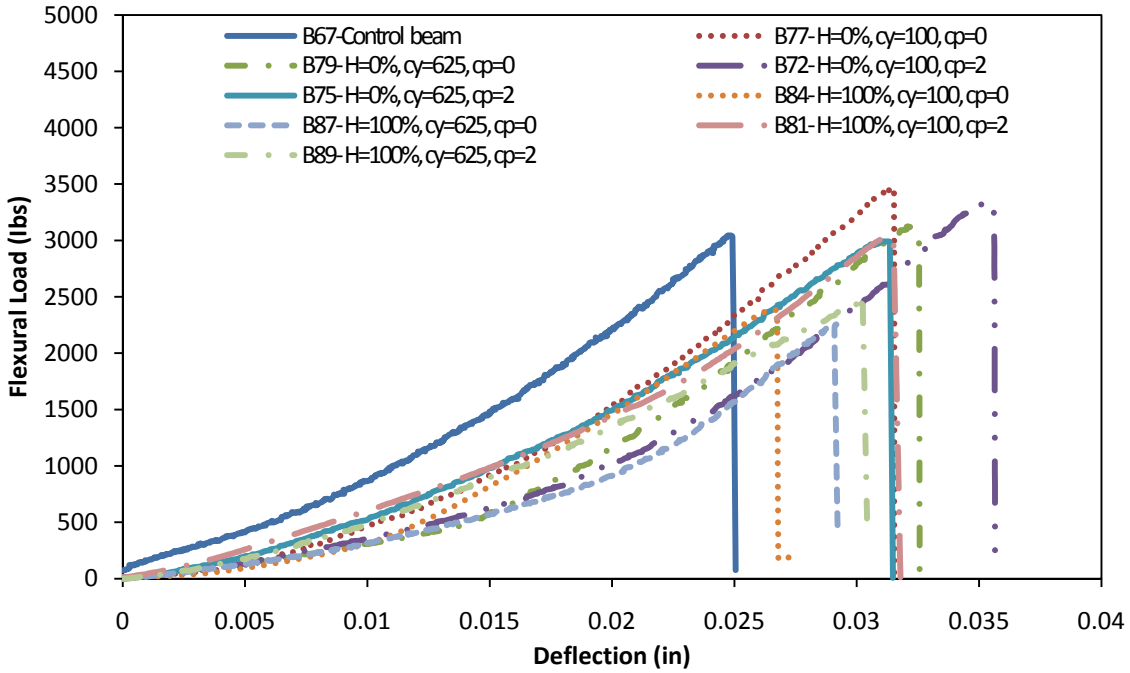

Figure 6.8: Concrete beams, flexural load-max. deflection results - 180°C

Figure 6.9: Flexural failure of concrete beam-180^{o}C

Table 6.4 shows a comparison of the maximum deflection, max flexural load and the stiffness of the 100^{o}C temperature concrete beam specimens and the control specimens. The data that is tabulated in table 6.4 is the average results of two same condition specimens.

Table 6.4: Concrete beam specimen results, T= 100^{o}C

Number of Cycles	T (^{o}C)	RH %	CP (hrs)	Max. Deflect on (in)	Max. flexural load (lbs)	Stiffness (lbs/in)
Control	LT	LH	-	0.0262	3061.6	102679
100	100	0	2	0.0248	4335.9	136449
625	100	0	2	0.0354	3788.9	74730
100	100	100	2	0.0282	4022.5	110330
250	100	100	2	0.0613	4348.5	45943
625	100	100	2	0.0812	3858.7	17592

Figure 6.10 represents the maximum deflections vs. number of cycles, the results of this figure shows that the deflection increases with increasing the time of exposing to the environmental conditions. The increase was much more significant when the relative humidity

was 100%. At 100 cycles of exposing, the deflection results were almost same of the deflection of control specimen results.

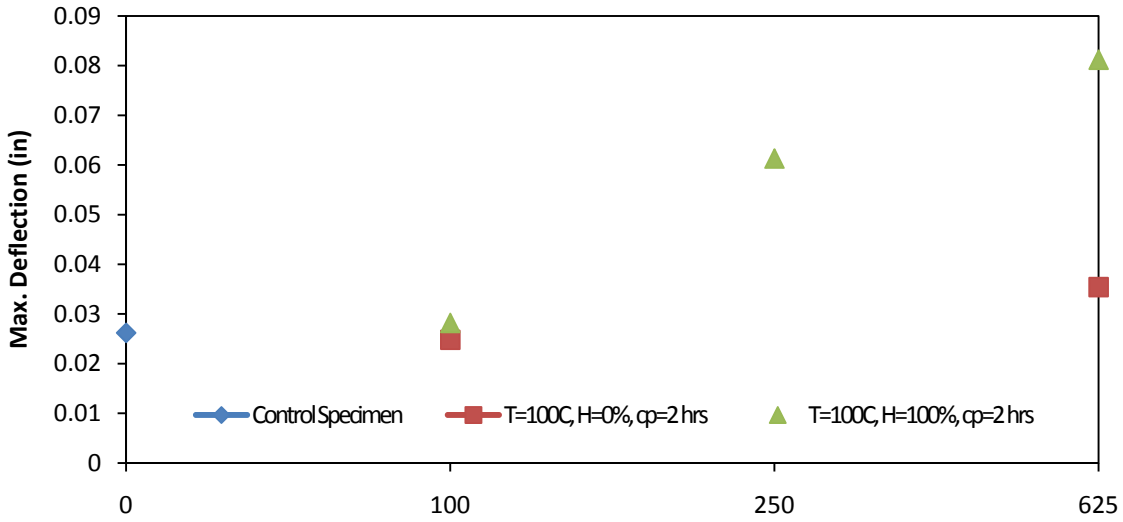

Figure 6.10: Max. deflection vs. number of cycles at100^{o}C temperature

Comparing to the control specimens, the maximum flexural load of 100^{o}C temperature specimens increased about 42% after 100 cycles and 250 cycles, while the increase was 26% after 625 cycles. The relative humidity doesn't show any influence on the flexural strength of 100^{o}C concrete beam specimens (see figure 6.11). As shown in figure (6.12), the stiffness of these specimens has effected inversely by increasing the number of cycles.

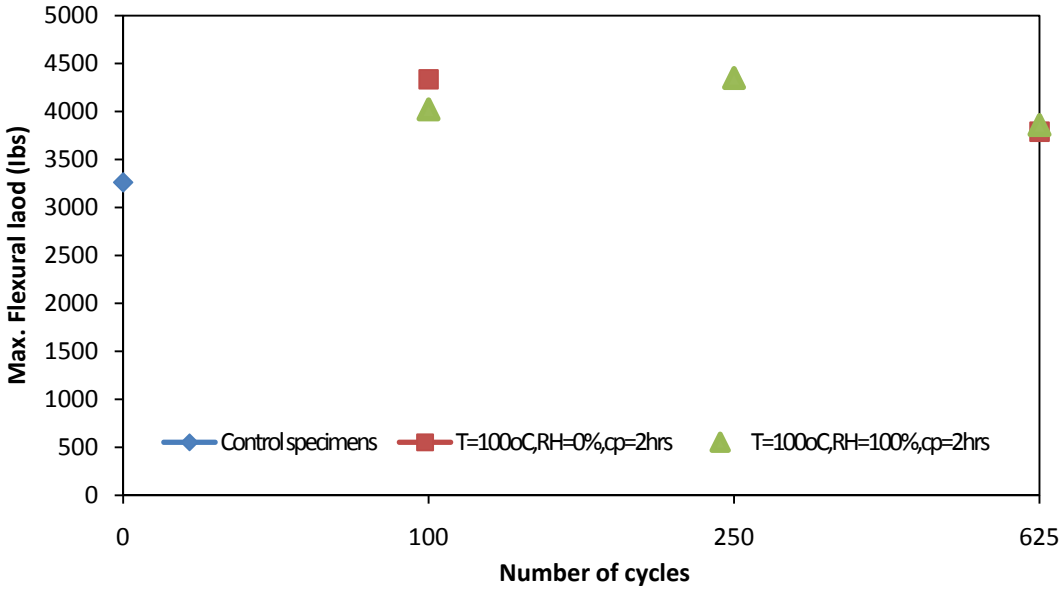

Figure 6.11: Max. flexural load vs. number of cycles scatter at100^{o}C temperature

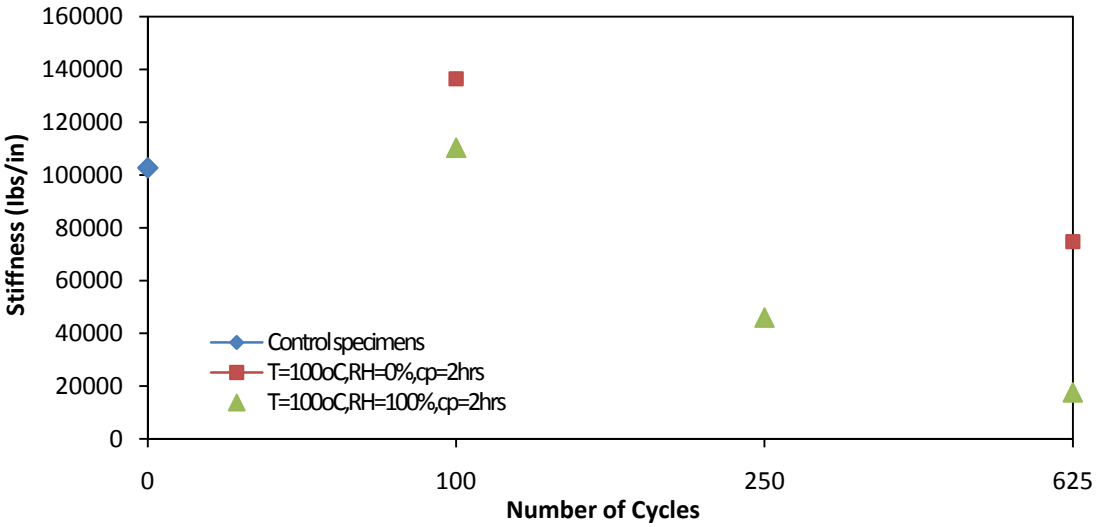

Figure 6.12: Stiffness vs. number of cycles scatter at100^{o}C temperature

More details are explained in table (6.5) about the plain concrete beam specimens that have been subjected to 180^{o}C, different relative of humidities, number of cycles, and cycle periods. These quantities include the maximum deflection, maximum flexural load, and the specimen stiffness. By the same way that is utilized in Table (6.4), the data that are tabulated in

table (6.5) are the average results of two same condition specimens.

Table 6.5: Concrete beam specimen results, T= 180°C

Number of Cycles	T (°C)	RH %	CP (hrs)	Max. Deflection (in)	Max. flexural load (Ibs)	Stiffness (Ibs/in)
Control	LT	LH	-	0.0262	3061.6	102679
100	180	0	0	0.0400	3501.8	70730
625	180	0	0	0.0281	3172.2	91774
100	180	0	2	0.0409	3606.7	68997
625	180	0	2	0.0309	3089.7	81756
100	180	100	0	0.0297	2504.9	74876
625	180	100	0	0.0326	2454.7	54621
100	180	100	2	0.0292	3254.6	97005
625	180	100	2	0.0324	2463.3	71534

Comparing with the control specimen results, the mid-span deflection of the 0% RH samples has increased after 100 cycles for both 2 hours cycle period and non-cycle period. But when the exposure time increased to 625 cycles, the deflection reduced to the magnitude similar to that of the control specimen.

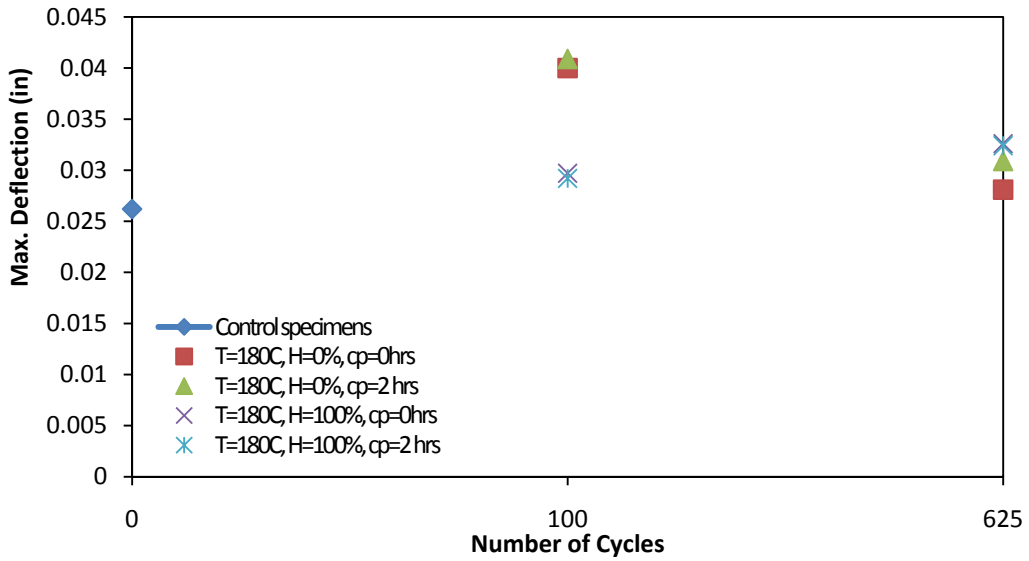

Figure 6.13: Deflection vs. number of cycles scatter at180°C temperature

Under the same 180°C of temperature and 0% relative humidity condition, the maximum flexural load showed an increase about 18% after 100 cycles and only 1% after 625 cycles comparing to the control specimen. While at 100% relative humidity and the same temperature of exposing, the flexural strength decreased 18% after 100 cycles and about 20% after 625 cycles comparing to control specimen, (see figure 6.14).

The relationship between the stiffness and the number of cycles is shown in figure 6.15. The stiffness result of 180°C of temperature is closed to the control specimen result regardless to the type of other environmental exposing.

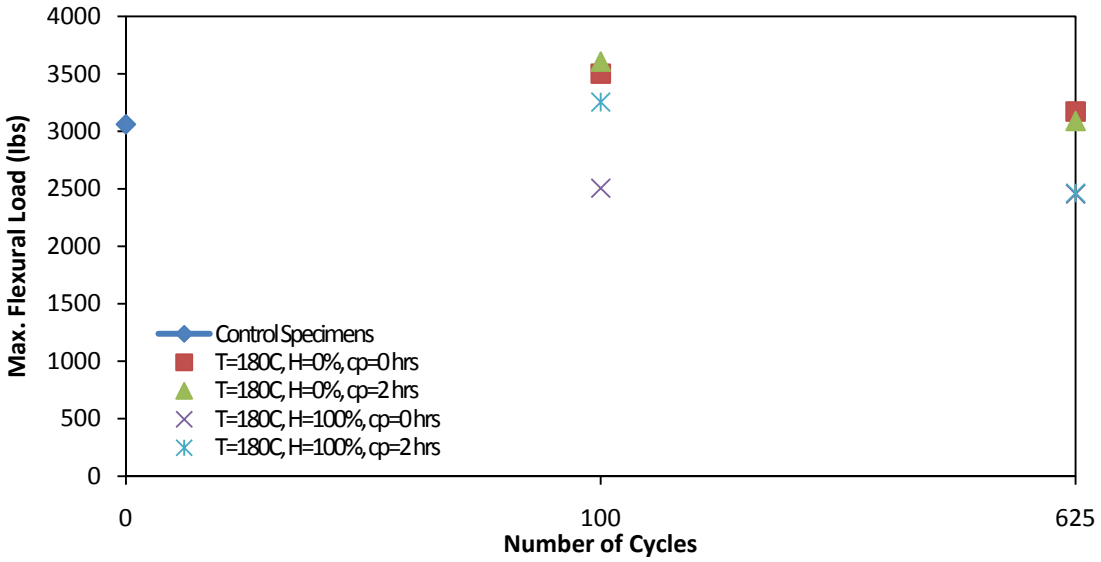

Figure 6.14: Max. flexural load vs. number of cycles scatter at180°C temperature

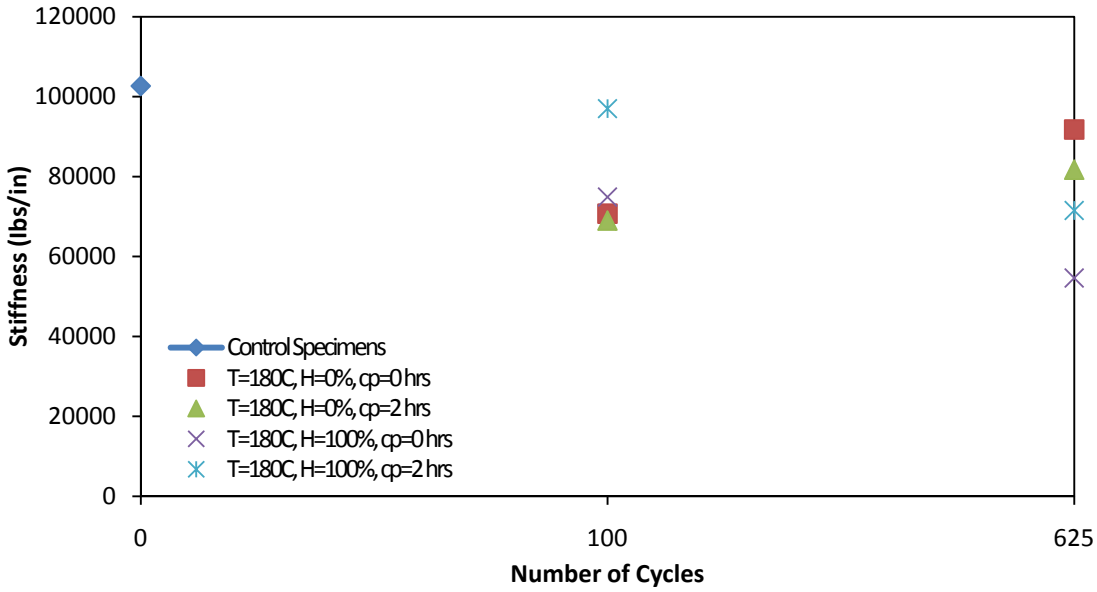

Figure 6.15: Deflection vs. number of cycles scatter at180^{o}C temperature

6.2.2 Experimental Results for Unstrengthened Concrete Columns

Two plain concrete columns C1 and C47 have been randomly selected and utilized as control. They were tested after 28 days of curing in water. All columns were tested for compressive strength according to ASTM C78-08, Figure (6.16). The mode of failure was concrete splitting failure, (see figure 6.17). Table 6.6 shows the deflection at maximum load, maximum compressive load, maximum compressive strength, stiffness, and the mode of failure of these two control specimens, where, the average maximum compressive strength of two specimens was 5502.0 psi, (38.0Mpa).

Figure 6.16: Compressive strength test C1 “control specimen”

Table 6.6: Compressive strength test results for control specimens (28 days)

Col. no.	Max. deflection^{+} (in)	Max. load (lbs)	Mean* (lbs)	Max. Compr. strength (psi)	Stiffness (lbs/in)	Failure mode
C1	0.0493	71981.1	69138.1	5728.243	1904956	Splitting failure
C47	0.0496	66295.1		5275.752	1932966	Splitting failure

*mean of the max. flexural load in *lbs*
$^{+}$ mid-span deflection at the maximum load

Figure 6.17: Concrete splitting failure of C1

Figure 6.18 represents the relationship between the compressive load and deflection of two control column specimens. The curve shows that the deflection at maximum load for both specimens is closed to each other.

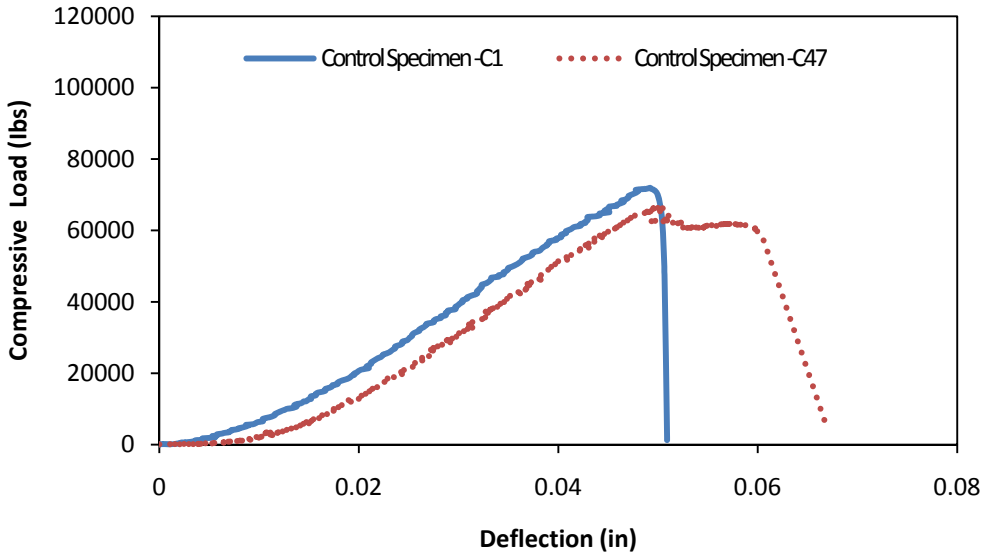

Figure 6.18: Compressive load- deflection curve results – "control specimens"

Six plain concrete column specimens had been exposed to 100^{o}C of temperature and other diverse environmental conditions as shown in table 6.7, and then were subjected to the compressive strength test, (Figure 6.19). The results demonstrate that the compressive strength of these specimens increased approximately 50% after 250 cycles, and about 25% after 625 cycles compared to the control specimen. Figure 6.20 illustrate the relationship curves between the compressive load and deflection of the 100^{o}C specimens, as well as the control specimen. As shown in figure 6.21 the mode of failure of all these six specimens were compression failure.

Table 6.7: Compressive strength test results of concrete column specimens 100°C

Col. no.	Temp. °C	RH %	Cy	CP[!] (Hr)	Max. load lbs	Mean lbs	Comp. strength (psi)	Difference[-] %	Failure mode
C48	100	0	625	2	96250.2	91976	7659.6	33.0	Compression
C49					87701.7		6979.3		Compression
C74		100	250		109826	103926	8739.9	50.3	Compression
C75					98027.2		7801.0		Compression
C50			625		86054.2	86369	6848.2	24.9	Compression
C51					86685.0				Compression

Figure 6.19: Compressive strength test C49 -100°C

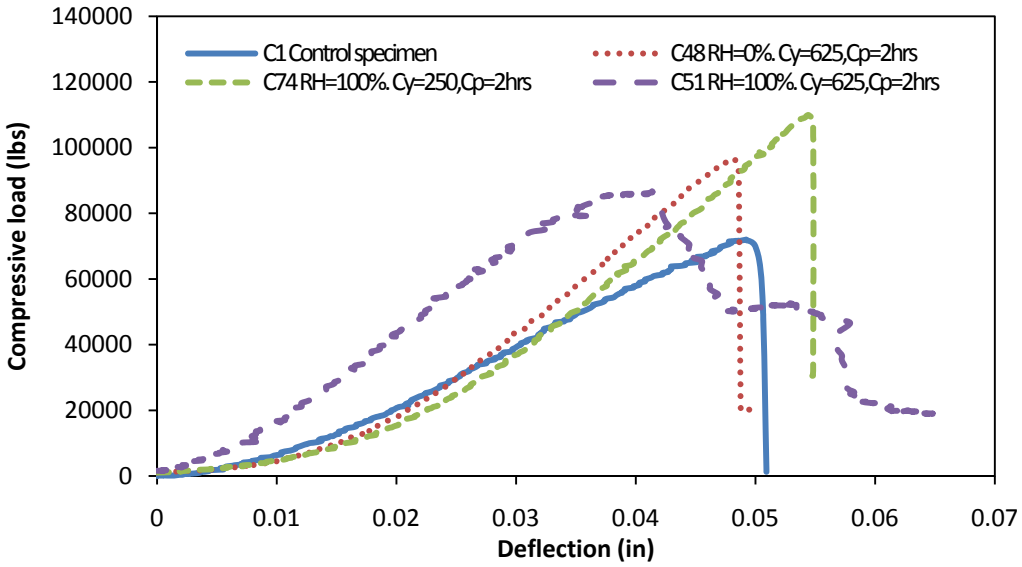

Figure 6.20: Compressive load- deflection curve results – 100°C

Figure 6.21: Compression failure of specimen C49 -100°C

Sixteen other plain concrete column specimens have been implemented and exposed to 180°C of temperature and different environmental conditions of relative humidities, number of cycles, and cycle periods, as summarized in table 6.8. All these 16 specimens were loaded under compression until fail, Figure (6.22). The mode of failure of all specimens was similar; the typical

compression failure has been observed for all of them. Figure 6.23 shows a typical of the failure shape.

Table 6.8: Compressive strength test results of concrete column specimens 180°C

Col. no.	Temp °C	RH %	Cy	CP[!] (Hr)	Max. load lbs	Mean lbs	Flex. strength (psi)	Difference - %	Failure mode
C52	180	0	100	0	74219.0	75412	5906.3	9.1	Compression
C53					76604.6		6096.2		Compression
C54			625		74176.7	75314	5903.0	8.9	Compression
C55					76452.0		6084.0		Compression
C56			100	2	75442.7	77281	6003.7	11.8	Compression
C57					79118.5		6296.2		Compression
C58			625		75206.6	74237	5984.9	7.4	Compression
C59					73267.5		5830.6		Compression
C60		100	100	0	70157.1	70739	5583.1	2.3	Compression
C61					71320.6		5675.7		Compression
C62			625		66215.0	64617	5269.4	-6.5	Compression
C63					63019.2		5015.1		Compression
C64			100	2	74550.8	74721	5932.7	8.1	Compression
C65					74890.4		5959.8		Compression
C66			625		62930.5		5008.0		Compression
C67					66463.2	64697	5289.1	-6.4	Compression

Figure 6.22: Compressive strength test C64 -180^{o}C

Figure 6.23: Compression failure of specimen C64 -180^{o}C

The test results are tabulated in table 6.8 and plotted in figures (6.24 and 6.25). Comparing with 100^{o}C of temperature, the 108^{o}C results indicate that the high temperature (180^{o}C) has an adversely influence on the compressive strength of the specimens regardless of the degree of relative humidity or the cycle periods. By comparing the results in figure 6.24 with figure 6.25, it

is evident that the strength reduction increased with increasing the exposure time.

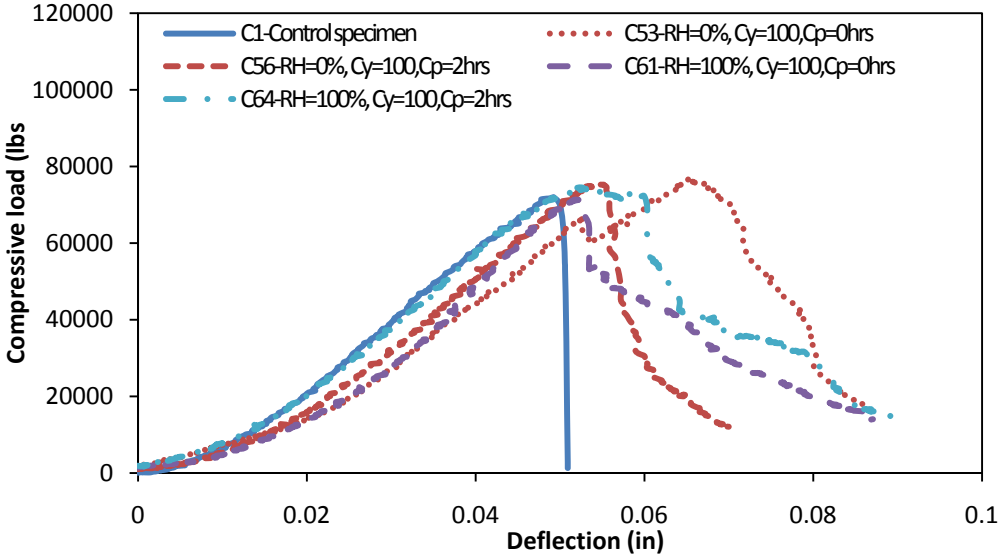

Figure 6.24: Compressive load-deflection curve results–180°C and 100 cycles

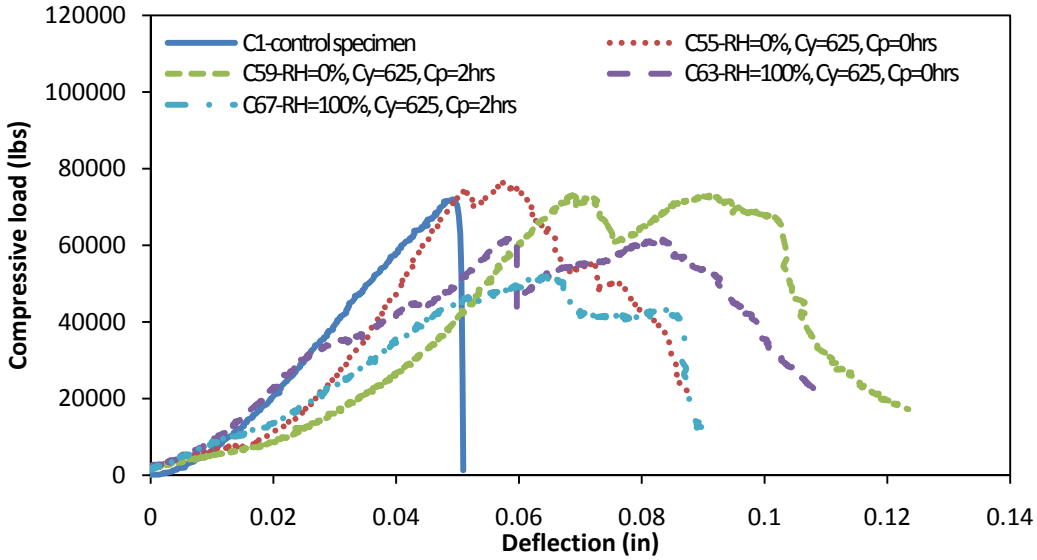

Figure 6.25: Compressive load-deflection curve results–180°C and 625 cycles

6.3 Experimental Results of Epoxy Beams

The resin material plays a vital role for the bonding between concrete surface and FRP strengthening material, where it is used as a bonding agent between the two surfaces. Therefore, in this research, much attention was paid to study this resin material. Investigation parameters included flexural strength, stiffness, and the hygrothermal effect on the strength of the resin material. To achieve this goal, 69 rectangular epoxy beam specimens with a dimension of 13″, 1.3″, 0.6″ (total length, width, thickness) respectively, were tested by center-point loading. The effective length was 9.6″ center to center support. These epoxy beams have been made from "Tyfo S epoxy" and cured for 14 days under standard laboratory conditions, where the temperature range was 21-25^{o}C (70-75^{o}F) and relative humidity was between 22% and 25%. Two specimens EB0 and EB01 were considered as control specimens; they have been tested right after the completion of the standard curing period of 14 days. Figure 6.26 shows the flexural strength test for one of the control beams by using center-point loading test. MTS 810 was used for this purpose, the rate of crosshead motion was calculated based on equation (6.1) of ASTM (D790-07) where found equal to 0.1066 mm/sec, (see equation 6.1).

$$R = \frac{ZL^2}{6d} \tag{6.1}$$

Where: R is the rate of crosshead motion, mm [in]/min,

L = support span, mm [in],

d = depth of beam, mm [in], and

Z = rate of starting of the outer fiber mm/mm/min, [in/in/min]. Z shall be equal to 0.01.

Figure 6.27 shows the deflection of the control specimen.

. The mode of failure for these two control specimens was flexural failure, Figure (6.28), where the specimen split at the mid-span into two parts and each part flew away from the test machine, which made it difficult to take pictures at the time of failure.

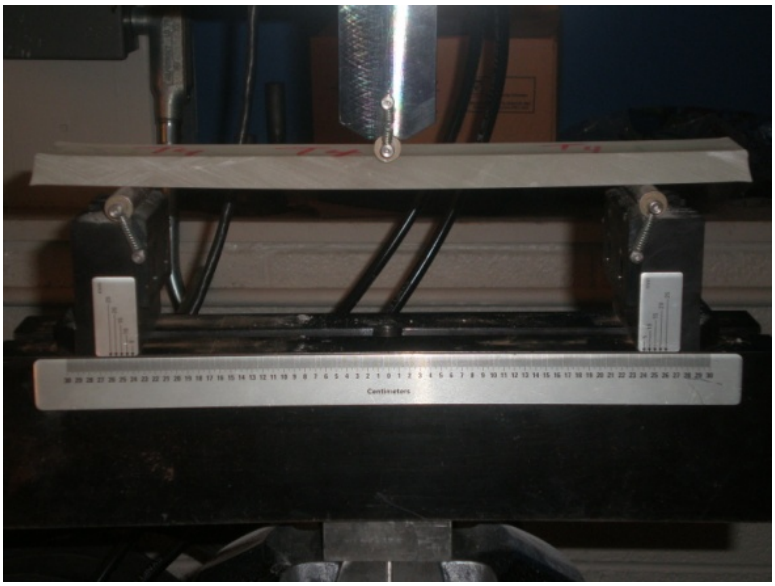

Figure 6.26: Center point-loading test of epoxy beam specimen loading

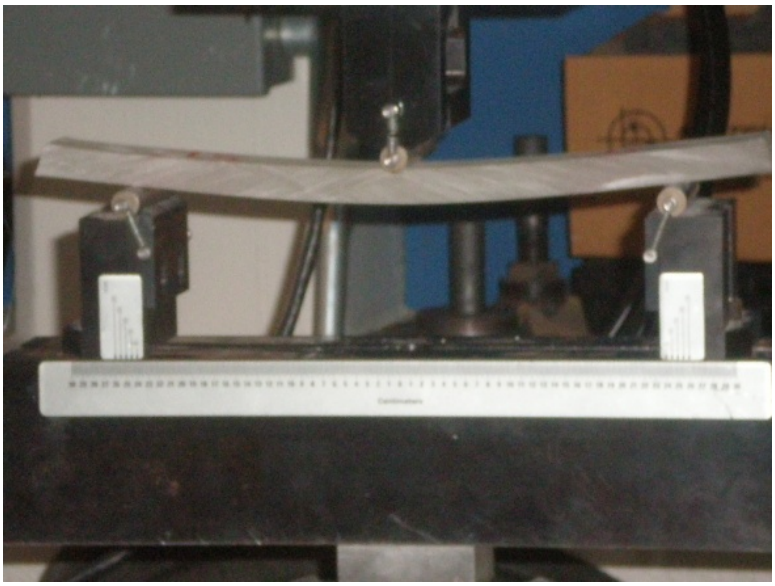

Figure 6.27: Deflection of the control specimen

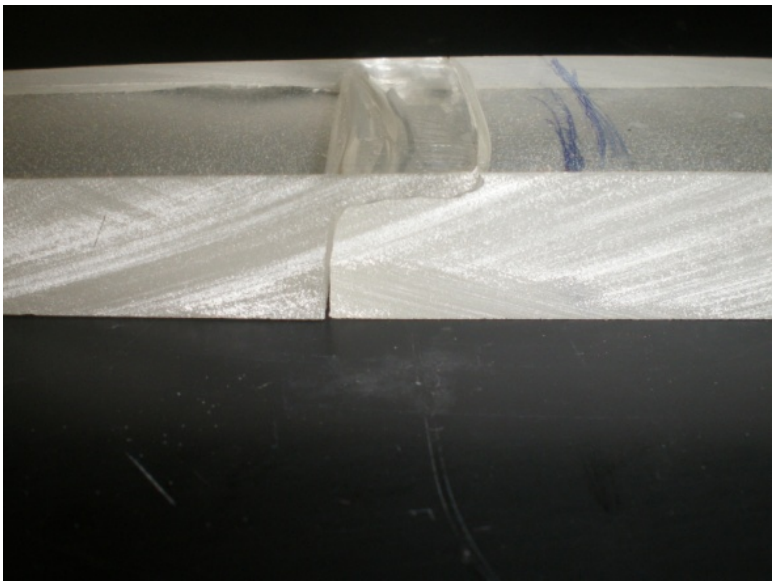

Figure 6.28: Failure mode of the control specimen

Table 6.9 shows the results of the control specimens, the maximum flexural load, maximum flexural strength, deflection at mid-span, stiffness, and the failure mode. All results of both specimens were close to each other. The stiffness of the specimens has been calculated by taking the trend (initial slope) of the flexural load- deflection curves. The average of the maximum flexural load of these two specimens was 243.0 lbs.

Table 6.9: Epoxy control beam specimen results

Beam no.	Max. deflection^{+} (*in*)	Max. load (*lbs*)	Mean* (*lbs*)	Stiffness (*lbs*/in)	Max. flexural strength (psi)	Failure mode
EB0	0.449	243.8	243	497.6	7501	Flexural
EB01	0.457	242.2		498.3	7452	Flexural

*mean of the max. flexural load in *lbs*

$^{+}$ mid-span deflection at the maximum load.

The relationship between the flexural load and the deflection is shown in figure 6.29. As mentioned in section 6.1 in this chapter, the deflection here represents the MTS crosshead movement.

All the specimens were subjected to a flexural strength test using center-point loading as well after being exposed to various environmental conditions. The results were

dissimilar depending on the type and the period of exposing condition.

It should be noted that all the specimens, subjected to the designated high temperature aging, are not tested immediately after removing from the ovens or the environmental chambers, but are left it in the air till cool.

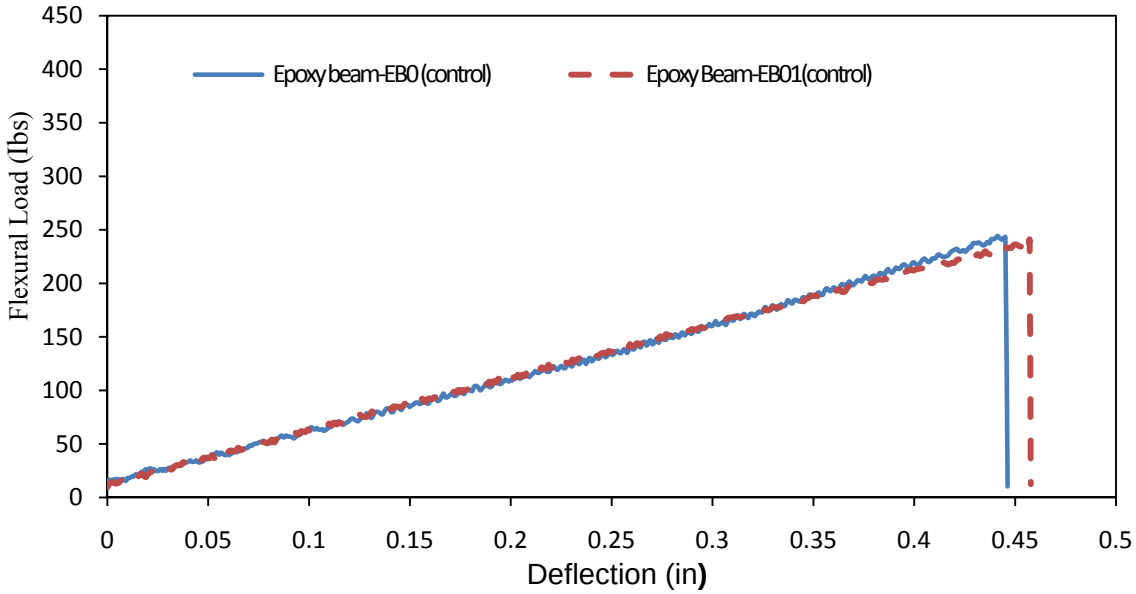

Figure 6.29: Flexural load-displacement curve of control epoxy beams

Ten epoxy beams EB1, EB2, EB9, EB10, EB17, EB18, EB25, EB26, EB33, and EB34 were subjected to different environmental cycling and tested after 40 cycles at a frequency of 2 hours (80 hours). Figure 6.30 shows the flexural-test setup for EB2. Epoxy beams EB1 and EB2 have been left under the standard lab condition for 80 hours which is equivalent to 40 cycles. While the other eight specimens were exposed to 100^{o}C of temperature and various conditions of relative humidity (RH) and cycle periods (Cp). Table 6.10 explains how each specimen has been treated and the results as well.

Comparing to the control specimens, after 40 cycles (Cy) of conditioning at various environments, the results show that the flexural strength increased by 9% under the standard lab condition and the change increased to 74% when the relative humidity was 100% and

0.0 cycles period. It is necessary to explain that the 0.0 cycle period means that the elevated temperature is constant during the time of environmental treatment. The results in table 6.10 show that the cycle period after 40 cycles of environmental exposure gave noticeable effect on the flexural strength of this resin material under both dry condition (0% of relative humidity) and 100%. In the case of 0% relative humidity, zero cycle period improved the strength by 42%, while at 2hrs period of cycles, the improvement was 60% compared to the control specimen results. When the relative humidity was 100% the difference between two hours cycle period and zero cycle periods (continuous cycle) was 38% (see table 6.10).

In addition, the effect of relative humidity (0% vs. 100%) was observed as well, it showed 13% difference in flexural strength after 40 cycles when the cycle of period was 2hrs, while at 0.0 period of cycles, the difference between 0% and 100% relative humidity was 74%. The type of failure of EB1 and EB2 which were subjected to the standard lab condition was flexural failure; figure 6.31 explains the flexural failure of EB2. The same failure has been observed for the both specimens EB17 and EB18 that exposed to 0.0% relative humidity and no cycles period. Also, similar type of failure was noticed on EB26 which was one of the two specimens that have been cured under 100% relative humidity and 0.0 period of cycle. Table 6.10 summarized the test results. Figure 6.32, shows the center-point loading test for specimen EB10. Figure 6.33 shows the deformation shape that occurred to specimen EB10 without any failure. Figure 6.34 shows the flexural strength verses mid-span deflection for the 40 cycle specimens. To make the curves easy to the reader and avoid any crowd of the curves on the same figure, for each two specimens have the same condition, one specimen result has been plotted.

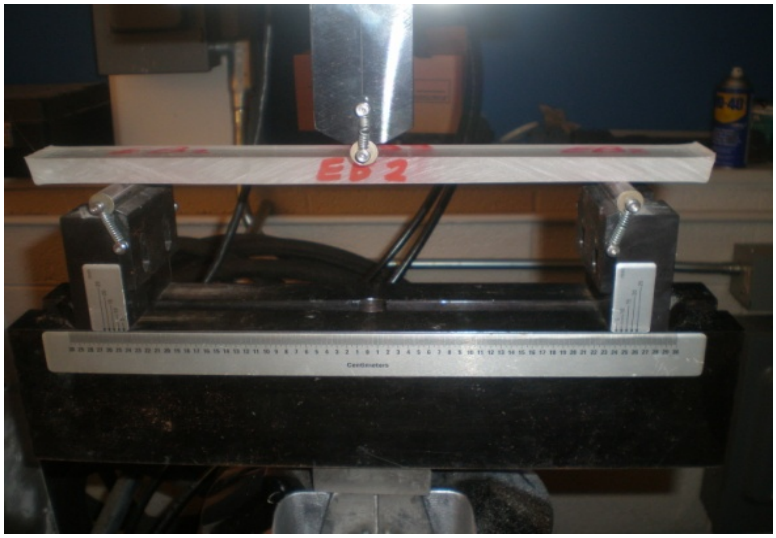

Figure 6.30: Flexural strength test for epoxy beam,(EB2) at 40 Cycles

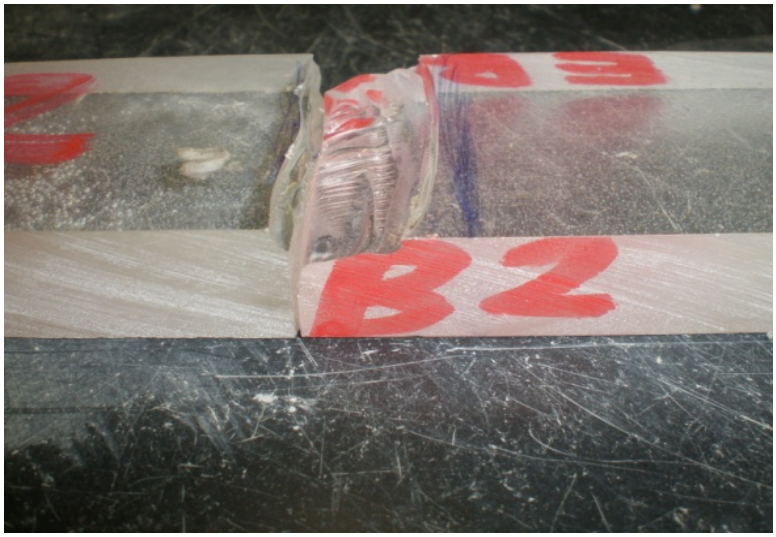

Figure 6.31: Flexural failure of the epoxy beam (EB2) at 40 Cycles

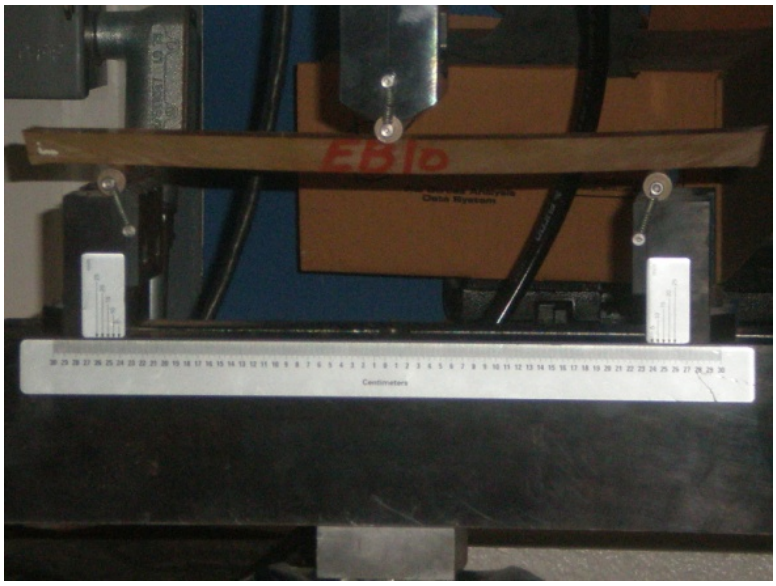

Figure 6.32: Flexural strength test for the epoxy beam (EB10) at 40 Cycles

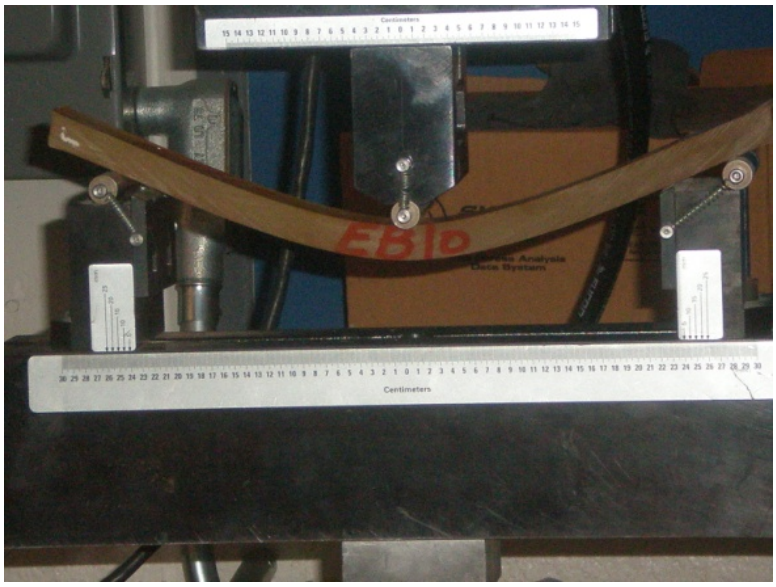

Figure 6.33: Deflection of the epoxy beam (EB10) at 40 Cycles

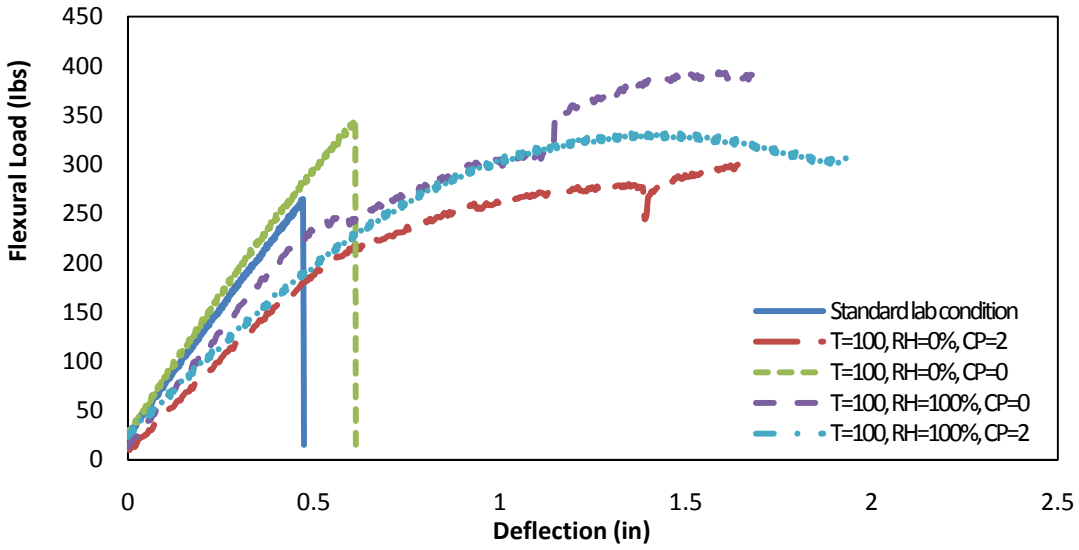

Figure 6.34: Flexural load-mid-span deflection curves of epoxy beams subjected to different environmental conditions with 100°C and 40 cycles

Table 6.10: Epoxy beam maximum flexural strength results subjected to different environmental conditions with 100°C and 40 cycles

Beam no.	Temp. °C	RH %	CP! (Hr)	Max. load lbs	Mean lbs	Flex. strength (psi)	Difference - %	Failure mode
EB1	LT*	LH+	-	265.5	264.9	8169.2	9.0	Flexural
EB2				264.4		8135.4		Flexural
EB9	100	0.0	2	384.7	389.7	11836.9	60.4	No failure
EB10				394.8		12147.7		No failure
EB17			0	344.7	346.3	10606.2	42.5	Flexural
EB18				348.0		10707.7		Flexural
EB25		100	0	393.0	422.6	12092.3	74	No failure
EB26				452.3		13916.9		Flexural
EB33			2	413.9	372.9	12735.4		No failure
EB34				332.0		10215.4	53.5	No failure

-Percentage difference of max. load increasing or decreasing compared with control result.
*Lab temperature,
+Lab humidity,
!Cycle period,

Further to the change of the strength and the mode of failure due to exposure to 100°C temperature and humidity, the color change of the specimens has been observed as well. While unexposed specimens show white color, this color changed gradually to light-to

brown depending on the temperature, humidity and the time of exposed, Figure (6.35).

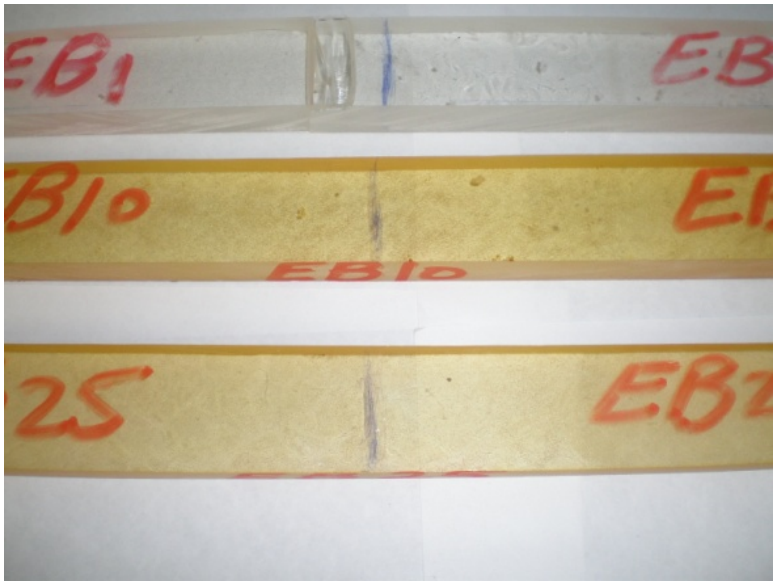

Figure 6.35: Changing of the specimens color at 40 cycles

The results of the other group which contains ten specimens as well and subjected to the same environmental condition that has been done for the first ten specimens but this time the number of cycles were 100 cycles (200 hours) are shown in table 6.11. These results comes to enhances the 40 cycles specimen results about how much the influence of the time of exposing to the environmental conditions on the characteristics of this resin material. The average maximum flexural strength of the specimens EB3 and EB4 which were exposed to the standard lab condition for a period of time that equivalent to 100 cycles increased 12.5% over the control specimen, due to time curing effect. Figure 6.36 shows the flexural strength test for specimen EB4. By exposing the specimens to the various environmental conditions for 100 cycles, flexural strength was increased to different degrees according to the type of the environmental conditions. For instance, when the relative humidity was 0% and the cycle period was 0.0, the increase in flexural strength reached 53.8% over the control specimens. The development of the mode of failure has been

observed, whereas except the standard lab condition specimens, most of the other specimens reached to the maximum deflection without failure, this is due to the changing that happened on the characteristic of the material caused by the hygrothermal effect, where the material turned into more ductile which allowed to a large deformation without rupture. Figures (6.37and 6.38) revealed the deformation shape for specimens EB20 (0% RH) and EB35 (100% RH) respectively. The flexural strength of the zero-cycle-period specimen was larger than the two-hour-cycle-period specimens either with or without humidity by 73% and 51% respectively, (see figure 6.39).

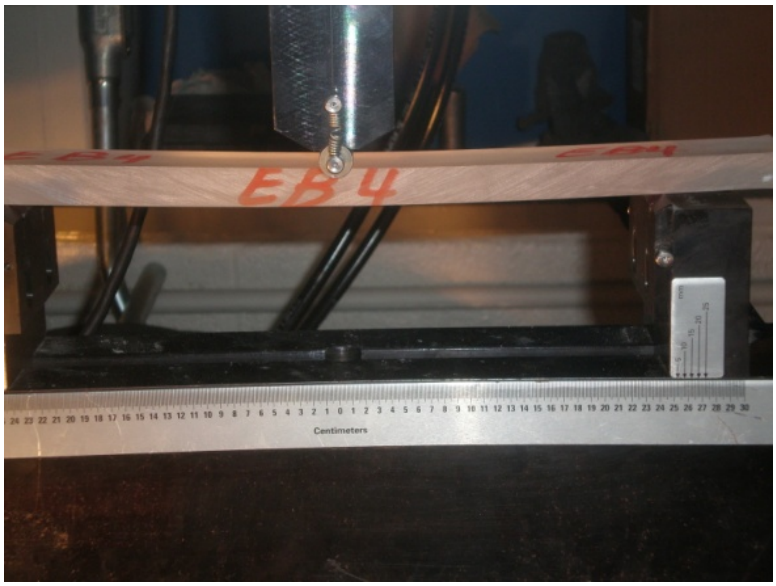

Figure 6.36: Flexural strength test for epoxy beam specimen (EB4) after exposed to standard lab condition and100 cycles

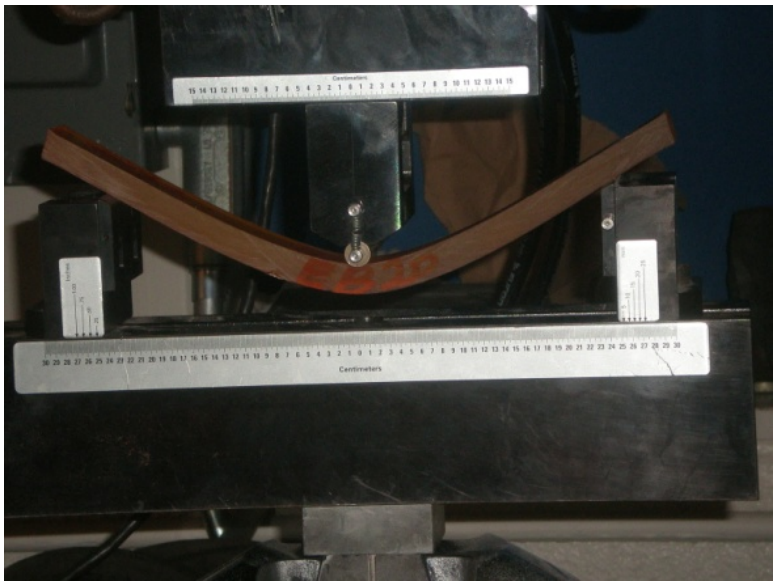

Figure 6.37: Deflection of the epoxy beam (EB20) at 100 Cycles

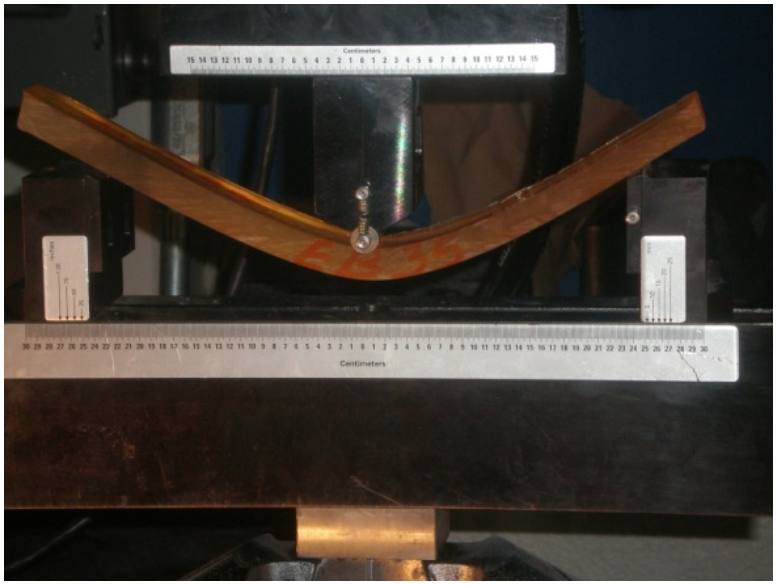

Figure 6.38: Deflection of the epoxy beam (EB35) at 100 Cycles

Table 6.11: Epoxy beam maximum flexural strength results subjected to different environmental conditions with 100°C and 100 cycles

Beam no.	Temp. °C	RH %	CP! (Hr)	Max. load lbs	Mean lbs	Flex. strength (psi)	Difference - %	Failure mode
EB3	LT*	LH+	-	249.6	273.4	7680	12.5	Flexural
EB4				297.1		9141		Flexural
EB11	100	0.0	2	272.3	329.5	8378	35.6	Flexural
EB12				386.6		11896		No failure
EB19			0	345.7	373.8	10637	53.8	No failure
EB20				401.9		12366		No failure
EB27		100	0	396.9	387.2	12212	59.3	No failure
EB28				377.5		11615		No failure
EB35			2	308.5	326	9492		No failure
EB36				343.4		10566	34.2	No failure

-Percentage difference of max. load increasing or decreasing compared with control result.
*Lab temperature,
+Lab humidity,
!Cycle period,

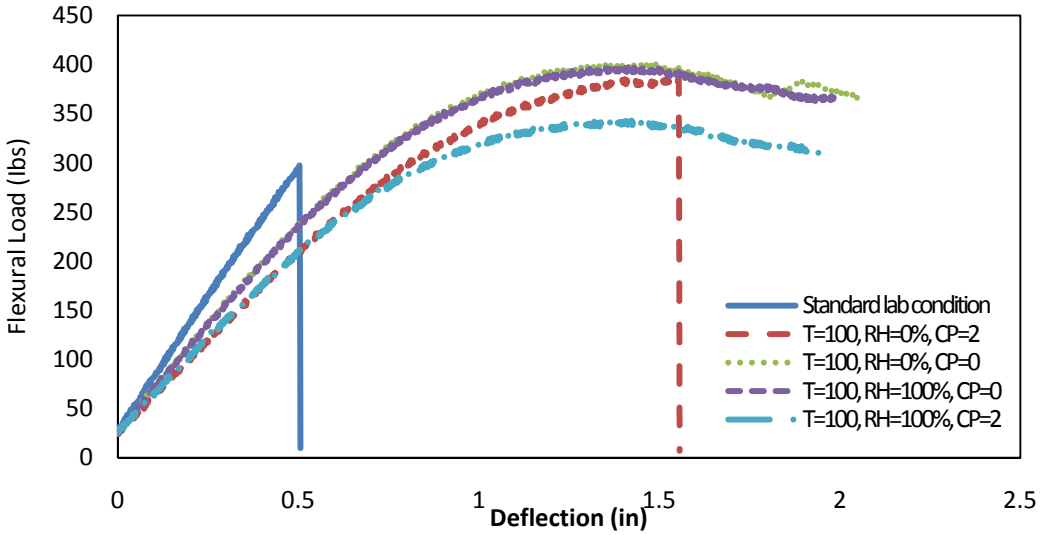

Figure 6.39: Flexural load-displacement curves of epoxy beams subjected to different environmental conditions with 100°C and 100 cycles

By increasing the number of cycles to 250 (500 hours), the changing of the material characteristics clearly appeared. By examing the results that are reported in table 6.12 and figure 6.40, the changes can be easily notified.

Table 6.12: Epoxy beam maximum flexural strength results subjected to different environmental conditions with 100°C and 250 cycles

Beam no.	Temp. °C	RH %	CP! (Hr)	Max. load lbs	Mean lbs	Flex. strength (psi)	Difference - %	Fail e mode
EB5	LT*	LH+	-	357.7	333.6	11006.4	37.3	Flexural
EB6				309.5		9523.3		Flexural
EB13	100	0.0	2	412.8	400	12701.9	64.6	No failure
EB14				387.1		11911.1		No failure
EB21			0	371.6	402.2	11434.1	65.5	No failure
EB22				432.8		13317.3		No failure
EB29		100	0	402.7	385.4	12391.1	58.6	No failure
EB30				368.1		11326.4		No failure
EB37			2	367	351.8	11292.6		No failure
EB38				336.5		10354.1	44.8	No failure

-Percentage difference of max. load increasing or decreasing compared with control result.
*Lab temperature,
+Lab humidity,
!Cycle period,

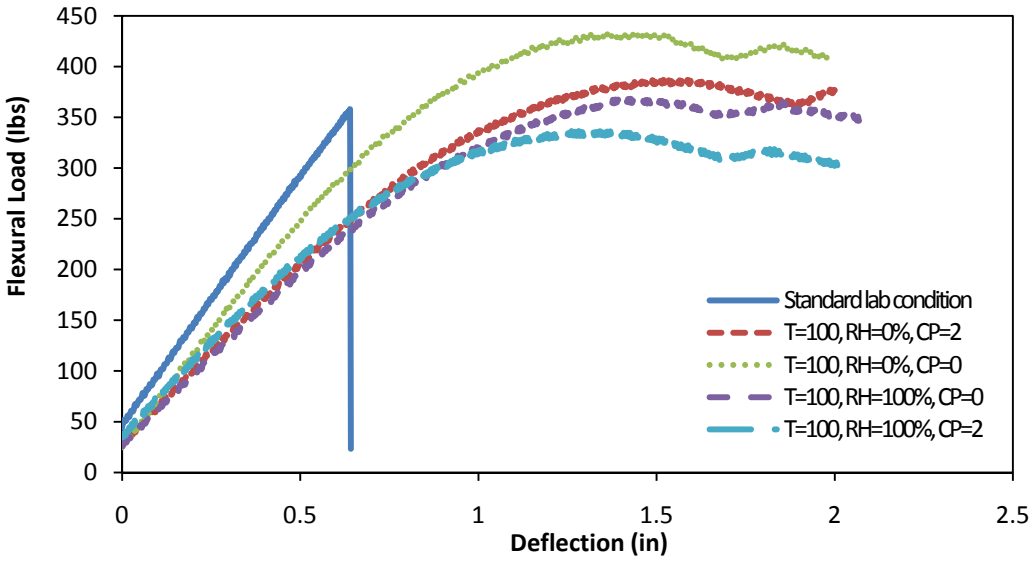

Figure 6.40: Epoxy subjected to different environmental conditions with 100°C and 250 cycles

For the standard lab condition specimens EB5 figure (6.41), and EB6, the flexural strength at failure increased by 37.3% over the control specimen; the mode of failure remained flexural failure. This result supports the effect of the specimen age at the same

condition on the strength.

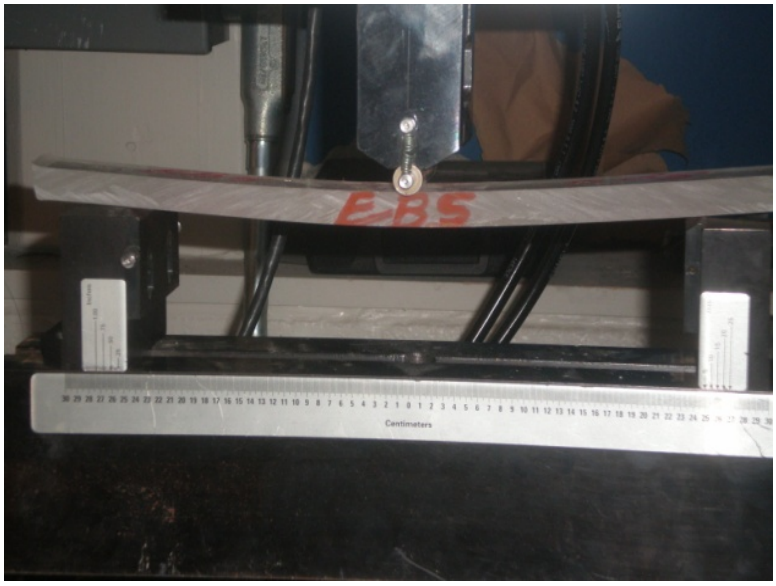

Figure 6.41: Flexural strength test for epoxy beam specimen, standard lab condition, 100 cycles

On the other hand, after 250 cycles of environmental aging at 100^{o}C, all the remaining eight specimens showed a large deformation without any failure. The large deflection exceeded the machine limit; hence the test must be terminated. Figures (6.42 and 6.43) show the deformation shape of specimens EB14 and EB37 during flexural testing.

Comparing with the results of the 40 and 100 cycles specimens, the 250 cycle specimens showed that the deference of the flexural strength results between 0.0 and 2hrs cycle periods diminished for both 0% and 100% relative humidity to be 0.55% and 9.5% respectively.

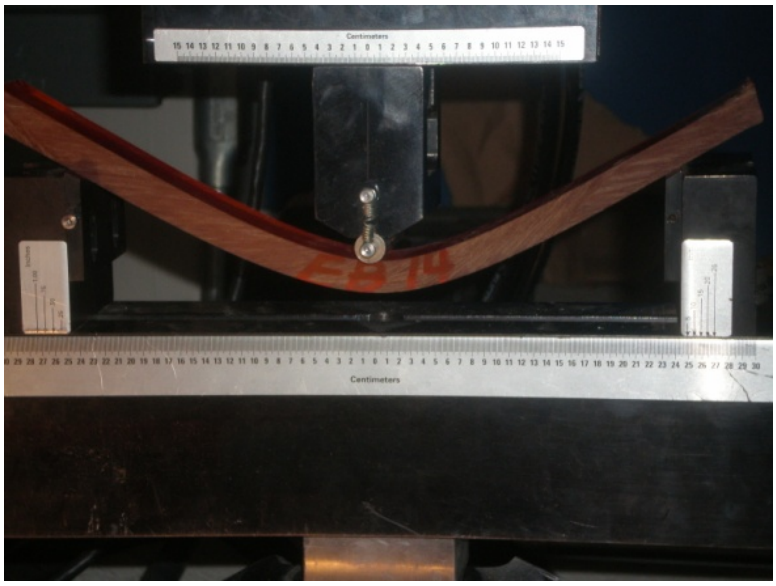

Figure 6.42: Deflection of the epoxy beam (EB14) at 250 Cycles

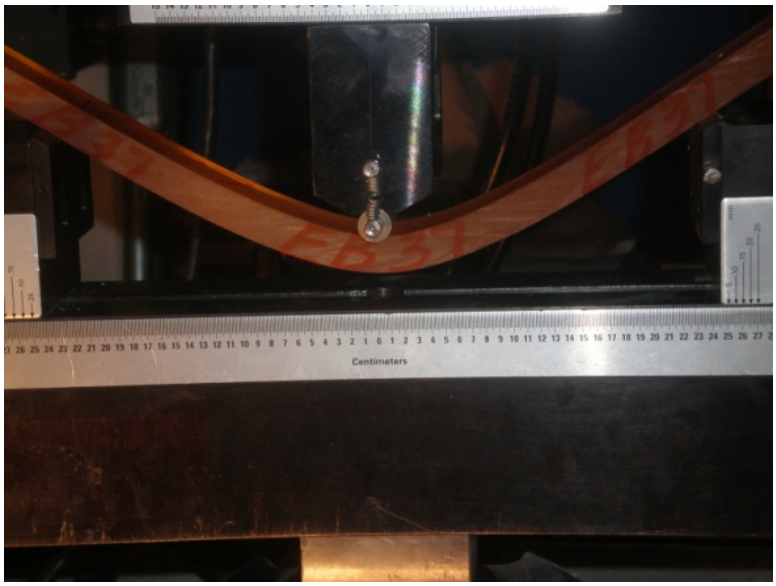

Figure 6.43: Deflection of the epoxy beam (EB37) at 250 Cycles

Besides that, aging also caused color changes of the specimens. The specimens that were aged treated in a “100% relative humidity” environment showed much lighter brown color than those which were exposed to 0.0% relative humidity, Figure (6.44).

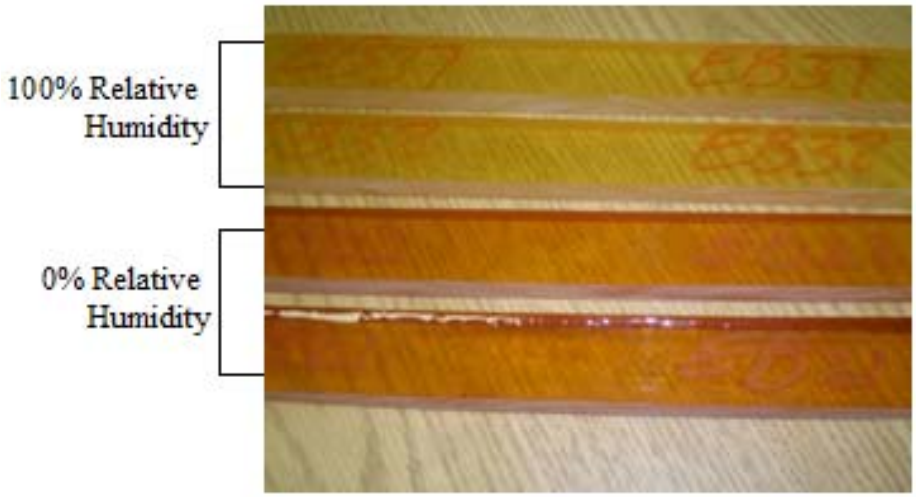

Figure 6.44: Variation in specimens color between 100% and 0% relative humidity condition, 250 cycles

After 625 cycles (1250 hours) of exposure to the environmental conditions at the elevated temperature (100^{o}C), significant reductions in flexural strength were evident. Under 100% relative humidity, the strength reduced by 16.5% and 41% for the 2 hour-cycle period specimens and for the zero-cycle-period specimens, respectively, when being compared with the control specimens. Under the standard lab conditions, the average of the maximum flexural load of EB7 and EB8 increased by 38.2% over the control specimen. The mode of failure of all these ten specimens was flexural failure. By increasing the number of cycles to 625 cycles which is (1250 hours at 2-hour frequency), the specimens became stiffer and the ductility reduced. Table 6.13 and figure 6.45 show the flexural strength and deflection results for these epoxy beam specimens.

Another thing was noticed after 625 cycles of environmental exposure, in contrast to the results of 40, 100, and 250 cycles, the flexural strength of the 2hrs cycle period specimens showed an increase of 65% and 60% than that of the 0.0 cycle period specimens under both 0% and 100% relative humidity condition.

Table 6.13**:** Epoxy beam maximum flexural strength results subjected to different environmental conditions with 100^{o}C and 625 cycles

Beam no.	Temp. ^{o}C	RH %	CP$^{!}$ (Hr)	Max. load lbs	Mean lbs	Flex. reng th (psi)	Difference^{-} %	ailure mode
EB7	LT*	LH^{+}	-	350.5	335.9	10784.9		Flexural
EB8				321.3		9886.4	38.2	Flexural
EB15			2	276.8	289.7	8517.1		Flexural
EB16				302.5		9307.9	19.2	Flexural
EB23		0.0	0	280.8	271.1	8640.2		Flexural
EB24	100			261.3		8040.2	11.6	Flexural
EB31			0	152.6	142.7	4695.5		Flexural
EB32		100		132.8		4086.3	-41.3	Flexural
EB39			2	218.8	203.0	6732.5		Flexural
EB40				187.3		5763.2	-16.5	Flexural

$^{-}$Percentage difference of max. load increasing or decreasing compared with control result.
*Lab temperature,
+Lab humidity,
!Cycle period,

Additionally, by examing to table 6.13 and figure 6.45, we can easily investigate the influence of the relative humidity on flexural strength. The flexural strength of the specimens which have been subjected to 100^{o}C and tested after 625 cycles when the relative humidity was 0% gave flexural strength results higher than of those were exposed to the same conditions but the relative humidity was 100% for both 2 hours cycle periods and 0.0 cycle period conditions.

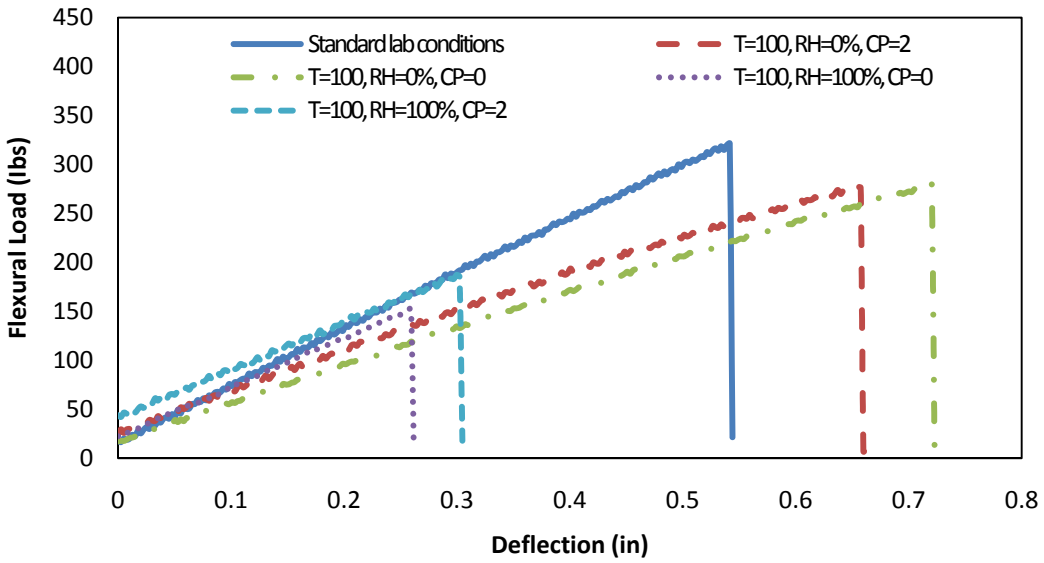

Figure 6.45: Epoxy subjected to different environmental conditions with 100°C and 625 cycles

More experimental tests have been performed in this research to further investigate the effect of high temperature on the durability and the characteristics of the resin material which has been used in this study. The environmental temperature was raised from 100°C to 180°C. The number of cycles have been used here were 40, 100, 250, and 350 cycles, and the cycle period was 2 hours. Table 6.14 shows that the flexural strength of the specimens decreased to about 59% below the flexural strength of the control specimens. The mode of failure remained flexural failure for all these 20 specimens. Besides the strength reduction, the coloration of the material has been noticed too, where the color of all specimens changed to black, (see figure 6.46).

Table 6.14: Epoxy beam maximum flexural strength results subjected to different environmental conditions with 180°C and 2 hrs cycle periods

Beam no.	RH! %	Cy~	Max. load (*lbs*)	Mean (*lbs*)	Max. Flex. Strength (*psi*)	Difference - %	Failure mode
EB51	0.0	40	180.6	174.0	5557.1	-28.4	Flexural
EB52			171.5		5277.1		Flexural
EB59			169.8		5224.7		Flexural
EB45		100	140.4	144.2	4320.1	-40.7	Flexural
EB46			148.0		4554.0		Flexural
EB47		250	245.5	243.4	7554.0	0.16	Flexural
EB48			241.3		7424.8		Flexural
EB55		350	94.8	100.8	2917.0	-58.5	Flexural
EB56			106.7		3283.2		Flexural
EB49	100	40	153.4	159.3	4720.1	-34.4	Flexural
EB50			159.0		4892.4		Flexural
EB61			165.4		5089.4		Flexural
EB41		100	149.8	141.0	4609.3	-42.0	Flexural
EB42			131.9		4058.6		Flexural
EB53			141.4		4350.9		Flexural
EB43		250	170.9	183.7	5258.6	-24.4	Flexural
EB44			196.4		6043.2		Flexural
EB57		350	145.8	150.4	4486.3	-38.1	Flexural
EB58			156.3		4809.4		Flexural
EB63			149.2		4590.9		Flexural

!Relative humidity
~Cycle period
-Percentage difference of max. load increasing or decreasing compared with control result.

Figure 6.46: Color change to black after exposed to temperature of 180^{o}C

The test results of flexural strength verses deflection of the 40 cycle specimens are shown in figure 6.47. The maximum flexural strength decreased by 28.4% and 34.4% when the specimens have been exposed to 0% and 100% relative humidity respectively. On the other hand as shown in figure 6.47, at 40 cycles of exposing, both results of 0% and 100% relative humidity specimens show that the maximum deflection, maximum flexural load, and the stiffness are closed to each other.

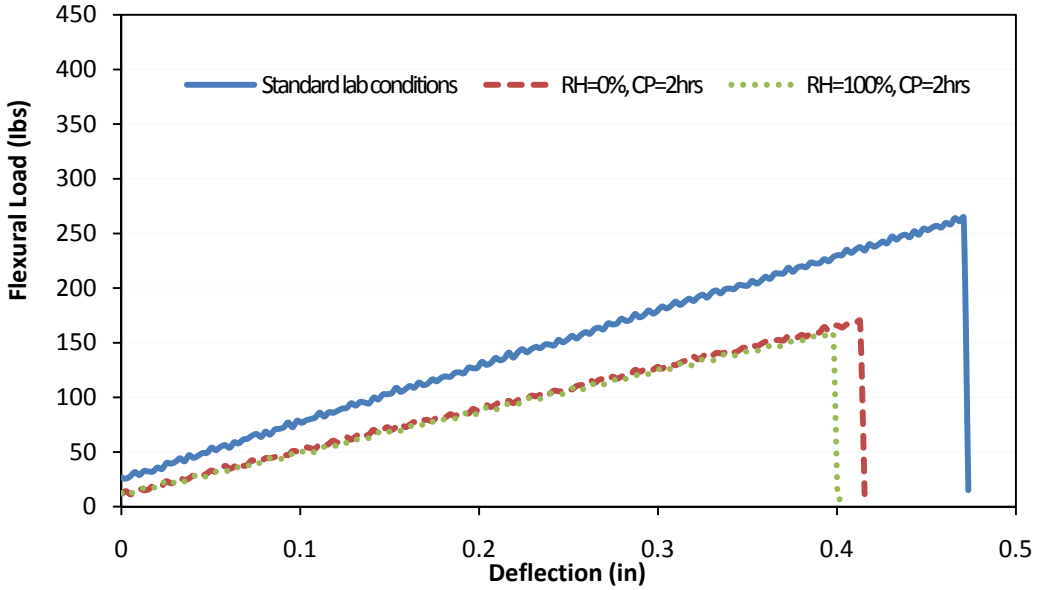

Figure 6.47: Flexural load-deflection curves of epoxy beams subjected to different environmental conditions with 180°C and 40 cycles

By increasing the time of exposing to 100 cycles (200 hours), the flexural strength at both 0% relative humidity and 100% relative humidity specimens further reduced to 58.5% and 42% respectively of the control specimens, figure (6.48).

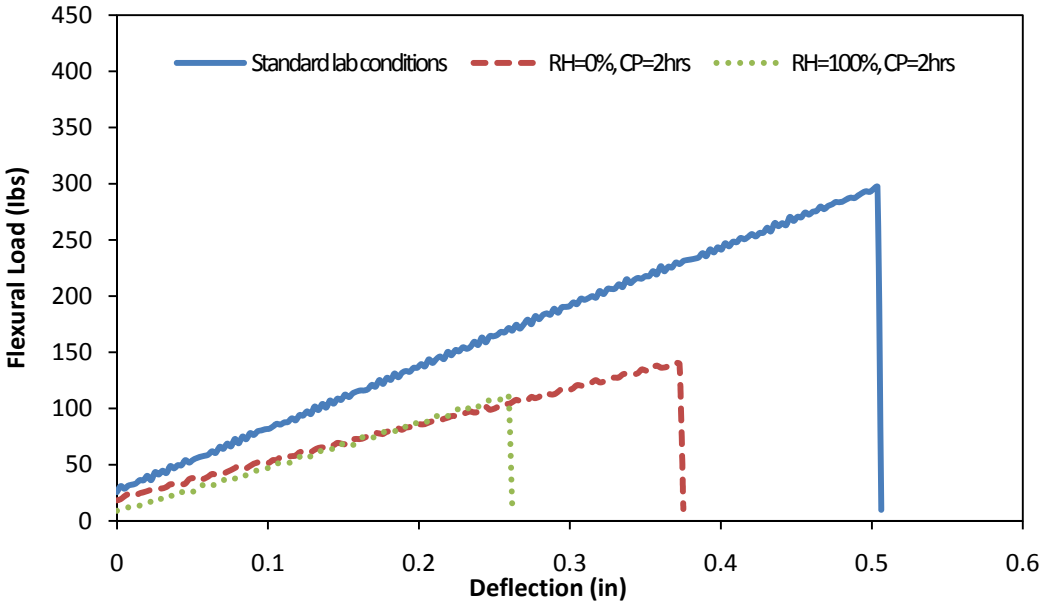

Figure 6.48: Flexural load-deflection curves of epoxy beams subjected to different environmental conditions with 180°C and 100 cycles

By increasing the number of cycles to 250 (500 hours) figure (6.49), and 325 cycles (650 hours) figure (6.50), the variation of flexural strength and deflection between 0 % and 100% relative humidity specimen results increased. But the stiffness of both cases is almost equal.

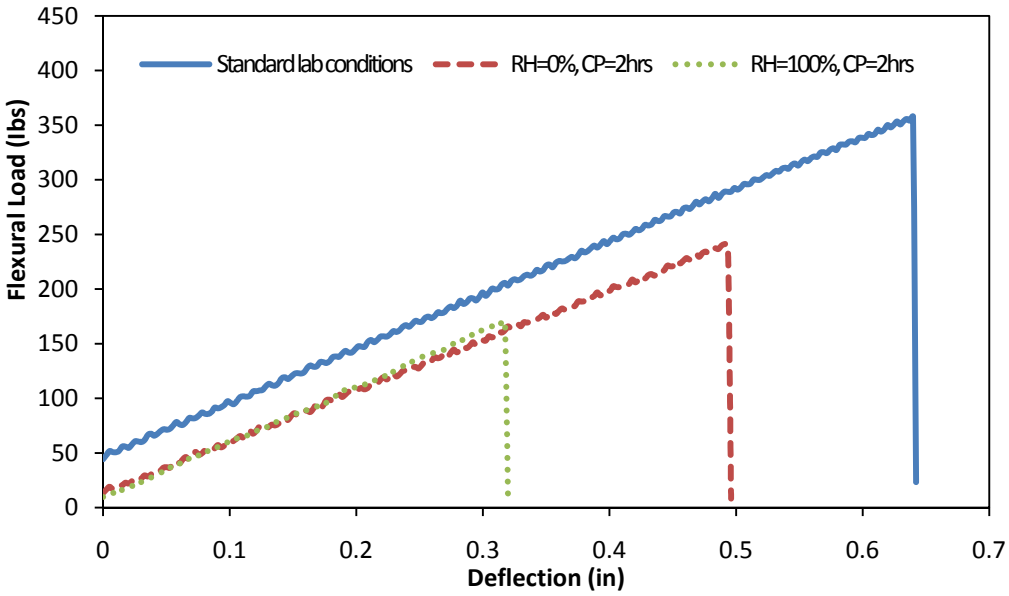

Figure 6.49: Flexural load-deflection curves of epoxy beams subjected to different environmental conditions with 180°C and 250 cycles

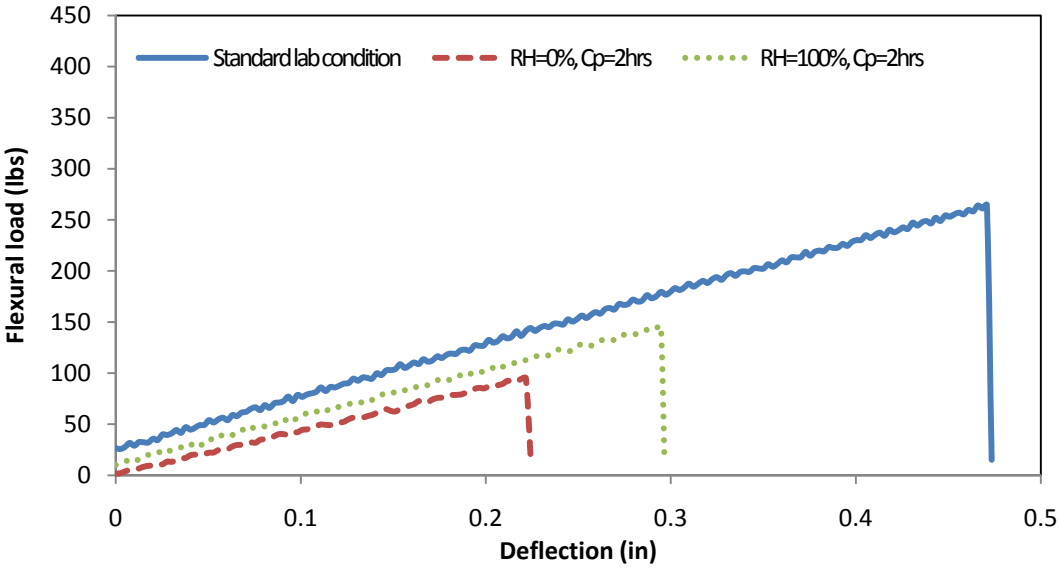

Figure 6.50: Flexural load-deflection curves of epoxy beams subjected to different environmental conditions with 180°C and 350 cycles

Regardless of any environmental conditions, the age of the specimens, which is related to the number of cycles, has an effected on the flexural strength results. Table 6.15 shows the average of maximum deflection, average of maximum flexural load, and the average stiffness results of the standard lab conditions specimens with respect to number of cycles. All these results explain that the time of exposure plays a role especially on the flexural strength results. Although, that the stiffness increased with increasing the time of exposure, all the standard lab conditions specimens have ruptured by brittle flexural failure.

Table 6.15: Standard lab conditions specimen results

Cycle	T (^{o}C)	RH %	CP (hrs)	Max. deflection (in)	Max. load (Ibs)	Stiffness (Ibs/in)
Control	LT	LH	-	0.453	243	503.3
40	LT	LH	-	0.457	265.0	532.1
100	LT	LH	-	0.467	273.4	537.3
250	LT	LH	-	0.599	333.6	506.5
625	LT	LH	-	0.606	380.9	612.7

Note: this result according to the average results of two specimens.

Tables (6.16 to 6.21) show the influence of the variation in the environmental conditions on the characteristics of the material corresponding to the average of deflection, average of the maximum load, and the average of the stiffness.

Table 6.16: Deflection, flexural load, and stiffness results, T=100^{o}C,RH=0%, Cp=2

# of Cycle	T (^{o}C)	RH %	CP (hrs)	Max. deflection (in)	Max. Load (lbs)	Stiffness (lbs/in)
Control	LT	LH	-	0.453	243.0	503.3
40	100	0.0	2	1.602	389.8.	468.8
100	100	0.0	2	1.550	329.5	364.5
250	100	0.0	2	1.593	400.0	369.9
625	100	0.0	2	0.655	289.7	451.8

Note: this result according to the average results of two specimens.

Table 6.17: Deflection, flexural load, and stiffness results, T=100°C,RH=0%, Cp=0

Cycle	T (°C)	RH %	CP (hrs)	Max. deflection (in)	Max. Load (lbs)	Stiffness (lbs/in)
Control	RT		-	0.453	242.5	503.3
40	100	0.0	0	1.480	346.0	355.3
00	100	0.0	0	1.056	373.8	362.0
250	100	0.0	0	1.536	402.2	394.7
625	100	0.0	0	0.805	271.1	387.9

Note: this result according to the average results of two specimens.

Table 6.18: Deflection, flexural load, and stiffness results, T=100°C,RH=100%, Cp=0

Cycle	T (°C)	RH %	CP (hrs)	Max. deflection (in)	Max. Load (lbs)	Stiffness (lbs/in)
Control	RT		-	0.453	243	503.3
40	100	100	0	1.501	422.7	472.1
100	100	100	0	1.426	387.2	418.4
250	100	100	0	1.417	385.4	449.8
625	100	100	0	0.268	142.7	462.9

Note: this result according to the average results of two specimens.

Table 6.19: Deflection, flexural load, and stiffness results, T=100°C,RH=100%, Cp=2

Cycle	T (°C)	RH %	CP (hrs)	Max. deflection (in)	Max. Load (lbs)	Stiffness (lbs/in)
Control	RT		-	0.453	242.5	503.3
40	100	100	2	1.483	373.0	399.9
100	100	100	2	1.444	326.0	336.6
250	100	100	2	1.319	351.8	381.6
625	100	100	2	0.377	168.1	458.4

Note: this result according to the average results of two specimens.

Table 6.20: Deflection, flexural load, and stiffness results, T=180°C, RH=0%

Cycle	T (°C)	RH %	CP (hrs)	Max. deflection (in)	Max. Load (lbs)	Stiffness (lbs/in)
Control	LT	LH	-	0.453	242.5	503.3
40	180	0.0	2	0.457	174.0	389.8
100	180	0.0	2	0.407	144.2	333.9
250	180	0.0	2	0.526	243.4	442.9
350	180	0.0	2	0.352	100.8	426.9

Note: this result according to the average results of two specimens.

Table 6.21: Deflection, flexural load, and stiffness results, T=180°C, RH=100%

Cycle	T (°C)	RH %	CP (hrs)	Max. deflection (in)	Max. Load (lbs)	Stiffness (lbs/in)
Control	RT		NA	0.453	242.5	503.3
40	180	100	2	0.257	159.3	379.1
10	180	100	2	0.292	141.0	420.7
250	180	100	2	0.322	183.7	505.2
350	180	100	2	0.442	150.4	453.9

Note: this result according to the average results of two specimens.

In conclusion, tables (6.22 to 6.26) supported by the figures (6.51 to 6.55) summarize the influence of the changing in the environmental conditions on the resin material that has been investigated in this study. Table 6.22 examines the effect of the different environmental conditions on the specimens' deflection. For the standard lab condition specimens, the maximum deflection has been observed to be increased slightly by increasing the time of exposing. At standard lab conditions, comparing to the control specimen results, the increases of deflection were very small at 40 and 100 cycles, but at 250 and 625 cycles of exposure the increasing clearly showed up comparing to the control specimens. At 250 cycles, the maximum deflection was very close to the 625 cycles result.

With 100°C of temperature, no strong effect of the cycle period on the deflection has been noticed, especially when the number of cycles was 250 cycles or less (see figure 6.51).

Table 6.22 and figure 6.51 show that at the same cycle period, the level of relative humidity has an important influence on the maximum deflection. After 625 cycles, the deflection of the 0% humidity specimens was 2-4 times higher than that of the 100% humidity specimens.

Table 6.22: Maximum deflection results for different conditions at 100°C

Number of Cycles	Lab Temp	Temperature= 100°C			
		Relative humidity 0.0%		Relative humidity 100%	
		Cp=2hrs	Cp=0.0	Cp=0.0	Cp=2
0	0.449	-	-	-	-
40	0.457	1.601	.480	1.501	1.483
100	0.467	1.113	1.055	1.425	1.444
250	0.599	1.593	1.536	1.417	1.318
625	0.606	1.046	0.805	0.268	0.376

As shown in figure 6.51, the maximum deflection of the 0% humidity specimens, of both 2hrs and 0.0 hrs periods, reduced to 1.1″ after 100 cycles from 1.6″ after 40 cycles. The maximum deflection then increased to 1.6″ again after 250 cycles and finally dropped to 0.8″ after 625 cycles. The overall trend suggests a gradual stiffening effect over time about strength increase and stiffness increase with 100 of cycles that might be because at 100 cycles the specimens became stiffer. While the specimens that have been subjected to 100°C of temperature and 100% relative humidity, the maximum deflection vs. number of cycles plot shows an overall trend similar to the 0% humidity case; the maximum deflection after 625 cycles was only 0.4", a 50% reduction from the 0% humidity counterpart, Table (6.22) and Figure (6.51).

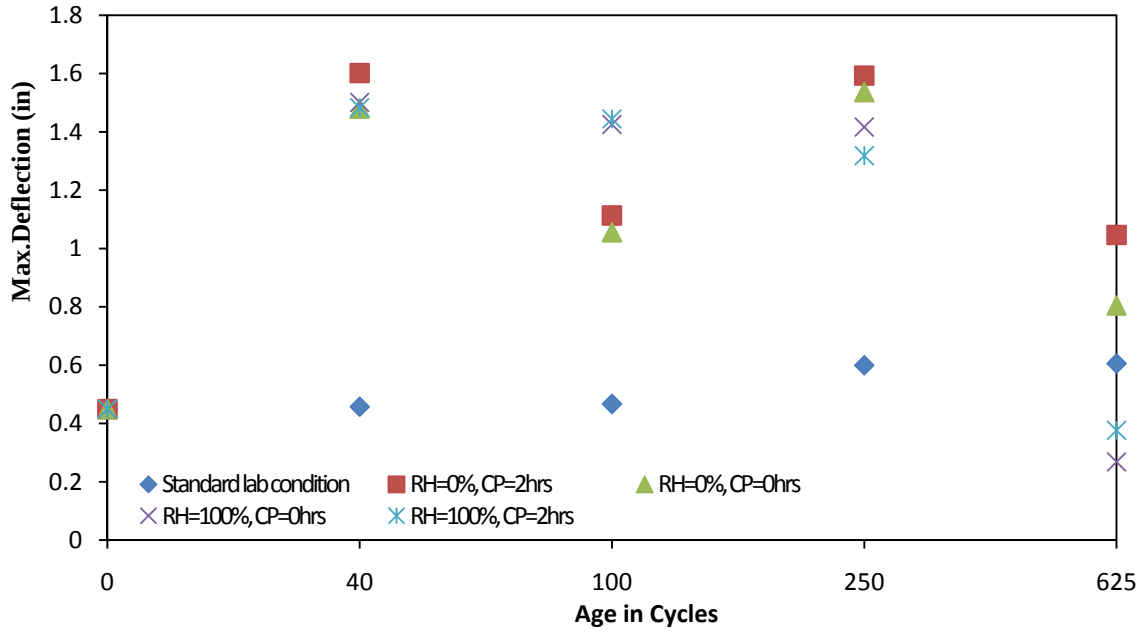

Figure 6.51: Deflection vs. number of cycles scatter after100^{o}Ctemperature

Table 6.23 summarizes the effects of various environmental conditions on flexural strength. These results have been represented on figure 6.52 by plotting the maximum flexural load verses the number of cycles. Under the standard lab conditions, the flexural strength increases with increasing curing time which is related to the number of cycles. This confirms that the durability of this material increases by time under standard lab conditions. When the relative humidity was 0%, the 2-hour cycle period seems to produce higher strengths over time than that of the 0 cycle period at the same numbers of cycles. When the humidity level was 100%, the opposite is true except for the 625-cycle specimens.

Table 6.23: Max. flexural load results for different conditions at 100°C

Number of Cycles	Lab Temp	Temperature= 100°C			
		Relative humidity 0%		Relative humidity =1 0%	
		Cp=2hrs	Cp=0.0	Cp=0.0	Cp=2
0	243.0	-	-	-	-
40	265.0	374.8	346.4	422.8	372.9
100	273.3	379.7	353.3	387.2	325.9
250	333.6	399.9	383.2	444.4	351.7
625	380.9	364.6	311.3	142.7	203.1

Comparing to the control under standard lab conditions, the curing at 100°C temperature showed strength increases up to 250 cycles. However, the flexural strength was greatly reduced after 625 cycles, regardless humidity levels and cycle periods. Such strength reductions were especially significant when 100% humidity was present.

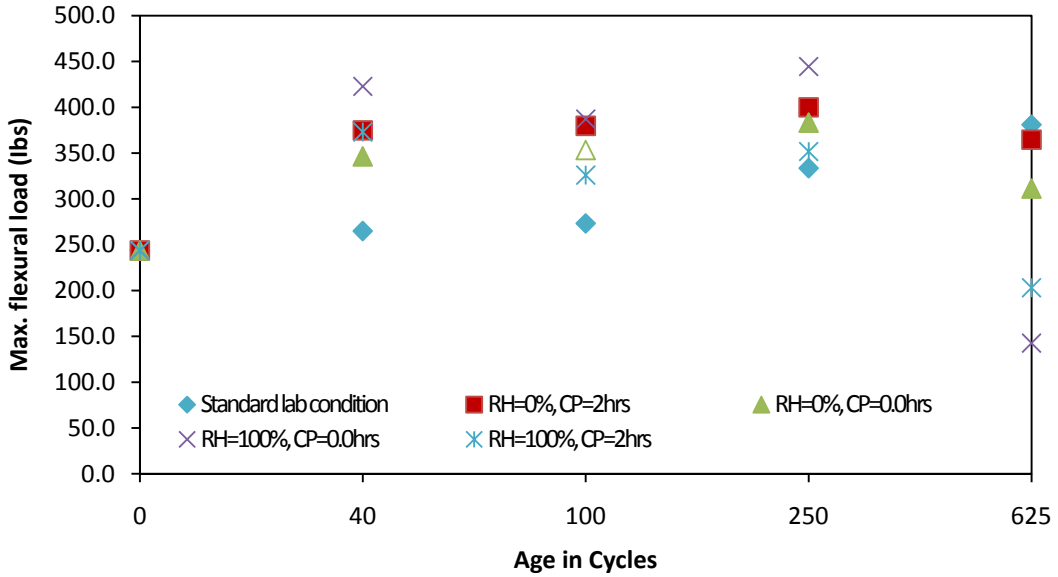

Figure 6.52: Max. flexural load vs. number of cycles scatter after100°C temperature

As shown in table 6.24, the overall trend of the stiffness reduced after being aged under 100°C, 0% or 100% relative humidity, 0.0 or 2hrs cycle periods. The specimens also

became more ductile; most of the specimens showed large deformations and these tests were terminated without failure since the crosshead movement of the test machine already exceeded its capacity. When the specimens were aged under 100% humidity for an extended period (after 625 cycles), the specimens lost their apparent ductility and once again showed a brittle failure mode similar to the control specimens but with reduced deflections (see figure 6.51) and reduced strengths (see figure 6.52). The reasons are yet to be discovered. A comparison of the stiffness results among control specimens, standard lab condition, and 100^{o}C temperature with different exposing time and humidity specimens are showing in figure 6.53.

Table 6.24: Stiffness results for different conditions at 100^{o}C

		Temperature= 100^{o}C			
Number of Cycles	Lab Temp	Relative humidity 0.0%		Relative humidity =100%	
		Cp=2hrs	Cp=0.0	Cp=0.0	Cp=2
0	503.3	-	-	-	-
40	532.1	468.8	355.3	472.1	399.9
100	537.3	364.5	362.0	418.4	336.6
250	506.5	369.9	394.7	449.8	381.6
625	612.7	451.8	387.9	462.9	458.4

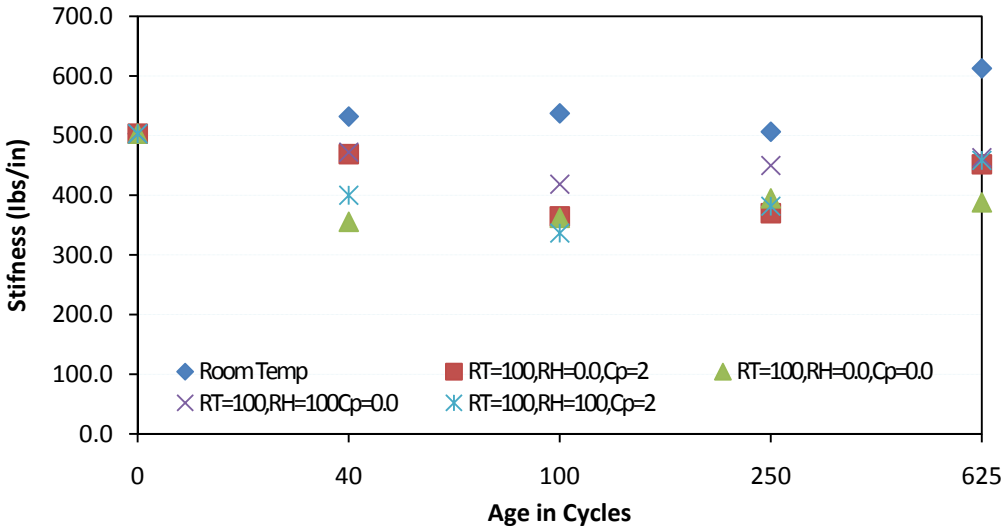

Figure 6.53: Stiffness vs. number of cycles scatter at100°C temperature

By raising temperature to 180°C, the maximum deflections under relative humidity 100% seemed to have large reductions then the 0% humidity counterparts, which were similar to the control under standard lab conditions, table 6.25 and figure 6.54.

Table 6.25: Deflection results for different conditions after 180°C

		Temperature= 180°C	
Number of Cycles	Lab Temp	CP =2 (hrs)	
		RH=0.0%	RH=100%
0	0.449	-	-
40	0.457	0.457	0.257
100	0.467	0.407	0.292
250	0.599	0.526	0.322
350	-	0.352	0.442

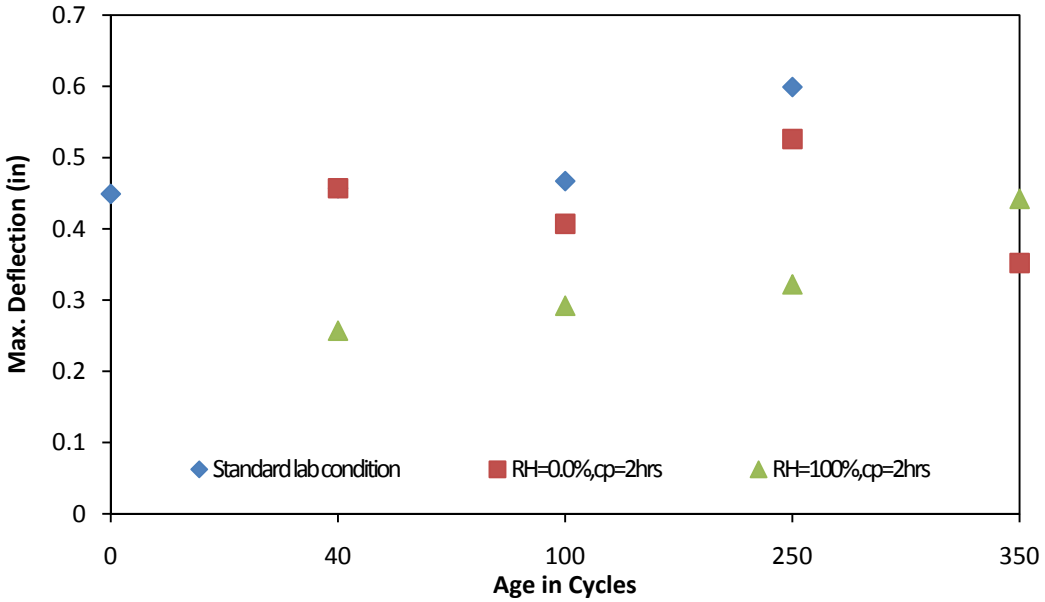

Figure 6.54: Deflection vs. number of cycles scatter after180^{o}Cof temperature

Table 6.26 shows the summary of maximum flexural loads of the 180^{o}C specimens in comparison to the control and standard lab condition specimens. The results in this table and figure 6.55 shows that the flexural loads of the 180^{o}C specimens under both 0% and 100% relative humidity decreased with the numbers of cycles. However, a slight increase in strength from 100 cycles to 250 cycles was observed for both humidity levels, and the reasons are unknown.

Table 6.26: Max. flexural load results for different conditions after 100^{o}C

		Temperature= 180^{o}C	
Number of Cycles	Lab Temp	Cycle Period =2 (hrs)	
		RH=0.0 %	RH=100%
0	243	-	-
40	264.0	174.0	159.3
100	273.4	144.2	141.0
250	333.	243.4	183.7
350	-	100.8	150.4

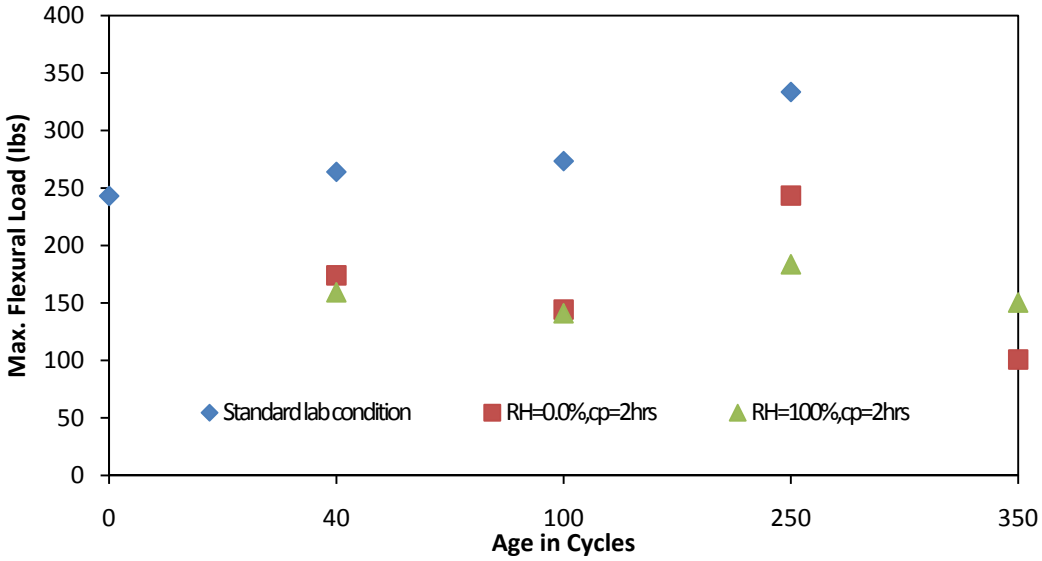

Figure 6.55: Max. flexural load vs. number of cycles scatter after180^{o}Cof temperature

As shown in table 6.27 and figure 6.56, at 180^{o}C of temperature, the stiffness of the specimens for both 0% and 100% relative humidity decreased slightly when it was compared with that of the control.

Table 6.27: Stiffness results for different conditions after 180^{o}C

		Temperature= 180^{o}C	
umber of Cycles	Lab Temp	Cycle Period =2 (hrs)	
		RH=0.0 %	RH=100%
0	503.3	-	-
40	532.1	389.8	379.1
100	537.3	333.9	420.7
250	506.5	442.9	505.2
325	-	426.9	453.9

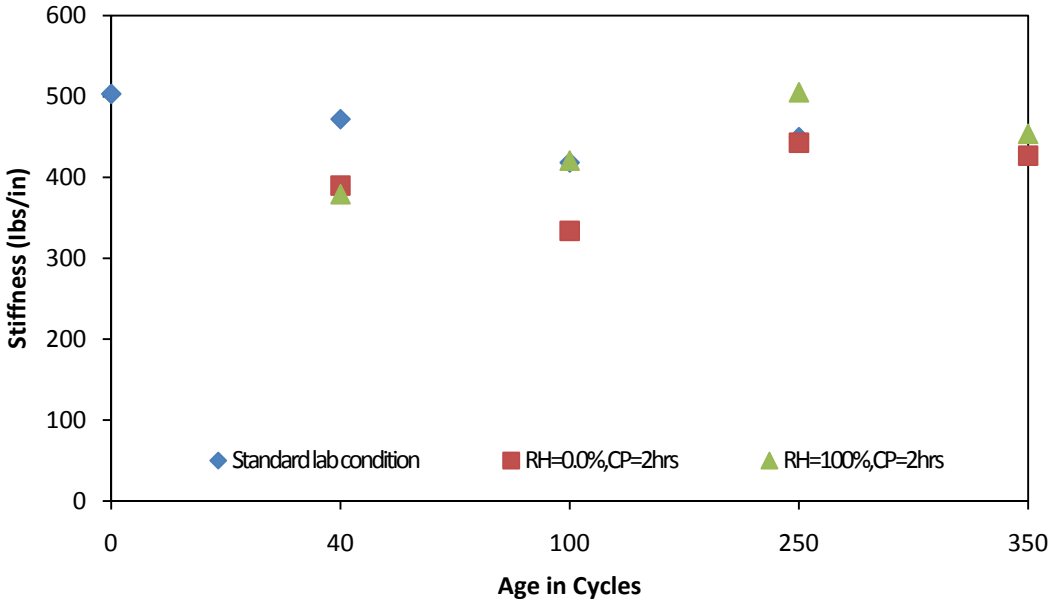

Figure 6.56: Stiffness vs. number of cycles scatter after180^{o}C of temperature

6.4 FRP Strengthened Specimens

As mentioned early in Chapter Three, the strengthening materials were obtained from two different sources, SIKA and Fyfe companies. Sika materials were bi-directional carbon fiber fabric (SikaWrap Hex 113C), uni-directional E-glass fiber fabric (SikaWrap Hex 100G), and Sikadur 300 as a resin material. While the materials from Fyfe company were uni-directional carbon fabric (Tyfo SCH-41composites), uni-directional glass fabric (Tyfo SHE-51A composites), in addition the resin material was Tyfo S saturant epoxy. The properties of all these materials were tabulated in chapter three.

In this research, prior to select a specific material, several different procedures of strengthening for beam and column specimens have been done, taking into account the main aim of this study which is the bonding between concrete and FRP materials. Both Sika and Fyfe materials were tested as follows:

6.4.1 SIKA Company Materials

Two beams B6 and B7 have been strengthened with one layer of Sika carbon fiber and sikadur 300, these two beams were subjected to flexural load test after 14 days of air curing. The mode of failure for both of them were concrete crushing figures (6.57a, 6.58a) followed by FRP rupture figures (6.57b, 6.58b).

a) Concrete crushing, beam B6

b) FRP rupture, beam B6

Figure 6.57: Concrete flexural crack and FRP rupture, B6

a) Concrete flexural crack, beam B7

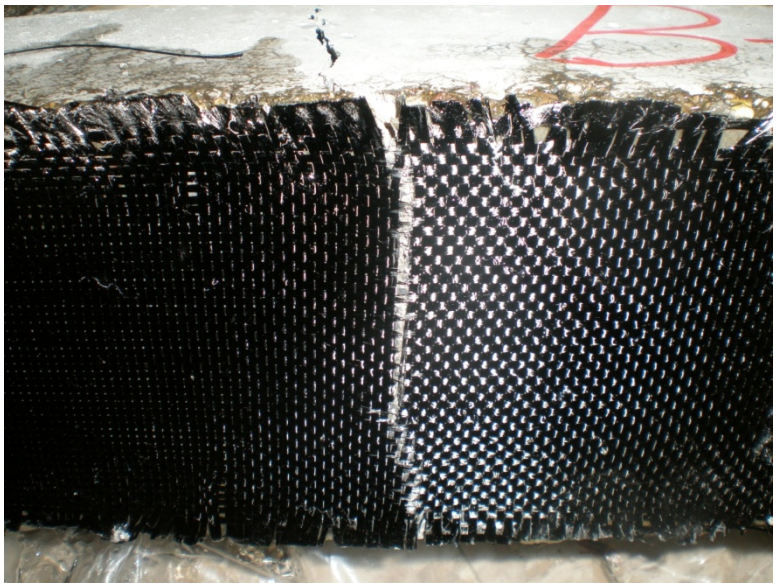

b) FRP Rupture, beam B7

Figure 6.58: Concrete flexural crack and FRP rupture, B7

At the time of FRP rupture of B6 and B7 a blast like sound was heard and the load started decrease.

Concrete beam B1 has been strengthened by using two layers of Sika CFRP and sikadur300 epoxy. This beam failed by crushing of concrete at the loading point, Figure (6.59a), followed by FRP delamination. The CFRP sheet was separated from the concrete surface, starting from the mid-span point and propagating through the left end of the beam. No evidence of FRP rupture was observed, (Figure 6.59b).

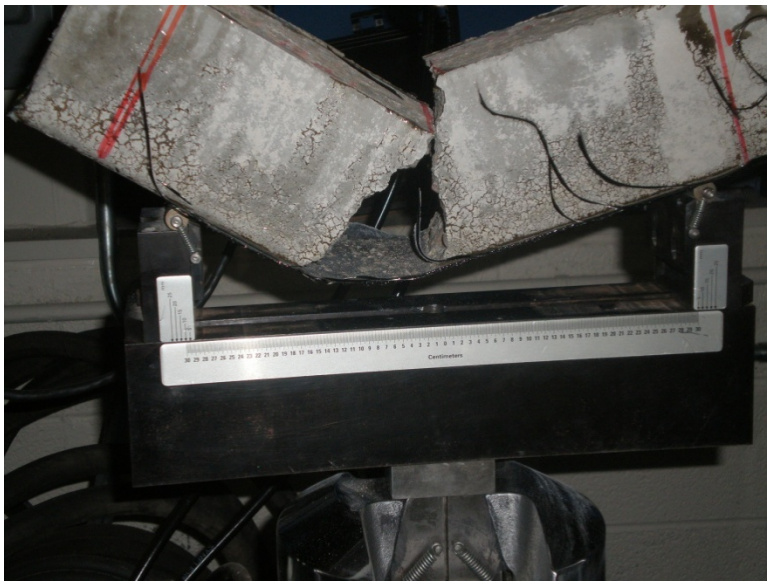

a) Concrete flexural crack, beam B1

b) FRP delamination on concrete surface, beam B1

Figure 6.59: Concrete flexural crack and FRP delamination, B1

Two other beam specimens B8, B11 were strengthened by using SIKA E-glass fiber (SikaWrap Hex 100G) and sikadur 300 epoxy, and subjected to flexural strength test as shown in figures (6.60 and 6.61).

Figure 6.60: Beam specimen B8 strengthened by Sika GFRP

Figure 6.61: Beam specimen B11 strengthened by Sika GFRP

As a result of the flexural test, both B8 and B11 failed by crushing of concrete at the point of loading followed by FRP delamination on one side of the specimen. The dominant mode of failure was FRP delamination for both of them. FRP debonding started closed to the center of the specimen under the point of loading and extended on one side toward the end support. Also for both specimens B8 and B11, the GFRP thin sheet showed splitting damage along the longitudinal direction, figures (6.62 and 6.63)a,b. This is probably due to the use of unidirectional glass fibers. Such splitting was not observed in the case of bi-axial carbon fiber sheet.

On the other hand, for the GFRP specimens, more ductility was shown on both specimens after the first crack of concrete. As shown in figure 6.64, for all specimens that were strengthened with one layer of CFRP or GFRP, the first crack has occurred approximately at the same load. The maximum load of one layer CFRP specimens was increased by 36% over the plain concrete beams, and about of 76% for GFRP specimens compared to the plain concrete control specimen results. The GFRP showed that when the first crack of concrete occurred, the load decreased about 30% then increased again and exceeded the first crack load. The CFRP specimens showed continuous load reductions after the first crack loads. Table 6.28 shows the maximum flexural load and flexural strength for all the Sika FRP Strengthened beam specimens.

a) Concrete flexural crack and FRP delamination, B8

b) FRP Strips rip at the time of failure, B8

Figure 6.62: Concrete flexural crack and FRP delamination and strips rip, B8

a) Concrete flexural crack and FRP delamination, B11

b) FRP Strips rip at the time of failure, B11

Figure 6.63: Concrete flexural crack and FRP delamination-FRP strips rip, B11

Table 6.28: Concrete beam specimens strengthened by various Sika FRP materials

Beam no.	FRP Type	# FRP Layers	Max. load lbs	Max. Flexural Strength (psi)	Mean Load (lbs)	Failure Mode
B6	CFRP	1	4008	1126.2	4092	FRP Rupture
B7	CFRP	1	4335	1218.1		FRP Rupture
B1	CFRP	2	4987	1401.3	4967	FRP delamination
B8	Glass	1	5179	1455.3	5393	FRP delamination
B11	Glass	1	5606	1575.3		FRP delamination

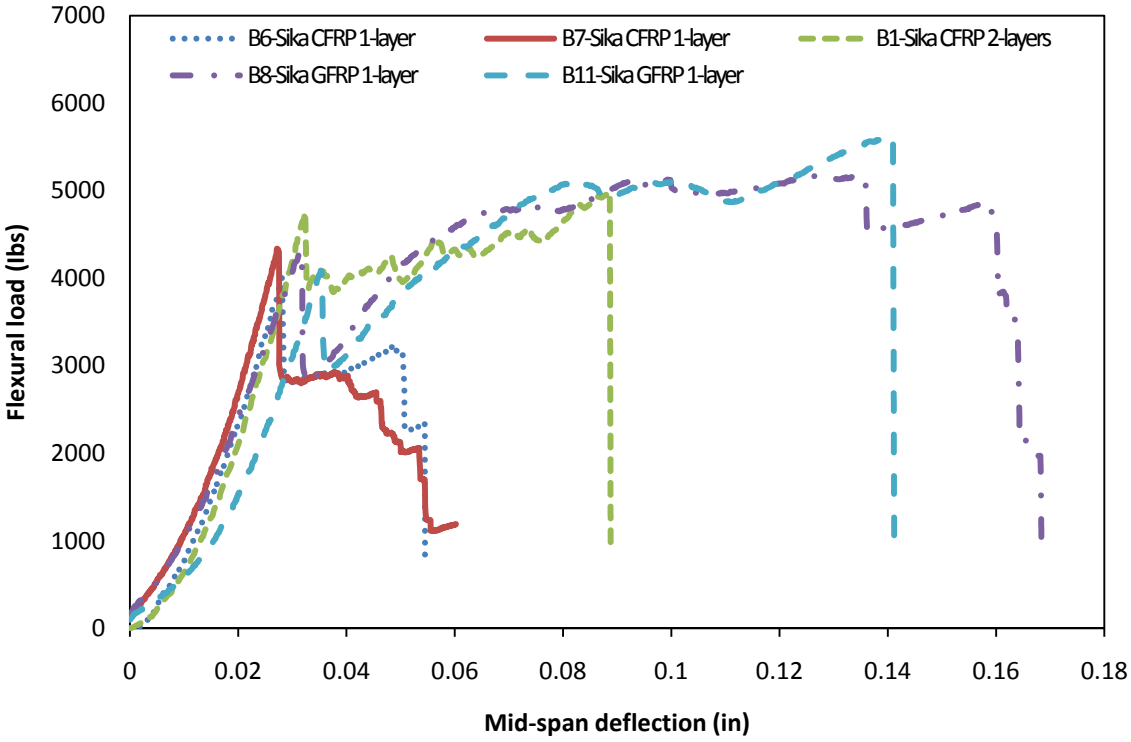

Figure 6.64: Flexural load- mid-span deflection of Sika FRP strengthened beams

Two concrete cylindrical specimens C3 and T were retrofitted by using one layer Sika CFRP then were tested for compressive strength after cured for 14 days. Both specimens failed as a result of FRP rupture, (see figures 6.65 and 6.66). At the time of failure, a blast like sound was heard and the load decreased.

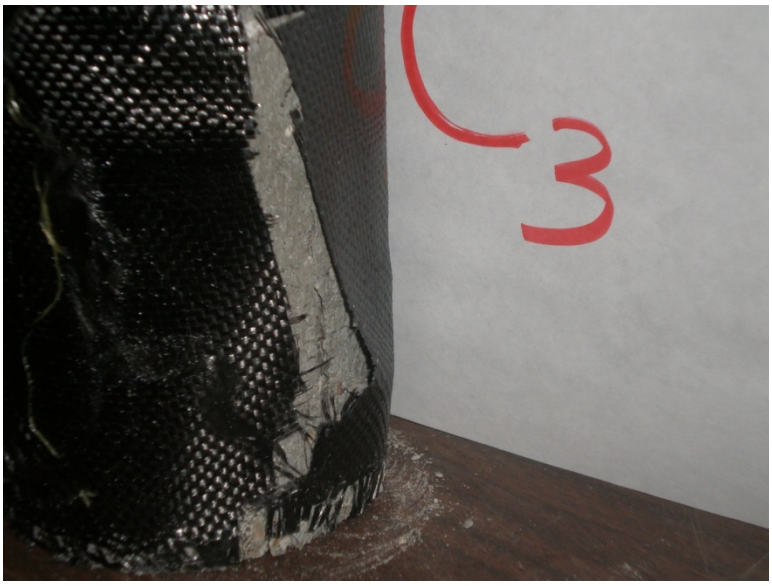

Figure 6.65: FRP rupture of concrete cylindrical specimen C3

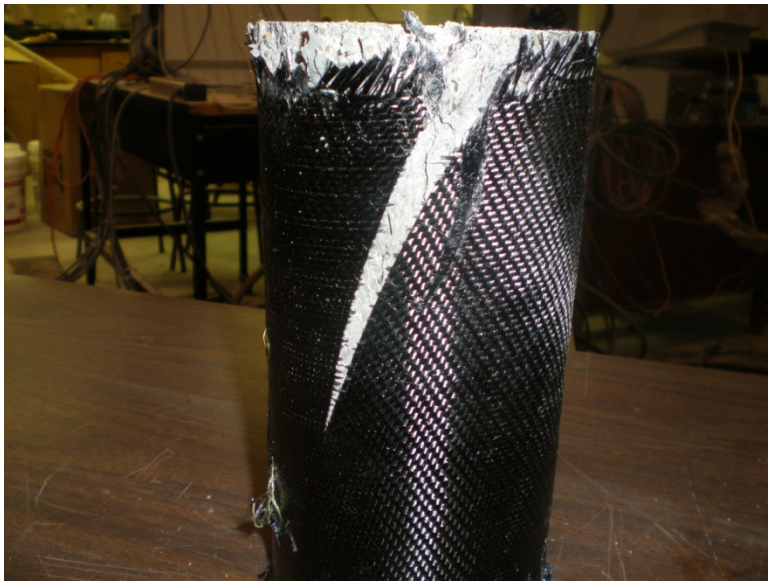

Figure 6.66: FRP rupture of concrete cylindrical specimen T

Two column specimens, C4T1 and C9 were wrapped by utilizing SIKA GFRP. Same procedures for surface preparation, epoxy applying and curing have been followed for all specimens in this research. Both cylindrical specimens C4T1 and C9 were subjected to the compressive strength test according to ASTM 39-08 until failure, (see figures 6.67, 6.68).

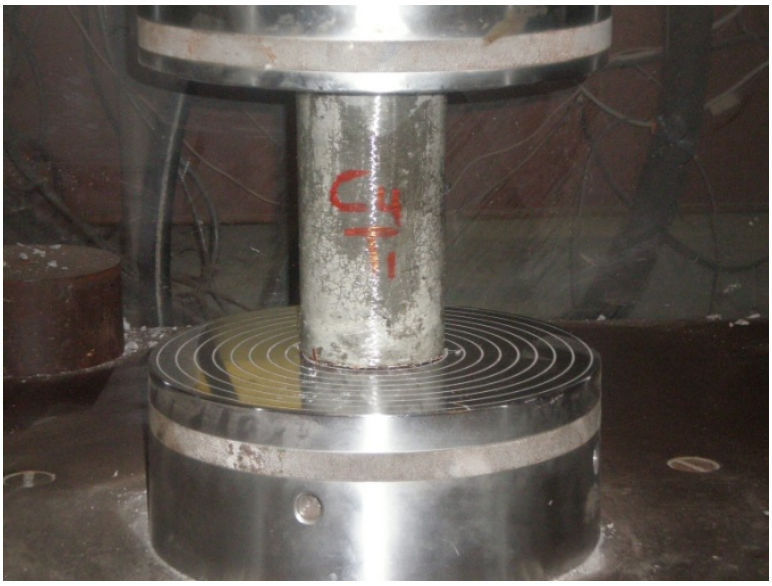

Figure 6.67: Compressive strength test for C4T1 specimen wrapped by Sika GFRP

Figure 6.68: Compressive strength test for C9 specimen wrapped by Sika GFRP

The concrete crushing followed by transverse rupture of the GFRP wrap, figures (6.69 and 6.70)a,b. Prior to the instant FRP failure, a sound of FRP rupture was heard for both specimens that followed by high sound at the time of failure.

a) Concrete crushing and GFRP rupture of C4T1

b) GFRP rupture and strips rip of C4T1

Figure 6.69: Concrete crushing and Sika GFRP rupture of C4T1

a) Concrete crack and GFRP rupture in hoop direction of C9

b) GFRP rupture and strips rip of C9 on the opposite side to (a)

Figure 6.70: Concrete crushing and Sika GFRP rupture of C9

The results of Concrete cylindrical specimens that were strengthened by utilizing one layer of Sika GFRP materials are shown in table 6.29 and figure 6.71. These results suggest that

the Sika GFRP columns have flexural strength stronger than the Sika CFRP columns; probably due to the high strength of the GFRP composites (see chapter 3-table 3.9). The much larger ductility of the GFRP column (C9) is likely due to the larger ultimate strain of the GFRP composites. While CFRP rupture was the mode of failure of the CFRP columns (as shown in Fig 6.65 and 6.66), the two GFRP strengthened specimens failed due to a complex mix of GFRP rupture, GFRP splitting failure in the transverse direction, and GFRP delamination (Fig 6.69, and 6.70).

Table 6.29: Concrete cylindrical specimens strengthened by various Sika FRP materials

Column no.	FRP type	Max. load lbs	Max. Comp. Strength (psi)	Mean Load (lbs)	Failure Mode
C3	CFRP	86394.2	6875.032	87150.9	FRP Rupture
CT	CFRP	87907.6	6995.465		FRP Rupture
C4T1	GFRP	99039.4	7881.305		Mixed modes
C9	GFRP	105527.2	8397.588	102283.3	Mixed modes n

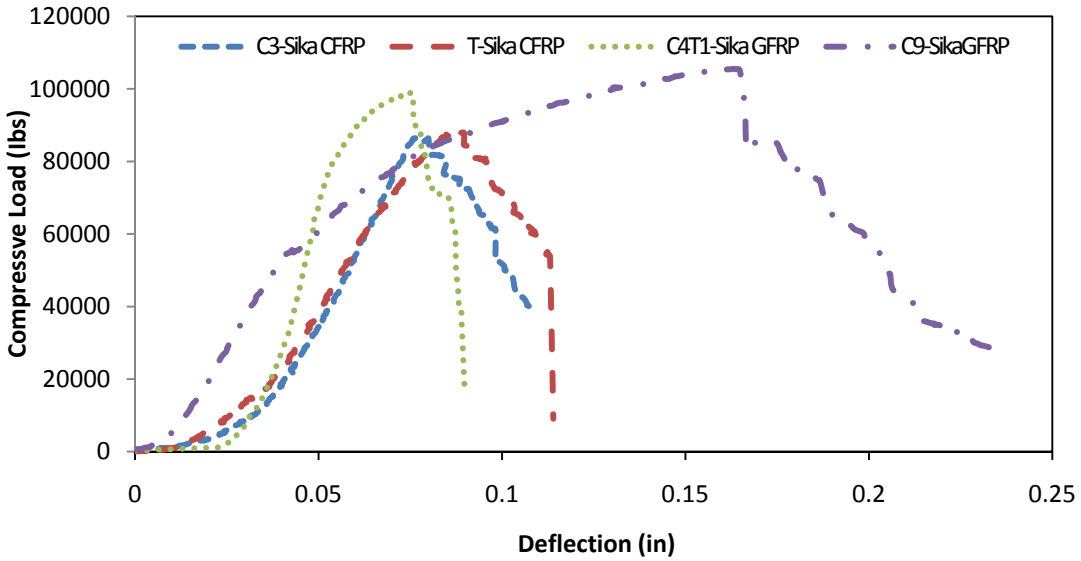

Figure 6.71: Compression load- deflection relationships of Sika FRP strengthened columns

6.4.2 Fyfe Company Materials

Two beams B4 and B5 have been strengthened by using one layer of Fyfe CFRP and Fyfe epoxy. The mode of failure was shear failure followed by FRP delamination, figures (6.72 and 6.73). The separation of CFRP sheet from the concrete surface occurred only on one side; it started at the point of initial shear crack and extended towards through the length of the beam until the support. No CFRP delamination was detected on the other side of the specimens.

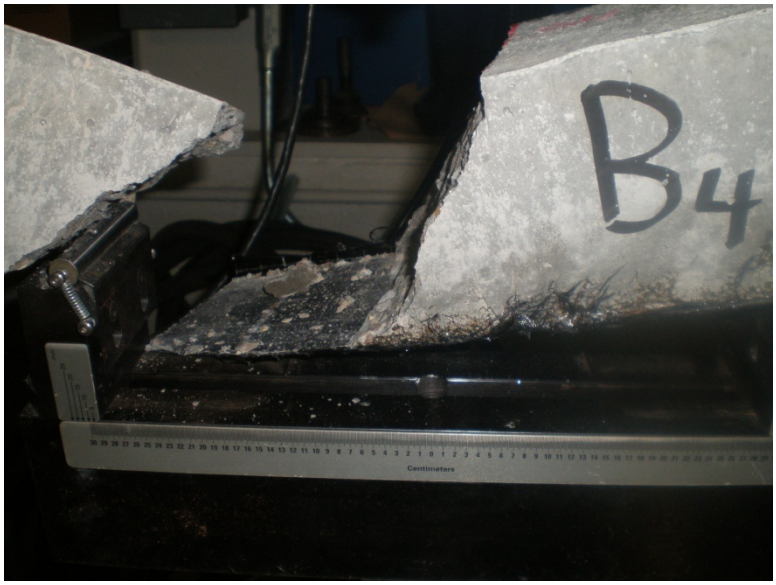

Figure 6.72: Shear failure with CFRP delamination, B4

Figure 6.73: Shear failure with CFRP delamination, B5

One beam B3 was strengthened with two layers of CFRP. This beam failed by shear failure in concrete then followed by delamination between the concrete and FRP interface, Figure (6.74). The crack started from the bottom face and extended diagonal through the beam depth then distributed horizontally bout half inch above the bottom surface at one direction of the beam till the support

Figure 6.74: Shear failure of two layers Fyfe CFRP beam specimen, B3

Other two beam specimens B12 and B15 have been strengthened by utilizing one layer of Fyfe GFRP and epoxy materials. Both specimens were loaded and tested for flexural strength (see figures 6.75 and 6.76).

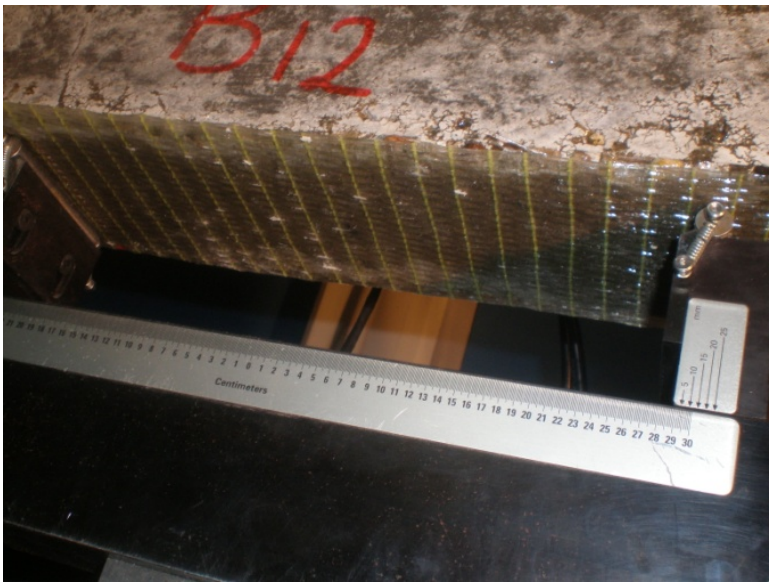

Figure 6.75: Fyfe GFRP strengthened beam specimen B12

Figure 6.76: Fyfe GFRP strengthened beam specimen B15

In spite that the first crack was due to flexure, the final failure was caused by a separate shear crack. The shear crack started from the bottom of the specimen and then propagated upward to near the center load point following a 45^{o} degree angle. The mode of failure of B12 and B15 were shear failure. Moreover, at the time of failure, FRP delamination between concrete and FRP sheet was observed only on one side. No FRP rupture was evident, (see figures 6.77 and 6.78).

a) Concrete flexural crack followed by shear crack of specimen B12

b) Shear failure and FRP delamination, B12

Figure 6.77: Concrete cracks and GFRP delamination of beam B12

a) Concrete flexural crack followed by shear crack of specimen B15

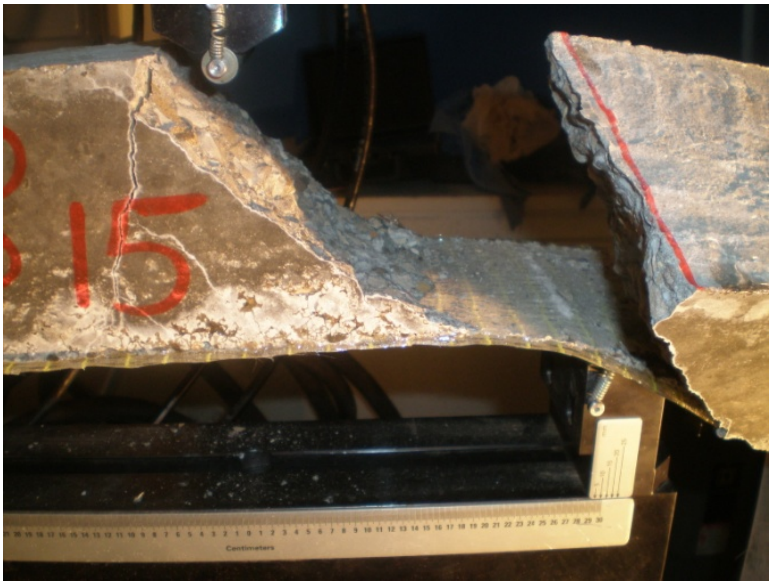

b) Shear failure and FRP delamination, B15

Figure 6.78: Concrete cracks and GFRP delamination of beam B15

Table 6.30 summarizes the flexural test results of different Fyfe FRP strengthened beams. As shown in table 6.30 and figure 6.79, the Fyfe CFRP beams showed slightly higher flexural strength than Fyfe GFRP beams. The flexural strength of the two layers CFRP strengthened

specimen increased about 18% comparing to one layer CFRP strengthened specimens. The mode of failure of all these five specimens was shear crack followed by FRP delamination. As shown in figure 6.79, although, the flexural strength of the CFRP strengthened specimens were greater than those of the GFRP strengthened specimens, the GFRP strengthened specimens showed much higher ductility after the first crack than those specimens strengthened by CFRP.

Table 6.30: Concrete beam specimens strengthened by various Fyfe FRP materials

Beam no.	FRP Type	# FRP Layers	Max. load lbs	Max. Flexural Strength (psi)	Mean Load (lbs)	Failure Mode
B4	CFRP	1	9273.7	2643	8704.8	Shear crack + FRP delamination
B5	CFRP	1	8135.9	2290		Shear crack + FRP delamination
B3	CFRP	2	10236.7	2882	10236.7	Shear failure
B12	Glass	1	7777.2	2189	7950.6	Shear crack + FRP delamination
B15	Glass	1	8124.0	2287		Shear crack + FRP delamination

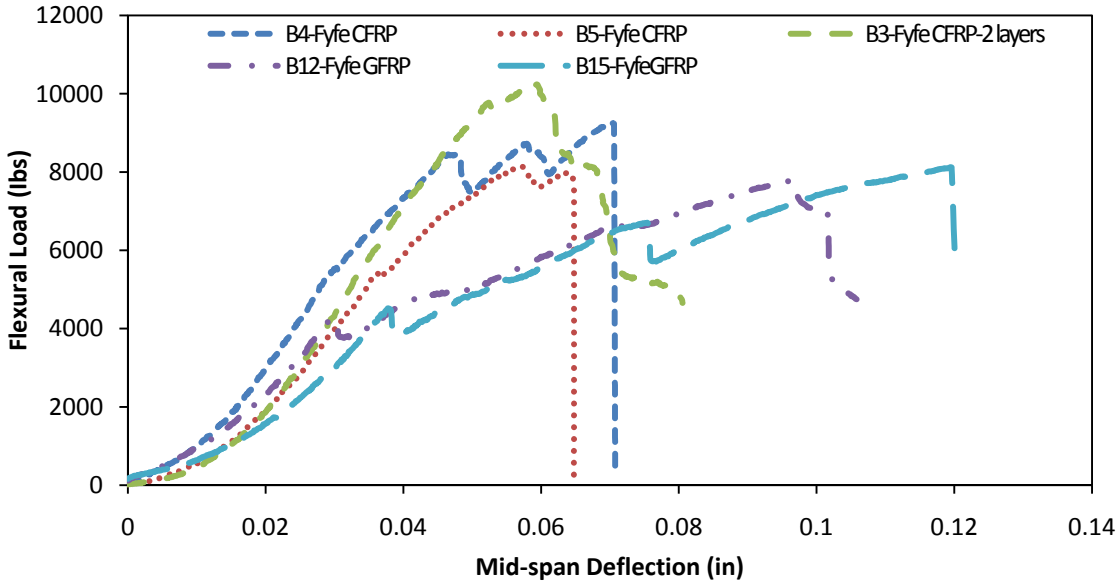

Figure 6.79: Flexural load vs. mid-span deflection of Fyfe FRP strengthened beams

Two concrete cylindrical specimens C2 and C4 were strengthened by using one layer Fyfe CFRP, and one concrete cylindrical specimen C5 was strengthened by 2-layers of Fyfe CFRP as well. All these specimens were loaded by compression until failure. The mode of failure was CFRP rupture in both the longitudinal and hoop (transverse) direction for all three specimens, figures (6.80, 6.81, and 6.82). A partial delamination between the two CFRP layers was observed at the time of failure for the 2-layers CFRP strengthened specimen, (see figure 6.83). The top layer was separated and ejected away a distance of 12 feet from the specimen. At the time of failure of these three specimens, a violent sound was heard.

Figure 6.80: Compression test- FRP ruptures, C2

Figure 6.81: Compression test- FRP ruptures, C4

Figure 6.82: Compression test- FRP ruptures, C5

Figure 6.83: Delamination failure between two CFRP layers, a large portion of the top layer (on left) was ejected from the specimen at the time of failure, C5

Two column specimens, C7 and C11 were wrapped by using 1 layer Fyfe GFRP and were also tested until failure, figures (6.84, 6.85). Both specimens C7, and C11 failed due to concrete crushing and GFRP rupture in hoop direction figures (6.86, 6.87, and 6.88). Prior to the instant of failure; a sound of FRP rupture was heard for all specimens that followed by high sound at the time of failure and concrete grains Scattered.

Figure 6.84: Compressive strength test for column specimens, C7 wrapped by FYFE GFRP

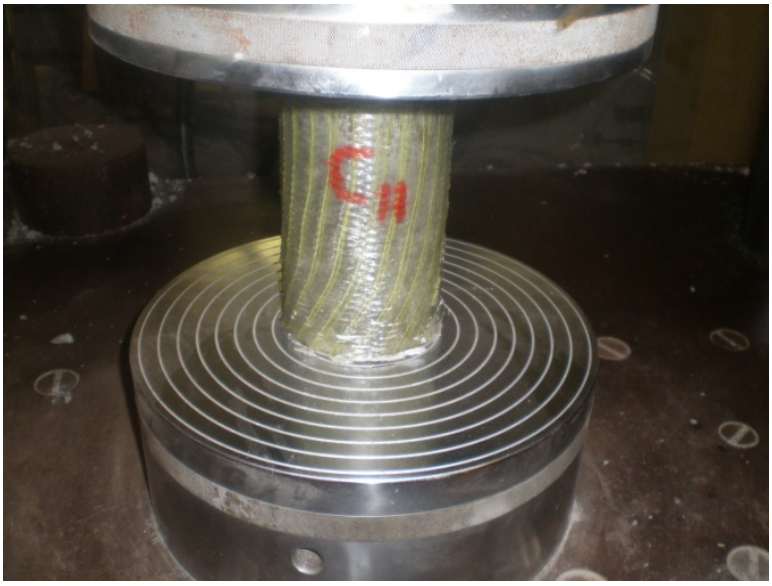

Figure 6.85: Compressive strength test for column specimens, C11 wrapped by FYFE GFRP

Figure 6.86: Concrete crushing and GFRP rupture of C7

Figure 6.87: Concrete crushing and GFRP rupture of C7, opposite side of Fig 6.86

Figure 6.88: Concrete crushing and FRP rupture of C11

The test results of all cylindrical specimens which have been strengthened by utilizing Fyfe CFRP or Fyfe GFRP strengthening materials are shown in table 6.31 and figure 6.89. The results show that the CFRP strengthened specimens gave a compressive strength about 72% stronger than the GFRP strengthened specimens. Also, when evaluating the results of the one-

layer vs. two-layer CFRP specimens, it was found that the strength of the two-layer specimen is about 36% higher than that of one-layer CFRP specimens.

In spite of the lower strength of the GFRP strengthened specimen, the GFRP show a higher ductility, as shown in figure 6.89. The same conclusion also was applied to the Fyfe specimens under flexural loading (see Fig 6.79). A larger ductility was also observed from the tests of the Sika GFRP specimens in comparison with the CFRP specimens.

Table 6.31: Concrete cylindrical specimens strengthened by various Fyfe FRP materials

Column no.	FRP type	# FRP Layers	Max. load lbs	Max. Comp. Strength (psi)	Mean Load (lbs)	Failure Mode
C2	CFRP	1	241901.2	19250	243280.2	FRP Rupture
C4	CFRP	1	244659.1	19469		FRP Rupture
C5	CFRP	2	330238.9	26280	330238.9	FRP Rupture
C7	GFRP	1	149873.4	11927	141453.2	FRP Rupture
C11	GFRP	1	133033.0	10586		FRP Rupture

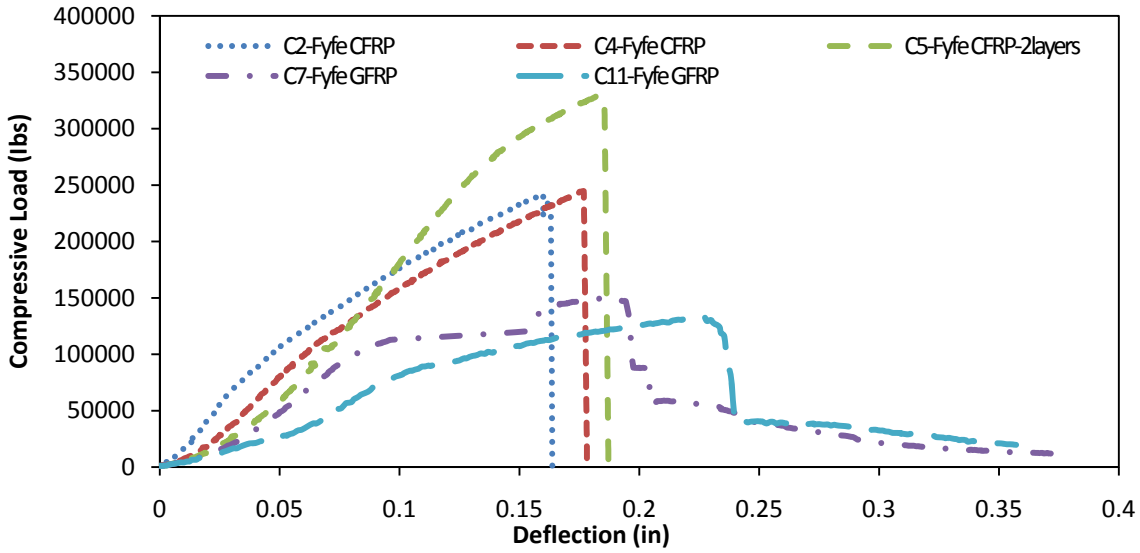

Figure 6.89: Compression load-deflection relationships of Fyfe FRP strengthened columns

In addition, comparison between the two resin materials has been included in this study to evaluate the bonding strength. Two beam and two column specimens had been strengthened by using SIKA CFRP and FYFE epoxy. Also, other two beam and two column specimens were

strengthened by FYFE CFRP and SIKA epoxy. Beam specimens B13 and B14 were strengthened by SIKA CFRP and the bonding material were FYFE epoxy, figures (6.90, and 6.91). Beam Specimens B9 and B10 were strengthened by FYFE CFRP and SIKA epoxy, figures (6.92, and 6.93).

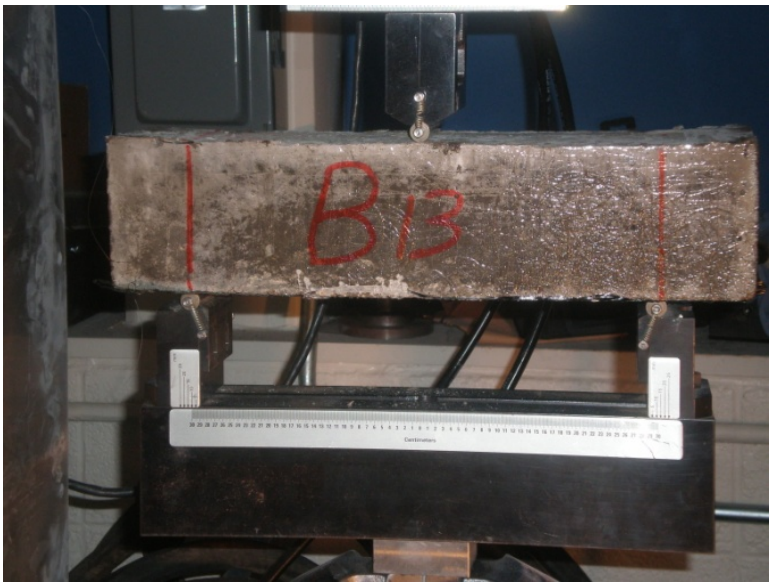

Figure 6.90: Beam specimens B13 strengthened by SIKA CFRP and FYFE epoxy

Figure 6.91: Beam specimens B14 strengthened by Sika CFRP and Fyfe epoxy

Figure 6.92: Beam specimens B9 strengthened by Fyfe CFRP and Sika epoxy

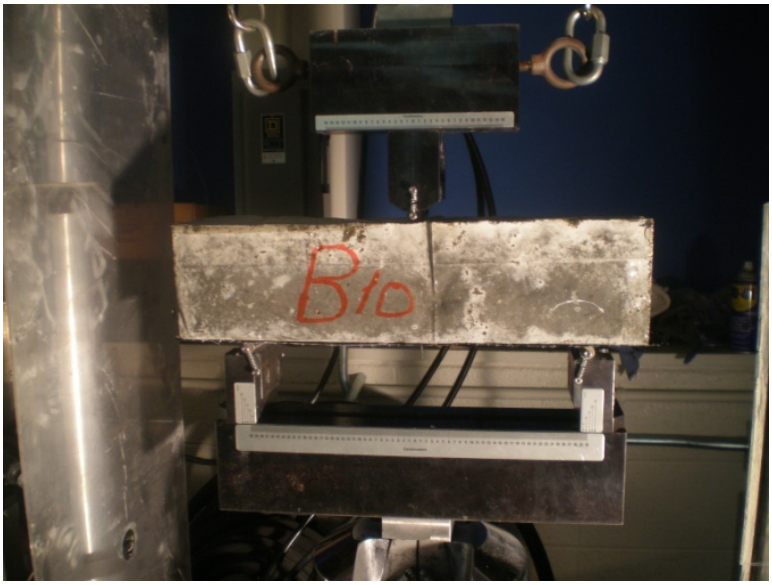

Figure 6.93: Beam specimens B10 strengthened by Fyfe CFRP and Sika epoxy

As shown in figures (6.94, 6.95), B13 and B14 failed due to FRP rupture. A concrete flexural crack first appeared at the center of the beam, the crack grew gradually followed by FRP

rupture through the beam width at the center of the bottom surface. No FRP delamination occurred.

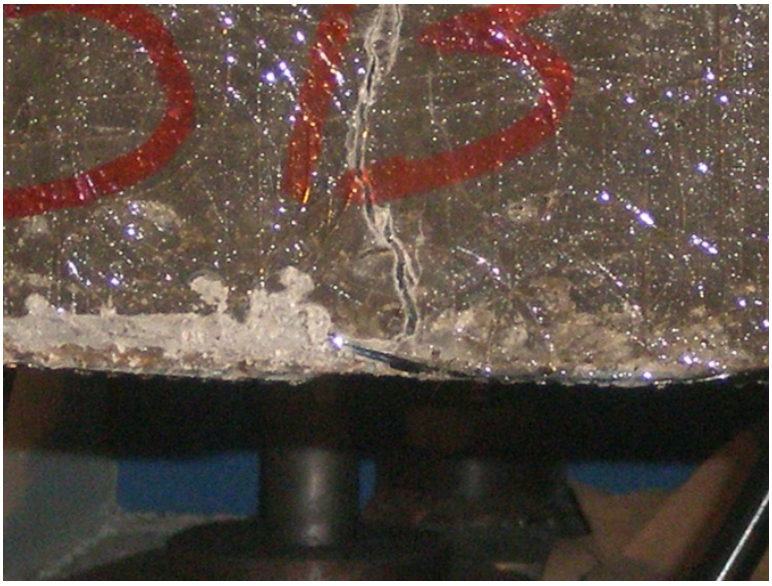

a) Concrete flexural crack, B13

b) CFRP Rupture, B13

Figure 6.94: Concrete flexural crack and FRP rupture, B13

a) Concrete flexural crack, B14

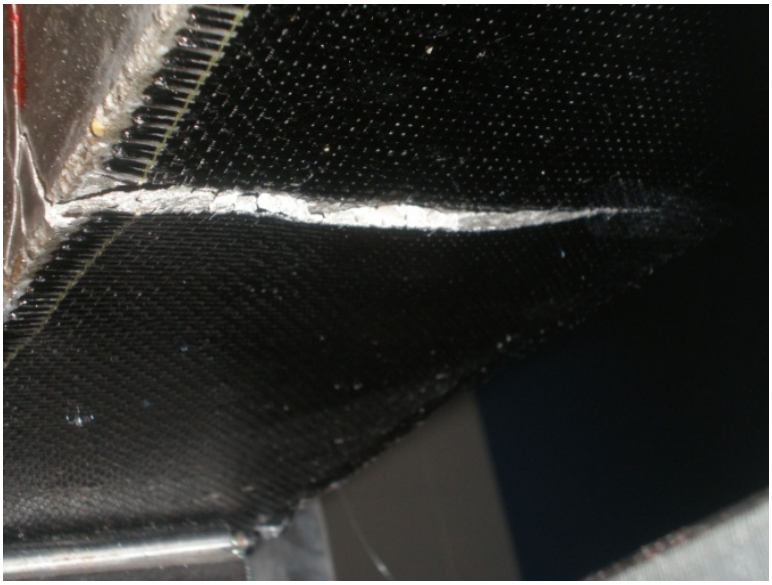

b) CFRP Rupture B14

Figure 6.95: Concrete flexural crack and FRP rupture, B14

The pattern of failure that had been noticed on beams B9 and B10 were concrete flexural cracking following by FRP delamination from the concrete. FRP rupture was not observed for both B9 and B10 specimen, (Figures 6.96, and 6.97).

a) CFRP delamination, B9

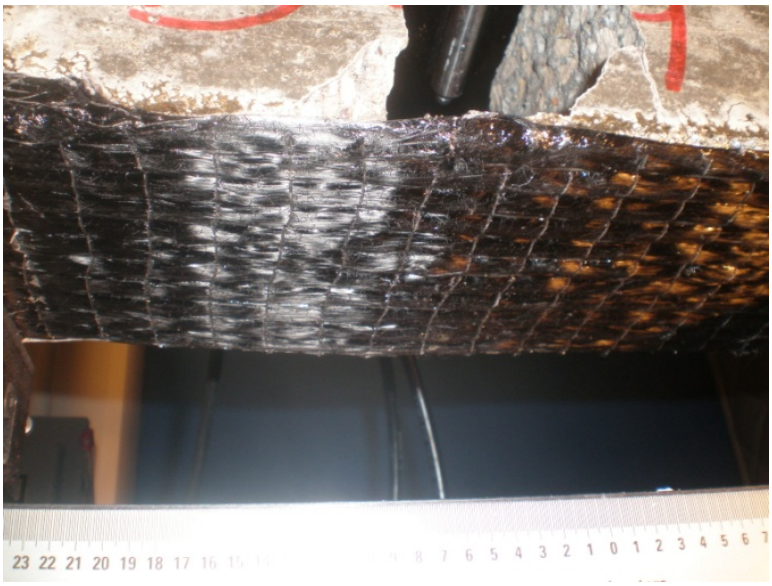

b) CFRP delamination, no rupture B9

Figure 6.96: Concrete flexural crack and FRP delamination, B9

a) Concrete flexural crack, B10

b) CFRP delamination, no rupture B10

Figure 6.97: Concrete Flexural Crack and FRP Delamination, B10

Table 6.32 shows a comparison of the flexural strength test results for four concrete beams were strengthened by using Sika carbon fiber and different resin materials. While the first two beams in this table were strengthened by utilizing Sikadur300 epoxy material, the Tyfo S saturant epoxy which produced by Fyfe Company were used to strength the other two beams (B13, B14). The results say that these two resin materials provided flexural strength values closed to each other.

Table 6.32: Concrete beam specimens strengthened by Sika CFRP and various epoxy materials

Beam no.	FRP type	Epoxy Type	Max. load lbs	Max. Comp. Strength (psi)	Mean Load (lbs)	Failure Mode
B6	CFRP	Sika	4008	1128	4171.5	FRP Rupture
B7	CFRP	Sika	4335	1177		FRP Rupture
B13	CFRP	Fyfe	3706.8	1043	3849.4	FRP Rupture
B14	CFRP	Fyfe	3991.9	1124		FRP Rupture

The flexural load versus mid-span deflection curves are plotted in figure 6.98. Strength and stiffness of the strengthened beams are all similar.

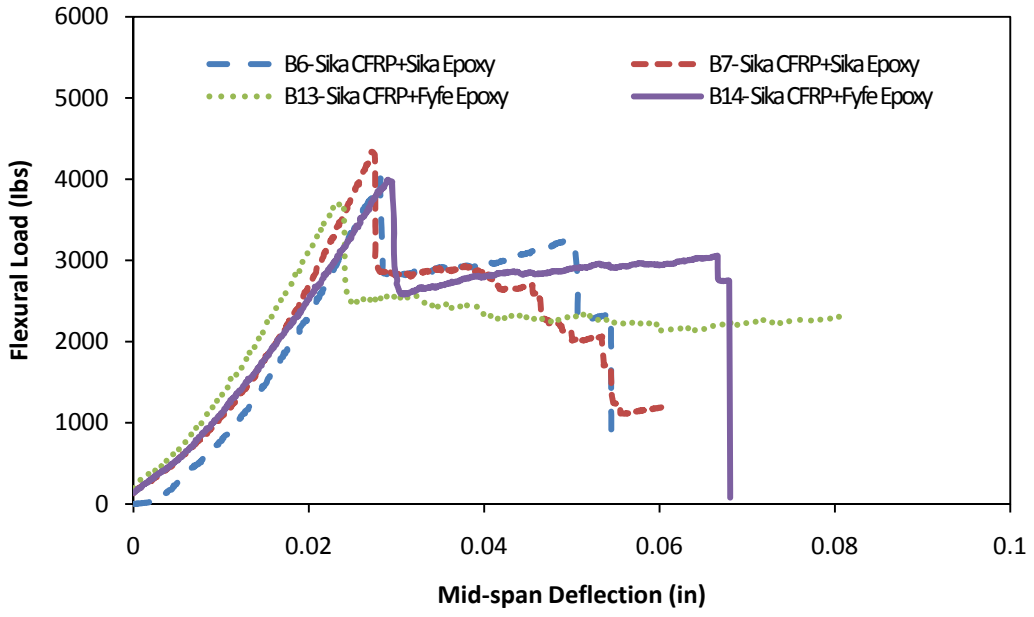

Figure 6.98: Flexural load- mid-span deflection of Sika CFRP strengthened beams

The comparison between Sika and Fyfe epoxy materials which have been used to bond the Fyfe carbon fiber to strength the concrete beam specimens is tabulated in table 6.33 and shown in figure 6.99 as well.

Table 6.33: Concrete beam specimens strengthened by Fyfe CFRP and various epoxy materials

Beam no.	FRP type	Epoxy Type	Max. load (lbs)	Max. Comp. Strength (psi)	Mean Load (lbs)	Failure Mode
B4	CFRP	Fyfe	9273.7	2643	8704.8	FRP delamination
B5	CFRP	Fyfe	8135.9	2290		FRP delamination
B9	CFRP	Sika	9458.9	2662.7	8814.9	FRP delamination
B10	CFRP	Sika	8170.9	2300.1		FRP delamination

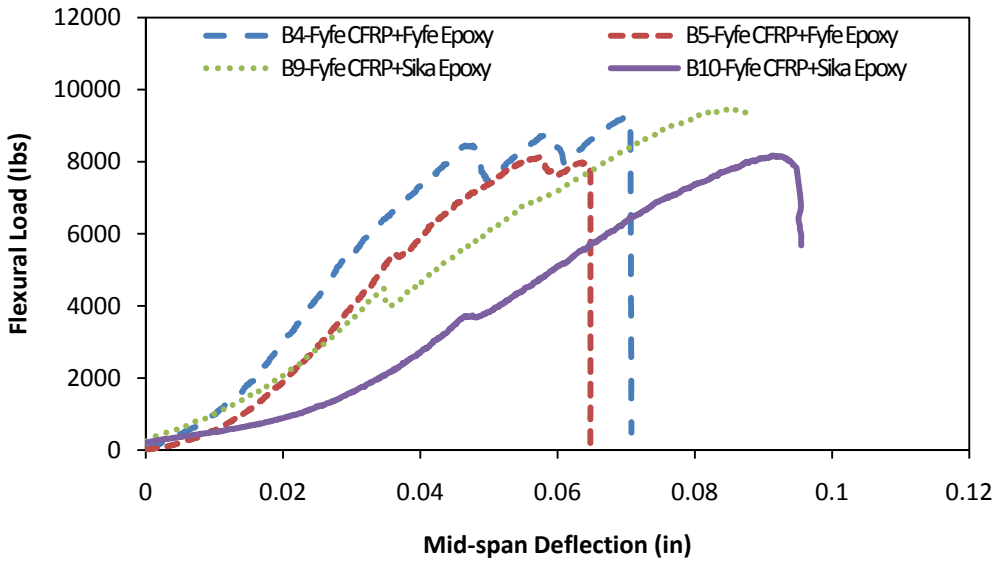

Figure 6.99: Flexural load- mid-span deflection of Fyfe CFRP strengthened beams

By the same way, two column specimens, C8 and C12 were wrapped by SIKA CFRP and FYFE epoxy. These two cylindrical specimens have been tested for compressive strength, figures (6.100, 6.101). The mode of failure was FRP rupture for both specimens, (see figures 6.102 and 6.103).

Figure 6.100: Compression strength test for column specimen strengthened by Sika CFRP and Fyfe epoxy

Figure 6.101: Compression strength test for column specimen strengthened by Sika CFRP and Fyfe epoxy

Figure 6.102: Concrete crushing and FRP rupture along the height of the specimen, C8

Figure 6.103: Concrete crushing and FRP rupture along the height of the specimen, C12

By comparing the results of these two specimens (C8 and C12) and the specimens C3, CT that were strengthened by utilizing Sika Epoxy material, the Fyfe epoxy seems to produce a 10% strength increase over the Sika epoxy. The mode of failure was the same in all cases,

(Table 6.34). The relationships between compressive load and deflection for these specimens are shown in figure 6.104.

Table 6.34: Concrete column specimens strengthened by Sika CFRP and various epoxy materials

Column no.	FRP type	Epoxy Type	Max. load (lbs)	Max. Comp. Strength (psi)	Mean Load (lbs)	Failure Mode
C3	CFRP	Sika	86391.42	6875.0	87150.9	FRP Rupture
CT	CFRP	Sika	87907.6	6995.5		FRP Rupture
C8	CFRP	Fyfe	98852.2	7866.4		FRP Rupture
C12	CFRP	Fyfe	93349.7	7428.5	96101.0	FRP Rupture

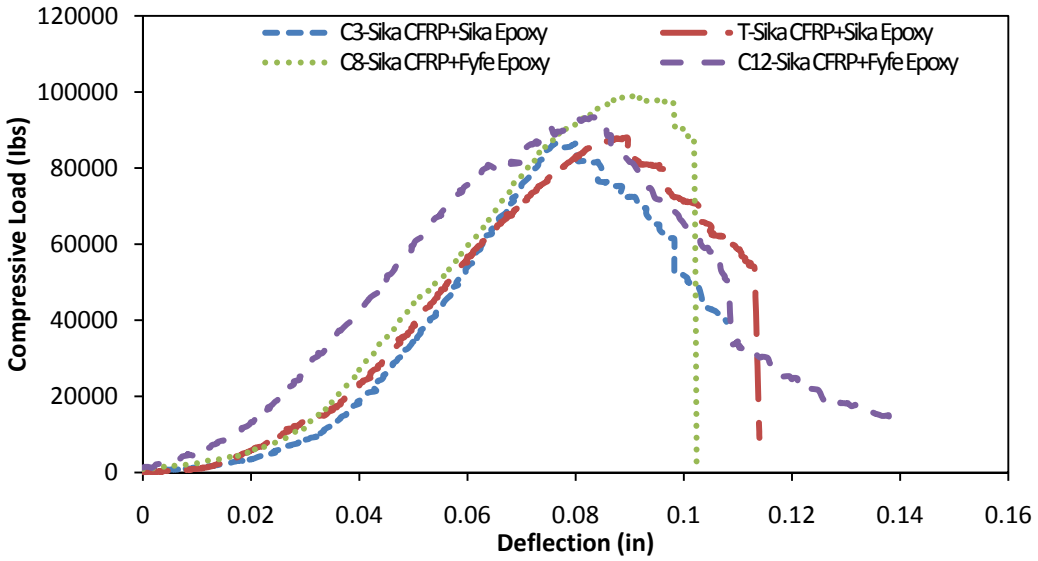

Figure 6.104: Compression load- deflection relationships of Sik FRP strengthened columns

On the other hand, two column specimens C6 and C10 were strengthened by FYFE CFRP and SIKA epoxy, figures (6.105, 6.106). The modes of failure were FRP rupture in both longitudinal and hoop direction for both specimens, Figures (6.107, 6.108).

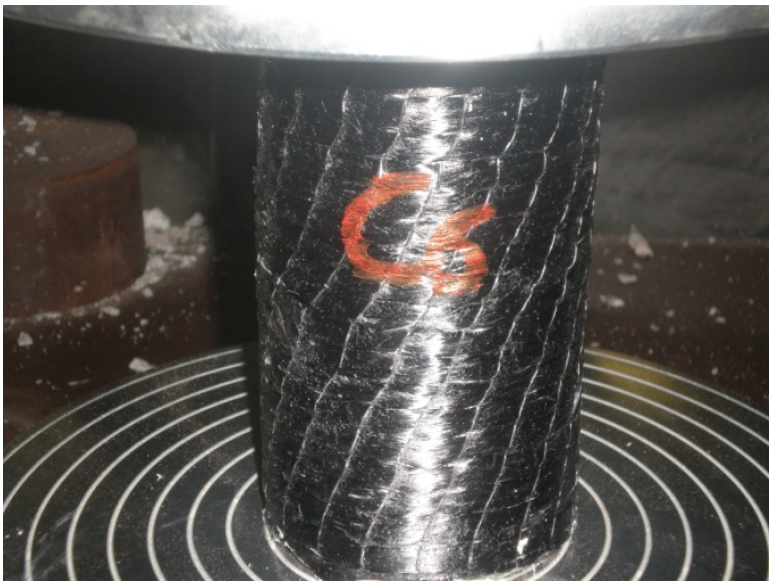

Figure 6.105: Compression strength test for column specimen strengthened by Fyfe CFRP and Sika epoxy

Figure 6.106: Compression strength test for column specimen strengthened by Fyfe CFRP and Sika epoxy

Figure 6.107: Hoop direction FRP rupture around the perimeter of the specimen, C6

Figure 6.108: Hoop direction FRP rupture around the perimeter of the specimen, C10

Table 6.35 presents the maximum flexural strength and the failure mode of all the four column specimens that were strengthened by Fyfe carbon fiber and different epoxy materials.

Both adhesive materials (Fyfe and Sika epoxy) provided satisfactory results. The Fyfe-epoxy specimens show a strength increase of 32% over the Sika-epoxy specimens. Figure (6.109) plots the relationship between the flexural load and deflection of these four specimens.

Table 6.35: Concrete column specimens strengthened by Fyfe CFRP and various epoxy materials

Column no.	FRP type	Epoxy Type	Max. load lbs	Max. Comp. Strength (psi)	Mean Load (lbs)	Failure Mode
C2	CFRP	Fyfe	241901.2	19250	243280.2	FRP Rupture
C4	CFRP	Fyfe	244659.1	19469		FRP Rupture
C6	CFRP	Sika	186777.6	14863		FRP Rupture
C10	CFRP	Sika	181271.1	14435	184024.4	FRP Rupture

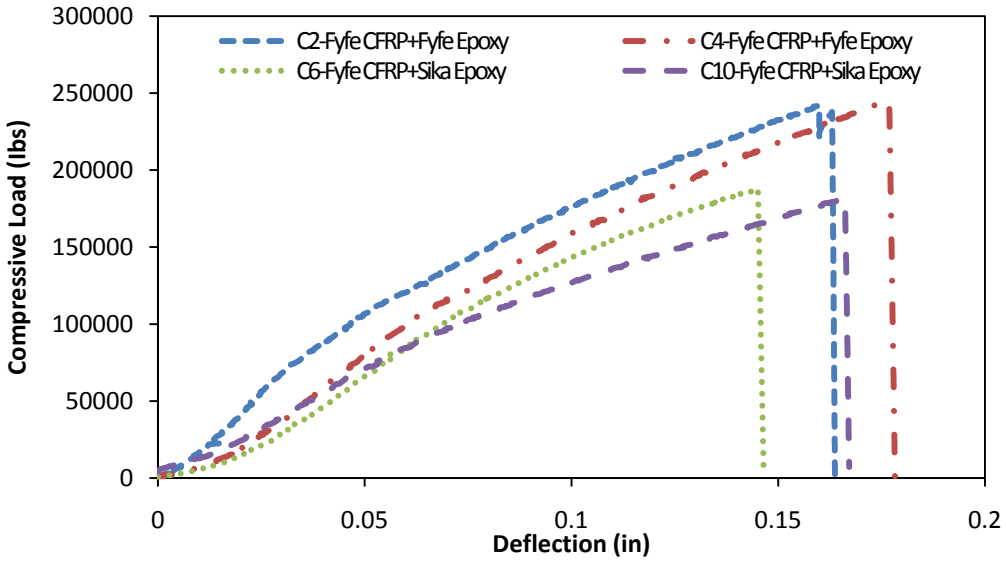

Figure 6.109: Compression load- deflection relationships of Fyfe FRP strengthened columns

6.4.3 Summary

As a result of all above tests, the mode of failure of all concrete beams strengthened by one layer of Sika CFRP regardless of the type of resin material was FRP rupture. While FRP delamination was noticed between the concrete surface and the FRP sheets in the case of the two-layer Sika CFRP strengthened beam specimen.

As for the Sika GFRP, Fyfe CFRP, and Fyfe GFRP beam specimens, all failed owing to FRP delamination no matter Sika or Fyfe resin was used. All the column specimens strengthened

by using the Sika GFRP, Fyfe CFRP, or Fyfe GFRP failed due to FRP rupture in the longitudinal and hoop (transverse) direction. All the concrete column specimens strengthened by Sika CFRP failed due to FRP rupture in the meridian (longitudinal) direction.

According to the above results and observations, the following conclusions have been drawn.

1. To achieve the main objectives of this study on bond properties between concrete surface and FRP strengthening material, delamination of FRP from concrete should be avoided. Hence, a weaker fiber system (Sika CFRP) was chosen to strengthen the remaining beam and column specimens.
2. Despite both Sika and Fyfe resin materials showed satisfactory results of bonding, the Fyfe epoxy was chosen for further study. This choice was based on the higher strength of the Fyfe resin (Tyfo S Saturant Epoxy) according to the manufacturer data sheets and the findings from the preliminary tests.
3. Although, according to the above two points, the focus in this study was placed on the Sika CFRP and Fyfe resin system, additional tests also were carried out with beam and column specimens that were strengthened by using Sika GFRP, Fyfe CFRP, Fyfe GFRP, and Fyfe or Sika resin materials. These additional specimens also were subjected to different environmental conditions to study to what extent the influence of temperature and relative humidities on the flexural and compressive strength of these strengthened specimens. It was also important to determine how temperature and humidity affect the mode of failure. These results will be presented at the end of this chapter.

6.5 Environmental Effect on FRP Strengthened Beam Specimens

6.5.1 FRP Strengthened Beams at 40 Cycles and 100°C Temperature

Eight concrete beam specimens were first strengthened by using Sika CFRP and Fyfe epoxy. These specimens were then subjected to environmental aging at 100°C temperature, different relative humidities and cycle periods up to 40 cycles (80 hours for a 2-hour cycle period). Also, two other beams B22 and B23 were strengthened by the same FRP materials and subjected to the standard lab conditions for a period equivalent to 40 cycles. Table 6.36 shows the test results of these beams. Comparing with the control concrete beam specimens, the CFRP strengthening material improved the flexural strength by 34% for the standard lab conditions specimens. While for the specimens that were exposed to the specified environmental conditions, flexural strength increase ranged from 27% to 53%. The maximum improvement on flexural strength was 53% for the specimens conditioned at 100°C, relative humidity 100%, and 2-hour cycle period. All these 10 specimens failed due to FRP rupture; figure (6.110) shows the mode of failure of B23.

Figure 6.110: Concrete flexural failure and FRP rupture of B23

The flexural load vs. mid-span deflection curves of these specimens are shown in figure (6.111), only one of two specimens of the same group has been plotted in this figure.

Table 6.36: FRP strengthened beam maximum flexural test results subjected to different environmental conditions with 100°C and 40 cycles

Beam no.	Temp °C	RH %	CP! (Hr)	Max. load lbs	Mean lbs	Flex. strength (psi)	Difference - %	Failure mode
B22	LT*	LH+	-	4061.5	4110	1143.3	34.2	FRP rupture
B23				4158.6		1170.6		FRP rupture
B38	100	0.0	0	3883.3	3875	1093.1	26.6	FRP rupture
B39				3865.8		1088.2		FRP rupture
B30			2	4013.2	4111	1129.7	34.3	FRP rupture
B31				4209.2		1184.9		FRP rupture
B46		100	0	4189.4	4191	1179.3	36.9	FRP rupture
B47				4192.3		1180.1		FRP rupture
B54			2	4699.5	4685	1322.9		FRP rupture
B55				4670.9		1314.9	53.0	FRP rupture

-Percentage difference of max. load increasing or decreasing compared with control result.
*Lab temperature,
+Lab humidity,
!Cycle period,

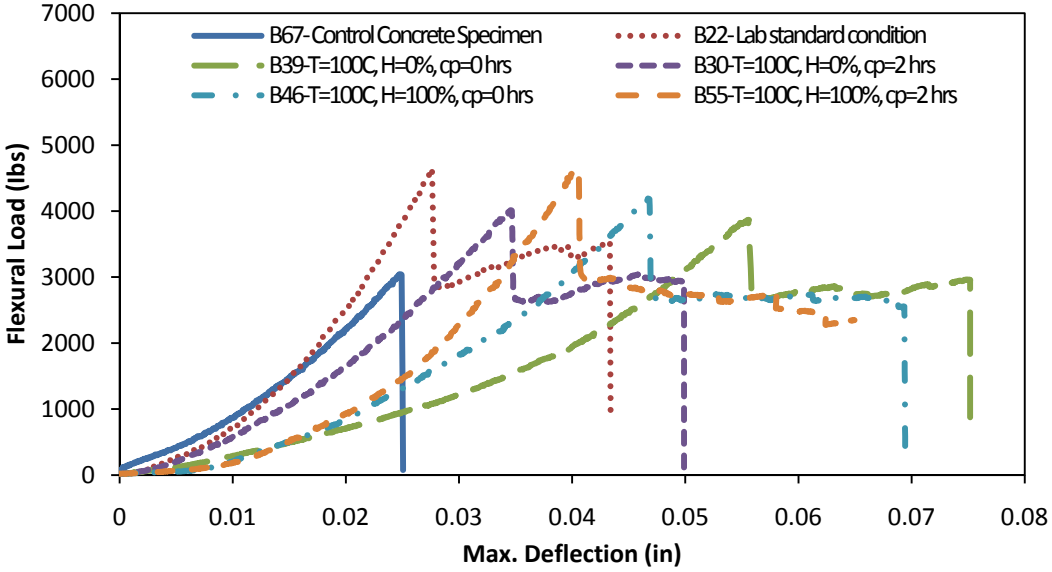

Figure 6.111: Flexural load vs. mid-span deflection of strengthened beams – 100°C and 40 cycles

6.5.2 FRP Strengthened Beams at 100 Cycles and 100°C Temperature

Two strengthened beams B24 and B25 were subjected to equivalent 100 cycles (200 hours) under standard lab conditions and other eight strengthened beam specimens were exposed to100°C of temperature and different environmental conditions as described in table 6.37.

Comparing with the control specimens, all these specimens have shown increases in flexural strength. Compared to the control, the increase was 36% for the standard lab conditioned specimens, whereas the improvements in flexural strength were in the range from 43% to 66% for those specimens conditioned at 100°C temperature and different environmental conditions. The mode of failure of all these 10 specimens was FRP rupture Figure (6.112). Figure 6.113 shows the relationships between flexural load and mid-span defection for these specimens; only one of two specimens from the same group was included in the plot for clarity.

Table 6.37: FRP strengthened beam maximum flexural test results subjected to different environmental conditions with 100°C and 100 cycles

Beam no.	Temp °C	RH %	CP[!] (Hr)	Max. load lbs	Mean lbs	Flex. strength (psi)	Difference[-] %	Failure mode
B24	LT[*]	LH[+]	-	4043.8	4171	1138.3	36.2	FRP rupture
B25				4297.6		1209.8		FRP rupture
B40	100	0.0	0	4656.2	4472	1310.7	46.1	FRP rupture
B41				4287.5		1206.9		FRP rupture
B32			2	4752.7	4595	1337.9	50.1	FRP rupture
B33				4437.0		1249.0		FRP rupture
B48		100	0	4093.9	4383	1152.4	43.2	FRP rupture
B49				4671.4		1315.0		FRP rupture
B56			2	5147.0		1448.9		FRP rupture
B57				5011.1	5079	1410.6	65.9	FRP rupture

[-]Percentage difference of max. load increasing or decreasing compared with control result.
*Lab temperature,
+Lab humidity,
!Cycle period,

Figure 6.112: Typical mode of failure "FRP rupture" for concrete beam specimens (B56) at 100°C and 100 cycles

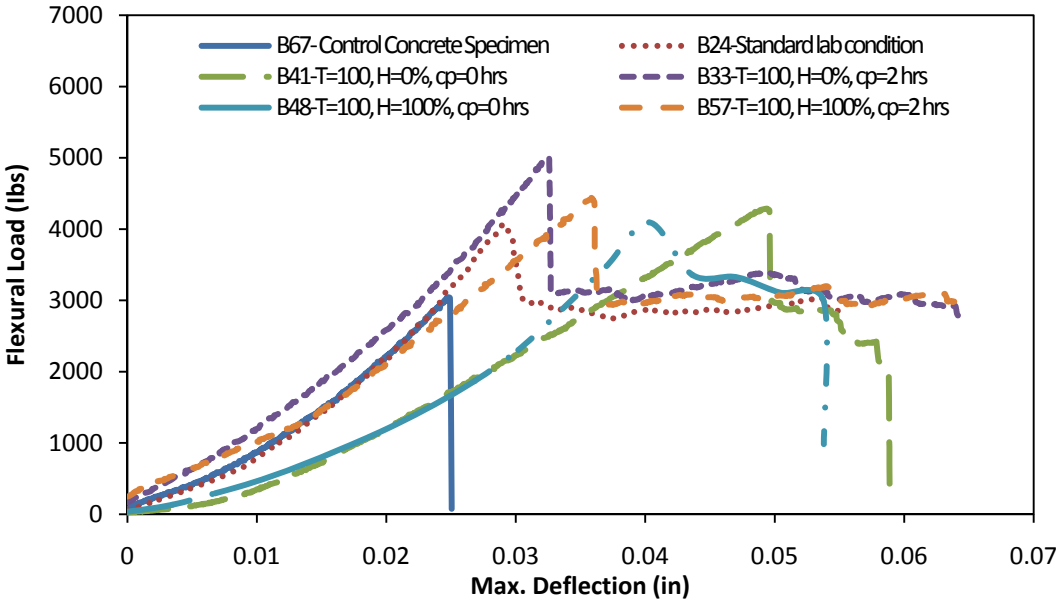

Figure 6.113: Flexural load vs. mid-span deflection of strengthened beams –100°C and 100 cycles

6.5.3 FRP Strengthened Beams at 250 Cycles and 100°C Temperature

An improvement in flexural strength has been observed by further increasing exposure time to 250 cycles (500 hours) under the 100°C of temperature. Two strengthened beams B26 and B27 recoded an increase in their flexural strength about 45% under the standard lab condition. While the other eight specimens have shown improvement in flexural strength ranging from 46% to about 55% over the control specimens (Plain concrete control specimen), Table (6.38). The results of the flexural tests are shown in figure 6.114. No change in the mode of failure was observed, where all these 10 specimens failed due to FRP rupture (see figure 6.115). FRP delamination was not observed in all cases.

Table 6.38: FRP strengthened beam maximum flexural test results subjected to different environmental conditions with 100°C and 250 cycles

Beam no.	Temp °C	RH %	CP! (Hr)	Max. load lbs	Mean lbs	Flex. strength (psi)	Difference - %	Failure mode
B26	LT*	LH+	-	4334.0	4445	1220.0	45.2	FRP rupture
B27				4556.6		1282.7		FRP rupture
B42	100	0.0	0	4491.9	4490	1264.5	46.7	FRP rupture
B43				4487.6		1263.3		FRP rupture
B34			2	4921.4	4762	1385.4	55.5	FRP rupture
B35				4603.1		1295.8		FRP rupture
B50		100	0	4621.4	4712	1300.9	53.9	FRP rupture
B51				4802.0		1351.7		FRP rupture
B58			2	4970.8	4755	1399.3	55.3	FRP rupture
B59				4540.1		1278.0		FRP rupture

-Percentage difference of max. load increasing or decreasing compared with control result.
*Lab temperature,
+Lab humidity,
!Cycle period,

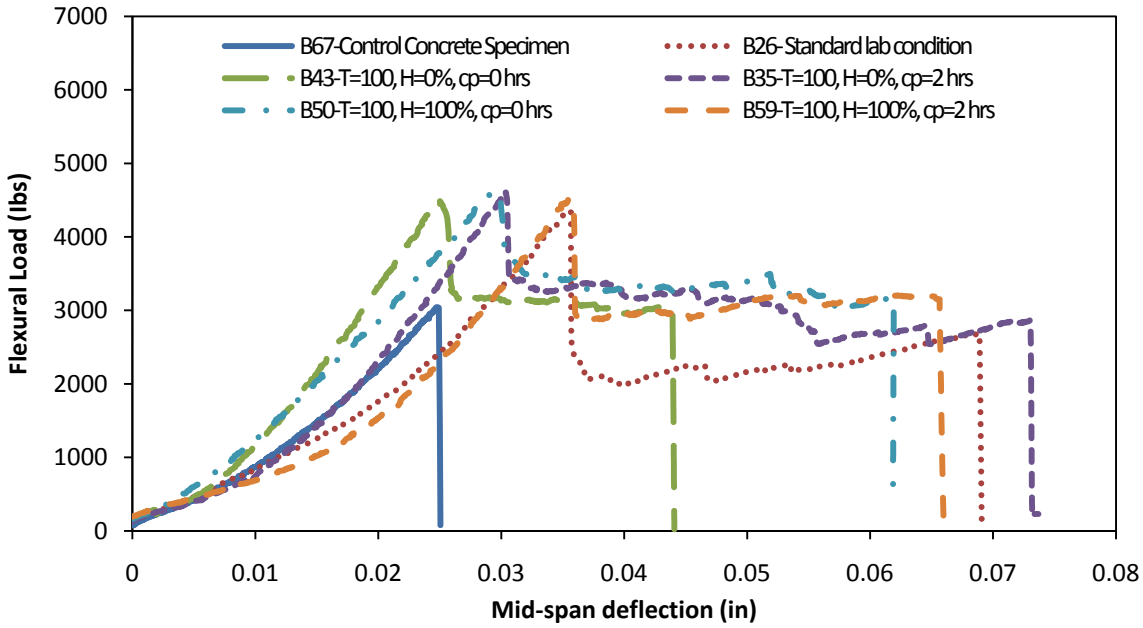

Figure 6.114: Flexural load vs. mid-span deflection of Strengthened beams – 100°C and 250 cycles

Figure 6.115: Typical mode of failure "FRP rupture" for concrete beam specimens (B51) at 100°C and 250 cycles

6.5.4 FRP Strengthened Beams at 625 Cycles and 100°C Temperature

Even when the time of exposure to the environmental conditions has been increased to 625 cycles which is equivalent to 1250 hours, the flexural strength of the strengthened specimens increased as shown in table 6.39. Such continuous increases in flexural strength indicate that the durability of the strengthened specimens is satisfactory, at least up to 625 cycles. No change in failure mode was observed; all specimens failed owing to FRP rupture, (Figure 6.116). The relationships of flexural load vs. mid-span deflection are shown in figure 6.117. Again, only a typical curve of one of two specimens from the same group was plotted.

Table 6.39: FRP strengthened beam maximum flexural test results subjected to different environmental conditions with 100°C and 625 cycles

Beam no.	Temp °C	RH %	CP! (Hr)	Max. load lbs	Mean lbs	Flex. strength (psi)	Difference - %	Failure mode
B28	LT*	LH+	-	4391.3	4538	1236.2	48.2	FRP rupture
B29				4684.5		1318.7		FRP rupture
B44	100	0.0	0	4305.8	4327	1212.1	41.3	FRP rupture
B45				4348.6		1224.1		FRP rupture
B36			2	4635.4	4542	1304.9	48.4	FRP rupture
B37				4448.8		1252.3		FRP rupture
B52		100	0	4809.8	4923	1354.0	60.8	FRP rupture
B53				5035.3		1417.4		FRP rupture
B60			2	5321.1		1497.9		FRP rupture
B61				4895.4	5108	1378.1	66.8	FRP rupture

-Percentage difference of max. load increasing or decreasing compared with control result.
*Lab temperature,
+Lab humidity,
!Cycle period,

Figure 6.116: Typical mode of failure "FRP rupture" for concrete beam specimens (B52) at 100°C and 625 cycles

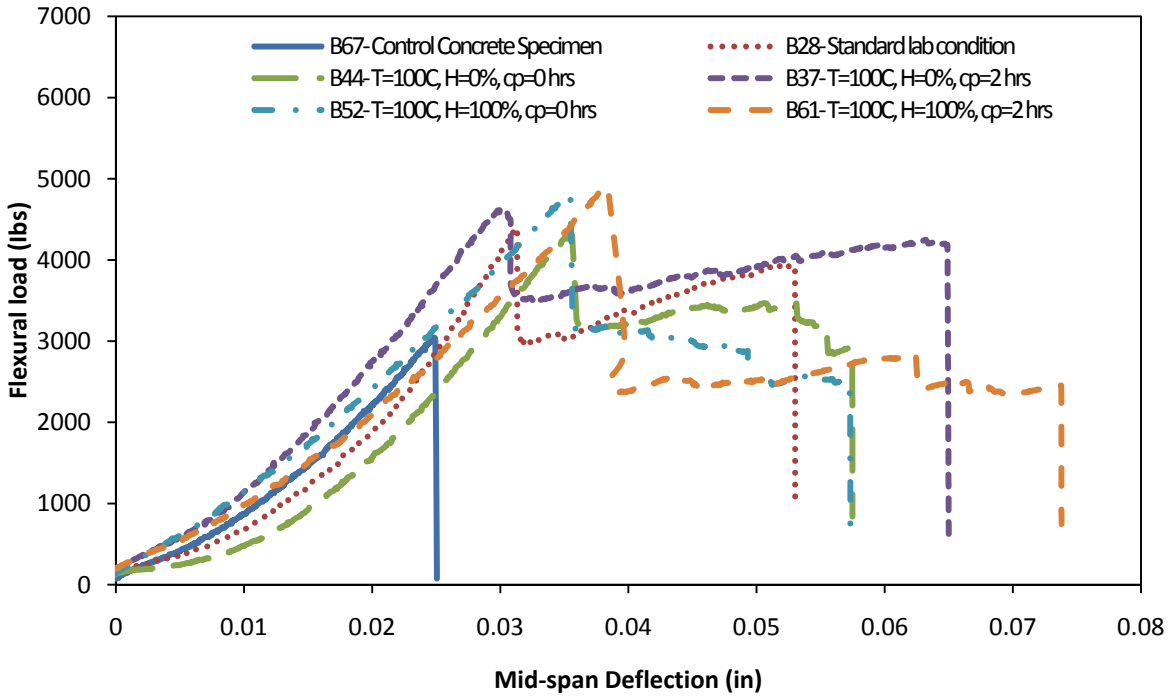

Figure 6.117: Flexural load vs. mid-span deflection of strengthened beams – 100°C and 625 cycles

6.5.5 FRP Strengthened Beams at 40 Cycles and 180°C Temperature

More interesting work has been done in this study by increasing the temperature of exposing to 180°C rather than 100°C. The higher test temperature would provide further insight into the effects of temperature on the behavior of the strengthening materials and their retrofit efficiencies. Under the 100°C temperature environments, all strengthened specimens showed an increase in flexural strength over time comparing to the control concrete specimens. The mode of failure was the same for all specimens. Under the 180°C environments, the results were very different. Eight strengthened beam specimens B90, B91, B102, B103, B96, B97, B110, and B111 were conditioned at 180°C temperature, and different relative humidity and cycle periods for 40 cycles (which equals 80 hours). Then these specimens were tested to failure by flexural testing, Figure (6.118). As shown in table 6.40, despite of exposure to 40 cycles, an increase in flexural strength was still observed, compared to the control specimens. However, these improvements were less than those of the 100°C temperature specimens or the standard lab condition specimens at same numbers of cycles. Moreover, all these eight specimens showed FRP delamination as the mode of failure. This represents a significant change from FRP rupture that was observed in all 100°C specimens. Figure 6.119 shows a typical delamination of the FRP sheet from concrete beams. As a result of exposure to 180°C temperature, the color of all the concrete specimens was changed to dark brown due to partial melting of the resin material, (see figure 6.118).

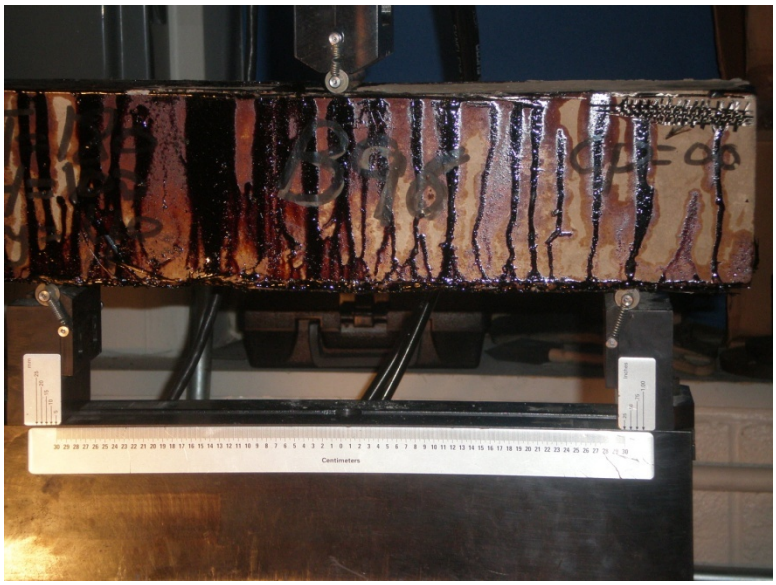

Figure 6.118: Flexural load test of B96

The relationships between the flexural load and mid-span deflection are shown in figure (6.120). The results suggest that most of 180°C specimens showed a higher ductility after the development of first crack and prior to the FRP was completely delaminated.

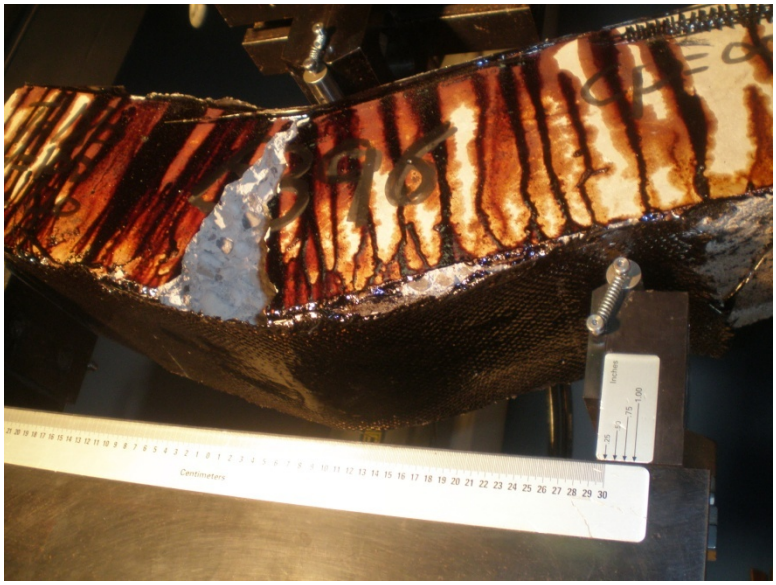

Figure 6.119: FRP delamination of concrete beam specimen, 180°C and 40 cycles

Table 6.40: FRP strengthened beam maximum flexural test results subjected to different environmental conditions with 180°C and 40 cycles

Beam no.	Temp °C	RH %	CP! (Hr)	Max. load lbs	Mean lbs	Flex. strength (psi)	Difference - %	Failure mode
B22	LT*	LH+	-	4061.5	4110	1142.3	34.24	FRP rupture
B23				4158.6		1169.6		Delamination
B90	180	0.0	0	3970.2	4116	1116.6	34.44	Delamination
B91				4260.8		1198.4		Delamination
B102			2	3275.3	3522	921.2	15.04	Delamination
B103				3769.1		1060.1		Delamination
B96		100	0	3933.9	3977	1106.4	29.90	Delamination
B97				4019.5		1130.5		Delamination
B110			2	4102.0		1153.7		Delamination
B111				3750.9	3926	1054.9	28.23	Delamination

-Percentage difference of max. load increasing or decreasing compared with control result.
*Lab temperature,
+Lab humidity,
!Cycle period,

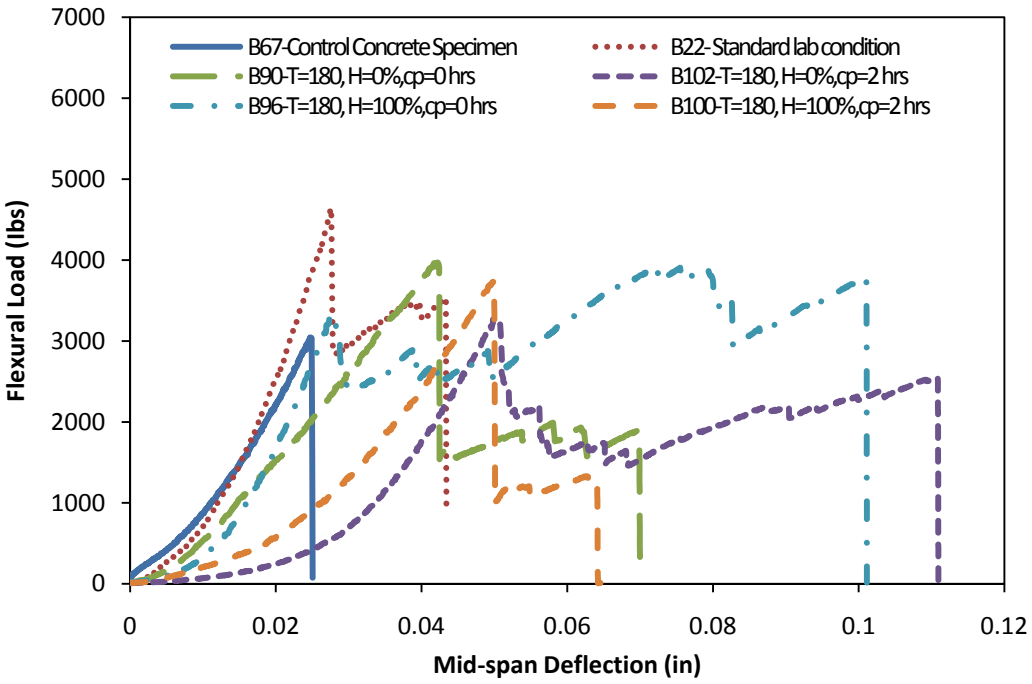

Figure 6.120: Flexural load vs. mid-span deflection of strengthened beams – 180°C and 40 cycles

6.5.6 FRP Strengthened Beams at 100 Cycles and180^{o}C Temperature

Further reductions in flexural strength were found when the specimens were exposed to the 180^{o}C environments after 100 cycles (200 hours). Specimens B92, B93, B104, B105, B98, B99, B112, and B113 showed reduced flexural strength, comparing to the 100^{o}C specimens or the 180^{o}C specimens after 40 cycles. Table 6.41 shows the maximum flexural load, flexural strength, and the modes of failure for all these specimens. Figure 6.121 illustrated a typical FRP delamination from one of these specimens. The relationships between the flexural load and deflections are plotted in figure 6.122.

Table 6.41: FRP strengthened beam maximum flexural test results subjected to different environmental conditions with 180^{o}C and 100 cycles.

Beam no.	Temp ^{o}C	RH %	CP$^{!}$ (Hr)	Max. load lbs	Mean lbs	Flex. strength (psi)	Difference^{-} %	Failure mode
B24	LT*	LH^{+}	-	4043.8	4171	1137.3	36.2	FRP rupture
B25				4297.6		1208.7		Delamination
B92	180	0.0	0	3405.4	3373	957.8	10.2	Delamination
B93				3340.0		939.4		Delamination
B104			2	3106.2	3189	873.6	4.2	Delamination
B105				3271.9		920.2		Delamination
B98		100	0	3157.9	3205	888.2	4.7	Delamination
B99				3252.3		914.7		Delamination
B112			2	3722.8		1047.0		Delamination
B113				3941.4	3832	1108.5	25.2	Delamination

$^{-}$Percentage difference of max. load increasing or decreasing compared with control result.
*Lab temperature,
+Lab humidity,
!Cycle period,

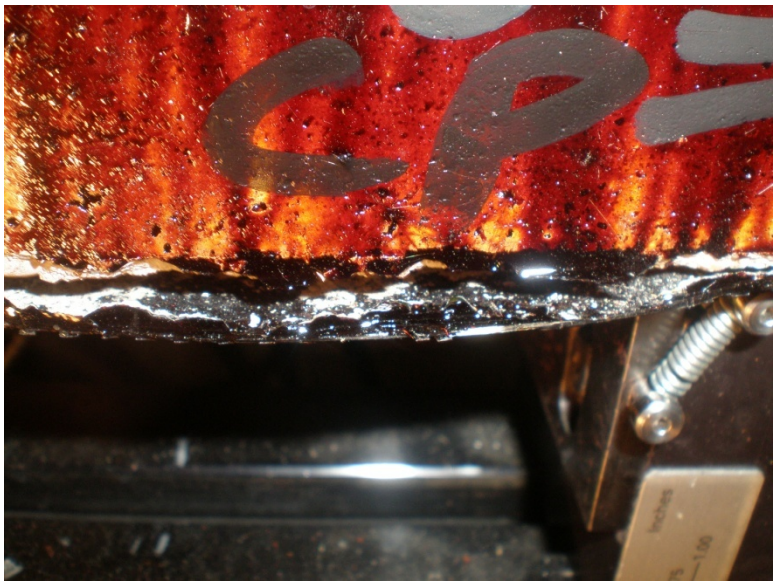

Figure 6.121: FRP delamination of concrete beam specimen, 180°C and 100 cycles

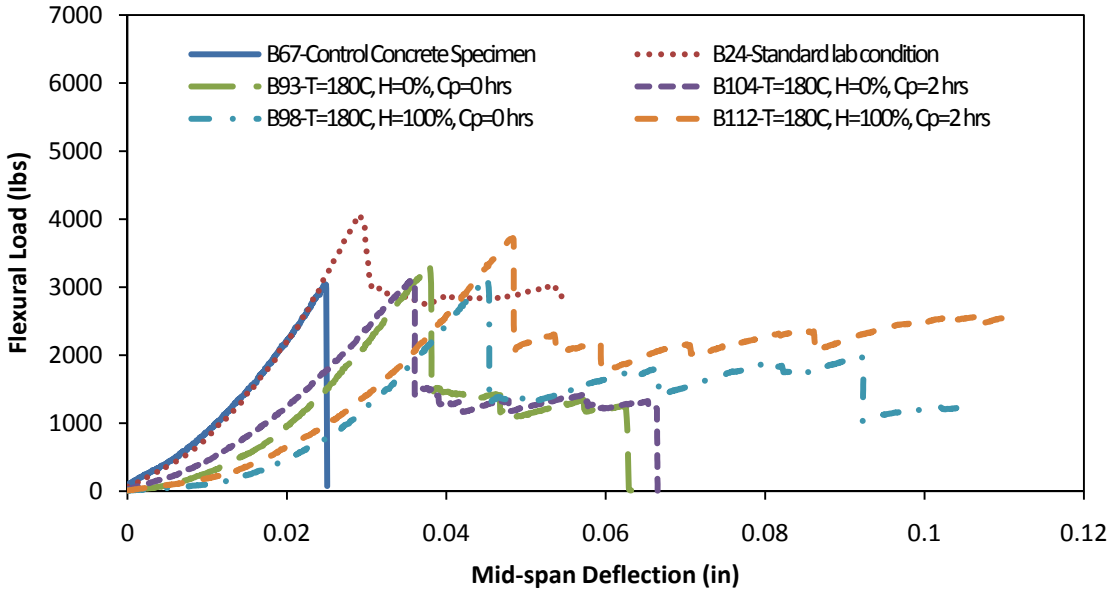

Figure 6.122: Flexural load vs. mid-span deflection of strengthened beams – 180°C and 100 cycles

6.5.7 FRP Strengthened Beams at 250 Cycles and180°C Temperature

By subjecting another eight specimens B94, B95, B106, B107, B100, B101, B114, and B115 to the 180°C environments for 250 cycles, a significant reduction in flexural strength was

found in all these specimens (Table 6.42). All specimens failed due to FRP delamination, as shown in figures 6.123.

Figure 6.123: FRP delamination of concrete beam specimen, 180°C and 250 cycles

Table 6.42: FRP strengthened beam maximum flexural test results subjected to different environmental conditions with 180°C and 250 cycles

Beam no.	Temp °C	RH %	CP[!] (Hr)	Max. load lbs	Mean lbs	Flex. strength (psi)	Difference[-] %	Failure mode
B26	LT[*]	LH[+]	-	4334.0	4445	1218.9	45.2	FRP rupture
B27				4556.6		1281.5		Delamination
B94			0	2801.5	2852	787.9	-6.8	Delamination
B95		0.0		2903.1		816.5		Delamination
B106			2	3174.8	3327	892.9	8.7	Delamination
B107	100			3479.9		978.7		Delamination
B100			0	3074.3	2910	864.6	-5.0	Delamination
B101		100		2746.0		772.3		Delamination
B114			2	3094.1		870.2		Delamination
B115				3198.4	3146	899.6	2.8	Delamination

[-]Percentage difference of max. load increasing or decreasing compared with control result.
*Lab temperature,
+Lab humidity,
!Cycle period,

The flexural load verses mid-span deflection curves are shown in figure 6.124. Regardless the degrees of humidity and cycle periods, the flexural strength significantly reduced after 250 cycles conditioned in the 180°C environments, when being compared with the corresponding standard lab condition specimens. Such strength values are approximately the same as the control plain concrete specimens. That is the strengthening effect of the CRFP sheet is almost vanished, most likely due to a severely weakened bond between concrete and the CFRP. Such bond deterioration became very evident after 250 cycles conditioned at 180°C.

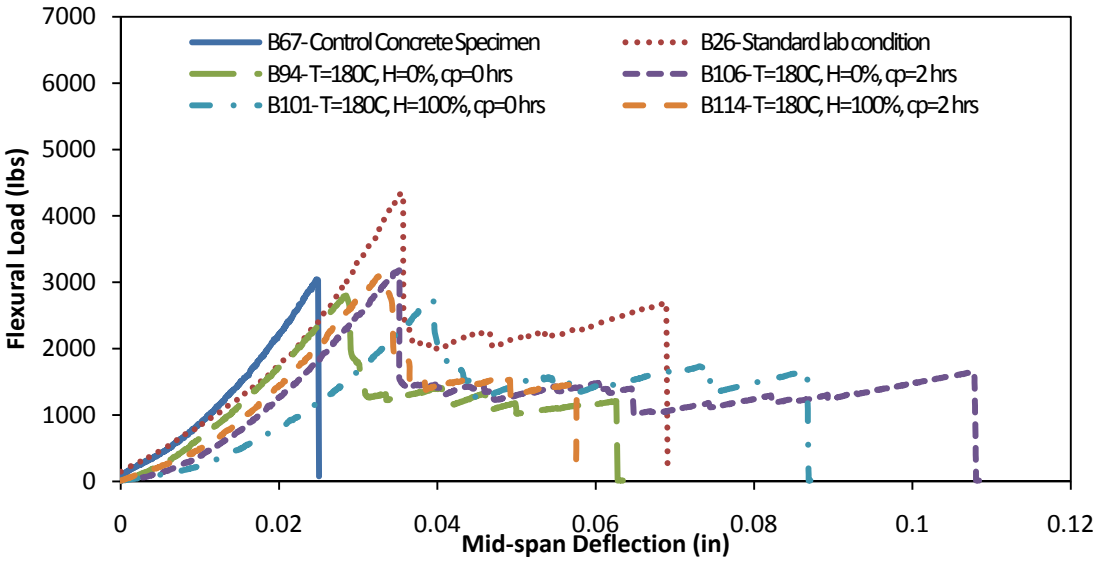

Figure 6.124: Flexural load- mid-span deflection of Strengthened beams – 180°C and 250 cycles

Tables (6.43 to 6.47) show the summary results of the specimens subjected to 100°C temperature and different environmental condition. The reported numbers represented the averaged maximum deflection, maximum flexural load, and stiffness of two beam specimens.

Table 6.43: Standard lab condition strengthened beam specimen results

# of Cycle	Temp (°C)	RH (%)	CP	Average max. Deflection (in)	Average max. Load (lbs)	Average Stiffness (lbs/in)
Control	LT	LH	-	0.0290	3991.9	143731
40	LT	LH	-	0.0405	4110.0	119719
100	LT	LH	-	0.0409	4170.7	118892
250	LT	LH	-	0.0305	4445.3	156218
625	LT	LH	-	0.0292	4537.9	161544

Table 6.44: Strengthened beam specimen results (RH=0%, Cp=2)

# of Cycle	Temp (°C)	RH (%)	CP	Average max. Deflection (in)	Average max. Load (lbs)	Average Stiffness (lbs/in)
Control	LT	LH	-	0.0290	3991.9	143731
40	100	0.0	2	0.0347	4111.2	125413
100	100	0.0	2	0.0273	4881.9	175560
250	100	0.0	2	0.0295	4762.2	183055
625	100	0.0	2	0.0314	4542.1	179442

Table 6.45: Strengthened beam specimen results (RH=100%, Cp=2)

# of Cycle	Temp (°C)	RH (%)	CP	Average max. Deflection (in)	Average max. Load (lbs)	Average Stiffness (lbs/in)
Control	LT	LH	-	0.0290	3991.9	143731
40	100	100	2	0.0385	4685.2	145623
100	100	100	2	0.0357	4792.0	127058
250	100	100	2	0.0354	4755.5	146383
625	100	100	2	0.0323	5108.3	160448

Table 6.46: Strengthened beam specimen results (RH=0%, Cp=0)

# of Cycle	Temp (°C)	RH (%)	CP	Average max. Deflection (in)	Average max. Load (lbs)	Average Stiffness (lbs/in)
Control	LT	LH	-	0.0290	3991.9	143731
40	100	0	0	0.0522	3874.6	83806
100	100	0	0	0.0393	4471.9	118905
250	100	0	0	0.0295	4489.7	118603
625	100	0	0	0.0323	4327.2	155525

Table 6.47: Strengthened beam specimen results (RH=100%, Cp=0)

# of Cycle	Temp (^{o}C)	RH (%)	CP	Average max. Deflection (in)	Average max. Load (lbs)	Average Stiffness (lbs/in)
Control	LT	LH	-	0.0290	3991.9	143731
40	100	100	0	0.0441	4190.8	120181
100	100	100	0	0.0377	4382.6	131354
250	100	100	0	0.0449	4911.7	111345
625	100	100	0	0.0361	4922.6	135892

The maximum deflections, flexural loads, and stiffnesses after exposure to 100^{o}C of temperature are shown in Tables (6.48 to 6.50) respectively, as well as Figures (6.125 to 6.127).

Table 6.48: Maximum deflection results for different conditions at 100^{o}C

		Temperature= 100^{o}C			
# of Cycles	Lab Temp	Relative humidity 0%		Relative humidity 100%	
		Cp=0 hrs	Cp=2 hrs	Cp=0 hrs	Cp=2 hrs
0	0.0290	-	-	-	-
40	0.0405	0.0385	0.0347	0.0522	0.0441
100	0.0409	0.0357	0.0273	0.0393	0.0377
250	0.0305	0.0354	0.0295	0.0295	0.0449
625	0.0292	0.0323	0.0314	0.0323	0.0361

Deflection's unit [inch]

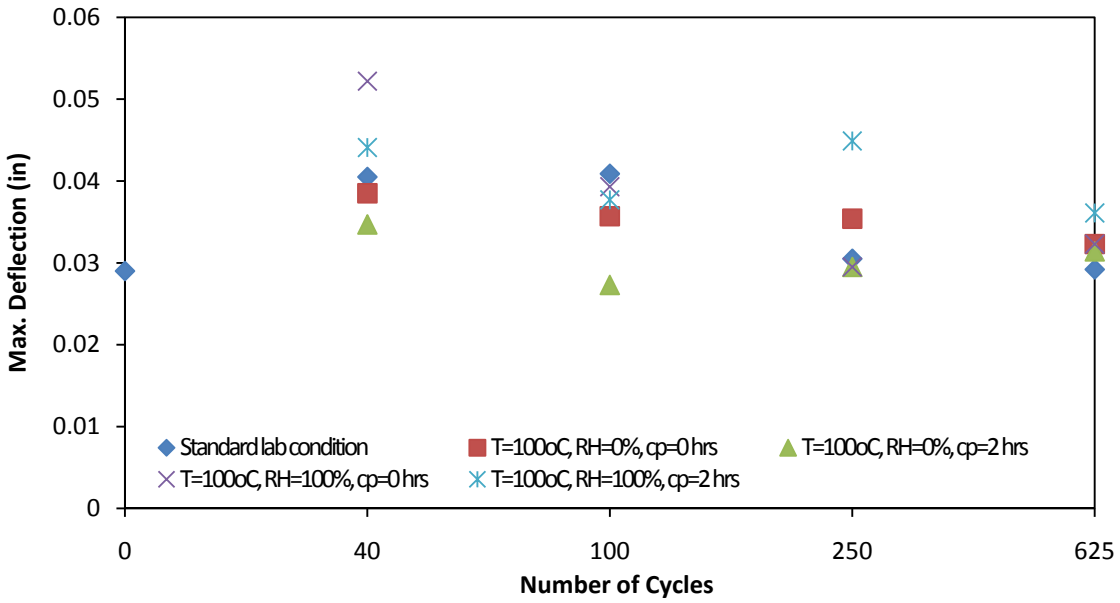

Figure 6.125: Deflection vs. number of cycles after 100°C temperature

Table 6.49: Maximum Flexural load results for different conditions at 100°C

# of Cycles	Lab Temp	Temperature= 100°C			
		Relative humidity 0%		Relative humidity 100%	
		Cp=0 hrs	Cp=2 hrs	Cp=0 hrs	Cp=2 hrs
0	3849.4	-	-	-	-
40	4110	3875	4111	4191	4685
100	4170.7	4472	4595	4383	5075
250	4445.3	4490	4762	4712	4755
625	4537.9	4327	4542	4923	5108

flexural load's unit [lbs]

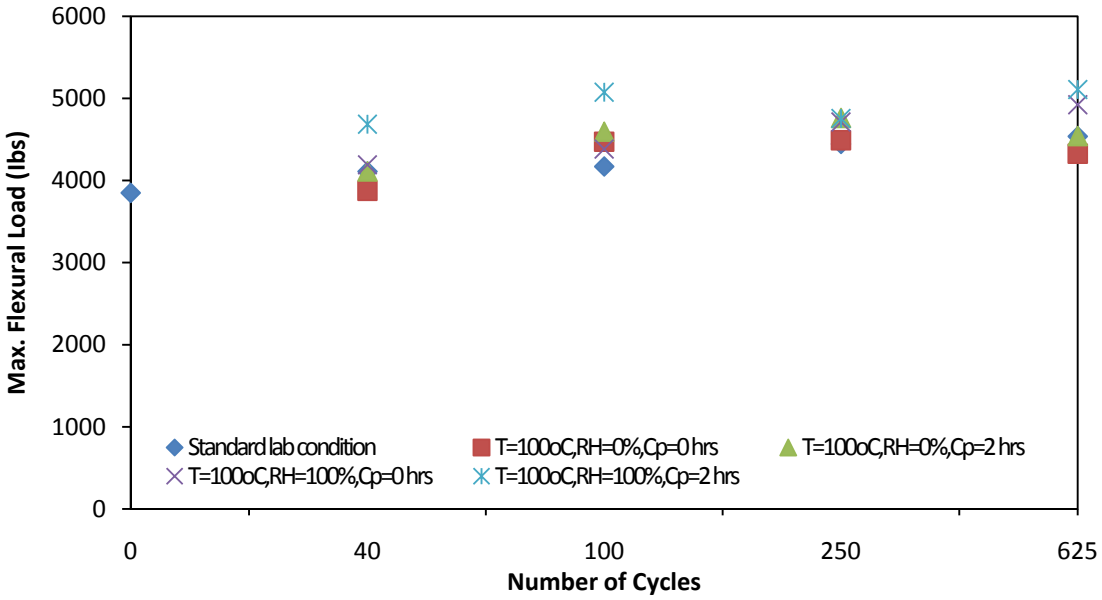

Figure 6.126: Max. flexural load vs. number of cycles after 100°C temperature

Table 6.50: Maximum stiffness results for different conditions at 100°C

		Temperature= 100°C			
# of Cycles	Lab Temp	Relative humidity 0%		Relative humidity 100%	
		Cp=0 hrs	Cp=2 hrs	Cp=0 hrs	Cp=2 hrs
0	143731	-	-	-	-
40	119719	145623	125413	83807	120182
100	118892	127058	175560	118905	131355
250	156218	146383	183055	118603	111345
625	161544	160448	179442	155525	135892

stiffness's unit [lbs/in]

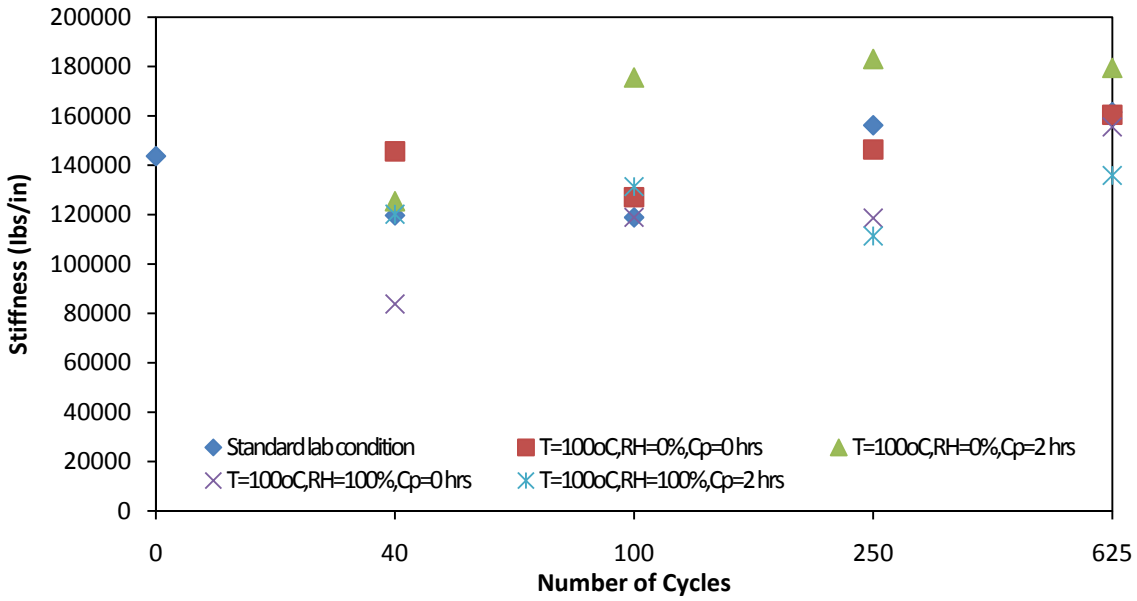

Figure 6.127: Stiffness vs. number of cycles after 100°C temperature

On the other hand, tables (6.51 to 6.54) show the test results of the 180°C specimens. Each numerical numbers represented the averaged maximum deflection, maximum flexural load, and stiffness of two strengthened beam specimens.

Table 6.51: Strengthened beam specimen results (RH=0%, Cp=2)-180°C

# of Cycle	Temp (°C)	RH (%)	CP	Average max. Deflection (in)	Average max. Load (lbs)	Average Slope (lbs/in)
Control	LT	LH	-	0.0290	3991.9	143731(one order higher?)
40	180	0.0	2	0.053106	3522.0	43584.44
100	180	0.0	2	0.044582	3189.0	63372.93
250	180	0.0	2	0.032659	3327.0	80548.44

Table 6.52: Strengthened beam specimen results (RH=100%, Cp=2)-180°C

# of Cycle	Temp (°C)	RH (%)	CP	Average max. Deflection (in)	Average max. Load (lbs)	Average Slope (lbs/in)
Control	LT	LH	-	0.0290	3991.9	143731
40	180	100	2	0.044857	3926.0	66187.25
100	180	100	2	0.057089	3832.0	45121.58
250	180	100	2	0.031741	3146.0	84167.38

Table 6.53: Strengthened beam specimen results (RH=0%, Cp=0)-180°C

# of Cycle	Temp (°C)	RH (%)	CP	Average max. Deflection (in)	Average max. Load (lbs)	Average Slope (lbs/in)
Control	LT	LH	-	0.0290	3991.9	143731
40	180	0.0	0	0.046959	4116.0	73138.45
100	180	0.0	0	0.046849	3373.0	57950.6
250	180	0.0	0	0.038438	2852.0	68574.17

Table 6.54: Strengthened beam specimen results (RH=100%, Cp=0)- 180°C

# of Cycle	Temp (°C)	RH (%)	CP	Average max. Deflection (in)	Average max. Load (lbs)	Average Slope (lbs/in)
Control	LT	LH	-	0.0290	3991.9	143731
40	180	100	0	0.064815	3977.0	67424.03
100	180	100	0	0.04666	3205.0	52943.3
250	180	100	0	0.039332	2910.0	58365.49

The maximum deflections, flexural loads, and stiffness after exposing to 180°C are shown in table (6.55 to 6.57) respectively, as well as Figures (6.128 to 6.130).

Table 6.55: Maximum deflection results for different conditions at 180°C

		Temperature= 180°C			
# of Cycles	Lab Temp	Relative humidity 0%		Relative humidity 100%	
		Cp=0 hrs	Cp=2 hrs	Cp=0 hrs	Cp=2 hrs
0	0.0290	-	-	-	-
40	0.0405	0.046959	0.053106	0.064815	0.044857
100	0.0409	0.046849	0.044582	0.04666	0.057089
250	0.0305	0.038438	0.032659	0.039332	0.031741

deflection's unit [in]

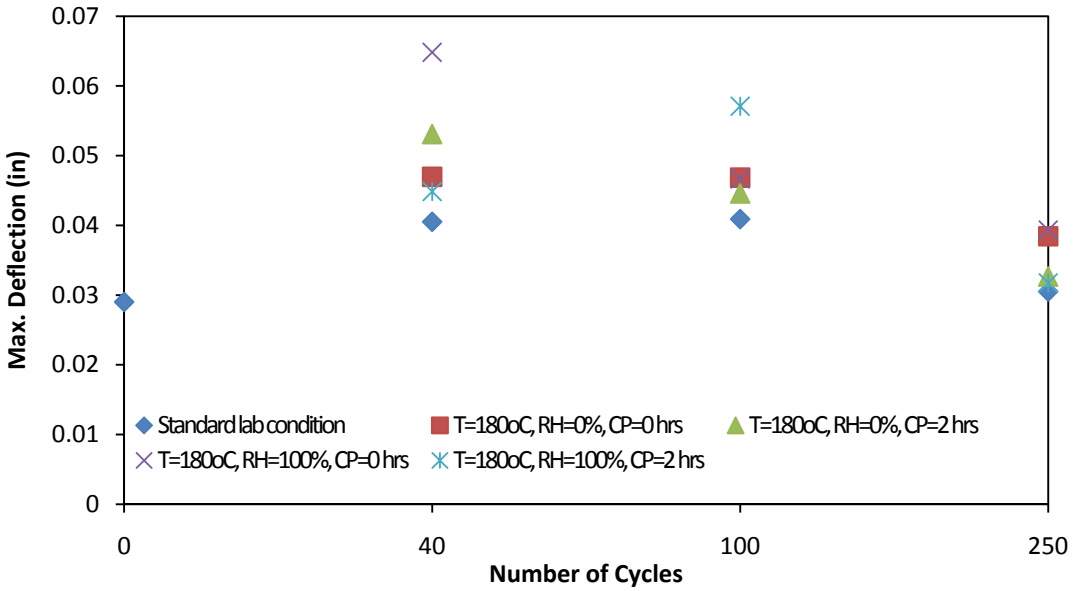

Figure 6.128: Deflection vs. number of cycles after 180°C temperature

Table 6.56: Maximum flexural load results for different conditions at 180°C

# of Cycles	Lab Temp	Temperature= 180°C			
		Relative humidity 0%		Relative humidity 100%	
		Cp=0 hrs	Cp=2 hrs	Cp=0 hrs	Cp=2 hrs
0	3849.4	-	-	-	-
40	4110	4116	3522	3977	3926
100	4170.7	3373	3189	3205	3832
250	4445.3	2852	3327	2910	3146

Flexural load's unit [lbs]

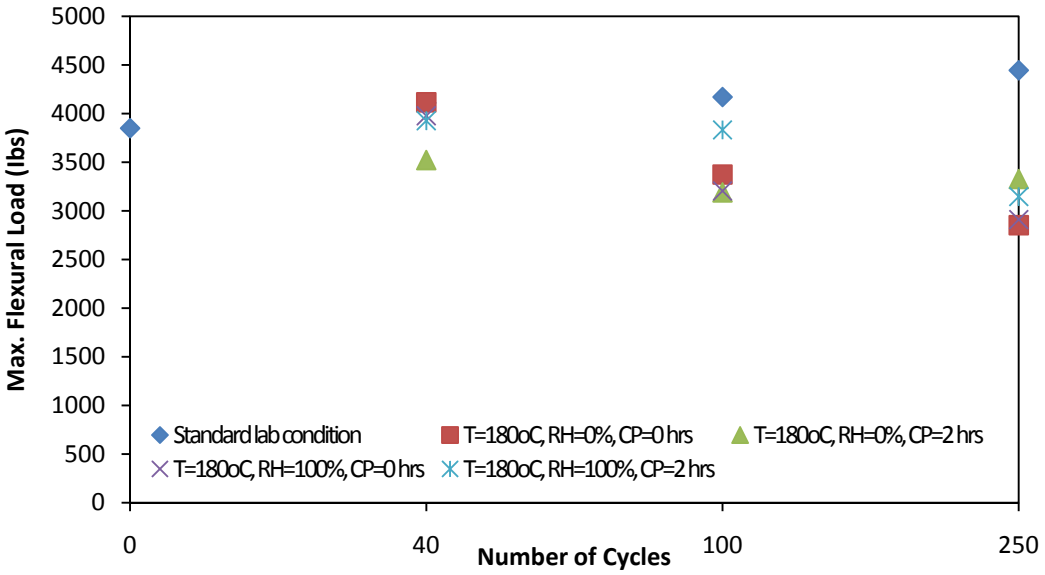

Figure 6.129: Max. flexural load vs. number of cycles after 180°C temperature

Table 6.57: Maximum stiffness results for different conditions at 180°C

# of Cycles	Lab Temp	Temperature= 180°C			
		Relative humidity 0%		Relative humidity 100%	
		Cp=0 hrs	Cp=2 hrs	Cp=0 hrs	Cp=2 hrs
0	143731	-	-	-	-
40	119719	73138.45	43584.44	67424.03	66187.25
100	118892	57950.6	63372.93	52943.3	45121.58
250	156218	68574.17	80548.44	58365.49	84167.38

stiffness's unit [lbs/in]

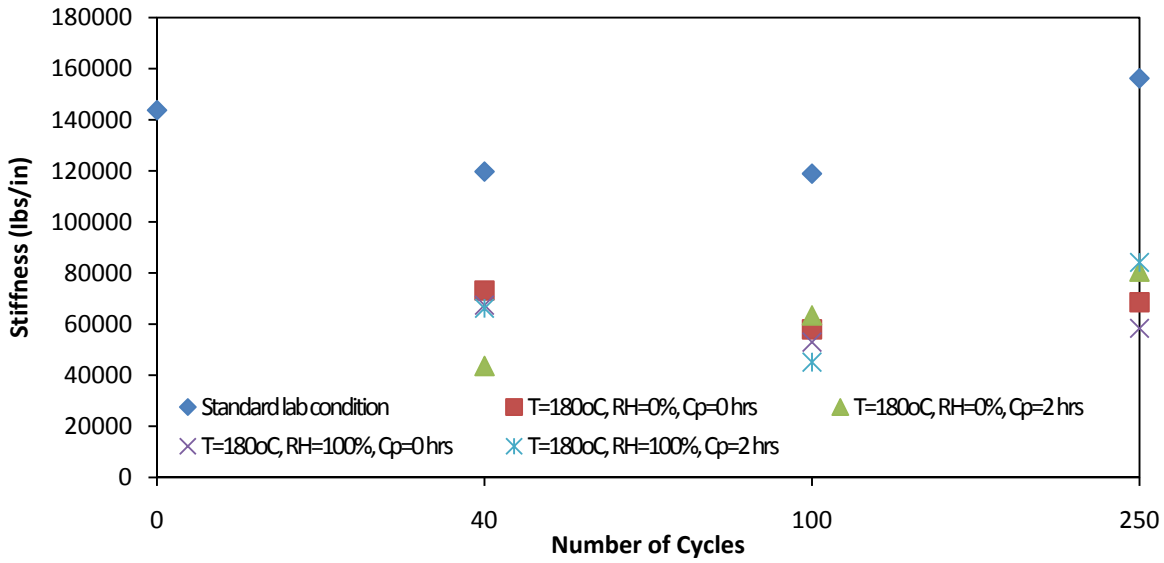

Figure 6.130: Stiffness vs. number of cycles after 180°C temperature

6.6 FRP Strengthened Concrete Column Specimens

The effects of hygrothermal influence on bond strength between concrete and FRP strengthening wraps of cylindrical specimens also were studied. 40 strengthened concrete column specimens were prepared and exposed to different environmental conditions. 8 of these specimens were subjected to the lab standard conditions, 16 specimens were subjected to 100°C of temperature, and 16 were exposed to 180°C. The time of exposure, relative humidity, and cycle periods varied for both cases.

6.6.1 FRP Strengthened Columns at 40 Cycles and100°C Temperature

One set of column specimens, consisting of 8 specimens, were strengthened, then, exposed to 100°C temperature, two RH levels, and two cycle periods for 40 cycles (80 hours). The results are tabulated in table 6.58. All these specimens were subjected to compressive loading until failure, (see figure 6.131).

Table 6.58: FRP strengthened column compression test results subjected to different environmental conditions with 100°C and 40 cycles

Col. no.	Temp °C	RH %	CP! (Hr)	Max. Load (lbs)	Mean lbs	Comp. strength (psi)	Difference - %	Failure mode
C22	LT	LH		92812		7386. 0		FRP Rupture
C23				91940	92376.0	7316.6	33.6	FRP Rupture
C34	100	0	0	104958.6	103016.5	8352.6	49.0	FRP Rupture
C35				101074.5		8043.5		FRP Rupture
C30			2	107444.3	107234.3	8550.4	55.1	FRP Rupture
C31				107024.4		8517.0		FRP Rupture
C38		100	0	109910.8	108161.8	8746.7	56.4	FRP Rupture
C39				106412.8		8468.3		FRP Rupture
C42			2	104555.2		8320.5		FRP Rupture
C43				102337.1	103446.1	8144.0	49.6	FRP Rupture

-Percentage difference of max. load increasing or decreasing compared with control result.
*Lab temperature,
+Lab humidity,
!Cycle period,

Figure 6.131: Compressive strength Test, C43

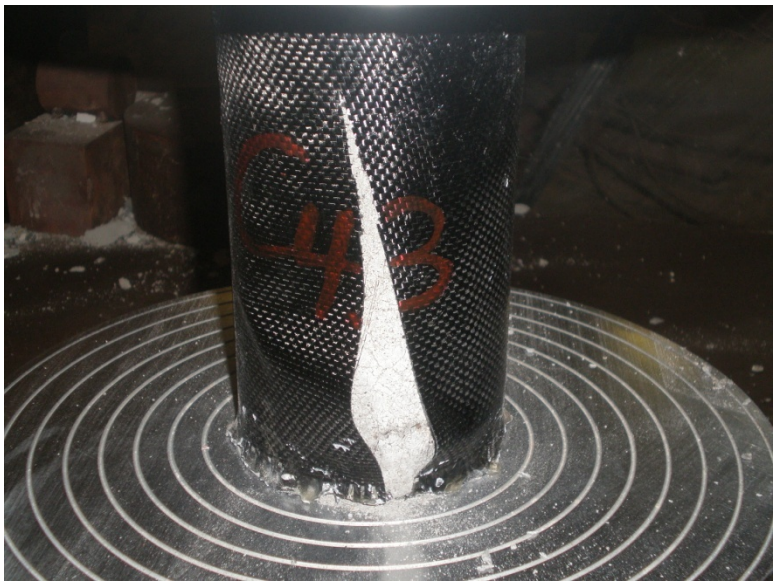

Figure 6.132: FRP rupture of C38-100^{o}C, 40cycles

As shown in table 6.58 the maximum compressive load results, indicate that after 40 cycles of exposure, the strength increases about 56% when the relative humidity was 100% and the cycle periods =0. At standard lab conditions, the strength improved 33.6% over the plain concrete cylinder specimen results. Both relative humidity and period of cycles did not show a significant effect on strength gains. The mode of failure was FRP rupture for all these specimens. Figure (6.132) shows the typical failure mode. The curves of compressive load verses deflection are shown in figure (6.133).

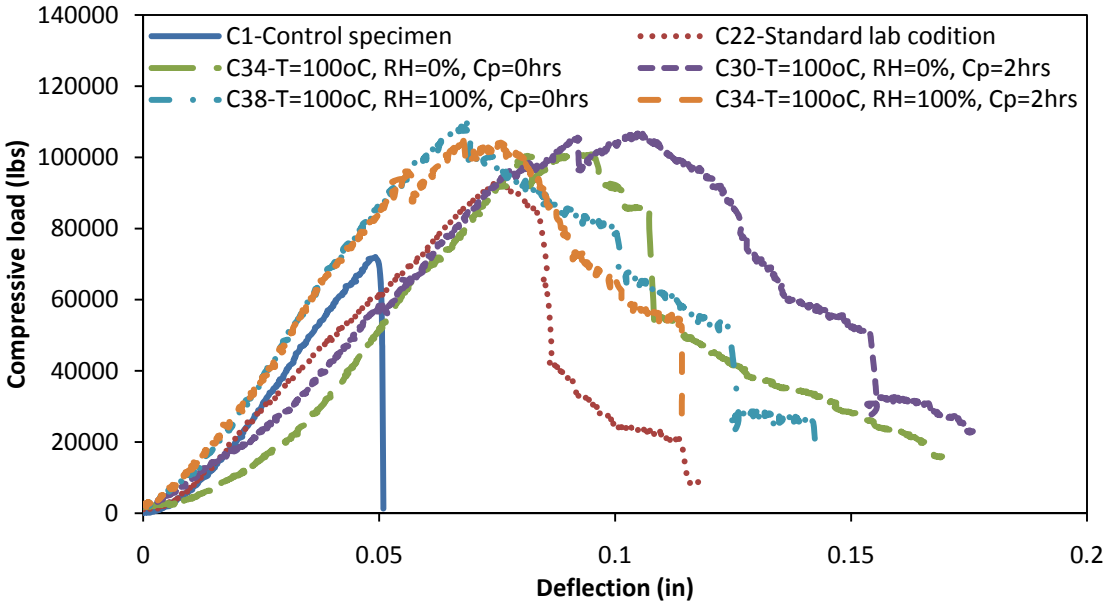

Figure 6.133: Compressive load- deflection of strengthened columns–100°C and 40 cycles

6.6.2 FRP strengthened Columns at 625 Cycles and 100°C temperature

Another 8 strengthened column specimens have been subjected to 100°C temperature for 625 cycles (1250 hours) and different environmental conditions of relative humidities and cycle periods. The results are shown in table 6.59. The mode of failure was FRP rupture. Figure 6.134 shows a typical failure mode of these 8 specimens.

By comparing tables 6.58 and 6.59, the compressive strength decreased due to exposure to 625 cycles and 100°C of temperature. While at the standard lab conditions, after 625 cycles (1250 hrs), the compressive strength increased about 12% compared to 40 cycles of exposure. On the other hand, when comparing with the control specimens, the compressive strength of these aged specimens still represented 35-38% increases regardless the degrees of humidity and periods of cycles, (Figure 135).

Table 6.59: FRP strengthened column compression test results subjected to different environmental conditions with 100°C and 625 cycles

Col. no.	Temp °C	RH %	CP! (Hr)	Max. load (lbs)	Mean lbs	Comp. strength (psi)	Difference - %	Failure mode
C28	LT	LH	-	96258.62	95204.6	7660.2	37.7	FRP Rupture
C29				94150.5		7492.5		FRP Rupture
C36	100	0	0	91775.75	93561.1	7303.5	35.3	FRP Rupture
C37				95346.48		7587.7		FRP Rupture
C32			2	93033.85	95338.1	7403.6	37.9	FRP Rupture
C33				97642.28		7770.4		FRP Rupture
C40		100	0	94776.49	93169.4	7542.3	34.8	FRP Rupture
C41				91562.31		7286.5		FRP Rupture
C44			2	90455.52	93020.9	7198.4	34.5	FRP Rupture
C45				95586.24		7606.7		FRP Rupture

-Percentage difference of max. load increasing or decreasing compared with control result.
*Lab temperature,
+Lab humidity,
!Cycle period,

Figure 6.134: FRP rupture of C36-100°C, 625cycles

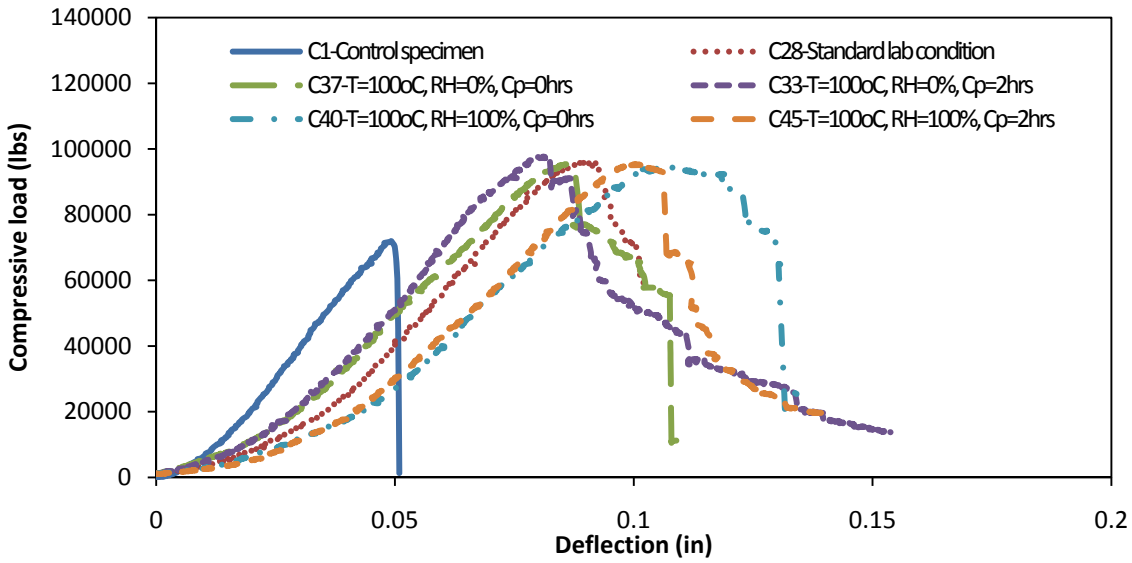

Figure 6.135: Compressive load- deflection of strengthened Columns –100°C and 625 cycles

6.6.3 FRP strengthened Columns after 40 Cycles and 180°C temperature

As discussed above, the compressive strengths of 100°C strengthened column specimens were not affected by the variation of relative humidity. Consequently, additional four strengthened concrete column specimens C82, C23, C86, and C87 were exposed to 180°C temperature and 0% relative humidity, while two cycle periods were used, (Table 6.60).

Following the same procedures that were used for all previous column specimens, all these four specimens were subjected to the compressive strength test. As stated in table 6.60 and figure 6.137, owing to exposing to 180°C temperature, the compressive strength was only in the range between 14-16% above the control specimens. Nevertheless, the modes of failure, FRP rupture, were unchanged for all specimens. Figure 6.136 depicted the mode of failure of one of these four specimens. It should be noted that no separation/debonding occurred along the overlapped area of the FRP wraps for all concrete column specimens.

Table 6.60: FRP strengthened column compression test results subjected to different environmental conditions with 180°C and 40 cycles

Col. no.	Temp °C	RH %	CP! (Hr)	Max. load (lbs)	Mean lbs	Comp. strength (psi)	Difference - %	Failure mode
C22	LT	LH		92812		7386. 0		FRP Rupture
C23				91940	92376.0	7316.6	33.6	FRP Rupture
C82			0	84544.5	78921.5	6728.0	14.2	FRP Rupture
C83	180	0		73298.5		5833.1		FRP Rupture
C86			2	76812.8		6112.8		FRP Rupture
C87				83529.0	80170.9	6647.2	16.0	FRP Rupture

-Percentage difference of max. load increasing or decreasing compared with control result.
*Lab temperature,
+Lab humidity,
!Cycle period,

Figure 6.136: FRP rupture of C86-180°C, 40 cycles

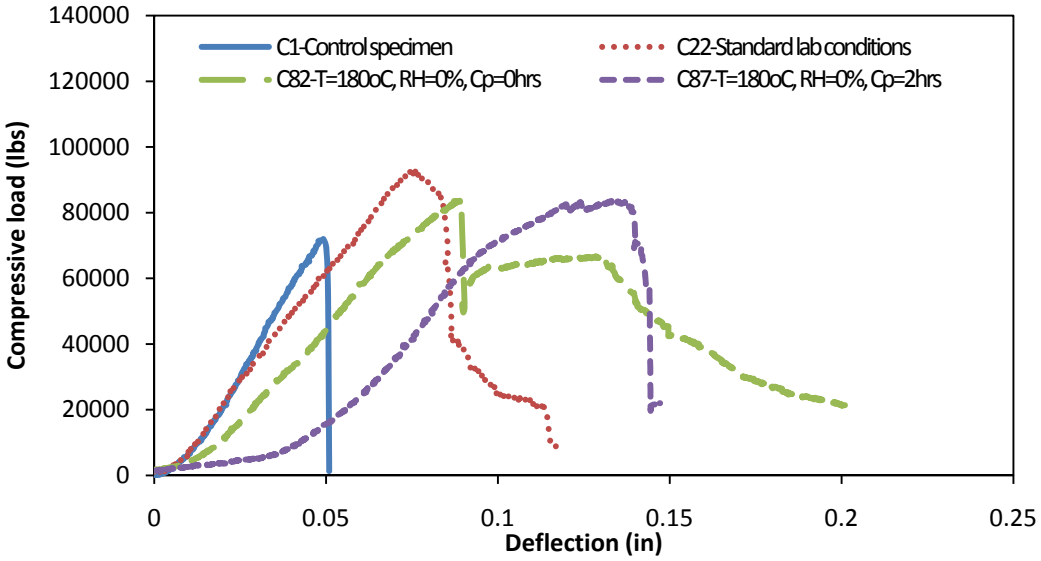

Figure 6.137: Compressive load-deflection of strengthened columns–180°C and 40 cycles

6.6.4 FRP Strengthened Columns at 100 Cycles and180°C Temperature

More experimental work has been implemented by strengthening extra column specimens and exposing them to 180°C temperature and 100 cycles, but unlike of the 40-cycle specimens, the relative humidity was changed to 100% as shown in table 6.61. Figure 6.138 shows the mode of failure of one of these column specimens. The relationships between compressive load and deflection are explained in figure 6.139.

Table 6.61: FRP strengthened column compression test results subjected to different environmental conditions with 180°C and 100 cycles

Col. no.	Temp °C	RH %	CP! (Hr)	Max. load lbs	Mean lbs	Comp. strength (psi)	Difference - %	Failure mode
C24	LT	LH	-	88241.94		7022.3		FRP Rupture
C25				97516.75	92879.3	7760.4	34.3	FRP Rupture
C92				78697.4	78028.1	6262.7	12.9	FRP Rupture
C93	180	100	0	77358.7		6156.2		FRP Rupture
C96			2	71176.2	72897.9	5664.2	5.4	FRP Rupture
C97				74619.5		5938.2		FRP Rupture

-Percentage difference of max. load increasing or decreasing compared with control result.
*Lab temperature,
+Lab humidity,
!Cycle period,

Figure 6.138: FRP rupture of C93-180°C, 100 cycles

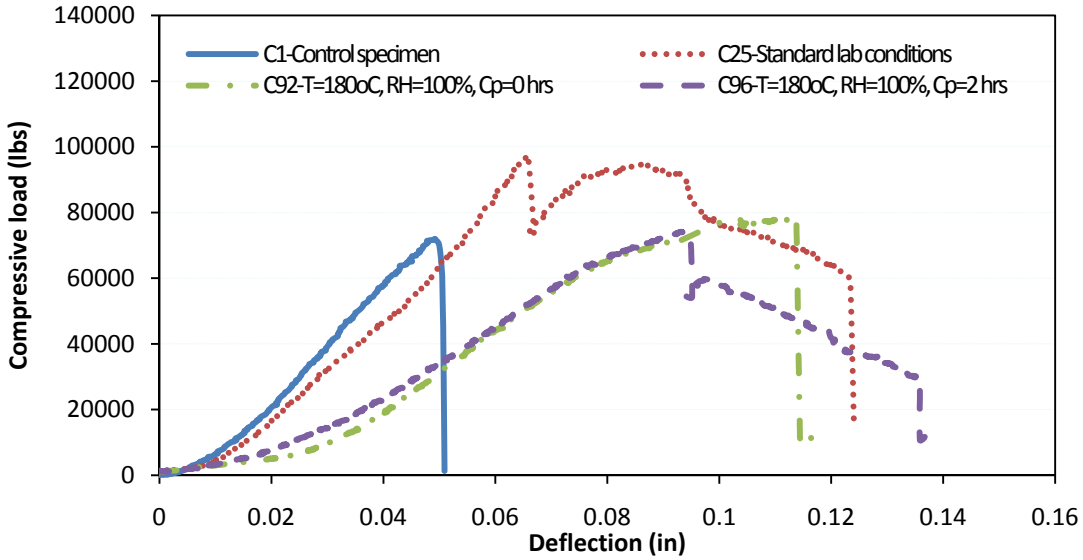

Figure 6.139: Compressive load- deflection of strengthened columns–180°C and 100 cycles

6.6.5 FRP Strengthened Columns at 250 Cycles and 180°C of Temperature

Another set of strengthened concrete column specimens, consisting of 8 specimens, was exposed to 180°C temperature under various relative humidity and cycle period environments up to 250 cycles (500 hours). By increasing the numbers of cycles to 250 cycles, a detrimental influence on compressive strength was noted. Comparing with the control specimens, when the

relative humidity was 0% and the cycle period was zero, the compressive strength reduced to the range between (0.5- 2.4)% below the plain concrete control specimen results. While it was 7% above the control specimen when the relative humidity was 100% and the cycle period was 2 hours; and 4.2% when zero cycle period was used. The mode of failures "FRP rupture" remained the same for all specimens, Figure (6.140). More details are tabulated in table 6.62 and shown in figure 6.141.

Table 6.62: FRP strengthened column compression test results subjected to different environmental conditions with 180°C and 250 cycles

Col. no.	Temp °C	RH %	CP! (Hr)	Max. load (lbs)	Mean lbs	Comp. strength (psi)	Difference - %	Failure mode
C26	LT	LH		96258.62	95204.6	7660.2	37.7	FRP Rupture
C27				94215.05		7492.5		FRP Rupture
C84	180	0	0	68243.41	67513.3	5430.8	-2.4	FRP Rupture
C85				66783.28		5314.6		FRP Rupture
C88			2	73460.91	72256.5	5846.0	4.5	FRP Rupture
C89				71052.18		5654.3		FRP Rupture
C94		100	0	70095.11	68810.1	5578.2	-0.5	FRP Rupture
C95				67525.12		5373.6		FRP Rupture
C98			2	74612.29	74081.4	5937.6	7.1	FRP Rupture
C99				73550.47		5853.1		FRP Rupture

-Percentage difference of max. load increasing or decreasing compared with control result.
*Lab temperature,
+Lab humidity,
!Cycle period,

Figure 6.140: FRP rupture of C95-180°C, 250 cycles

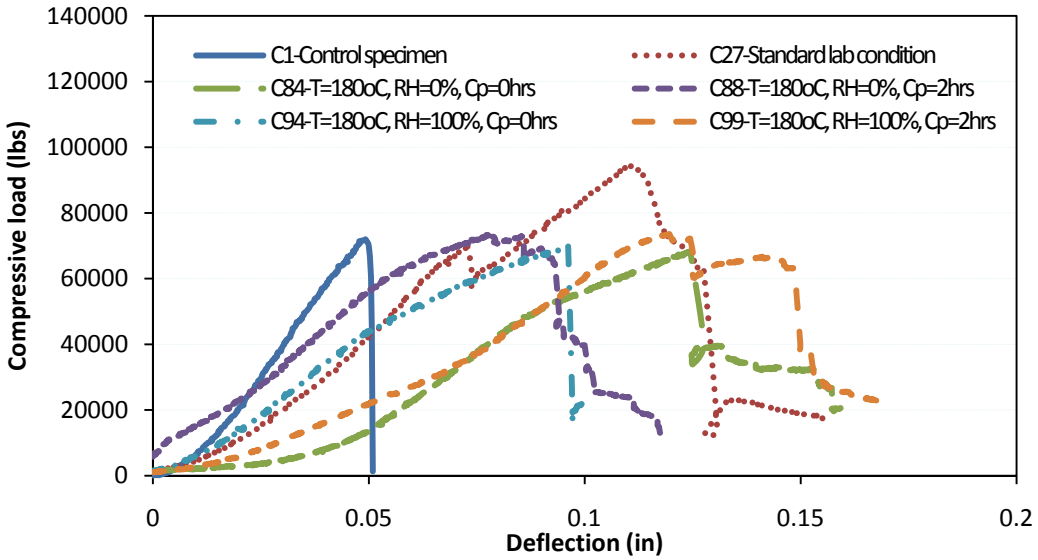

Figure 6.141: Compressive load- deflection of Strengthened columns–180°C and 250 cycles

6.7 Strengthened Concrete Beam/Column Specimens Using Miscellaneous FRPs and Epoxy Materials

Additional beam and column specimens have been strengthened by utilizing various FRP sheets and resin materials. These specimens were exposed to 180°C temperature and 100%

relative humidity. The times of exposing to the environmental conditions were 100 and 250 cycles. The cycle period was 2 hours for all specimens.

6.7.1 Strengthened Beam Specimens Using Miscellaneous FRPs and Epoxy Materials

Four concrete beam specimens B120, B121, B122, and B123 have been strengthened by using one layer Fyfe carbon fiber and epoxy and subjected to 180^{o}C temperature. Two of these four specimens were tested after 100 cycles, while the other two specimens were tested after 250 cycles. All specimens have been tested by using central- point flexural load test until failure (figure 6.142). The flexural strength results that are shown in table 6.63 demonstrate that the flexural strength of standard-lab-condition specimens have increased 184% comparing with the control specimen while the increase was 22% after 100 cycles and just 10% after 250 cycles under the aging conditions.

Figure 6.142: Flexural load test, B120

FRP delaminated was the mode of failure for all these specimens, (Figure 6.143). The relationships between flexural load and mid-span deflection are concluded in figure 6.144.

Table 6.63: Strengthened beam specimens with Fyfe carbon and Fyfe epoxy- (Cp=2hr)

Beam no.	Temp °C	RH %	Cy	Max. load lbs	Mean lbs	Flex. strength (psi)	Difference - %	Failure mode
B4	LT*	LH+	-	9273.7		2605.9		FRP delamination
B5				8135.9	8704.8	2286.2	184	FRP delamination
B120			100	4036.1		1134.1		FRP delamination
B121	180	100		3436.0	3736.1	965.5	22	FRP delamination
B122			250	3509.7		986.2		FRP delamination
B123				3213.7	3361.7	903.0	9.8	FRP delamination

-Percentage difference of max. load increasing or decreasing compared with control result.
*Lab temperature,

Figure 6.143: FRP delamination of B120-180°C, 100% RH

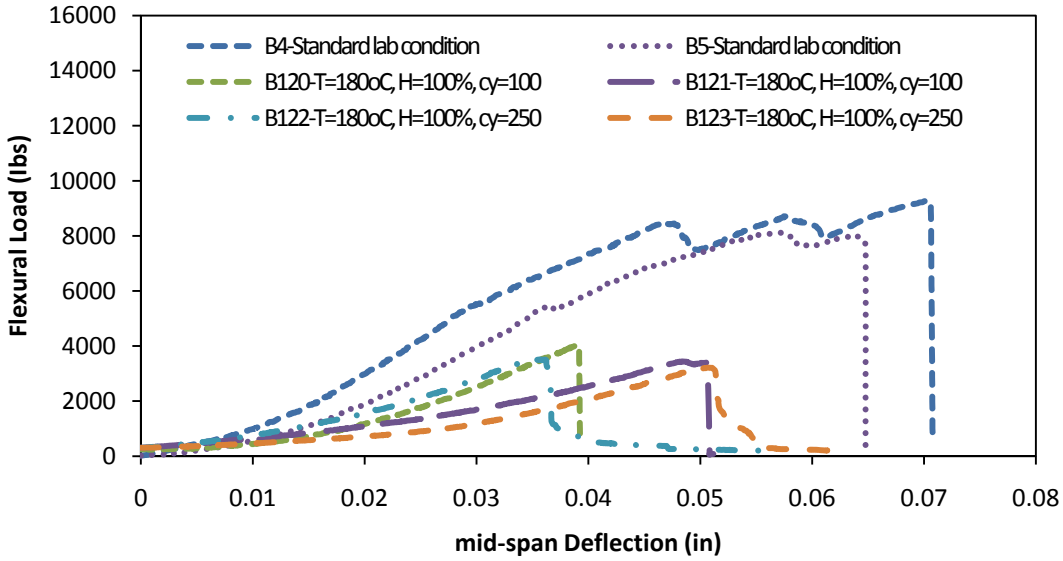

Figure 6.144: Flexural load vs. mid-span deflection curves of strengthened beams 180°C (Fyfe CFRP and epoxy)

One layer Fyfe GFRP and Fyfe epoxy have also been employed to strengthening four concrete beam specimens B116, B117, B118, and B119. These specimens were subjected to 180°C temperature and 100% RH. The numbers of cycles were 100 and 250 cycles as shown in table (6.64). Based on the results that are described on table 6.64 and figure 6.147, comparing with the control specimen results, the flexural strength of standard lab condition specimens recorded an increase about 160%. After 100 cycles of aging, the flexural strength was 62% more than the control specimens, and only 40% after 250 cycles. The modes of failure were FRP delamination for all specimens. Only a flexural crack in concrete was observed for B117, B118, and B119, (see figure 6.145). For B116, the first crack in concrete was due to flexure, which was followed by a diagonal crack (shear crack). The shear crack started from the top and propagated to the bottom along a 45 ° degree path, (Figure 6.146).

Table 6.64: Strengthened beam specimens with Fyfe glass and Fyfe epoxy - (Cp=2hr)

Beam no.	Temp ^{o}C	RH %	Cy	Max. load lbs	Mean lbs	Flex. strength (psi)	Difference $^{-}$ %	Failure mode
B12	LT*	LH^{+}	-	7777.2		2185.4		FRP delamination
B15				8124.0	7950.6	2282.8	159.7	FRP delamination
B116	180	100		5152.8		1447.9		FRP delamination
B117			100	4758.2	4955.5	1337.1	61.9	FRP delamination
B118				4240.0		1191.4		FRP delamination
B119			250	4331.9	4286.0	1217.3	40	FRP delamination

$^{-}$Percentage difference of max. load increasing or decreasing compared with control result.
*Lab temperature,

Figure 6.145: Concrete flexural crack and FRP delamination of B117-180^{o}C, 100% RH

Figure 6.146: Concrete shear crack and FRP delamination of B116-180°C, 100% RH

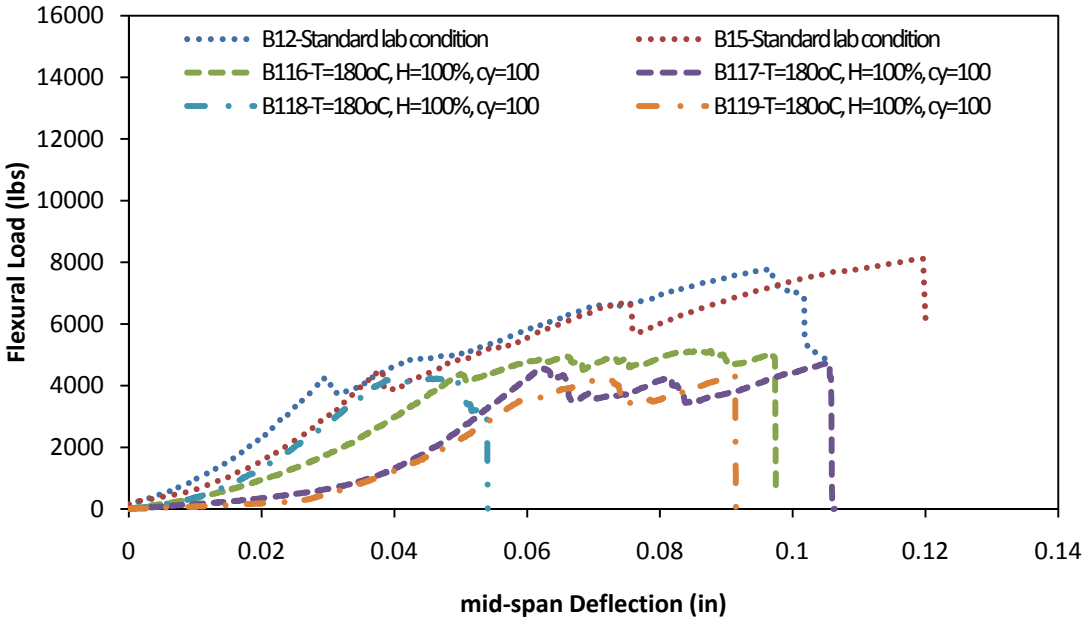

Figure 6.147: Flexural load vs. mid-span deflection curves of strengthened beams 180°C (Fyfe GFRP and epoxy)

Four concrete beams B124, B125, B126, and B127 have been strengthened by using Sika glass fiber and Sika epoxy materials and exposed to 180°C temperature and 100% relative humidity. As shown in table (6.65), the flexural strength after 100 cycles increased by 61%, and

after 250 cycles the increase was only 44%. Under the standard lab condition, the flexural strength was 76% higher than the control specimen. Figure 6.148 shows the flexural strength vs. the mid-span deflection curves. FRP delamination was the mode of failure for all these specimens, figure (6.149a). During debonding, the GFRP sheets split along the longitudinal direction (Fig 6.149b). Such splitting phenomenon was observed for all Sika GFRP strengthening sheets regardless the environmental conditions. A color change of the GFRP sheet to black has been found as well.

Table 6.65: Strengthened beam specimens with Sika glass and Sika epoxy-(Cp=2hr)

Beam no.	Temp °C	RH %	Cy	Max. load lbs	Mean lbs	Flex. strength (psi)	Difference - %	Failure mode
B8	LT*	LH+	-	5179		1455.3		FRP delamination
B11				5606	5392.5	1575.3	76.1	FRP delamination
B124	180	100	100	5049.0		1418.8		FRP delamination
B125				4848.2	4948.6	1362.3	61.6	FRP delamination
B126			250	4712.5		1324.2		FRP delamination
B127				4154.2	4433.4	1167.3	44.8	FRP delamination

-Percentage difference of max. load increasing or decreasing compared with control result.
*Lab temperature,

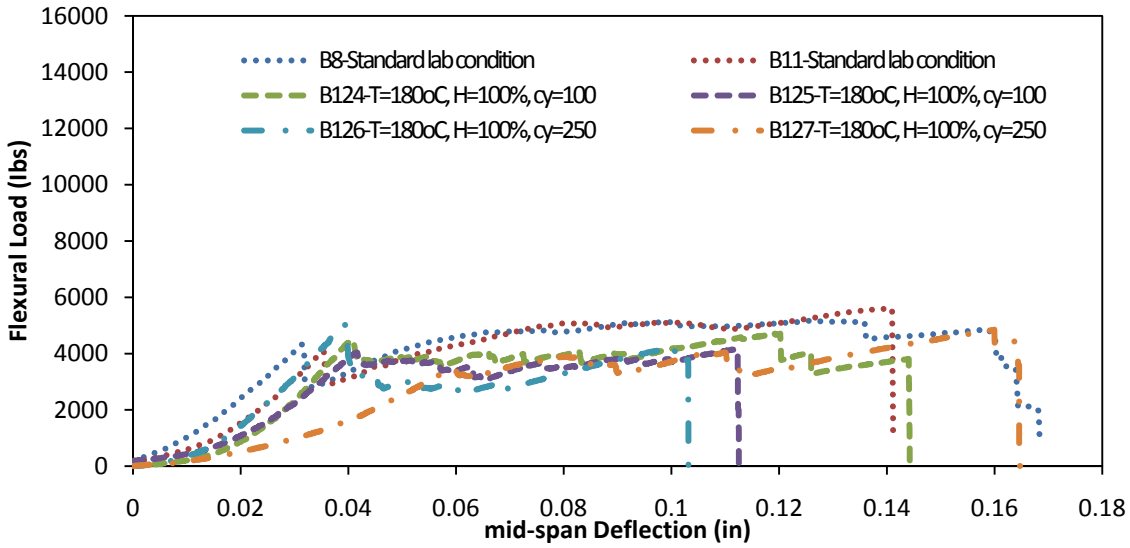

Figure 6.148: Flexural load- mid-span deflection curves of Strengthened beams 180°C (Sika GFRP and Epoxy)

(a)

(b)

Figure 6.149: FRP delamination of B125-180^{o}C, 100% RH

6.7.2 Strengthened Column Specimens Using Miscellaneous FRPs and Epoxy Materials

C68, C69, C70, and C71 concrete column specimens were strengthened by utilizing Fyfe CFRP and epoxy materials. C68 and C69 have been exposing to 180^{o}c temperature and

100% RH for 100 cycles, while C70 and C71 were subjected to 250 cycles under the same temperature and humidity conditions. As a result of compressive strength test, figure (6.150), the compressive load increased by 125% after 100 cycles and about 110% after 250 cycles comparing to the control specimen results. The increasing in compressive strength for the standard lab condition specimens was 207% comparing with the control specimens, table 6.66 and figure 6.151. As shown in figure 6.152, FRP rupture was the mode of failure for all these specimens.

Figure 6.150: Compressive strength test, C68 (Fyfe CFRP)

Table 6.66: Strengthened column specimens with Fyfe carbon and Fyfe epoxy-(Cp=2hr)

Col. no.	Temp ^{o}C	RH %	Cy	Max. load lbs	Mean lbs	Comp. strength (psi)	Difference - %	Failure mode
C2	LT	LH	-	241901.2		19250		Rupture
C4				244659.1	243280.0	19469	207.4	Rupture
C68	180	100	100	180684.4		14378		Rupture
C69				175337.8	178011.1	13953	125.0	Rupture
C70			250	169672		13502		Rupture
C71				162094.4	165883.2	12899	109.6	Rupture

-Percentage difference of max. load increasing or decreasing compared with control result.
*Lab temperature,
+Lab humidity,
!Cycle period,

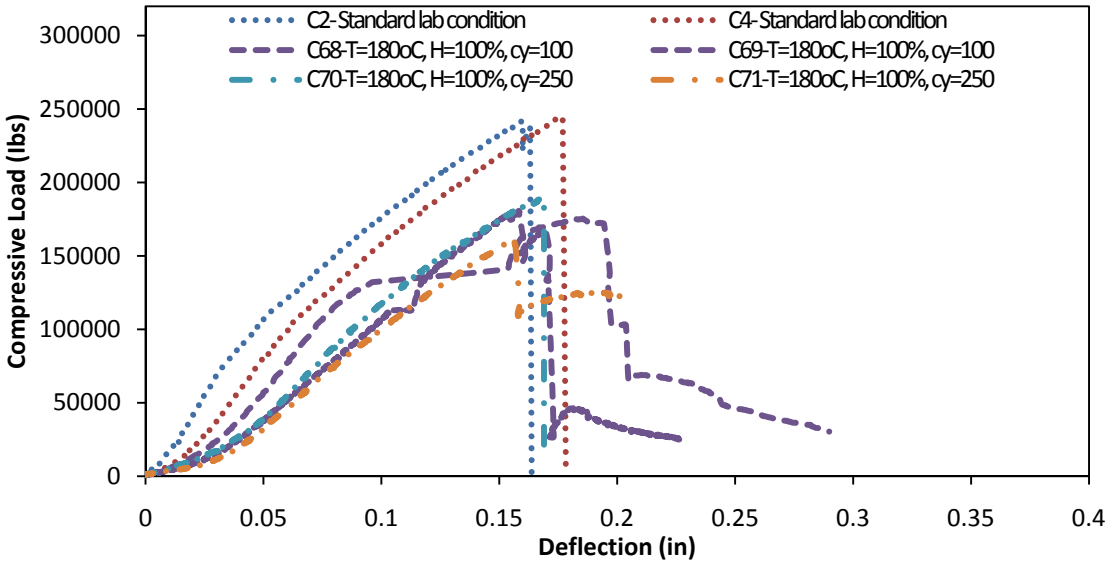

Figure 6.151: Compressive load- deflection curves of strengthened column 180°C (Fyfe CFRP and epoxy)

Figure 6.152: FRP rupture, C68 -180°C, 100% RH

Another four concrete column specimens C77, C79, C80, and C81 have been strengthened by using Fyfe GFRP and epoxy materials. Whilst the compressive strength of standard lab conditions specimens increased about 79% above the control specimens, after 100 cycles of exposing to 180°C temperature and 100% RH the compressive strength became 62.7%

above the control specimen results. By increasing the time of exposing to 250 cycles (500 hours), the compressive strength was only 49.7% higher than the control specimens. Table 6.67 shows the results of maximum compressive load and strength of these specimens. The relationships between the compressive load and deflection are plotted in figure 6.153. Figure 6.154 shows the typical mode of failure of these specimens.

Table 6.67: Strengthened column specimens with Fyfe glass and Fyfe epoxy-(Cp=2hr)

Col. no.	Temp °C	RH %	Cy	Max. load lbs	Mean lbs	Comp. strength (psi)	Difference - %	Failure mode
C7	LT	LH	-	149873.4	141453.2	11927	78.7	FRP Rupture
C11				133033.0		10586		FRP Rupture
C77	180	100	100	137764.5	128781.1	10963	62.7	FRP Rupture
C79				119797.6		9533		FRP Rupture
C80			250	113030.8	118446.9	8995	49.7	FRP Rupture
C81				123862.9		9857		FRP Rupture

-Percentage difference of max. load increasing or decreasing compared with control result.
*Lab temperature,
+Lab humidity,
!Cycle period,

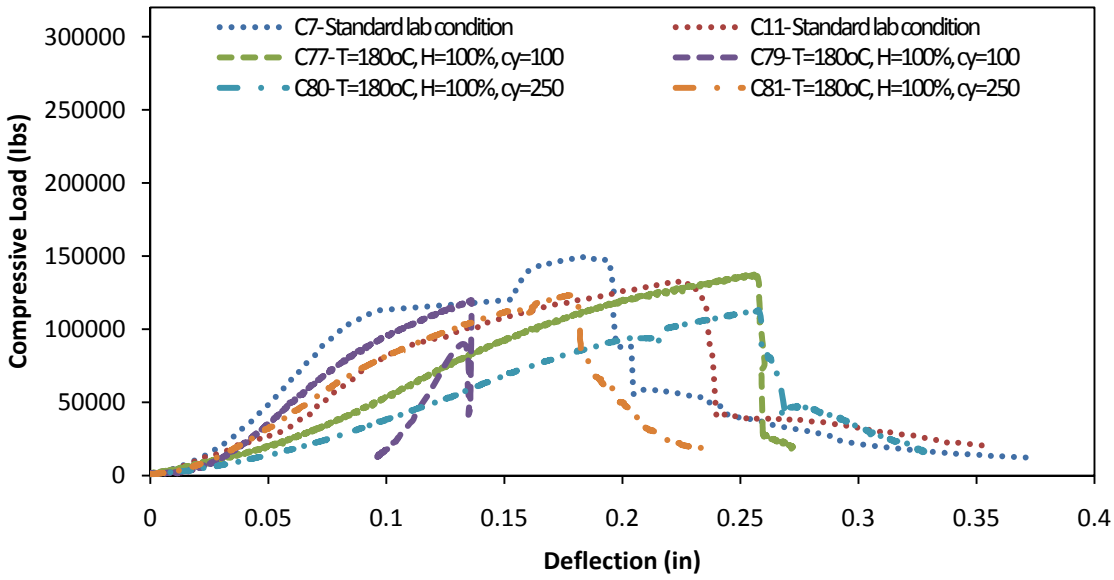

Figure 6.153: Compressive load- deflection curves of strengthened column 180°C (Fyfe GFRP and epoxy)

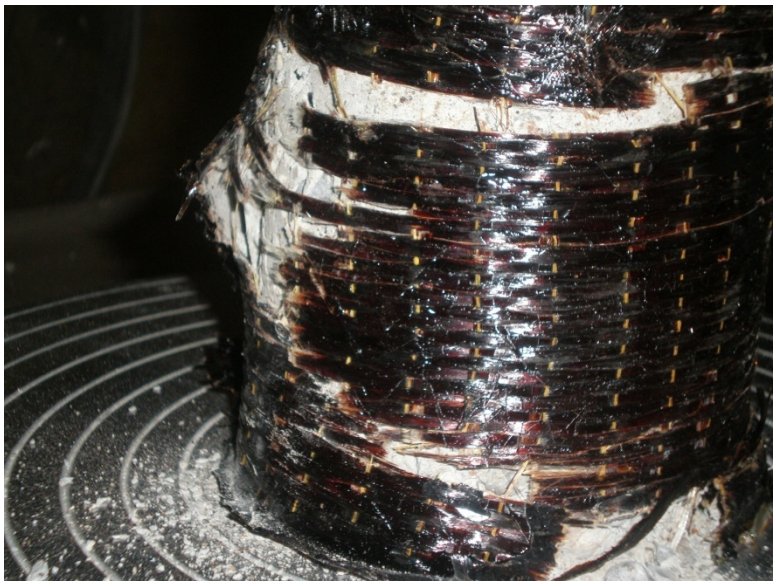

Figure 6.154: FRP rupture, C77 -180^{o}C, 100% RH

A set containing four concrete column specimens C104, C105, C106, and C107 have been strengthened by utilizing Sika GFRP and epoxy and were exposed to 180^{o}C and 100% relative humidity prior to compressive strength testing. Comparing to standard lab condition specimen results, a noticeable reduction on compressive strength has been observed, whereas, the compressive strength of standard lab condition specimens improved by 29% comparing with the control specimens, this improvement was reduced to be about 0% after 100 cycles and further reduced to 10% below the control specimens after 250 cycles, table 6.68 and figure 6.155. Figure 6.156 shows the mode of failure.

Table 6.68: Strengthened column specimens with Sika glass and Sika epoxy -(Cp=2hr)

Col. no.	Temp °C	RH %	Cy	Max. load lbs	Mean lbs	Comp. strength (psi)	Difference - %	Failure mode
$C4T_1$				99039.4		7881		FRP Rupture
C9	LT	LH	-	105527.2	102283.3	8398	29.2	FRP Rupture
C104			100	76421.6		6081		FRP Rupture
C105	180			81769.0	79095.3	6507	- 0.06	FRP Rupture
C106		100	250	73139.0		5820		FRP Rupture
C107				69014.8	71076.9	5492	-10.2	FRP Rupture

-Percentage difference of max. load increasing or decreasing compared with control result.
*Lab temperature,
+Lab humidity,
!Cycle period,

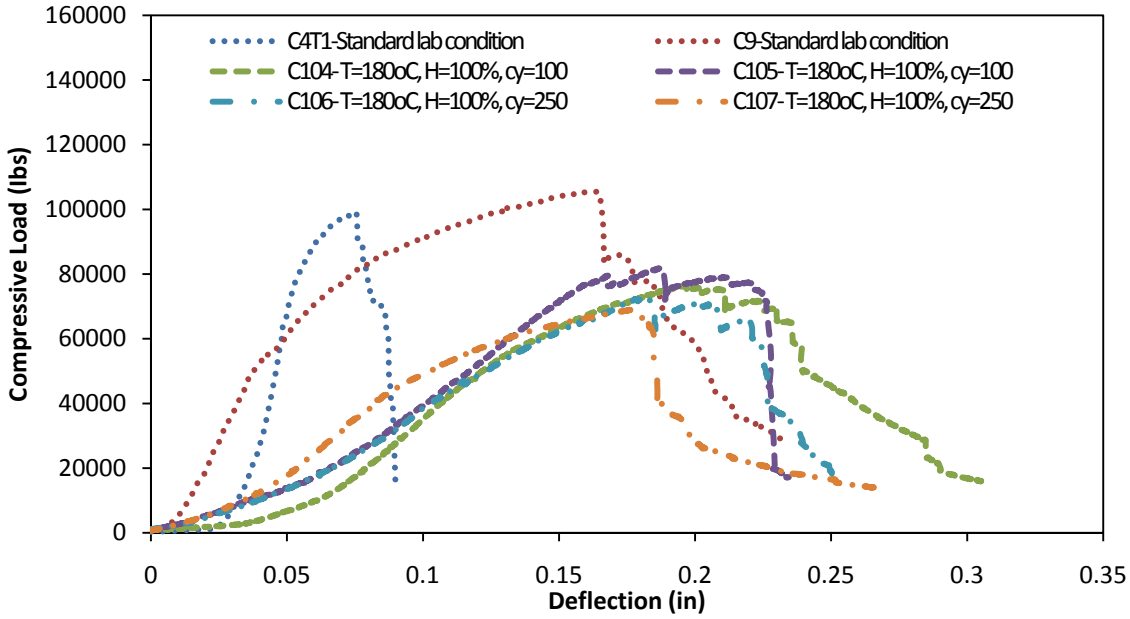

Figure 6.155: Compressive load- deflection curves of strengthened column 180°C (Sika GFRP and epoxy)

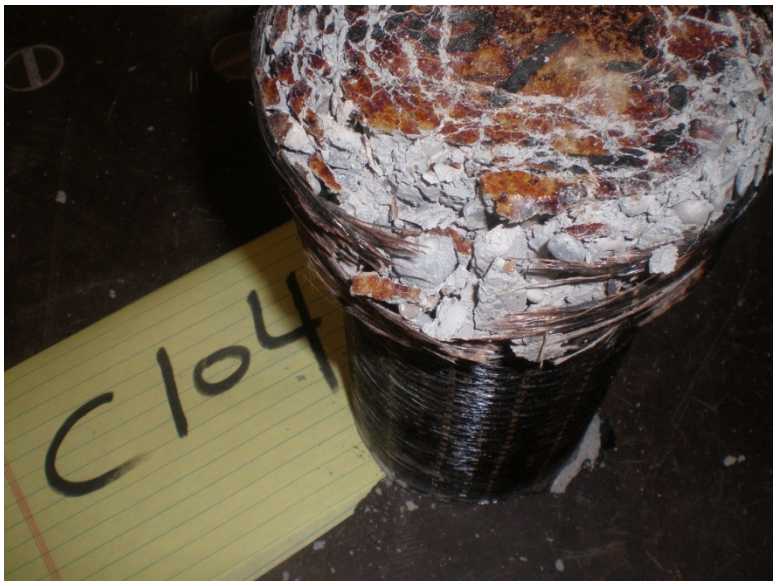

Figure 6.156: FRP rupture, C104 -180^{o}C, 100% RH

CHAPTER 7 DURABILITY PERFORMANCE PREDICTION USING ANALYTICAL AND NUMERICAL MODELING

7.1 Introduction

Temperature and humidity (hygrothermal) cycles cause degradation in composite strengthening materials by changing the properties of resin material due to plasticization and hydrolysis. Debonding between the fiber-matrix interface and the strengthened surface occurs as well. Although there is no comprehensive mechanistic modeling of the hygrothermal effect on durability/life-prediction including temperature, relative humidites, aging of exposure, and cycle periods, fairly precise predictions can be made through the sensible use of an equation based on micro mechanics and semi-empirical approaches that are based on extensive prior experimental testing results.

This chapter includes equations related to the prediction of hygrothermal effects, and then describes the predicting results on long-term strength and bonding of FRP strengthening materials that exposed to various environmental conditions. William-Landel-Ferry (WLF) equation was employed here to develop the shift factor for concrete and resin materials exposed to different environmental conditions. The shift factors were determined empirically based on experimental test results.

An extensive experimental research has been carried out throughout this study. The test results showed that the most influence on the strength of either concrete or resin material was temperature. While the change in relative humilities between 0% and 100% did not record significant aging effect on the properties of these materials.

7.2 Temperature and Aging effects

In chapter six of this dissertation, the accelerating aging effects on the strength behavior of plain concrete, resin material, and FRP strengthened concrete beams and columns have been

experimentally investigated. In this section, the temperature and aging effects are considered empirically for both concrete and resin materials by utilizing the -WLF- equation.

The combined effect of temperature and time on the strength of several materials could be represented by the time-temperature superposition (TTS) principle. One of the common applications of TTS is to expand the time range of short-term strength test results by taking such data at various temperatures and shifting them along the time axis, and then fitting the curve to find a master curve at the reference temperature which usually was the standard lab temperature (25^{o}C). The TTS principle was employed to construct the master curves for concrete and resin materials that were utilized in the experimental work of this research. The master curves were determined separately by using linear strength and time data, and also by logarithmic scale of these strength and time data.

7.2.1 Temperature and Aging Effects on Concrete Material

The experimental data of concrete beams was applied to obtain the master curve of concrete material.

The William-Landel-Ferry (WLF) equation is:

$$\log a_T = \frac{-c_1(T - T_r)}{c_2 + (T - T_r)} \tag{7.1}$$

Where:

a_T = temperature-dependent shift factor

T= temperature

T_r= reference temperature,

c_1 and c_2 are material constants.

By using the flexural strength data under various aging conditions for concrete beam specimens that were determined from the experimental tests, the original data on flexural

strength- time are plotted in figure 7.1 using linear scales. Figure 7.2 shows the logarithmic curves of these original data.

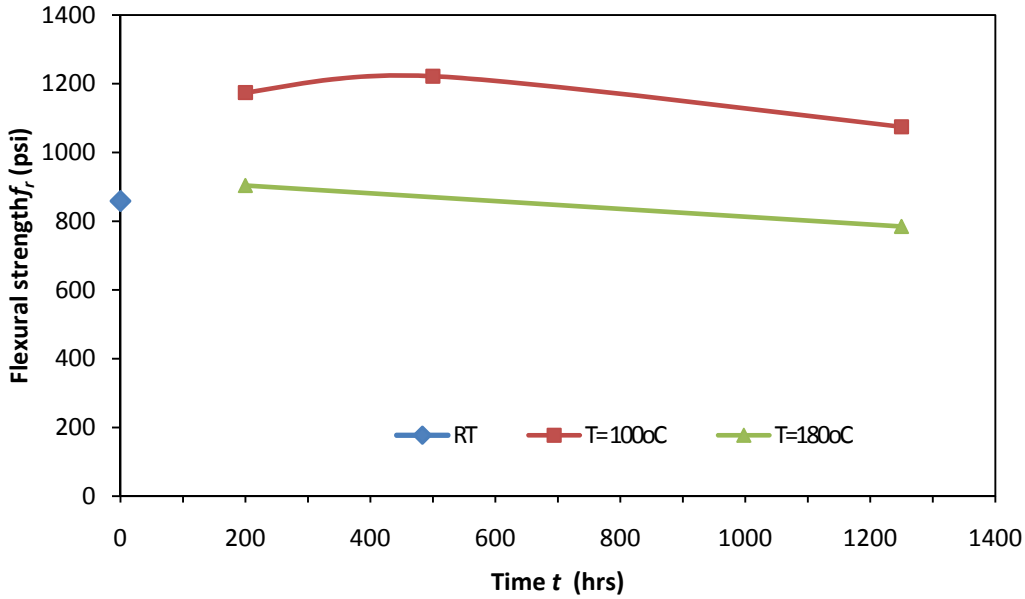

Figure 7.1: Flexural strength vs. time curves for concrete beams

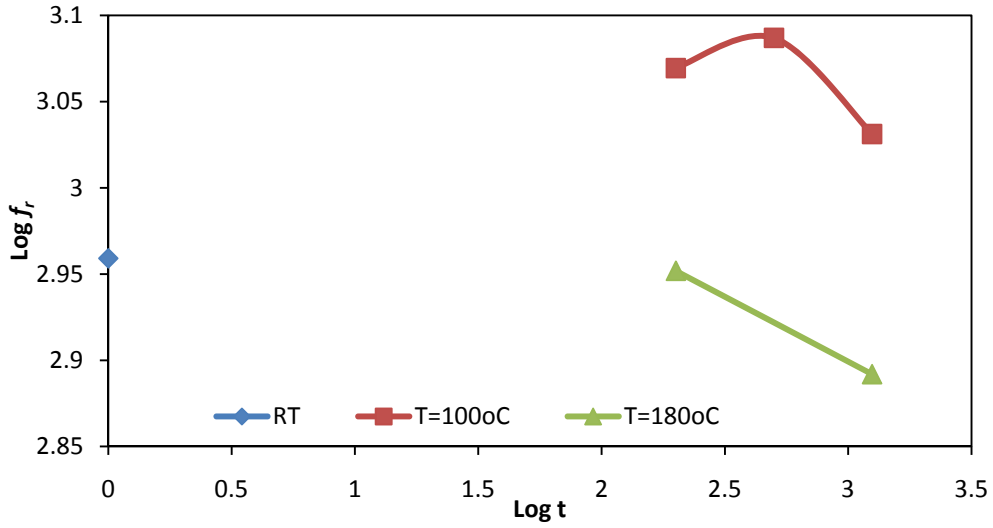

Figure 7.2: Flexural strength vs. time curves for concrete beams (logarithmic scale)

By using the WLF equation and substituting T by 100°C and 180°C while T_r was 25°C, we got two equations:

$$a_T = \frac{-c_1(100-25)}{c_2 + (100-25)} \tag{7.2}$$

$$a_T = \frac{-c_1(180-25)}{c_2+(180-25)} \tag{7.3}$$

By solving equations 7.2 and 7.3, the values of c_1= -8260.30 and c_2 = 146.26 (note: these values of c_1 and c_2 were obtained by using linear data). When the logarithmic data were used, the constants of c_1 and c_2 were equaled - 38.40 and 2325.0 respectively.

As a result of applying time-temperature superposition (TTS) using the available experimental data and shifting 100°C and 180°C data curves, the new curves were combined to generate the master curve (see figures 7.3 and 7.4).

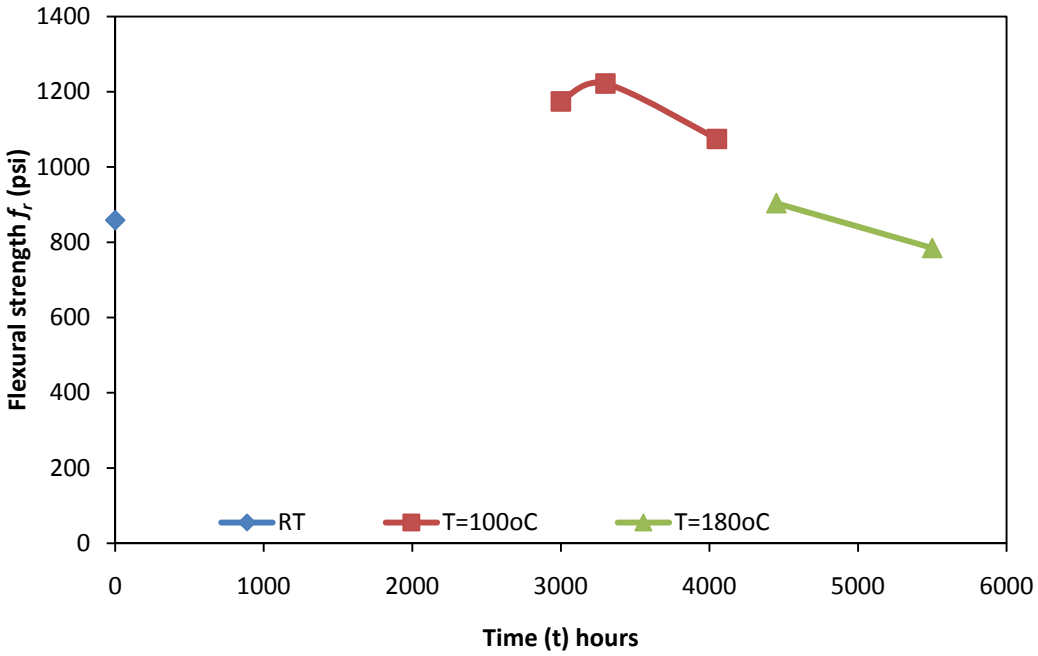

Figure 7.3: Shifting of flexural strength vs. time curves for concrete beams

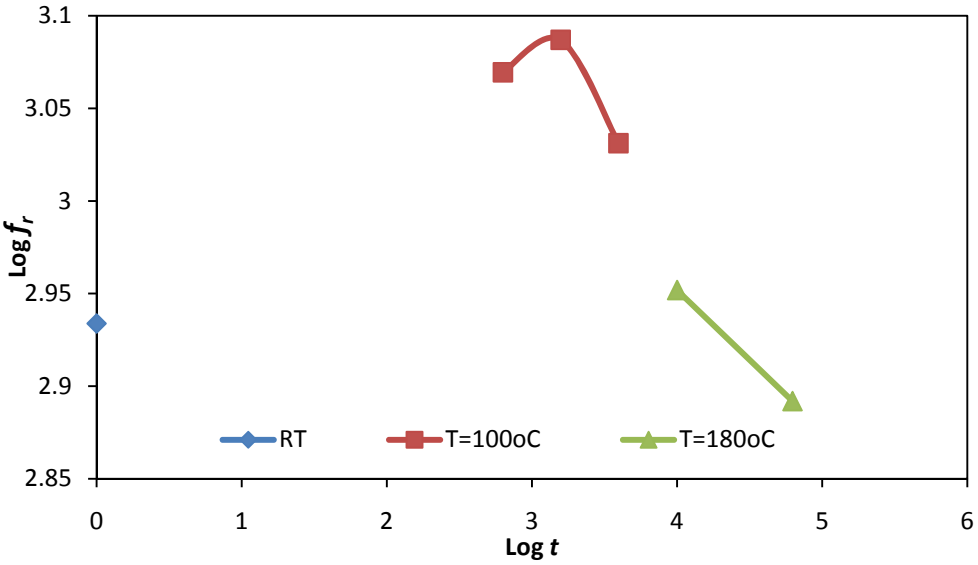

Figure 7.4: Shifting of Flexural strength vs. time curves for concrete beams (logarithmic scale)

The master curves at the reference temperature (25°C) were obtained by fitting all the data points in figures 7.3 and 7.4, and were shown in figures 7.5 and 7.6. The normalized strength equations as a function of time are equal:

$$f_{r(t)} = -5 \times 10^{-5} t^2 + 0.2551t + 864.95 \qquad \text{(linear scale)} \qquad (7.4)$$

$$f_{r(\log(t))} = -0.026 \log(t^2) + 0.1329 \log(t) + 2.9343 \qquad \text{(logarithmic scale)} \qquad (7.5)$$

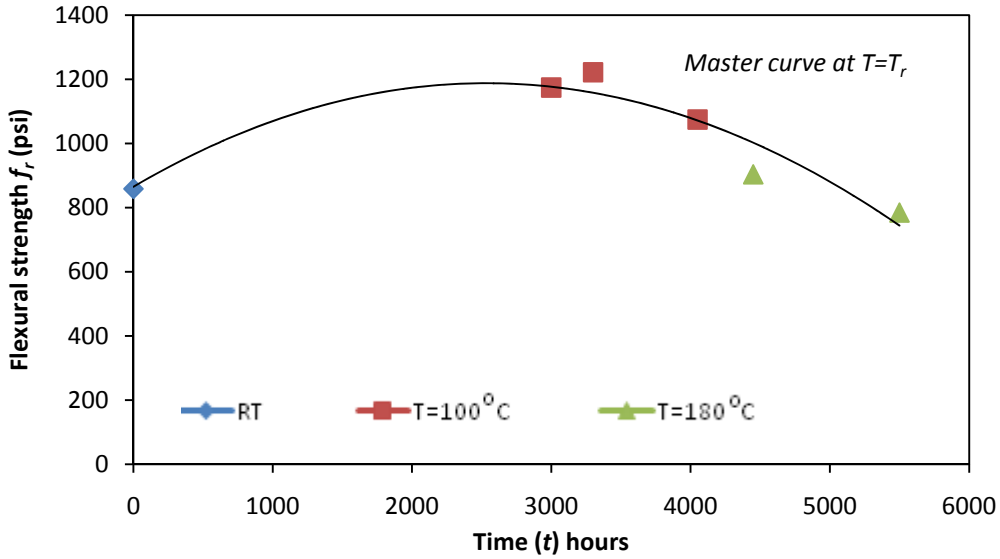

Figure 7.5: Master curve for concrete at reference temperature (linear scale)

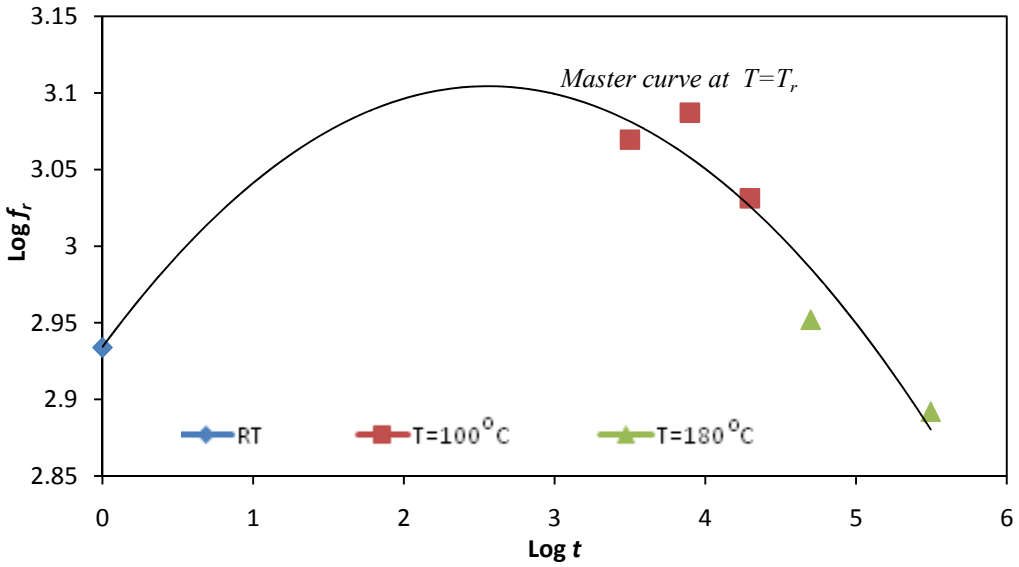

Figure 7.6: Master curve for concrete at reference temperature (logarithmic scale)

The temperature effect factors (k_{Tc}) after different number of cycles of exposure was determined according to the above master curves. Table 7.1 shows the values of this factor.

Table 7.1: Temperature effect factors for concrete material

Temp. (°C)	Number of cycles	Time of Exposing (hrs)	k_{Tc} (LMC)[1]	k_{Tc} (LGMC)[2]
RT*	0	0	1.0	1.0
100	40	80	1.38	1.055
	100	200	1.37	1.051
	250	500	1.35	1.041
	625	1250	1.25	1.03
180	40	80	1.19	1.029
	100	200	1.16	1.016
	250	500	1.07	0.9986
	350	700	1.04	0.9939
	625	1250	0.873	0.982

[1]- Linear data- master curve
[2]- Logarithmic data-master curve
- Reference temperature

The above master curves that are shown in figures 7.5 and 7.6, also the temperature effect factors which are tabulated in table 7.1 can be used to predict the compressive strength for concrete columns.

7.2.2 Temperature and Aging Effects on Resin Material

The resin materials, because of their viscoelastic nature, exhibit a deformation behavior which is both temperature and time dependent. For example, if a polymer is subjected to a constant load, the deformation exhibited by the material will increase over a period of time. This occurs because the material under a load undergoes molecular rearrangement in an attempt to minimize localized stresses. Hence, compliance or modulus measurements performed over a short time span result in lower/ higher values respectively than longer-term measurements.

The same procedures which were applied to plain concrete were performed to construct the master curve of the epoxies used in this study. The WLF equation was employed here to find the temperature-dependent shift factor for the resin material that was used in this research. The strength results, which were resulted from the experimental tests after exposing to different environmental conditions, have been utilized to predict the long-term environmental effects. Figures (7.7 and 7.8) show the original flexural strength-time curves of these test results by using linear and logarithmic scales respectively.

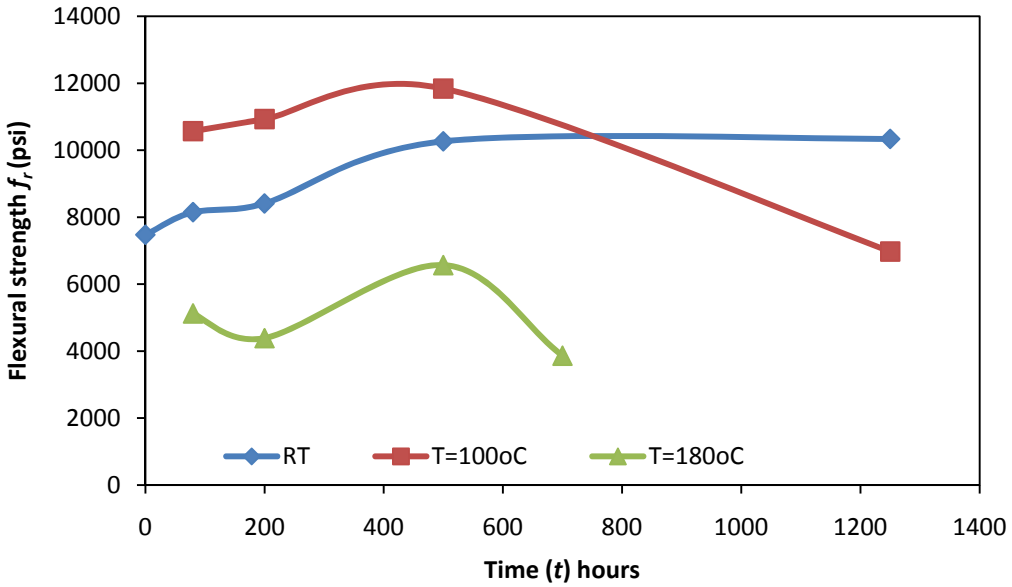

Figure 7.7: Flexural strength vs. time curves for epoxy beams (linear scale)

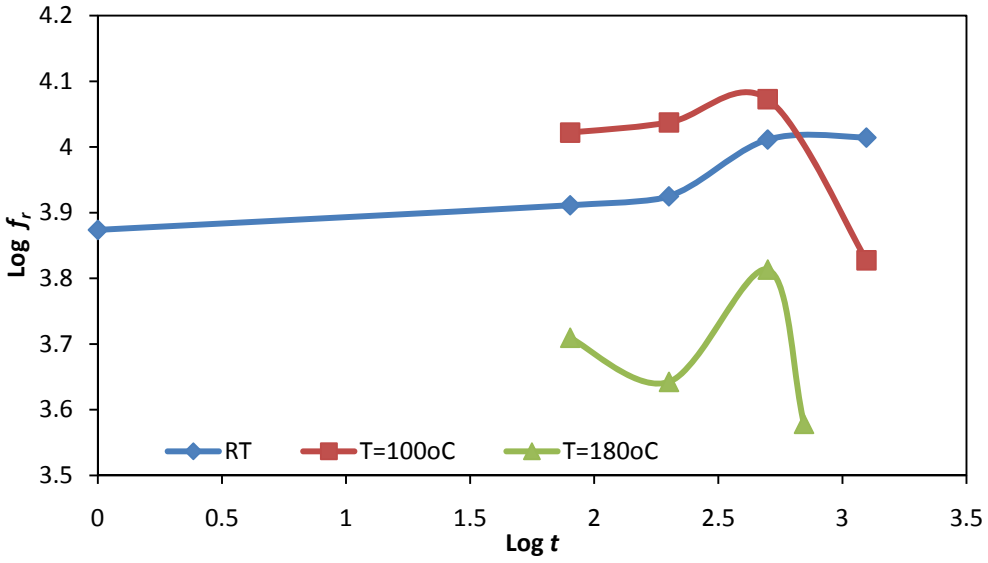

Figure 7.8: Flexural strength vs. time curves for epoxy beams (logarithmic scale)

The useful application of TTS was used to expand the range of short-term strength of resin material by shifting the data in figures 7.7 and 7.8 along the time axis. These curves were shifted according to temperature-dependent shift factor (see figures 7.9 and 7.10).

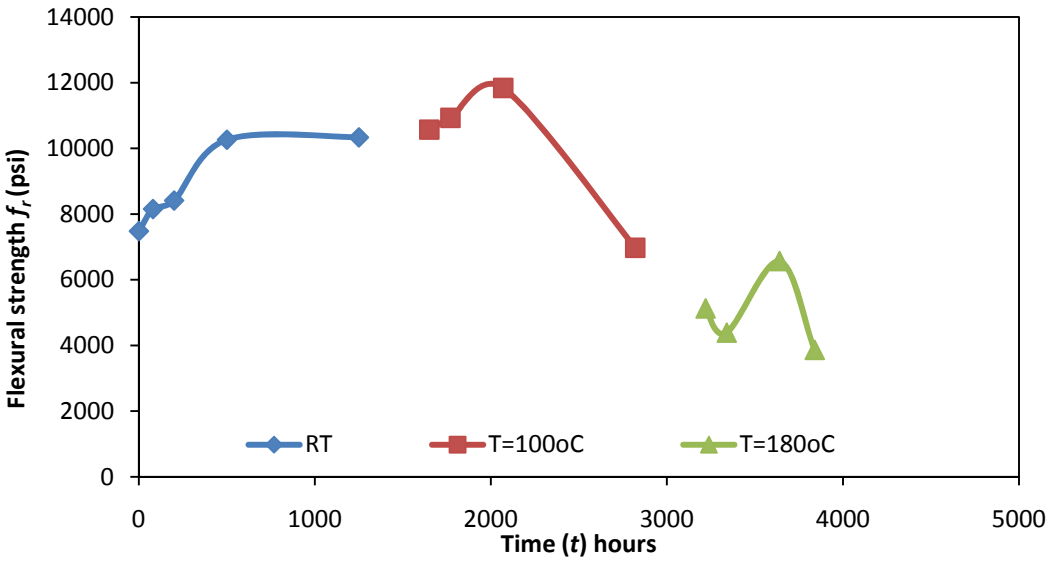

Figure 7.9: Shifting of flexural strength vs. time curves for epoxy beams (linear scale)

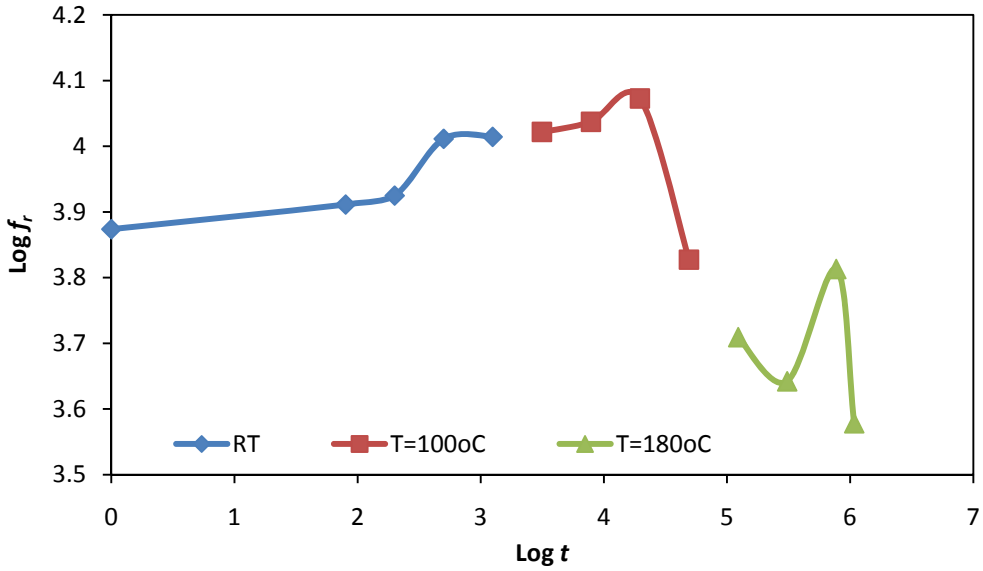

Figure 7.10: Shifting of flexural strength vs. time curves for epoxy beams (logarithmic scale)

By substituting into equation 7.1, where T one time is equal 100°C and again equal to 180°C, and T_r = 25°C, the constants c_1 and c_2 equaled -50240 and 2325 respectively. While c_1 = -51.0 and c_2 = 2325.0 when the logarithmic form of WLF equation was used.

The form master curves at reference temperature by using linear and logarithmic scales are shown in figures 7.11 and 7.12 respectively. The temperature effect factors (k_{Tm}) after different number of cycles of exposing was investigated according to the above master curves (see table 7.2). The normalized strength equations as a function of time are equal:

$$f_{r(t)} = -0.0014t^2 + 4.1899t + 7476.5 \qquad \text{(linear scale)} \qquad (7.6)$$

$$f_{r(\log(t))} = -0.0295\log(t^2) + 0.1469\log(t) + 3.8282 \quad \text{(logarithmic scale)} \qquad (7.7)$$

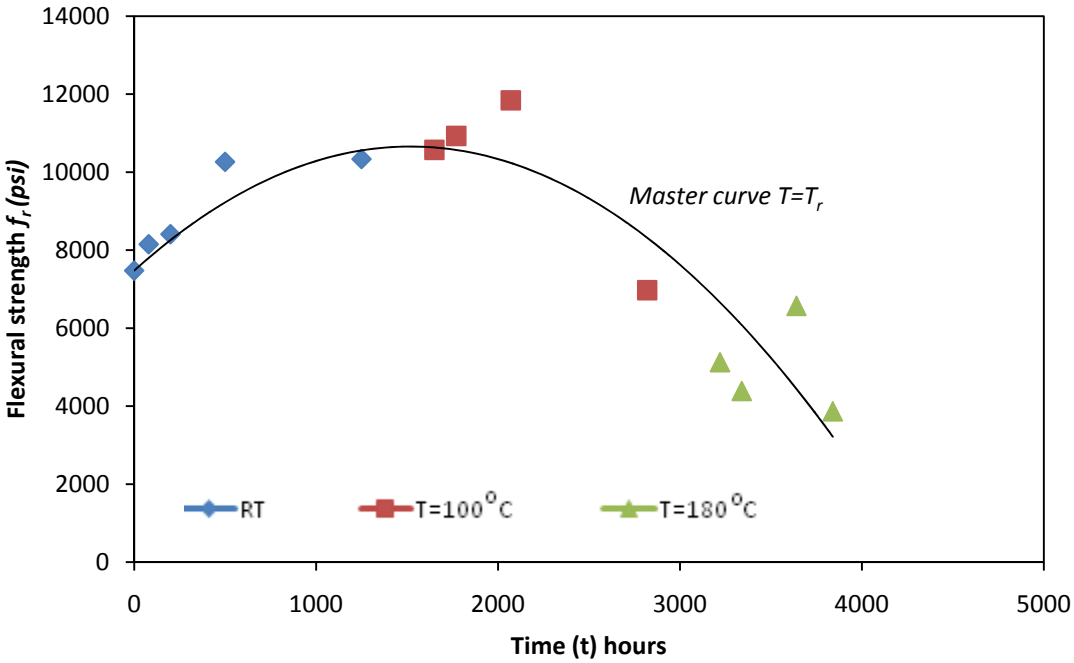

Figure 7.11: Master curve for epoxy material at reference temperature (linear scale)

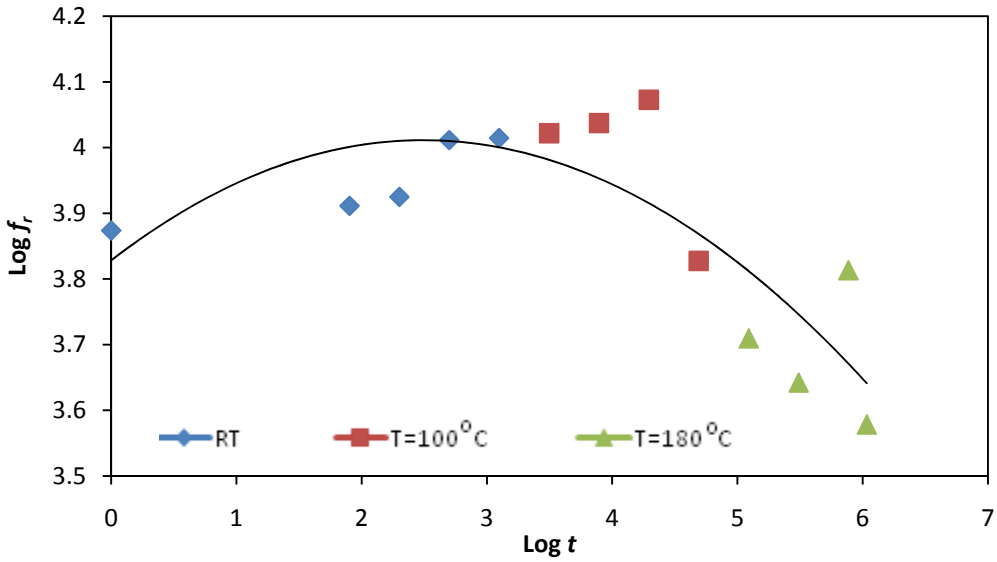

Figure 7.12: Master curve for epoxy material at reference temperature (logarithmic scale)

Table7.2: Temperature effect factors for epoxy material

Temp. (^oC)	Number of cycles	Time of Exposing (hrs)	k_{Tm} (LMC)[1]	k_{Tm} (LGMC)[2]
RT*	0	0	1.0	1.0
	40	80	1.05	1.043
	100	200	1.12	1.047
	250	500	1.25	1.047
	625	1250	1.42	1.043
100	40	80	1.41	1.037
	100	200	1.40	1.030
	250	500	1.38	1.023
	625	1250	1.11	0.965
180	40	80	0.880	0.99
	100	200	0.776	0.975
	250	500	0.602	0.954
	350	700	0.441	.949

[1]- Linear data- master curve
[2]- Logarithmic data-master curve
- Reference temperature

7.3 Analytical Model Results and Discussion

Analytical procedure, based on the ACI 318R-05 and ACI440.2R-02 requirements, was used to predict the flexural and compressive behaviors of unstrengthened and strengthened concrete beams and columns. This section includes the results and discusses of analytical procedures compared to the experimental findings

7.3.1 Non-Strengthened Concrete Beams

In general, when a concrete beam is subjected to gradually increasing load, initially the concrete is uncracked because the stress and strain are small. The tensile stresses f_t are smaller than the modulus of rupture f_r, but by increasing the loads, the stress and strain increases and the concrete begins to crack from the bottom of the beam (tensile zone). As a result of this increased load, the moment at which a crack starts to form is called the cracking moment $M_{cr.}$

$$M_{cr} = \frac{f_r I_g}{y_t} \tag{7.8}$$

Where f_r is the modulus of rupture, y_t is equal $h/2$, and I_g represents the moment of inertia of the gross cross-section.

$$f_r = 7.5\sqrt{f_c'} \tag{7.9}$$

$$I_{\mathrm{g}} = bh^3/12 \tag{7.10}$$

The above- equations were referred in section 4.2.1 of chapter four.

The modulus of rupture was modified by including the effect of temperature; the new equation will be:

$$f_r = 7.5K_{Tc}\sqrt{f_c'} \tag{7.11}$$

$$P_{cr} = \frac{4M_{cr}}{L_c} \tag{7.12}$$

Where P_{cr} is the cracking load and L_c represents the clear span (center to center).

k_{Tc} is the temperature factor of concrete and could be found from the master curve of concrete (see table 7.1), where f_c' represents the concrete compressive strength (= 5502 psi or 38.0MPa in this study).

In the case of reinforced concrete beams, after the concrete cracked, the steel will carry the load before a complete failure occurs. But in the case of plain concrete, as the case in this research, the concrete beam will fail at the onset of cracking of the concrete.

By applying the above equations (7.8 -7.12), the cracking moment and cracking load were found analytically. Table 7.3 shows the analytical results compared to the experimental results of different temperature aged samples. The moment of inertia of the beam gross cross-section is:

$$I_{\mathrm{g}} = \frac{4.3 * 4.1^3}{12} = 24.7\ in^4$$

$$y_t = \frac{4.1}{2} = 2.05\ in$$

Table7.3: Comparison of analytical failure load with experimental for non-strengthened concrete beams

Temp. (^oC)	Cy	k_{Tc}	f_r (pci)	M_{cr} (pci)	P_{cra}[a] (lbs)	P_{cre}[b] (lbs)	P_{cre}/P_{cra}
RT	0	1	556.32	6702.93	2234.31	3061.60	1.37
100	40	1.38	767.72	9250.04	3083.35	-	-
	100	1.37	762.15	9183.01	3061.00	4179.20	1.37
	250	1.38	767.72	9250.04	3083.35	4348.50	1.41
	625	1.25	695.40	8378.66	2792.89	3823.80	1.37
180	40	1.19	662.02	7976.49	2658.83	-	-
	100	1.16	645.33	7775.40	2591.80	3217.00	1.24
	250	1.07	595.26	7172.13	2390.71	-	-
	350	1.04	578.57	6971.05	2323.68	-	-
	625	0.9	500.68	6032.64	2010.88	2795.00	1.39

P_{cra}[a] =analytical failure load using ACI318-code chapter 9 (section 9.5.2.3)
P_{cre}[b]= experimental failure load

Figures 7.13 and 7.14 show the analytical and experimental load vs. the number of cycle curves of concrete beams that were exposed to 100°C and 180°C respectively.

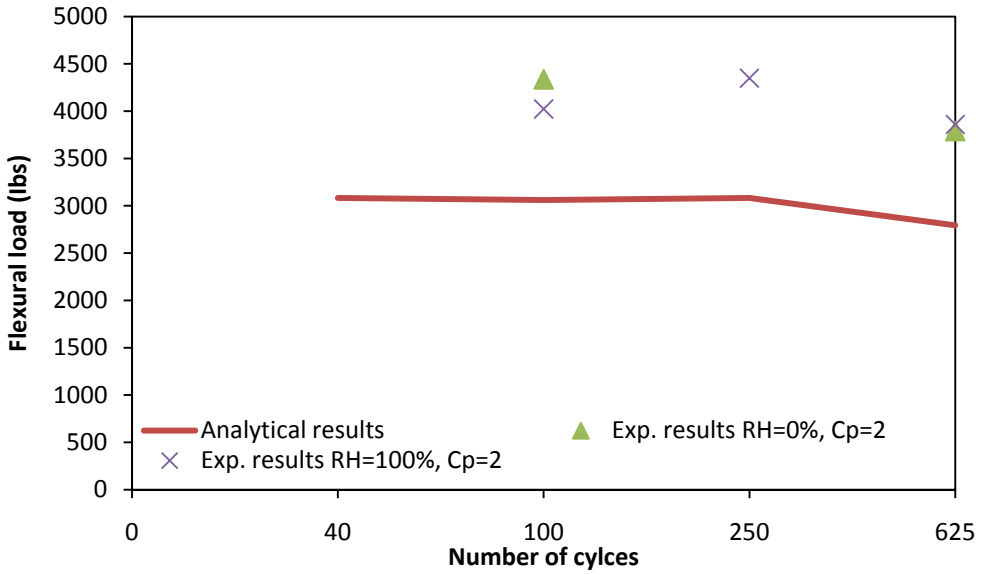

Figure 7.13: Analytical and experimental load/number of cycle curves of concrete beams T=100°C

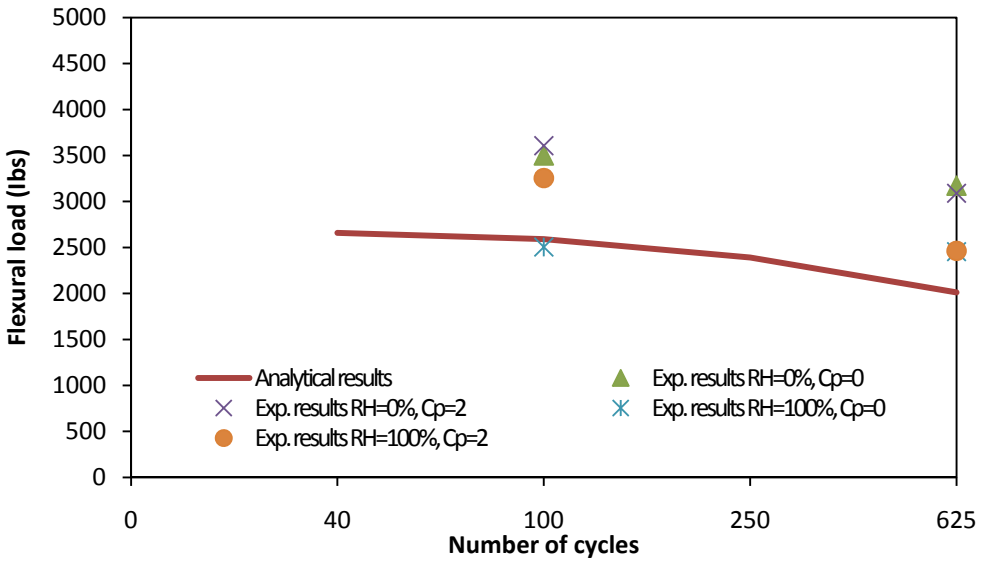

Figure 7.14: Analytical and experimental load/number of cycle curves of concrete beams T=180°C

The cracking loads of all beams conditioned at different temperatures were calculated using the analytical procedure including the temperature factors k_{Tc} (presented in table 7.3). These failure loads were compared with the experimental results as shown in figures 7.13 and 7.14. The pattern of the curves indicated that the analytical predictions underestimated the failure load by about 37%. This difference between the experimental and analytical results is considered as a factor of safety, as intended for design purposes in the modulus of rupture equation in ACI 318R-05.

7.3.2 Non-strengthened Concrete Columns

As mentioned in chapter four, section 4.2.2, the maximum nominal strength of RC column can be investigated by utilizing ACI318R-05 equation:

$$P_{n(\max)} = 0.85\emptyset[f_c'(A_g - A_{st}) + f_y(A_{st})] \quad (7.13)$$

All the symbols in the above equation were defined early in chapter four. When the effect of temperature is taken into account, the nominal strength of the column can be written in the form:

$$P_{n(\max)} = 0.85\emptyset[K_{TC}f_c'(A_g - A_{st}) + f_y(A_{st})] \quad (7.14)$$

By neglecting the steel effect, the above equation becomes:

$$P_{n(\max)} = 0.85[K_{TC} f_c' A_g] \tag{7.15}$$

In this research, the gross concrete area A_g is equal:

$$A_g = \frac{\pi D^2}{4} \tag{7.16}$$

Where D is diameter of the cylinder = $4''$

$$A_g = \frac{\pi(4)^2}{4} = 12.57\ in^2$$

As stated earlier, the compressive strength of the control concrete f_c' is 5502 psi. Thus: by substituting into equation 7.15, the maximum nominal axial load of the column specimens was found. Table 7.4 shows the analytical nominal axial loads and corresponding experimental loads.

Table 7.4: Comparison of Analytical Failure load with Experimental for non-strengthened concrete Columns

Failure Load							
Temp. (^oC)	Cy	k_{Tc}	$P_{na\,(1)}{}^a$ (lbs)	$P_{na\,(2)}{}^b$ (lbs)	$P_{ne}{}^c$ (lbs)	$P_{ne}/P_{na}{}^1$	$P_{ne}/P_{na}{}^2$
RT	0	1	58767.41	69138.13	69141.0	1.18	1.00
100	40	1.38	81099.03	95410.62	-		
	100	1.37	80511.35	94719.24	-		
	250	1.38	81099.03	95410.62	103926.0	1.28	1.09
	625	1.25	73459.27	86422.67	91781.0	1.25	1.06
180	40	1.19	69933.22	82274.38	-		
	100	1.16	68170.2	80200.23	75787.96	1.11	0.94
	250	1.07	62881.13	73977.8	-		
	350	1.04	61118.11	71903.66	-		
	625	0.9	52890.67	62224.32	67216.34	1.27	1.08

$P_{na(1)}{}^a$ =analytical ultimate load using ACI318-code ϕ=0.85
$P_{na(2)}{}^b$ =analytical ultimate load using ACI318-code ϕ=1.0
$P_{ne}{}^c$= experimental failure load

Comparisons between the analytical calculations and experimental results of the compressive load are represented by the relationship between the compressive load and number

of cycle curves (see figures 7.15 and 7.16). Two analytical compressive loads were calculated. In the first calculation, the reduction factor ϕ which is equal 0.85 was taken in to account as mentioned in the ACI318R-05. While in the second calculation, the reduction factor was neglected (ϕ=1.0). The analytical calculations considered the reduction factor showing that underestimated ultimate load, but in the column design, this conservative is important because the failure in the columns means structure failure. The pattern of the curves in figures 7.15 and 7.16 indicates that the analytical calculation without reduction (ϕ=1.0) were close to the experimental results (see figures 7.15 and 7.16).

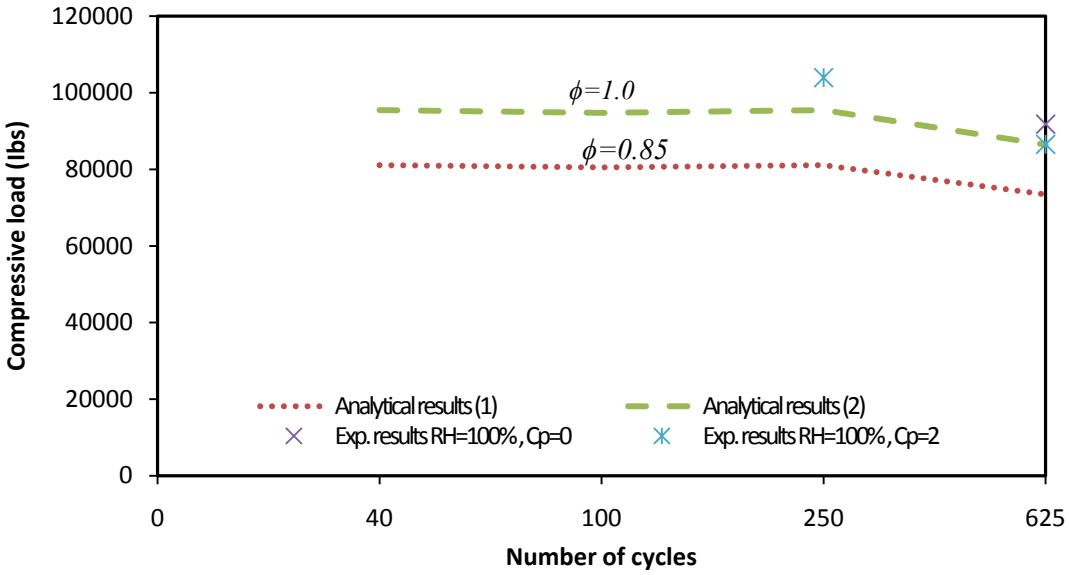

Figure 7.15: Analytical and experimental load/number of cycle curves of concrete columns T=100^{o}C

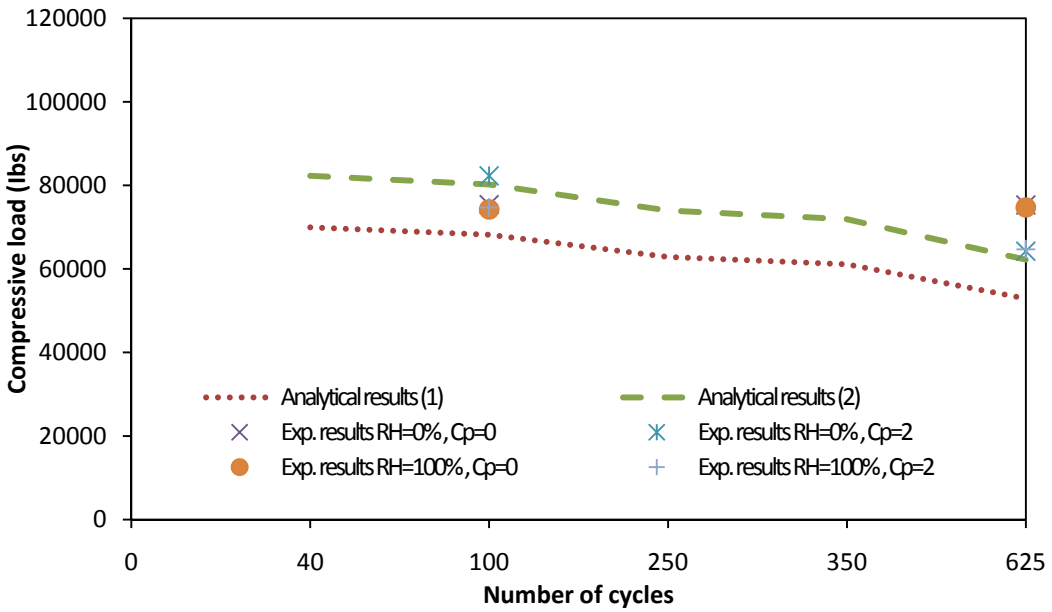

Figure 7.16: Analytical and experimental load/number of cycle curves of concrete columns T=180°C

7.3.3 Epoxy Beams

The failure flexural loads of the matrix materials aged at different temperatures were calculated by equation 7.16. All the symbols that are mentioned in this equation have been introduced in section 4.3-chapter four. The flexural stress of the control samples, σ_f, was 243psi. has been used as control stress to calculate the flexural stresses for different temperatures and number of cycles could be obtained by multiplying σ_f by appropriate temperature factors of the matrix material $k_{Tm,}$ as explained in equation 7.17.

$$P = \frac{2\sigma_f bd^2}{3L} \tag{7.16}$$

$$P = \frac{2k_{Tm}\sigma_f bd^2}{3L} \tag{7.17}$$

The analytical stress in the outer fibers at midpoint, the analytical flexural load, and the experimental flexural load at failure are tabulated in table 7.5. As shown in table 7.5 and figures 7.17,7.18, and 7.19, compared to the experimental results, the analytical procedure overestimated

in some cases but underestimated in other cases. Refined reduction factors might be needed for improving prediction accuracy.

Table7.5: Comparison of analytical failure load with experimental for epoxy beams

Temp. ($_{o}C$)	Cy	k_{Tm}	σ_f (psi)	Pa[a] (lbs)	Pe[b] (lbs)	Pa/Pe
RT	0	1.00	7476.50	242.99	242.99	1.00
	40	1.05	8152.00	255.14	264.94	1.04
	100	1.12	8410.50	272.14	273.34	1.00
	250	1.25	10264.85	303.73	333.61	1.10
	625	1.42	10335.65	345.04	335.91	0.97
100	40	1.41	10570.13	342.61	343.53	1.00
	100	1.4	10895.25	340.18	354.10	1.04
	250	1.38	11841.08	335.32	384.83	1.15
	625	1.11	6972.86	269.71	226.62	0.84
180	40	0.88	5126.80	213.83	166.62	0.78
	100	0.776	4378.58	188.56	142.30	0.75
	250	0.602	6570.15	146.28	213.53	1.46
	350	0.441	4017.36	107.16	130.56	1.22

[a] =analytical failure load
[b]= experimental failure load

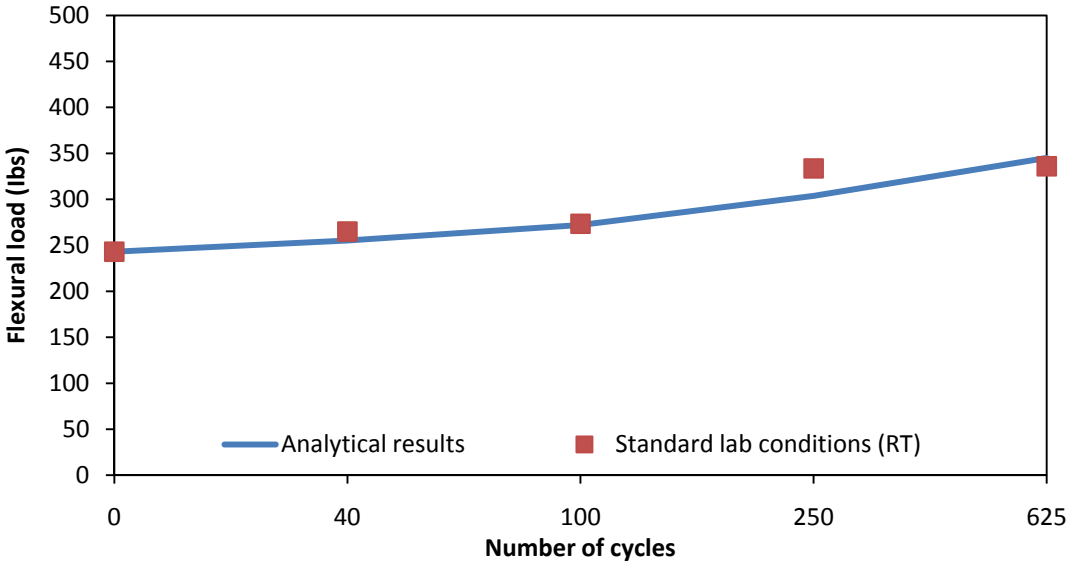

Figure 7.17: Analytical and experimental load/number of cycle curves of epoxy beams at RT

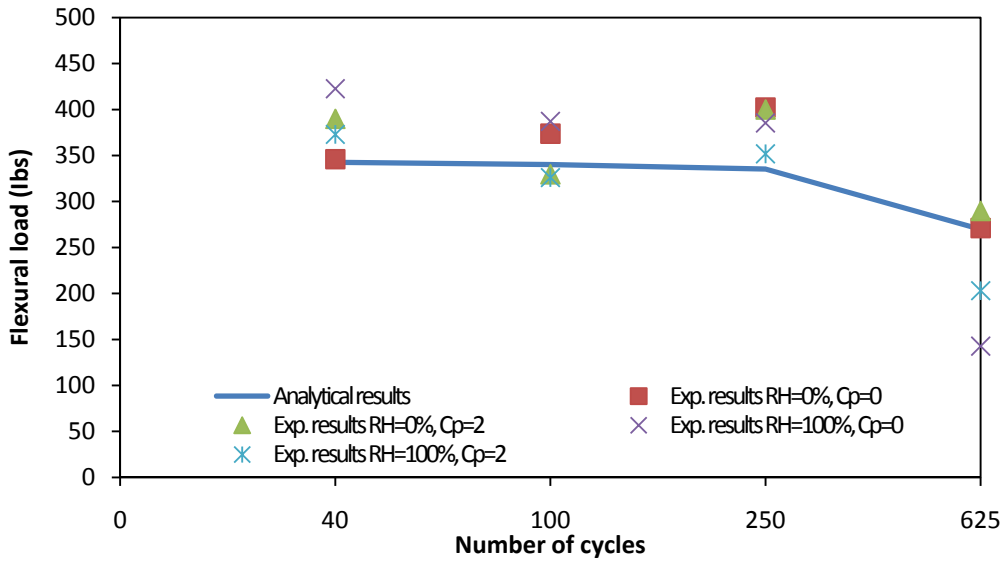

Figure 7.18: Analytical and experimental load/number of cycle curves of epoxy beams, T=100°C

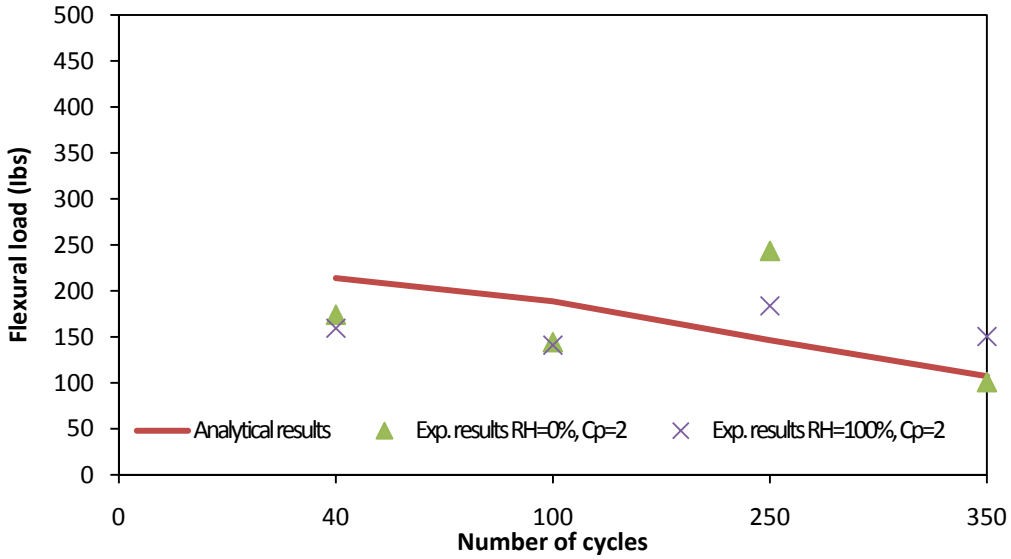

Figure 7.19: Analytical and experimental load/number of cycle curves of Epoxy beams, T=180°C

7.3.4 FRP Strengthened Concrete Beams

Based on the mechanical properties of fiber and matrix materials that are available, the actual tensile strength and tensile modulus of the composite materials can be calculated according to the following equations [6]:

$$\sigma_{com} = \sigma_f v_f + \sigma_m v_m \tag{7.18}$$

$$E_{com} = E_f v_f + E_m v_m \tag{7.19}$$

Where: σ_{com} is the tensile strength of the cured laminate composite, σ_f represents the tensile strength of dry fiber, σ_m is the tensile strength of matrix material, v_f is the volume fraction of fiber, and v_m represents the volume fraction of matrix. The tensile modulus, *E* of the fiber (subscript *f*) and matrix (subscript *m*) constituents an FRP composite (subscript *com*).

$$v_f = w_f \frac{\rho_c}{\rho_f} \tag{7.20}$$

$$v_m = w_m \frac{\rho_c}{\rho_m} \tag{7.21}$$

Where w_f is the weight or mass fraction of fiber,w_f, represents the weight or mass fraction of matrix, ρ_c , ρ_f , ρ_m are the weight density (or mass density) of composites, fiber, and matrix respectively.

$$w_f = \frac{W_f}{W_c} \tag{7.22}$$

$$w_m = \frac{W_m}{W_c} \tag{7.23}$$

W_f , W_m , W_c is the weight (or mass) of the fiber, matrix, and composites respectively.

The weight density of the matrix material used in the experimental work of this research was 0.8kg/m^3.

The density of the composite (fiber + matrix) can be found by this equation:

$$\rho_c = v_f \rho_f + v_m \rho_m = \frac{1}{w_f/\rho_f + w_m/\rho_m} \tag{7.24}$$

$$v_f + v_m = 1 \tag{7.25}$$

$$w_f + w_m = 1 \tag{7.26}$$

Based on the mechanical properties which are used in this research (tables 3.8-3.11), and by applying in the above equations, the actual ultimate tensile strength and tensile modulus were calculated. The volume fractions was calculated (see table 7.6)

Table 7.6: Mechanical properties of FRP composites

Fiber	Matrix	v_f	v_m	$\sigma_{com} = f_{fu}$ [a] (psi)	$E_{com} = E_f$ [b] (psi)
SikaWrap HEX 113C	Sikadur300	0.136	0.864	7.51E+05	4.77E+06
	Tyfo S	0.131	0.869	7.47E+04	4.78E+06
SikaWrap HEX 100G	Sikadur300	0.343	0.657	1.18E+05	3.76E+06
	Tyfo S	0.333	0.667	1.17E+05	3.80E+06
Tyfo SHE-41A	Sikadur300	0.349	0.651	1.97E+05	1.18E+07
	Tyfo S	0.339	0.661	1.94E+05	1.16E+07
Tyfo SHE-51A	Sikadur300	0.342	0.658	1.66E+05	3.76E+06
	Tyfo S	0.332	0.668	1.63E+05	3.80E+06

[a] = tensile strength of FRP composite
[b] = tensile modulus of FRP composite

This section explores the flexural behavior of FRP strengthened concrete beams. Analytical calculations were conducted to study the structural performance of FRP strengthened concrete beams under flexure according to ACI 440.2-2. Based on the force equilibrium and compatibility of deformations, the flexural behavior of the concrete beams strengthened with FRP can be predicted on the basis of the following assumptions:

- The strain distribution is linear throughout the beam section
- Shear deformation is very small and neglected.
- Failure of the beam occurs when either the maximum concrete strain reaches its ultimate strain which is 0.003 or the tensile strain of the FRP composite reaches its ultimate strain capacity.

To calculate the nominal load and moment for strengthened concrete beams, we need to determine the location of neutral axis, *c*. In the case of plain concrete beams, the depth *d* is the

total height of the beam *h*. By assuming a value of *c*, the effective tensile strain of the FRP can be calculated from the concrete strain (ε_c) by this equation:

$$\epsilon_{fe} = \varepsilon_c \left(\frac{h-c}{c}\right) - \varepsilon_{bi} \tag{7.27}$$

Where ε_{bi} represents the existing strain at the substrate at the time the FRP system is attached (in this analysis ε_{bi} was considered zero).

The ultimate tensile strength of FRP composite (cured laminate) equals:

$$f_{fu} = \sigma_{com} = \sigma_f v_f + k_{Tm}\sigma_m v_m \tag{7.28}$$

Where k_{Tm} is the temperature factor of the matrix, and equals 1.0 at time zero (right after the construction).

$$\varepsilon_c = \left(\varepsilon_{fe} + \varepsilon_{bi}\right)\frac{c}{h-c} \tag{7.29}$$

If ε_c =0.003, the concrete fails by crushing. Alternatively, the failure strain of concrete can be estimated by the ACI equation (ACI440.2R-02).

$$\varepsilon_c' = \frac{1.71 f_c'}{E_c} \tag{7.30}$$

Where f_c' is the compressive strength of concrete (= 5502 psi or 38Mpa in this study).

$$E_c = 57000\sqrt{f_c'} = 57000\sqrt{5502} = 4.23 \times 10^6 psi \tag{7.31}$$

$$\beta_1 = 2 - \frac{4[(\varepsilon_c/\varepsilon_c') - \tan^{-1}(\varepsilon_c/\varepsilon_c')]}{(\varepsilon_c/\varepsilon_c')\ln[1 + (\varepsilon_c/\varepsilon_c')^2]} \tag{7.32}$$

$$\gamma = \frac{0.9\ln[1 + (\varepsilon_c/\varepsilon_c')^2]}{\beta_1(\varepsilon_c/\varepsilon_c')} \tag{7.33}$$

Where β_1 and γ are the equivalent stress block.

Thus:

$$c = \frac{A_f f_{fu}}{\gamma f_c' \beta_1 b} \tag{7.34}$$

Where: A_f is the thickness of FRP sheet/fabric times the width of FRP sheet/fabric:

$$A_f = t_f w_f \tag{7.35}$$

Check the value of c. If it matches the assumed *c*, the correct neutral axis location has been found. Otherwise, assume another value of c and repeat the procedure until the c values converge. Several trials and iterations are needed. Therefore, a computer program by using MATLAB has been prepared to calculate the correct value of the neutral axis *c* of the section.

The nominal moment capacity of the strengthened concrete beam M_n is represented by this equation

$$M_n = \psi_f A_f f_{fu} \left(h - \frac{\beta_1 c}{2}\right) \tag{7.36}$$

ψ_f is an extra reduction factor of fiber = 0.85.

The nominal flexural load P_n is:

$$P_n = \frac{4M_n}{L_c} \tag{7.37}$$

By applying the above-mentioned equations, table 7.7 shows the experimental and analytical flexural loads at failure.

The flexural load at failure of all beams was calculated by using the analytical procedure based on ACI 440.2R-02 and are presented in table 7.7. Two analytical flexural load calculations are shown in table 7.7. The first one represents the analytical calculation including the reduction factor of fiber ψ_f (see equation 7.36), while the second computation ignored this reduction factor. The results of both analytical calculations were compared to the experimental results as shown in the figures (7.20, 7.21, and 7.22).

The pattern of the curves (figures 7.20, 7.21, and 7.22), point out that the two analytical solutions underestimated the failure load at standard lab conditions and after 100^{o}C of

temperature. While due to exposure to 180°C of temperature, the analytical results that included the FRP reduction factor, still conservative underestimated, but the second analytical results which was calculated without FRP reduction factor were overestimated failure load especially after 100 and 250 cycles of exposure. This explains that the FRP reduction factor is an important value must be considered at FRP strengthening design especially at hot environment.

Table 7.7: Comparison of analytical failure load with experimental for FRP strengthened beams

Temp. (°C)	Cy	k_{Tc}	k_{Tm}	Mna^a (1) (lbs-in)	Pna^b (1) (lbs)	Pna^c (2) (lbs)	Pne^d (lbs)	$\frac{P_{ne}}{P_{na}(1)}$	$\frac{P_{ne}}{P_{na}(2)}$
RT	0	1.00	1	10989.60	2905.8	3418.6	3849.35	1.32	1.13
	40	1.00	1.05	11014.50	2923.3	3439.2	4110.00	1.41	1.20
	100	1.00	1.12	11184.00	2947.8	3468.0	4170.00	1.41	1.20
	250	1.00	1.25	114054.00	2993.3	3521.5	4445.00	1.48	1.26
	625	1.00	1.42	114309.00	3052.7	3591.4	4538.00	1.49	1.26
100	40	1.38	1.41	114171.00	3057.7	3597.3	4215.50	1.38	1.17
	100	1.37	1.4	11389.20	3054	3592.9	4632.25	1.52	1.29
	250	1.35	1.38	110274.00	3046.6	3584.2	4679.75	1.54	1.31
	625	1.25	1.11	10720.80	2950	3470.6	4725.00	1.60	1.36
180	40	1.19	0.88	10582.20	2868.1	3374.2	3885.25	1.35	1.15
	100	1.16	0.776	10582.20	2831	3330.6	3399.75	1.20	1.02
	250	1.07	0.602	10345.80	2768	3256.5	3058.75	1.11	0.94

[a] =analytical failure moment using ACI 440.2R-02
[b]= analytical failure load when $\psi_f = 0.85$
[c]= analytical failure load when $\psi_f = 1.0$
[d]= experimental failure load

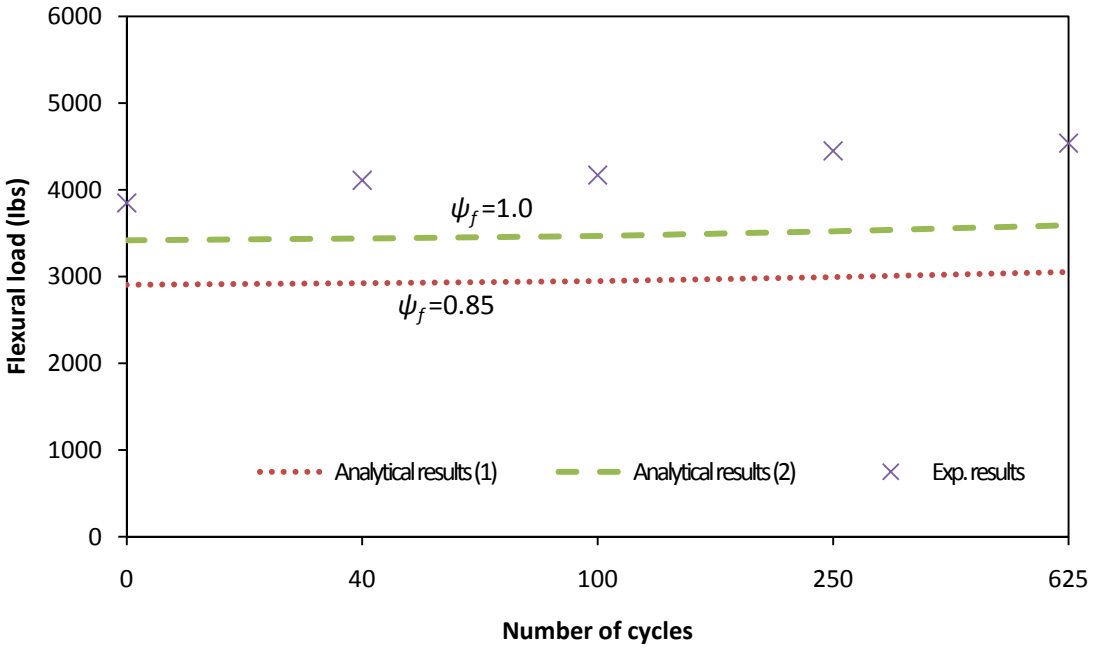

Figure 7.20: Analytical and experimental load/number of cycle curves of FRP strengthened beams at RT

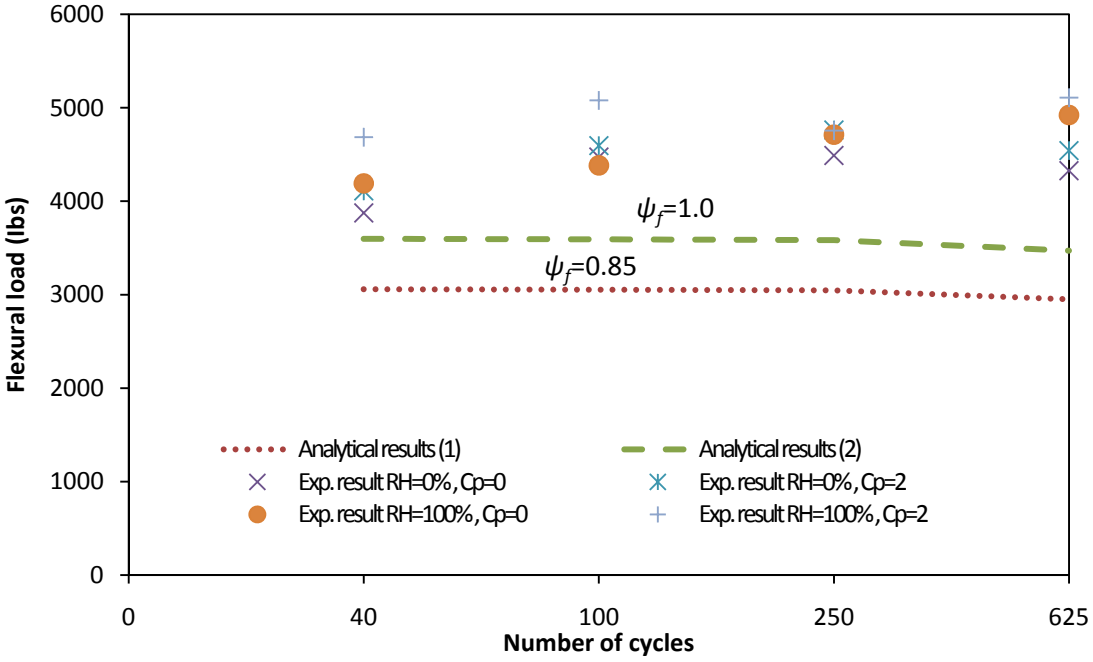

Figure 7.21: Analytical and experimental load/number of cycle curves of FRP strengthened beams T=100^{o}C

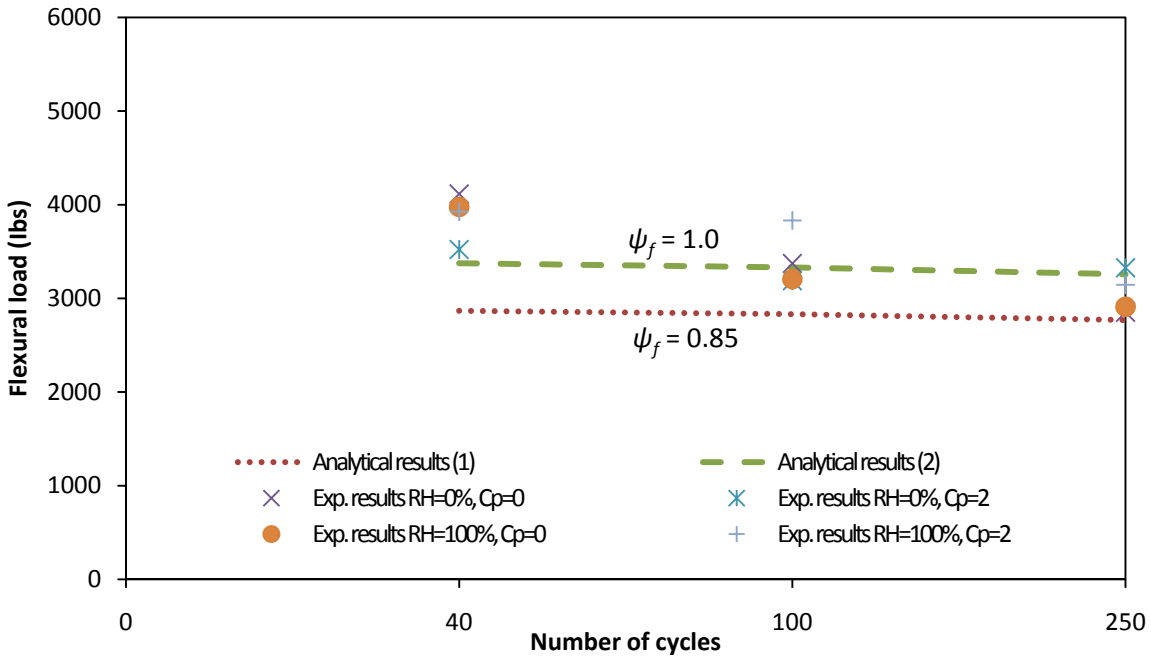

Figure 7.22: Analytical and experimental load/number of cycle curves of FRP strengthened beams T=180°C

7.3.5 FRP Strengthened Concrete Columns

ACI 440.2R-02 were utilized to calculate the failure axial concentrically load

The FRP ratio:

$$\rho_f = \frac{A_f}{A_c} = \frac{\pi D n t_f}{\pi D^2/4} = \frac{4nt_f}{D} \tag{7.38}$$

Where ρ_f represents the FRP strengthened ratio, A_f is the FRP area, and A_c is the gross concrete area.

$$f_1 = \frac{k_a \rho_f E_f \varepsilon_{fe}}{2} \tag{7.39}$$

f_1 is the confining pressure, k_a represents the efficiency factor which is taken as unity; for circular columns=1.0, E_f represents the tensile modulus of FRP, and ε_{fe} is the FRP effective strain.

$$f'_{cc} = f'_c\left(2.25\sqrt{1+7.9\frac{f_1}{f'_c}}-2\frac{f_1}{f'_c}-1.25\right) \tag{7.40}$$

f'_{cc} is the confined concrete compressive strength.

$$P_{n(\max)} = 0.85\left[0.85\psi_f f'_{cc}\left(A_g - A_{st}\right) + f_y A_{st}\right] \tag{7.41}$$

Where ψ_f is the FRP reduction factor = 0.95, A_{st} is the steel reinforcement area =0.0 in case of plain concrete, and f_y is the yielding stress of steel reinforcement. When steel reinforcements are not used, eqn (7.41) is reduced to

$$P_{n(\max)} = 0.85\left[0.85\psi_f f'_{cc}\left(A_g\right)\right] \tag{7.42}$$

$P_{n(\max)}$ represents the maximum nominal axial load.

A similar procedure was used with FRP strengthened beams to find two analytical results for the maximum compressive load. The extra FRP reduction factor was taken into account in the first calculation and the factor was neglected in the second calculation. A comparison among these two analytical solutions and experimental results are explained in table 7.8. The results show that at the standard lab condition (RT), the analytical calculation recorded underestimated failure load about of 36% by considering the reduction factor and by 29% without taking it into the account. This underestimating increased to reach 52% and 45% after exposure to 100^{o}C of temperature and 40 cycles for with and without reduction factor consideration respectively. With increases the number of cycles to 625 and 100^{o}C of temperature, the analytical results conservation backed down to only 8% and 3% respectively below the experimental results. After 250 cycles and 180^{o}C of temperature, the analytical results were 6% and 10% overestimated compared to the experimental results (see figure 7.23 to 7.25).

Table 7.8: Comparison of analytical failure load with experimental for FRP strengthened columns

Temp. (^{o}C)	Cy	k_{Tc}	k_{Tm}	Pna(1)[a] (lbs)	Pna(2)[b] (lbs)	Pne[c] (lbs)	Pne/Pna(1)	Pne/Pna(2)
RT	0	1.00	1	70568.00	74282.11	96101.00	1.36	1.29
	40	1.00	1.05	70623.00	74340	92304.75	1.31	1.24
	100	1.00	1.12	70700.00	74421.05	95877.00	1.36	1.29
	250	1.00	1.25	70844.00	74572.63	102970.00	1.45	1.38
	625	1.00	1.42	71032.00	74770.53	105759	1.49	1.41
100	40	1.38	1.41	71021.00	74758.95	108187.00	1.52	1.45
	100	1.37	1.4	92054.00	96898.95	-	-	-
	250	1.35	1.38	90898.00	95682.11	-	-	-
	625	1.25	1.11	84919.00	89388.42	91664.10	1.08	1.03
180	40	1.19	0.88	81251.00	85527.37	83159.60	1.02	0.97
	100	1.16	0.776	79429.00	83609.47	77003.10	0.97	0.92
	250	1.07	0.602	74114.00	78014.74	70029.80	0.94	0.90

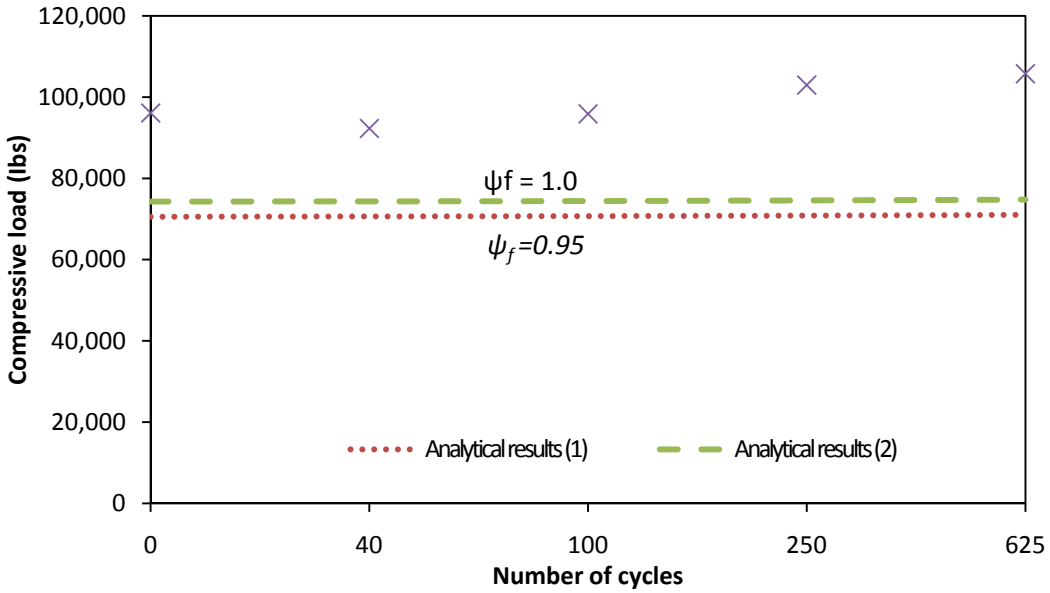

Figure 7.23: Analytical and experimental load/number of cycle curves of FRP strengthened columns at RT

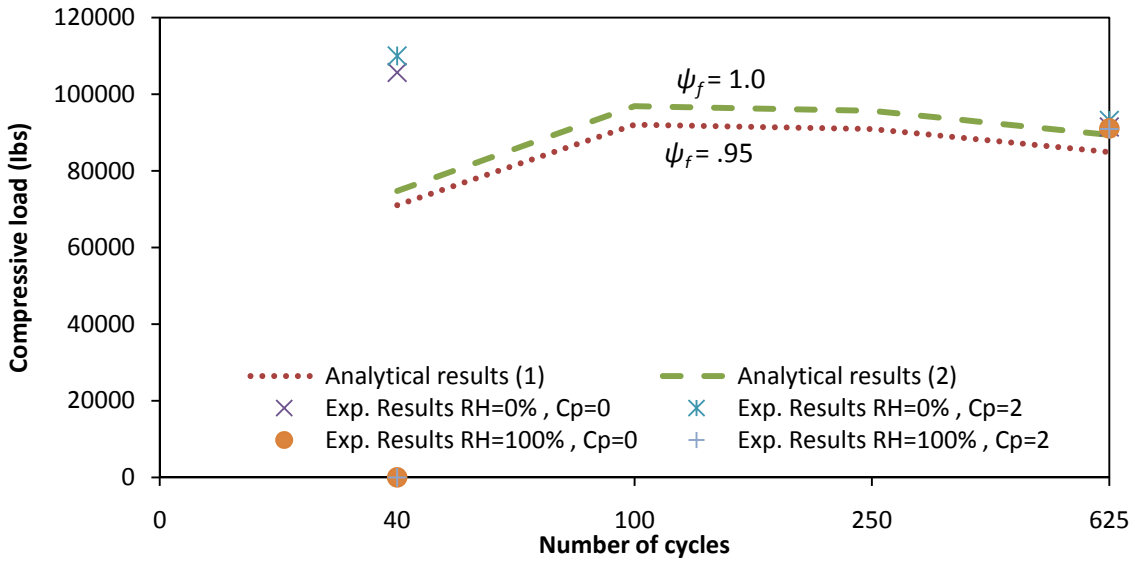

Figure 7.24: Analytical and experimental load/number of cycle curves of FRP strengthened columns T=100°C

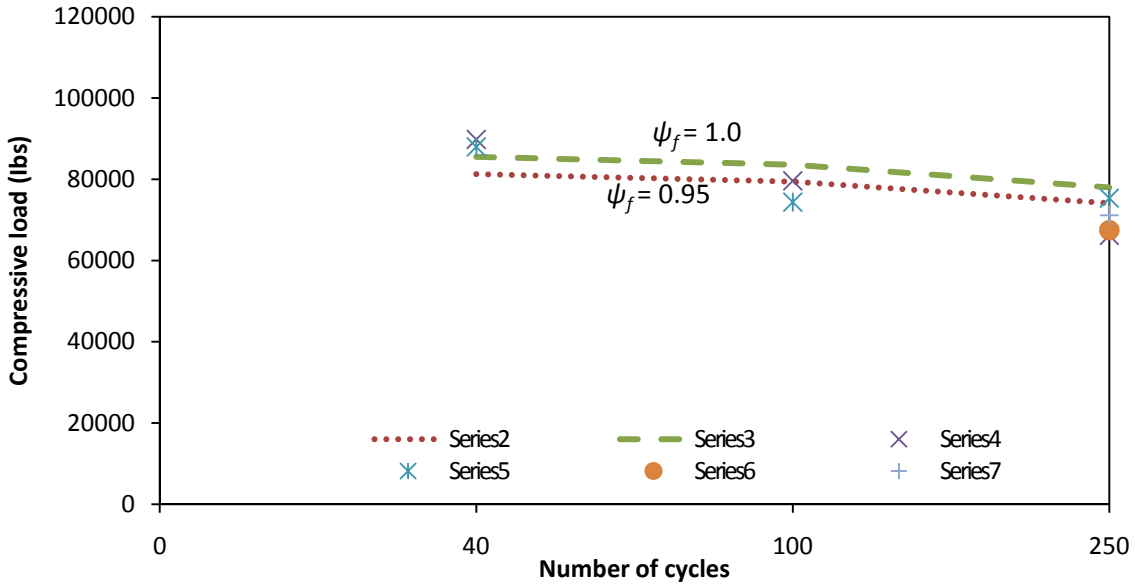

Figure 7.25: Analytical and experimental load/number of cycle curves of FRP strengthened columns T=180°C

7.4 Finite Element Model Predictions and Discussion

The behavior of unstrengthened and FRP strengthened concrete beams/columns and epoxy beams were studied experimentally in chapter six. The results were compared to analytical calculations in section 7.3 of this chapter. In this section, Extended Finite Element Method (X-

FEM) was used to model the behavior of those elements numerically to confirm these calculations, as well as to provide a valuable supplement to the experimental investigations in this study.

The ABQUS CAE finite element software (ABAQUS CAE 6.9-1) was adopted in this study to simulate the behavior of the experimental beams and columns, and predict the load - displacement response of the epoxy beams, unstrengthened and strengthened concrete beams and columns numerically**.**

7.4.1 Numerical Modeling of Non-Strengthened Concrete Beams

2D nonlinear extended finite-element (X-FE) model was developed to study the behavior of concrete beams (see figure 7.26). The section type was selected “deformed” and “Maxps Damage’ was chosen as the type of damage. The section was meshed by size of = 0.2; the total number of nodes was 1680 (figure 7.27); the element type was selected as “plane strain”, and the element shape was chosen “quad-dominated-structured’. The Poisson’s ratio was assumed as equal to 0.18; the concrete failure ratio was 1.16, and concrete density equal to 0.0867 lb/in^3. The average compressive strength of experimental test results was 5502 psi after 28 days, and the modulus of elasticity of concrete was 4228.0 ksi.

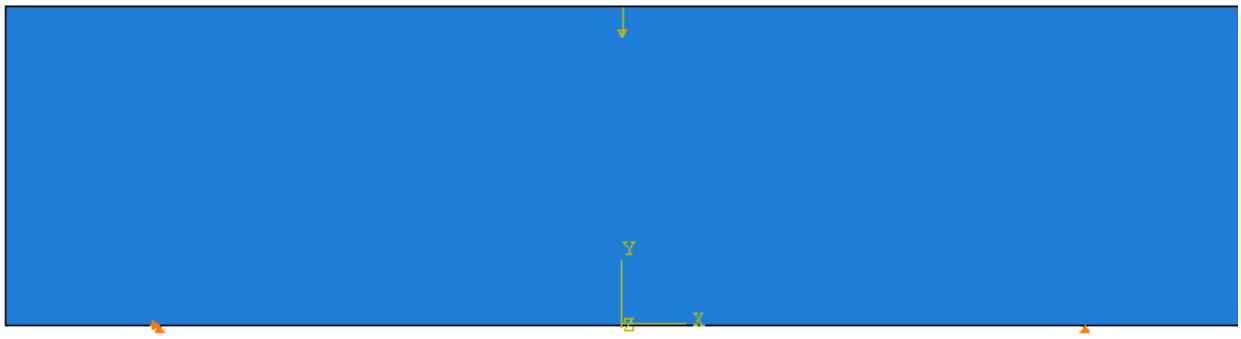

Figure 7.26: 2D Unstrengthened concrete beam model

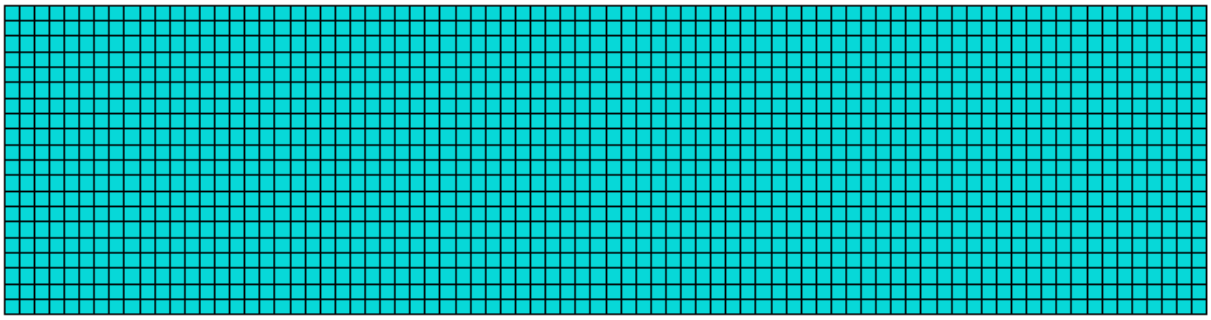

Figure 7.27: Unstrengthened concrete beam model meshing

By running the ABQUS-CAE software, the load started increase via steps and the section began deform until failed, figure 7.28 shows the crack propagation.

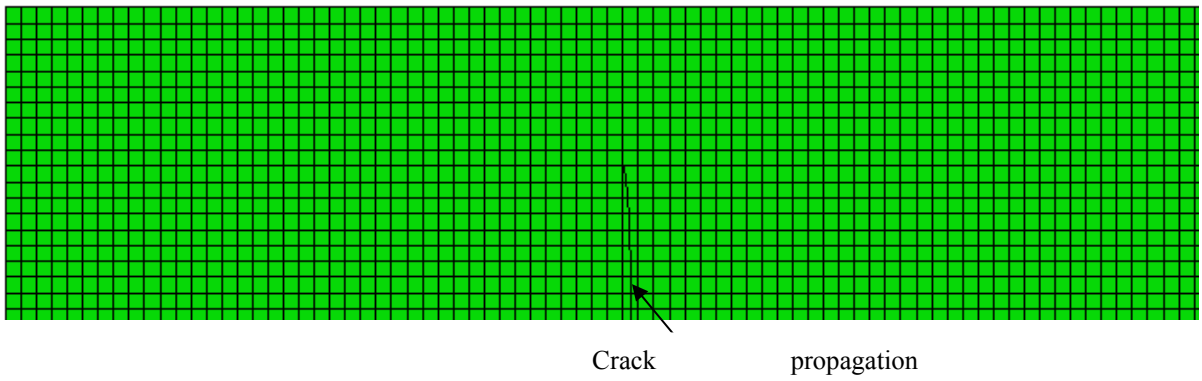

Figure 7.28: Crack propagation of unstrengthened concrete beam model

Figure 7.29 explains the typical crack shape of one model after exposure to 100^{o}C of temperature and 625 cycles, (the term CF in the legend means concentrated force). The crack started at the lowest node at mid-span then propagated gradually to the top of the section, the magnitude of the maximum flexural load was 3696.2 *lbs*. The mid-span deflection at maximum load was 0.002545″ (the term U_2 in the legend represents the vertical displacement "mid-span deflection", see figure 7.30).

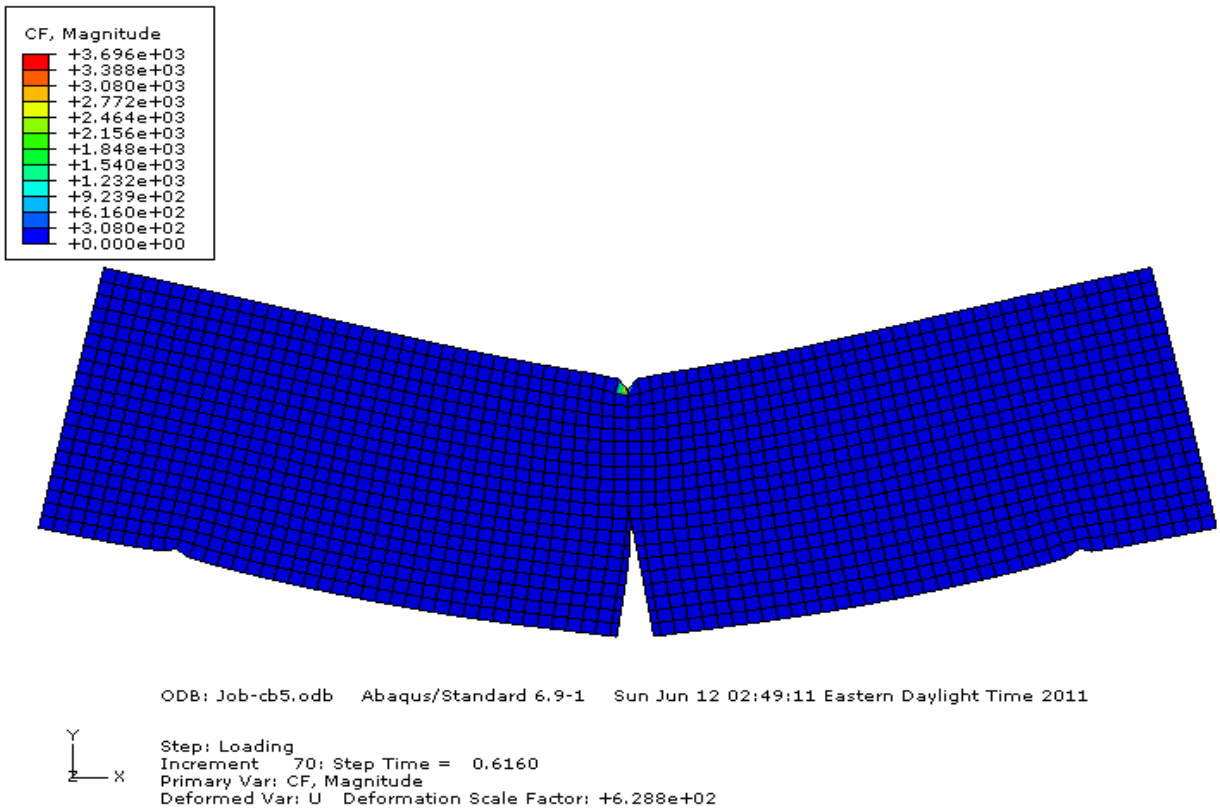

Figure 7.29: Unstrengthened concrete beam under flexural failure,(T=100^{o}C and Cy=625 cycles)

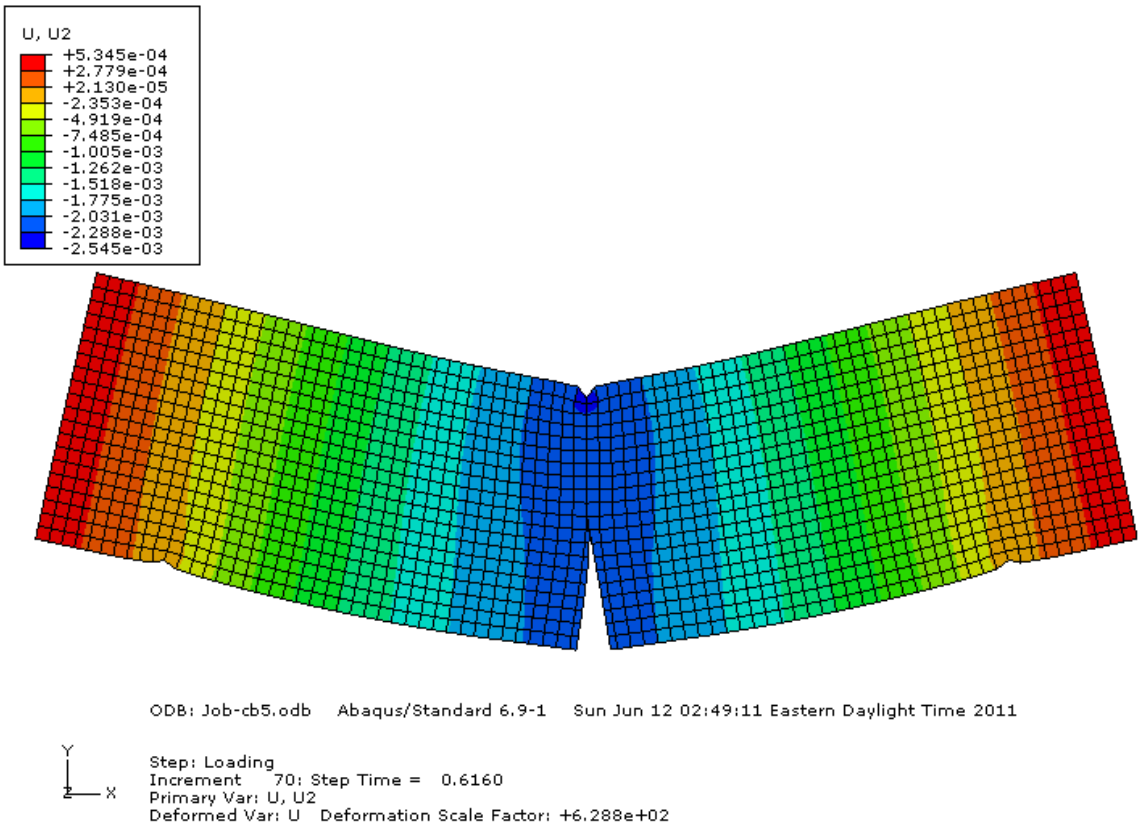

Figure 7.30: Maximum displacement of unstrengthened concrete beam (T=100^{o}C and Cy=625 cycles)

Table 7.9: Comparison of numerical failure load with experimental for FRP unstrengthened concrete beams

Temp ^{o}C	# 0f cycles	k_{Tc}	$k_{Tc}f'_c$ psi	$P_{(Num.)}$ lbs	$\delta_{(Num.)}$ in	Pe lbs	$\frac{P_e}{P_{(Num)}}$
RT	0	1	5502	2815.32	0.001802	3061.6	1.09
100	40	1.38	7592.76	4174.03	0.00284	-	-
	100	1.37	7537.74	4136.21	0.00283	4179.2	1.01
	250	1.38	7592.76	4174.03	0.00284	4348.5	1.04
	625	1.25	6877.5	3696.17	0.00254	3823.8	1.03
180	40	1.19	6547.38	3255.15	0.002098	-	-
	100	1.16	6382.32	3173.26	0.00199	3217.0	1.01
	250	1.07	5887.14	2836.01	0.001783	-	-
	350	1.04	5722.08	2777.43	0.00175	-	-
	625	0.9	4951.8	2531.11	0.01649	2795.0	1.10

The flexural load and mid-span deflection of non-strengthened concrete beam simulation at different environmental conditions of exposure compared to the experimental flexural load results are presented in table 7.9. The numerical results of flexural load was about 10% less than experimental results, which means the finite element model has been successful in prediction unstrengthened concrete beam failure load. A comparison between the experimental test results and the numerical results of the flexural load-number of cycles are plotted in figures (7.31 and 7.32).

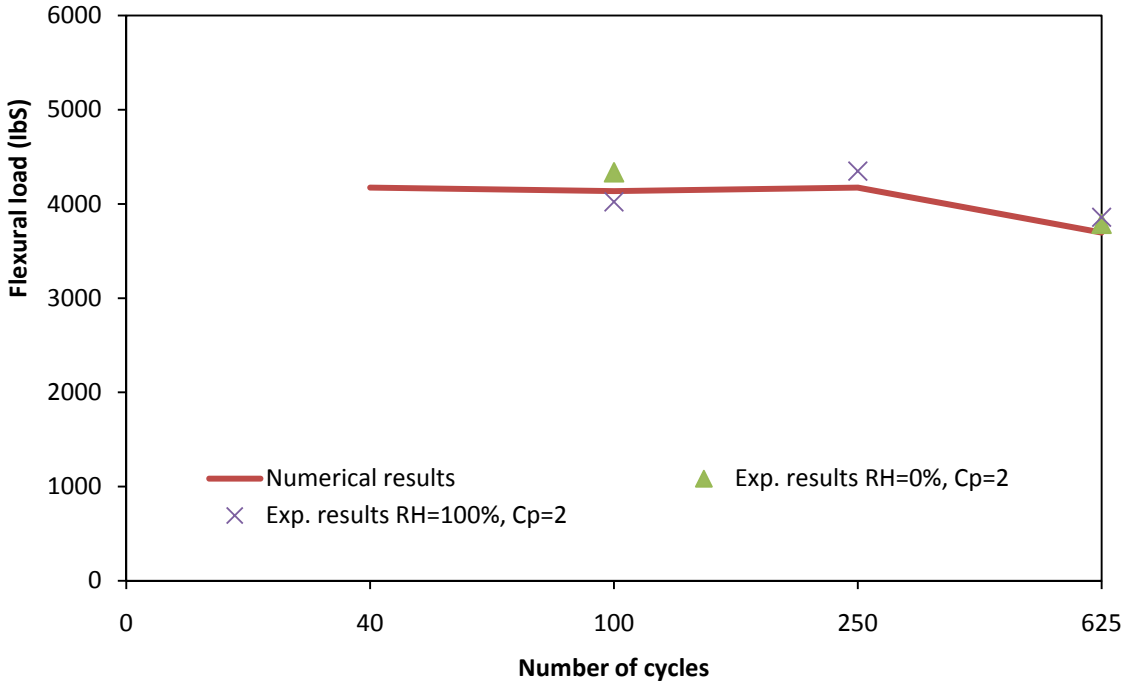

Figure 7.31: Numerical and experimental load/number of cycle curves of unstrengthened concrete beams, T=100^{o}C

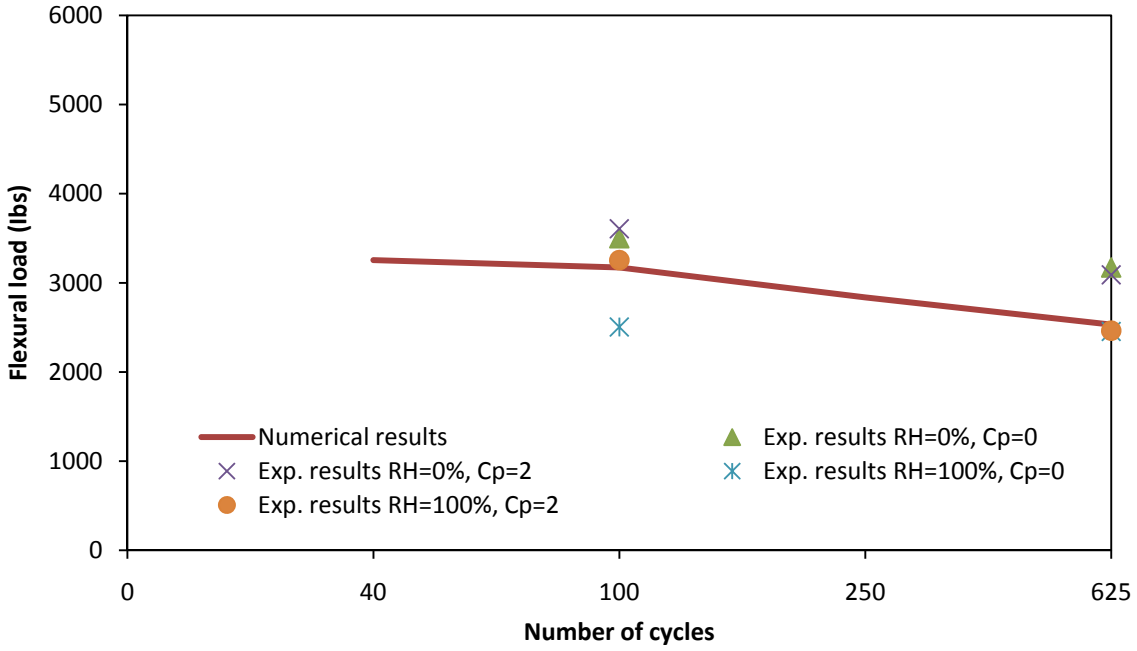

Figure 7.32: Numerical and experimental load/number of cycle curves of unstrengthened concrete beams, T=180^{o}C

7.4.2 Numerical Modeling of Non-Strengthened Concrete Columns

A three dimensional (3D) nonlinear extended finite-element (X-FE) model was developed to predict the behavior of concrete columns. The model was simulated based on the following assumptions. The model space was "3D", "deformable", and "solid". The section type was selected "homogeneous" and "Maxps Damage" was chosen as the type of damage. The total number of nodes was 790 nodes (see figure 7.33), the element type selected as "3D stress" and the element shape was chosen "quad-dominated-structured". The Poisson's ratio was assumed as equal to 0.18. The concrete failure ratio was 1.16, and concrete density equal to 0.0867 *lbs/in*^{3}. The average compressive strength of experimental test results was 5502 *psi* (38MPa) after 28 days, and the modulus of elasticity of concrete was 4228.0 *ksi*.

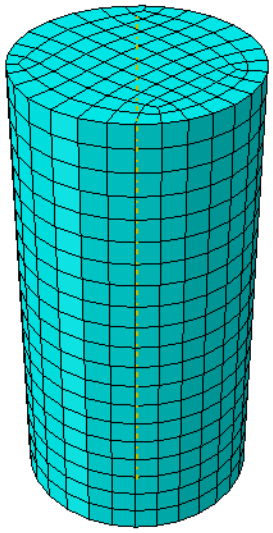

Figure 7.33: Meshing of 3-D unstrenghtened concrete column model

The results that are shown in table 7.10 and the pattern of compressive load and number of cycle curves (figures 7.34 and 7.35) indicate that the numerical model has a good prediction of compressive load compared to the experimental results. The maximum variation between numerical experimental results of compressive load was only 14%.

Table 7.10: Comparison of numerical failure load with experimental for FRP unstrengthened concrete columns

Temp.	Cy	k_{Tc}	$P_{(Num.)}$ lbs	Pe lbs	$\frac{P_e}{P_{(Num)}}$
RT	0	1.00	66914.0	69141.00	1.03
100	40	1.38	91413.0	-	-
	100	1.37	90329.0	-	-
	250	1.35	91413.0	103926.00	1.14
	625	1.25	82415.0	91781.00	1.11
180	40	1.19	78905.0		-
	100	1.16	76620.0	75787.96	0.99
	250	1.07	70603.0	-	-
	350	1.04	68672.0	-	-
	625	0.9	62498.0	67216.34	1.08

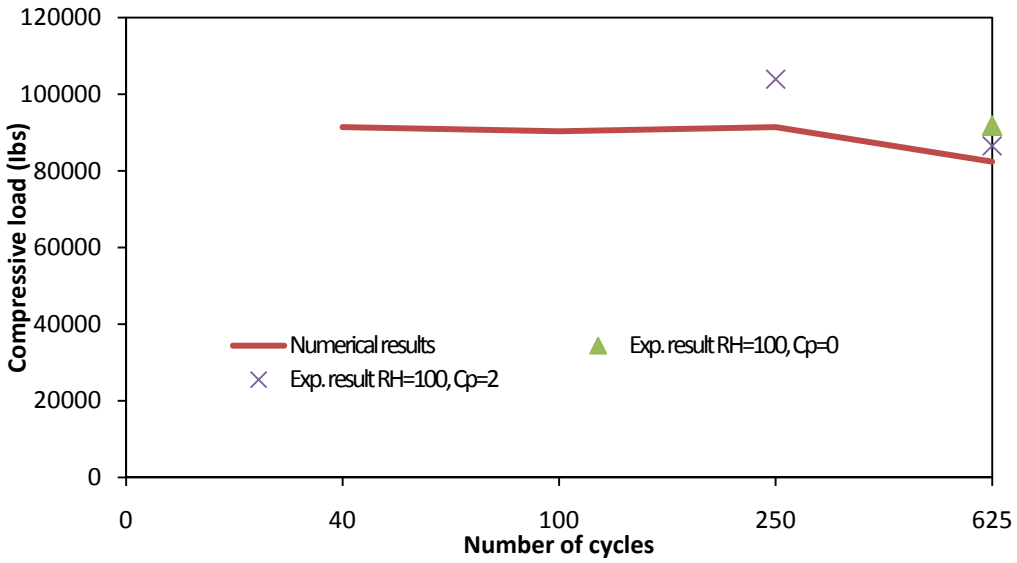

Figure 7.34: Numerical and experimental compressive load/number of cycle curves of unstrengthened concrete columns, T=100°C

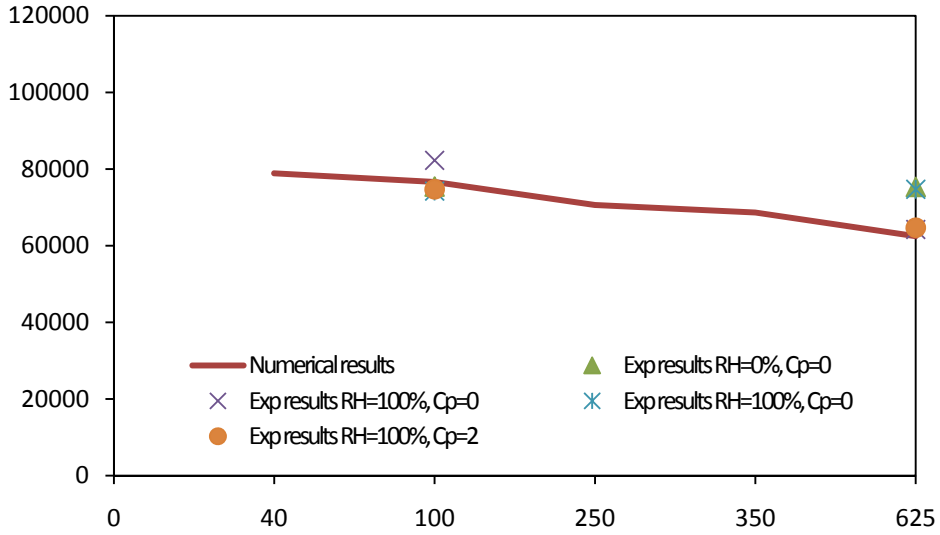

Figure 7.35: Numerical and experimental compressive load/number of cycle curves of unstrengthened concrete columns, T=180°C

7.4.3 Numerical Modeling of Epoxy Beams

ABAQUS-CAE software has been employed to simulate 2-D simply supported epoxy beam with size of 13″, 1.3″, and 0.6″ (total length, width, and depth) respectively. The distance

between the two supports was 9.6″ center to center. The concentrated load was applied at the mid-span of the simulation (see figure 7.36).

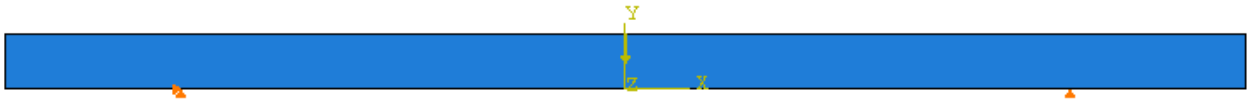

Figure 7.36: 2D planer Epoxy beam model (ABAQUS-CAE 6.9.1)

The section has been meshed by size where 0.12 was selected in vertical direction and 0.072 in the horizontal direction. The total number of nodes was 900, (see figure 7.37).

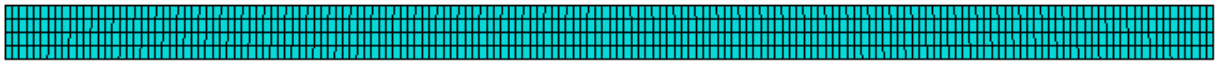

Figure 7.37: Epoxy beam meshed with 900 nodes (ABAQUS-CAE 6.9.1)

The mechanical properties of Tyfo-S saturant epoxy (see table 3.10) were utilized, and the temperature dependent factor k_{Tm} was taken into account. The Poisson's ratio was 0.3.

By clicking on the job function in ABAQUS-CAE software, the load began to increase by steps until the failure occur as shown in figure 7.38

Figure 7.38: The typical crack of epoxy beam (ABAQUS-CAE 6.9.1)

Figure 7.39 shows the flexural failure of one of the specimens before complete failure, while figure 7.40 shows the maximum deflection of the specimen prior to complete failure.

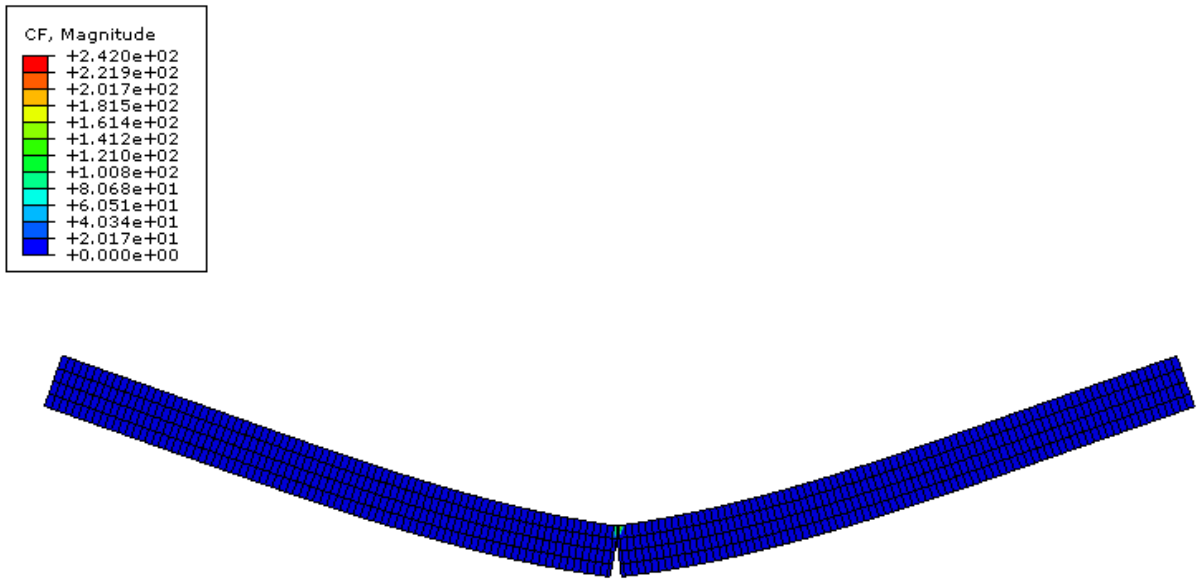

Figure 7.39: Flexural failure of epoxy beam at RT

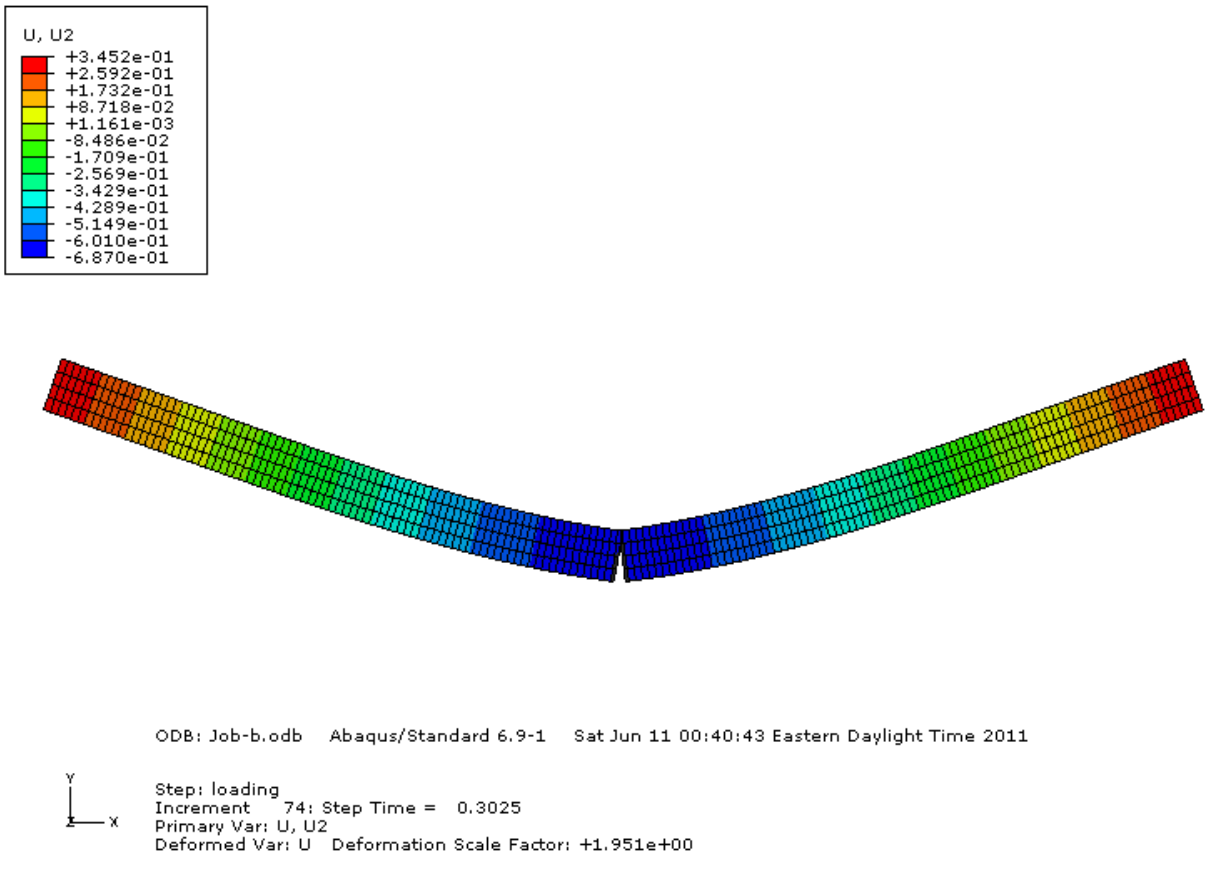

Figure 7.40: Maximum displacement of epoxy beam at RT

Table 7.11 represents the maximum flexural load of the numerical solution compared to the experimental results. Except the result of 180°C of temperature after 250 cycles of exposure, all the numerical results and experimental results are close to matching. The variation between the numerical results and experimental results at 180°C of temperature and 250 cycles might be due to some errors in the experimental test, or some changing in the material behavior that cannot be predicted in the numerical analysis.

Table 7.11: Comparison of Numerical failure load solution with Experimental results for epoxy beams

Temp °C	# 0f cycles	k_{Tm}	$P_{(Num.)}$ lbs	Pe lbs	$\frac{P_e}{P_{(Num)}}$
RT	0	1	242.00	242.99	1.00
	40	1.05	253.60	264.94	1.04
	100	1.12	268.70	273.34	1.02
	250	1.25	310.60	333.61	1.07
	625	1.42	351.50	335.91	0.96
100	40	1.41	334.00	343.53	1.03
	100	1.4	331.70	354.10	1.07
	250	1.38	326.80	384.83	1.18
	625	1.11	266.80	226.62	0.85
180	40	0.88	152.50	166.62	1.09
	100	0.776	141.50	142.30	1.01
	250	0.602	134.40	213.53	1.59
	350	0.44	112.00	130.5642	1.17

Figures 7.41 to 7.43 show a comparison of the flexural load- number of cycle curves between the numerical and experimental results at standard lab conditions, after 100°C, and 180°C of temperature respectively.

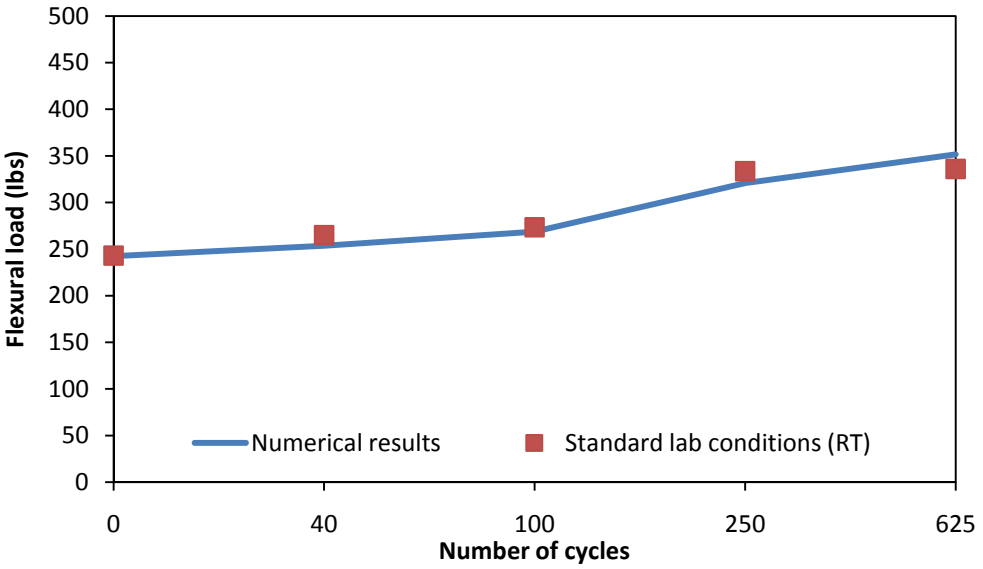

Figure 7.41: Numerical and experimental load/number of cycle curves of epoxy beams at RT

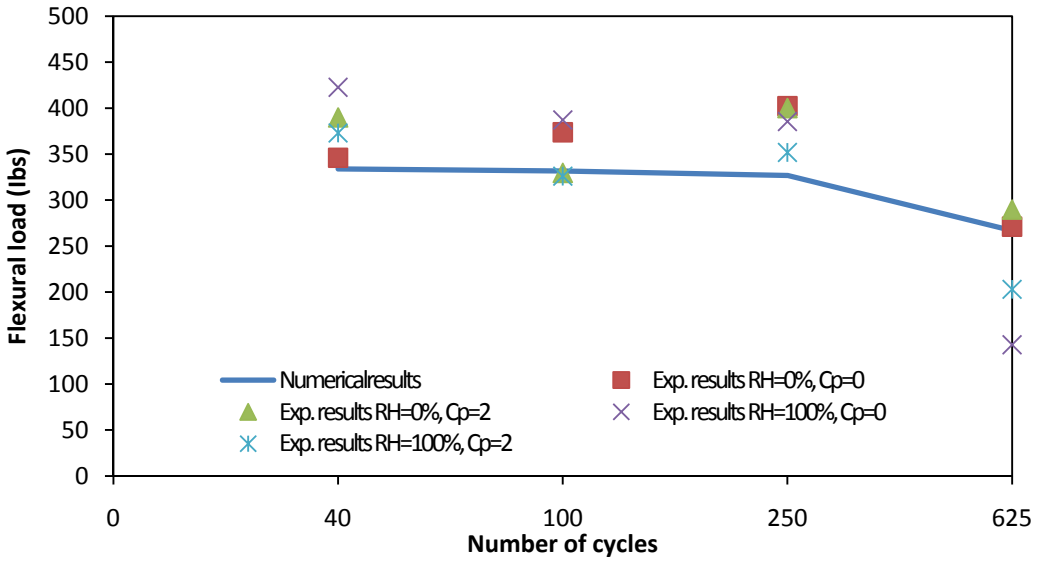

Figure 7.42: Numerical and experimental load/number of cycle curves of epoxy beams, T=100^{o}C

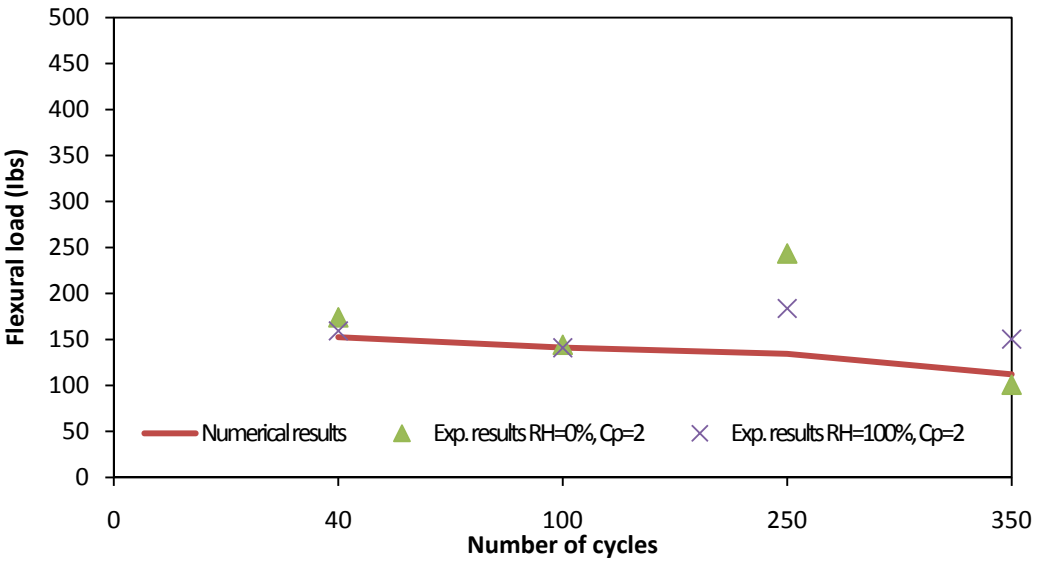

Figure 7.43: Numerical and experimental load/number of cycle curves of epoxy beams, T=180^{o}C

7.4.4 Numerical Modeling of FRP Strengthened Concrete Beams

The same procedures that were performed to model unstrengthened concrete beams have been followed here to obtain the numerical results of strengthened concrete beams. In this case, the model consists of two parts, the first part was the concrete beam and the second one was the FRP sheet. Two types of material properties were input to the ABAQUS-CAE; the first set of material properties was for concrete (first part), which applied the same data that were used for unstrengthened concrete beams, while the mechanical properties of FRP composite (second part) were used based on the data of table 7.3 and the other mechanical properties provided by the manufacture (see table 3.9). The two parts of 2D simulation were meshed by size; the total number of nodes was 451, as showing in figure 7.44 (the FRP part of the model does not clearly appear on the figure because its mesh thickness is very small compared to the concrete part). The concrete crack propagation is shown in figure 7.45.

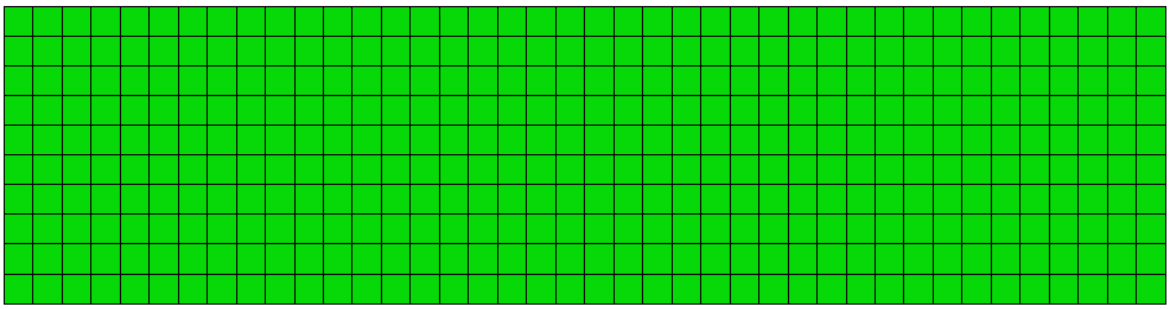

Figure 7.44: Strengthened concrete beam model meshed with 451 nodes

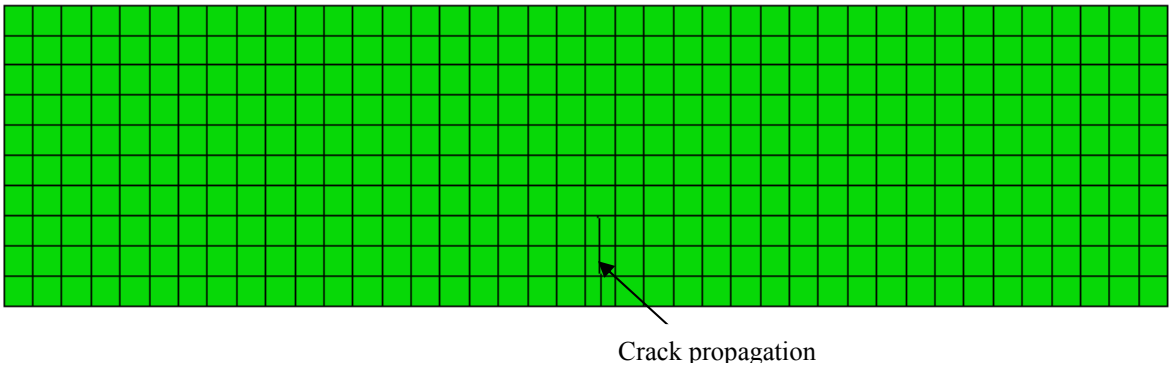

Figure 7.45: Crack propagation of strengthened concrete beam model

All prediction models at standard lab conditions and 100^{o}C of temperature showed that the mode of failure was FRP rupture; the crack began at the lowest point of the concrete part almost at the center and spread up proximately to the third of the section's height, and then propagated down to cut the FRP part. Figure 7.46 represents the failure mode of one beam at standard lab conditions and the number of cycles was zero (the control specimen), where the failure load was equal to 3761.2 *lbs* and the mid span deflection at the maximum failure load was equal 0.002262″. Figure 7.47 shows the mid-span deflection at the maximum flexural load.

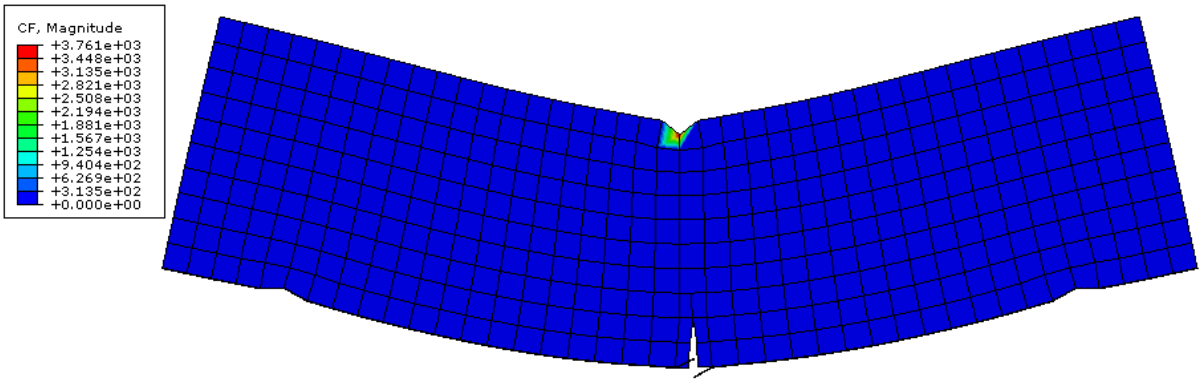

Figure 7.46: FRP rupture of strengthened concrete beam at RT

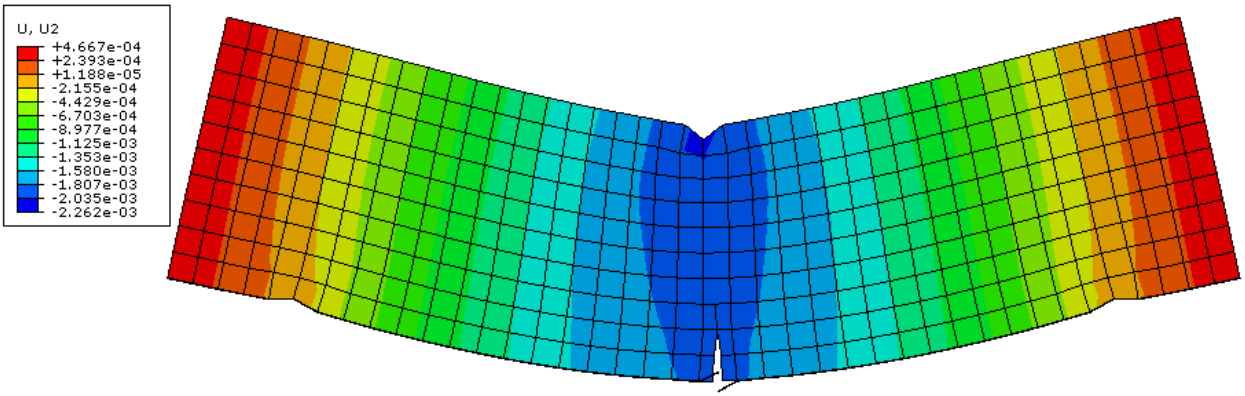

Figure 7.47: Maximum displacement of strengthened concrete beam at RT

The predictions for the 180^{o}C show that the mode of failures was FRP delamination for all number of cycles. The FRP delamination started at the center of the model and then spread to the both beam ends. (see figure 7.48a and 7.48b). The way of FRP delamination in the simulation was almost similar to the mode that was observed during the experimental tests.

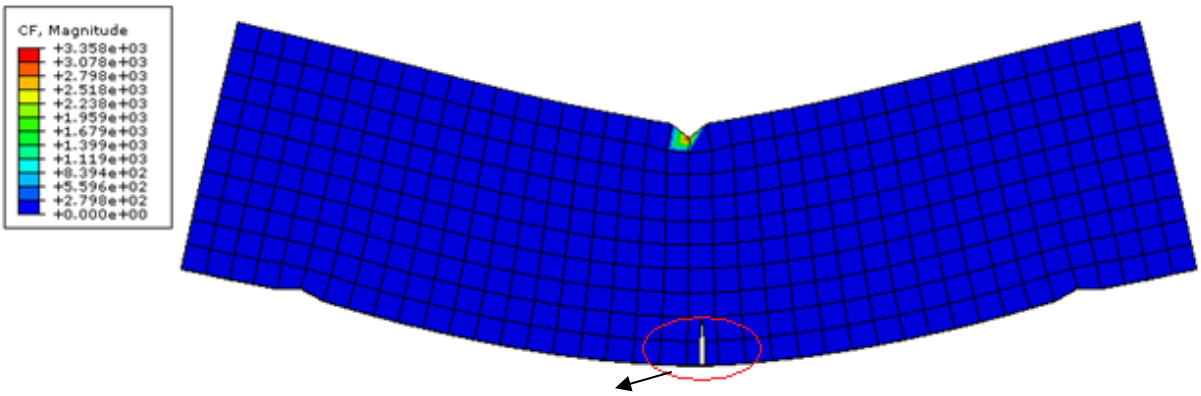

see figure 7.48b

(a)

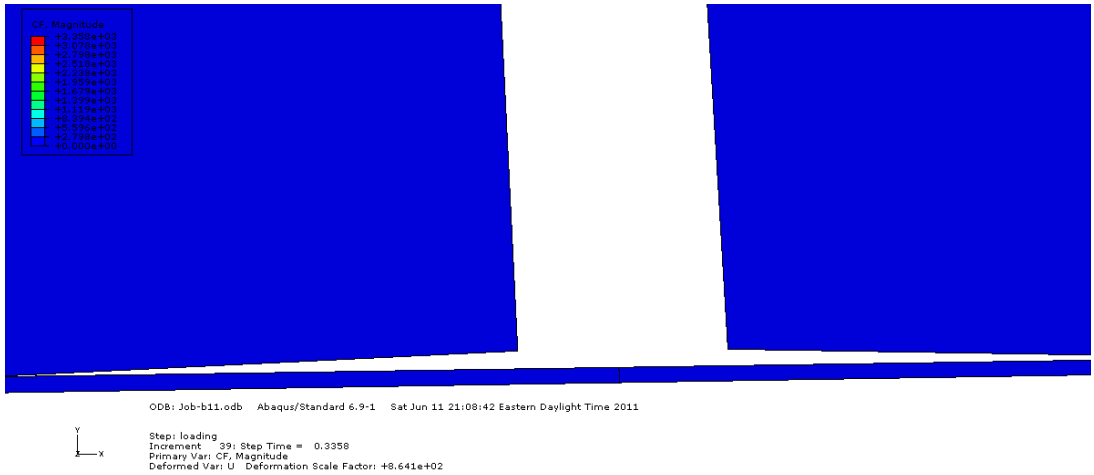

(b)

Figure 7.48: FRP delamination of strengthened concrete beam (T=180^{o}C and Cy=100)

The numerical solutions of the maximum flexural load compared to the experimental results are presented in tables 7.12, as well as the numerical mid-span deflection at the maximum load. The comparison shows that the numerical and experimental results close to each other.

Table 7.12: Comparison of numerical failure load solution with experimental results for FRP strengthened beams

Temp °C	# 0f cycles	k_{Tc}	k_{Tm}	$\delta_{(Num.)}$ in	$P_{(Num.)}$ lbs	Pe lbs	$\frac{P_e}{P_{(Num)}}$
RT	0	1.00	1	0.002262	3761.20	3849.35	1.02
	40	1.00	1.05	0.002577	4018.30	4110.00	1.02
	100	1.00	1.12	0.002576	4061.17	4170.00	1.03
	250	1.00	1.25	0.002707	4313.08	4445.00	1.03
	625	1.00	1.42	0.002691	4318.40	4538.00	1.05
100	40	1.38	1.41	0.002437	4191.80	4215.50	1.01
	100	1.37	1.4	0.002448	4190.40	4632.25	1.11
	250	1.35	1.38	0.002472	4185.35	4679.75	1.12
	625	1.25	1.11	0.002447	3956.21	4725.00	1.19
180	40	1.19	0.88	0.002236	3859.03	3885.25	1.01
	100	1.16	0.776	0.001852	3358.12	3399.75	1.01
	250	1.07	0.602	0.001779	3027.58	3058.75	1.01

A comparison between the numerical and experimental results is presented by the relationship of maximum flexural load and number of cycles in figures (7.49 to 7.51).

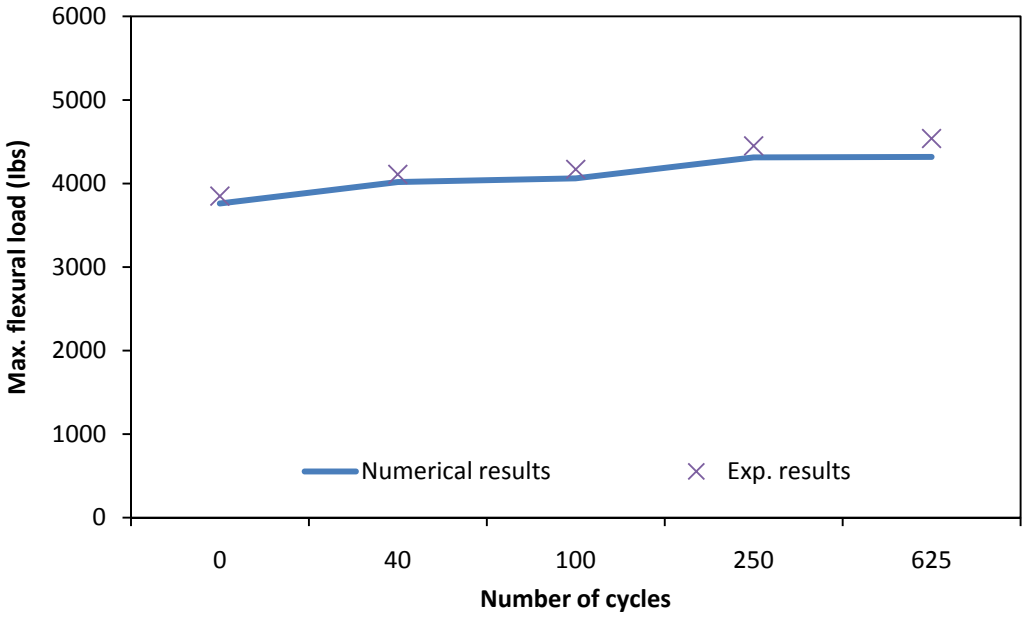

Figure 7.49: Numerical and experimental load/number of cycle curves of strengthened concrete beams at RT

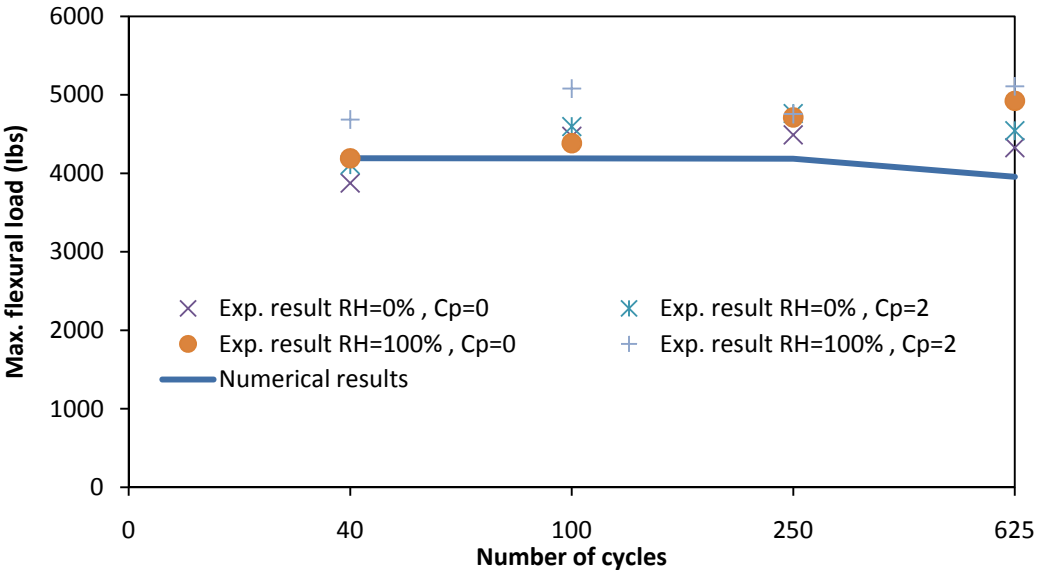

Figure 7.50: Numerical and experimental load/number of cycle curves of strengthened concrete beams, T=100°C

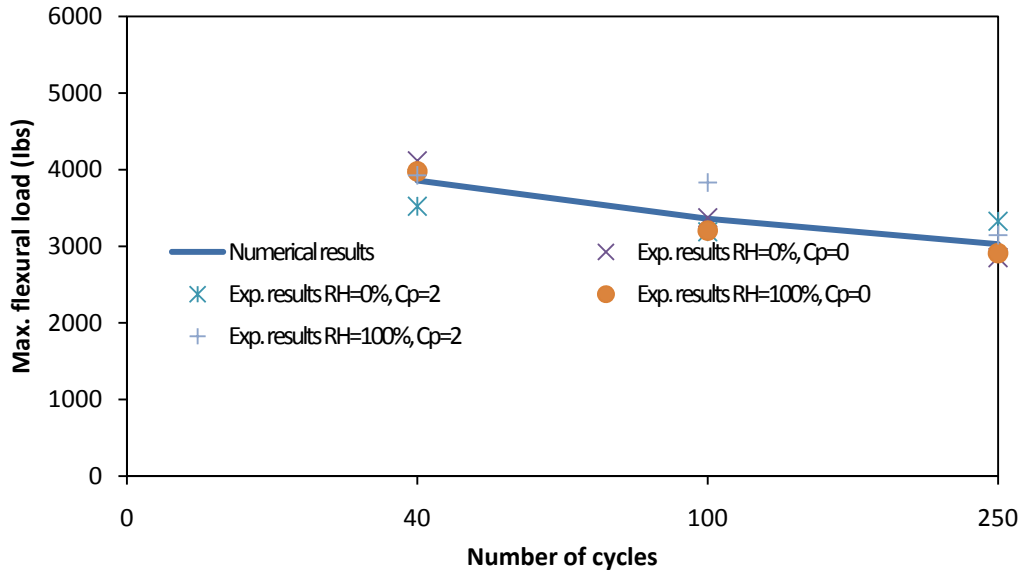

Figure 7.51: Numerical and experimental load/number of cycle curves of strengthened concrete beams, T=180°C

7.4.4 Numerical Modeling of FRP Strengthened Concrete Columns

ABAQUS-CAE software was adopted for predicting the compressive load, displacement response, and the mode of failure of strengthened columns numerically. The mesh model defined

810 nodes for the concrete part and 630 nodes for the FRP strengthening part (see figure 7.52). The same material properties which were used in the unstrenghtened concrete columns were used here in the concrete part. As for the FRP part, the same material properties that were used for the strengthened concrete beams have been used here.

By running the software, the pressure began to increase by steps until the failure occurred and the FRP rupture showed up (see figure7.53). In the case of columns, where the concrete is confided with the FRP sheets that makes it difficult to observe the concrete crack before the FRP fails during testing.

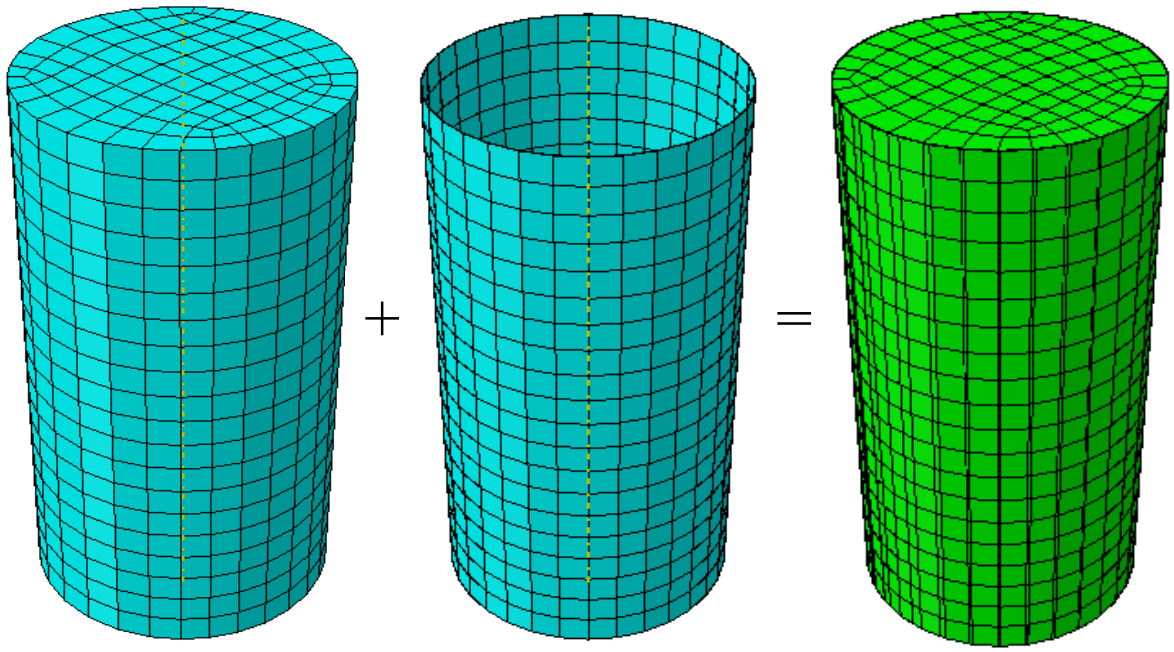

a) Concrete part b) FRP part c) FRP strengthened concrete model

Figure 7.52: Meshing of strengthened concrete column model

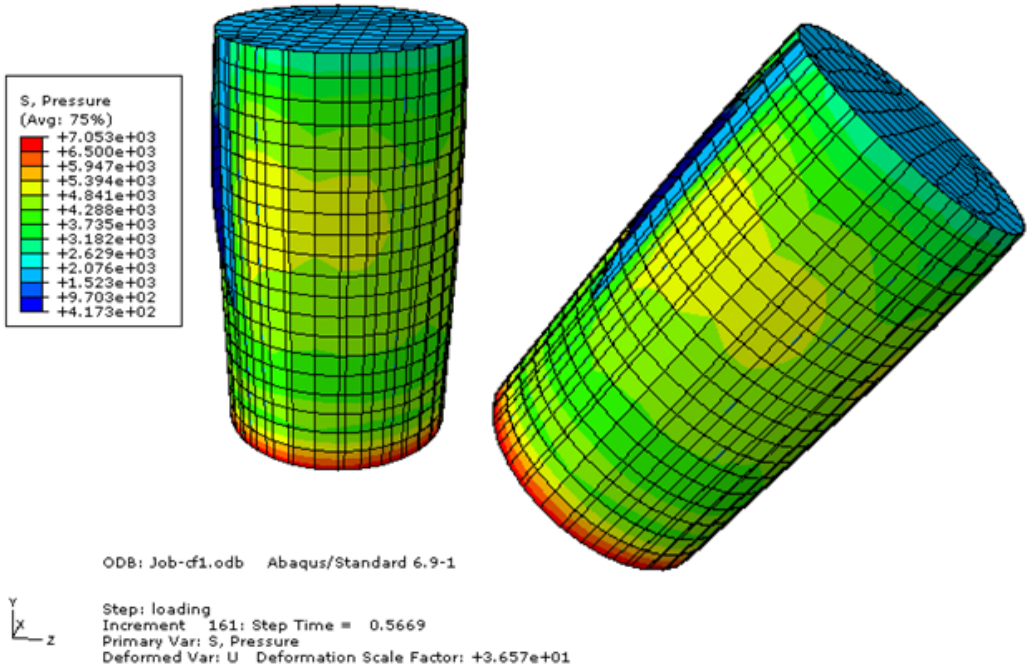

Figure 7.53: FRP rupture of strengthened concrete column

The simulated compressive loads of non-strengthened concrete columns at different environmental conditions of exposure comparing with the experimental compressive load results are presented in table 7.13. The numerical results of flexural load was about 13% less than experimental results after 500 hours of aging at the standard lab conditions, this difference between the prediction and experimental results was further reduced by increasing temperature and the time of exposure, and which means the finite element model has been reliable in predicting the behavior strengthened concrete columns failure load. A comparison between the experimental test results and the numerical results of the flexural load-number of cycles are plotted in figures 7.54 to7.56.

Table 7.13: Comparison of numerical failure load solution with experimental results for FRP strengthened columns

Temp.	Cy	k_{Tc}	k_{Tm}	$P_{(Num.)}$ lbs	Pe lbs	$\frac{P_e}{P_{(Num)}}$
RT	0	1.00	1	85371.19	96101.00	1.13
	40	1.00	1.05	86238.58	92304.75	1.07
	100	1.00	1.12	88628.00	95877.00	1.08
	250	1.00	1.25	90020.95	102970.00	1.14
	625	1.00	1.42	93224.12	105759.00	1.13
100	40	1.38	1.41	98310.54	108187.00	1.10
	100	1.37	1.4	97794.45	-	-
	250	1.35	1.38	91592.37	-	-
	625	1.25	1.11	84958.67	91664.10	1.08
180	40	1.19	0.88	80027.91	83159.60	1.04
	100	1.16	0.776	77326.76	77003.10	1.00
	250	1.07	0.602	74485.37	70029.80	0.94

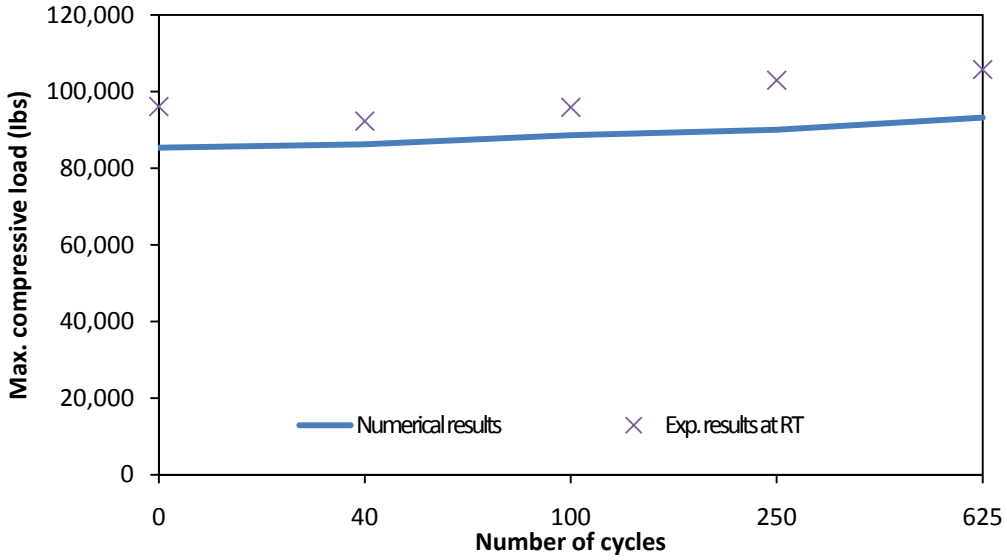

Figure 7.54: Numerical and experimental load/number of cycle curves of strengthened concrete columns at RT

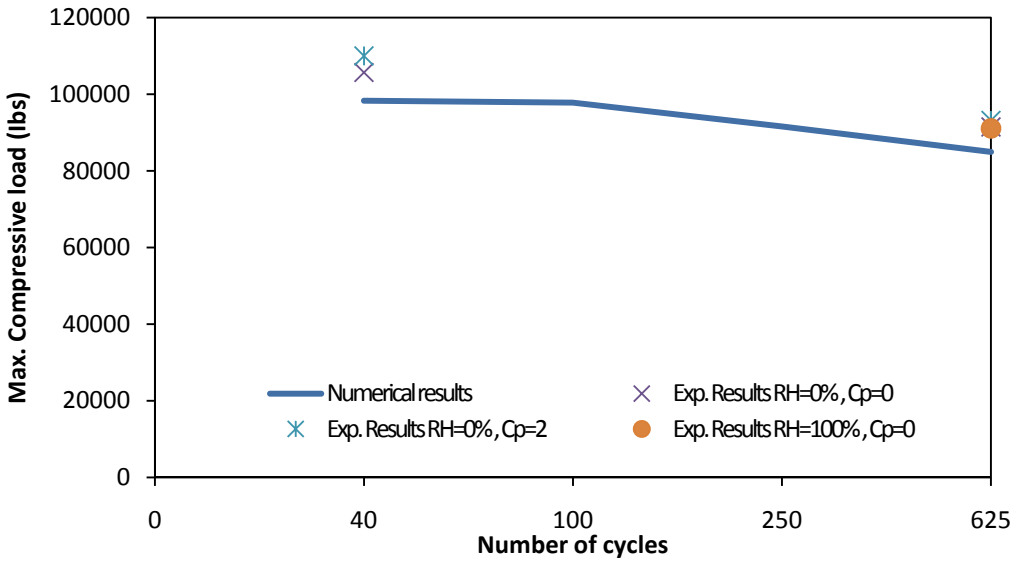

Figure 7.55: Numerical and experimental load/number of cycle curves of strengthened concrete columns, T=100°C

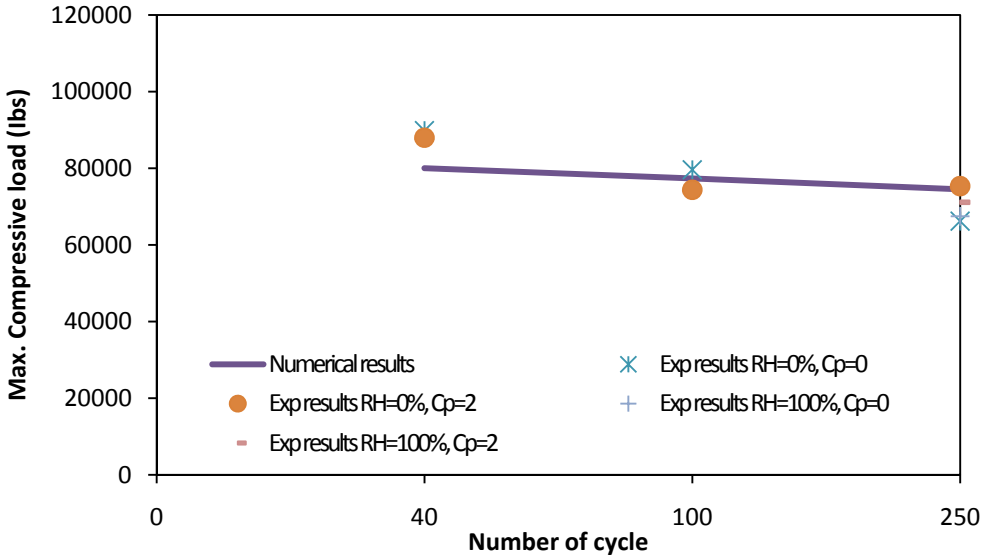

Figure 7.56: Numerical and experimental load/number of cycle curves of strengthened concrete columns, T=180°C

7.5 Comparison among Analytical, Numerical, and Experimental Results

7.5.1 Non-Strengthened Concrete Beams

Table 7.14: Comparison of flexural loads among analytical, numerical, and experimental results for concrete beams

Temp °C	# 0f cycles	$P_{(Analy.)}$ lbs	$P_{(Num.)}$ lbs	Pe lbs	$\frac{P_e}{P_{(Analy)}}$	$\frac{P_e}{P_{(Num)}}$
RT	0	2234.31	2815.32	3061.60	1.37	1.09
100	40	3083.35	4174.03	-	-	-
	100	3061.00	4136.21	4179.20	1.37	1.01
	250	3083.35	4174.03	4348.50	1.41	1.04
	625	2792.89	3696.17	3823.80	1.37	1.03
180	40	2658.83	3255.15	-	-	-
	100	2591.80	3173.26	3217.00	1.24	1.01
	250	2390.71	2836.01	-	-	-
	350	2323.68	2777.43	-	-	-
	625	2010.88	2531.11	2795.00	1.39	1.10

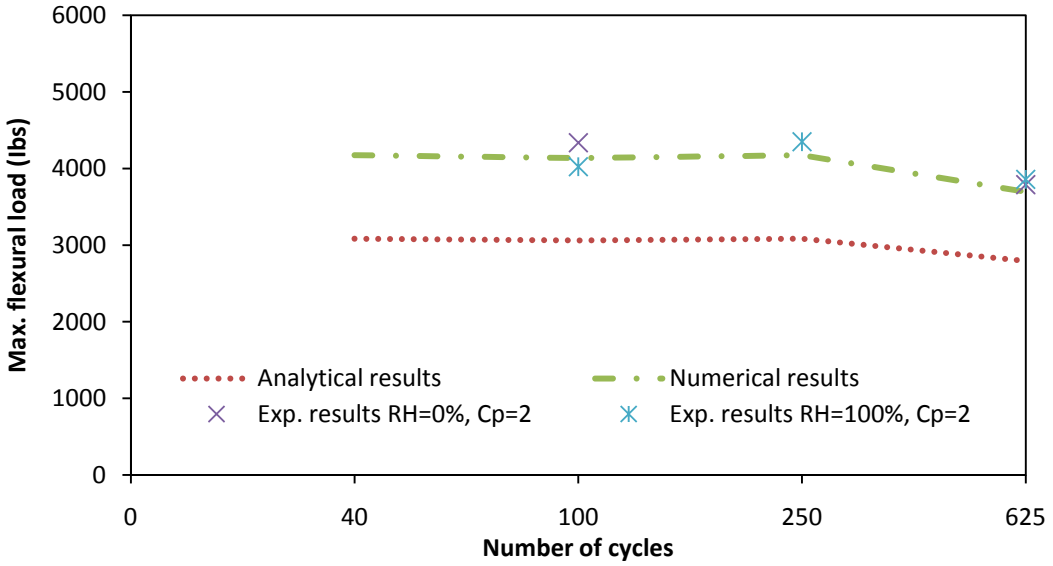

Figure 7.57: Flexural load-number of cycle curves unstrengthened concrete beams, T=100°C

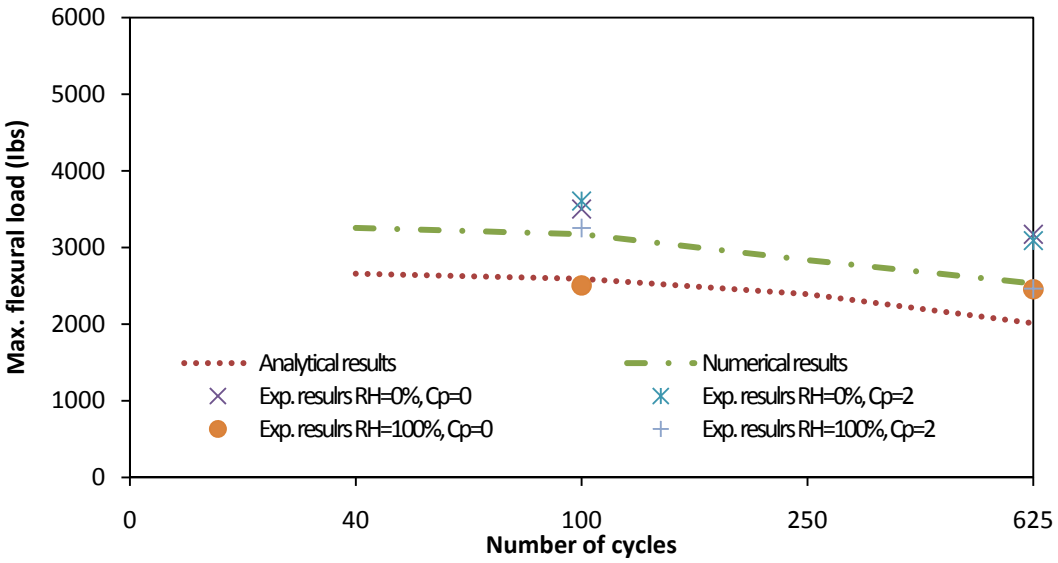

Figure 7.58: Flexural load-number of cycle curves unstrengthened concrete beams, T=180°C

7.5.2 Non-Strengthened Concrete Columns

Table 7.15: Comparison of compressive loads among analytical, numerical, and experimental results for concrete columns

Temp (°C)	Cy	$P_{(Analy.)}$ [a] lbs	$P_{(Analy.)}$ [b] lbs	$P_{(Num.)}$ [c] lbs	Pe [d] lbs	$\frac{P_e}{P_{(Analy1)}}$	$\frac{P_e}{P_{(Analy2)}}$	$\frac{P_e}{P_{(Num)}}$
RT	0	58767.4	69138.1	66914.	69141.0	1.18	1.0	1.03
100	40	81099.0	95410.6	91413.	-	-		-
	100	80511.4	94719.2	90329.	-	-		-
	250	81099.0	95410.6	91413.	103926.	1.28	1.09	1.14
	625	73459.3	86422.6	82415.	91781.0	1.25	1.06	1.11
180	40	69933.2	82274.3	78905.	-	-		-
	100	68170.2	80200.2	76620.	75787.9	1.11	0.94	0.99
	250	62881.1	73977.8	70603.	-	-		-
	350	61118.1	71903.6	68672.	-	-		-
	625	52890.7	62224.3	62498.	67216.3	1.27	1.08	1.08

[a]=analytical ultimate load using ACI318-code ϕ=0.85
[b] =analytical ultimate load using ACI318-code ϕ=1.0
[c] = Numerical failure load
[d]= Experimental failure load

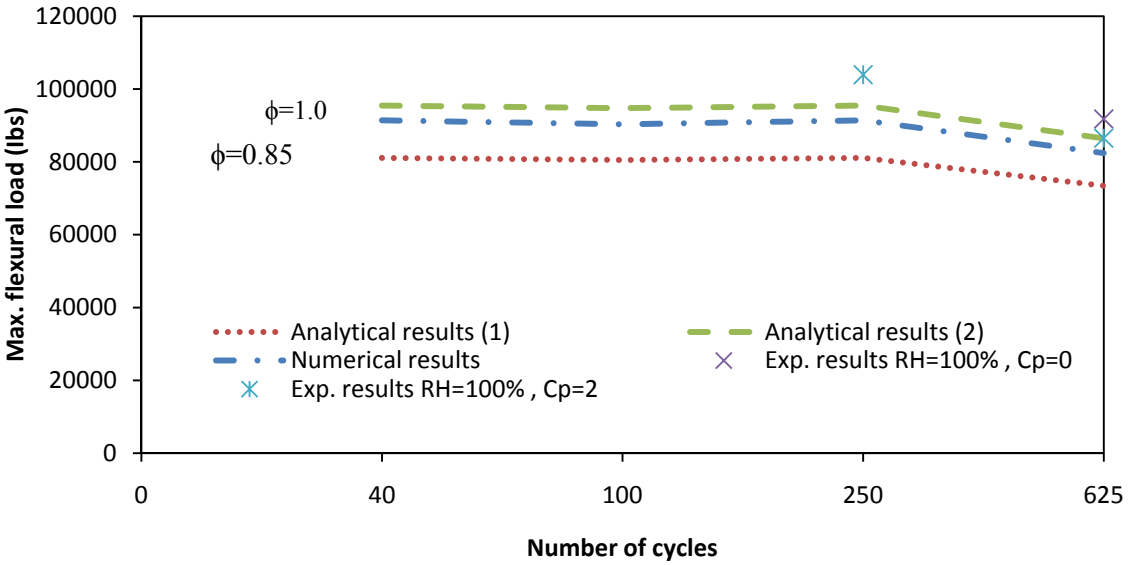

Figure 7.59: Compressive failure load-number of cycle curves for unstrengthened concrete columns, T=100°C

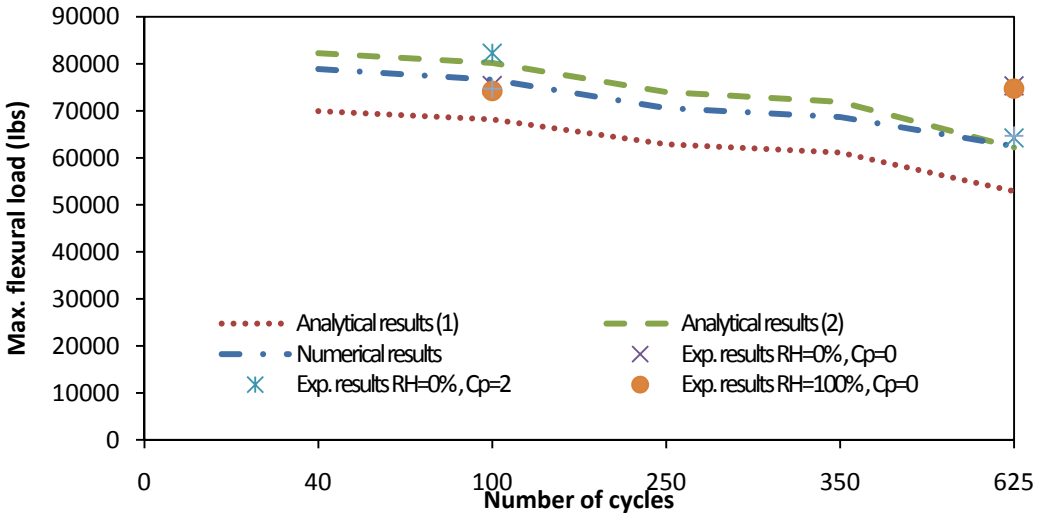

Figure 7.60: Compressive failure load-number of cycle curves for unstrengthened concrete columns, T=180°C

7.5.3 Epoxy Beams

Table 7.16: Comparison of failure flexural loads among analytical, numerical, and experimental results for epoxy beams

Temp °C	# 0f cycles	$P_{(Analy.)}$ lbs	$P_{(Num.)}$ lbs	Pe lbs	$\frac{P_e}{P_{(Analy)}}$	$\frac{P_e}{P_{(Num)}}$
RT	0	242.99	242.00	242.99	1.00	1.00
	40	255.14	253.60	264.94	1.04	1.04
	100	272.14	268.70	273.34	1.00	1.02
	250	303.73	310.60	333.61	1.10	1.07
	625	345.04	351.50	335.91	0.97	0.96
100	40	342.61	334.00	343.53	1.00	1.03
	100	340.18	331.70	354.10	1.04	1.07
	250	335.32	326.80	384.83	1.15	1.18
	625	269.71	266.80	226.62	0.84	0.85
180	40	213.83	152.50	166.62	0.78	1.09
	100	188.56	141.50	142.30	0.75	1.01
	250	146.28	134.40	213.53	1.46	1.59
	350	107.16	112.00	130.5642	1.22	1.17

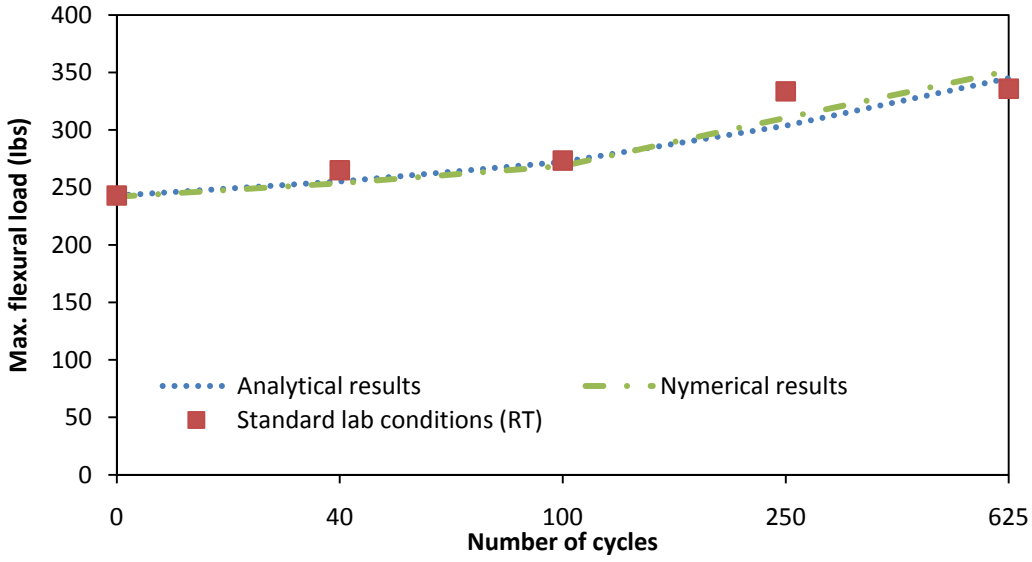

Figure 7.61: Flexural failure load-number of cycle curves for epoxy beams at RT

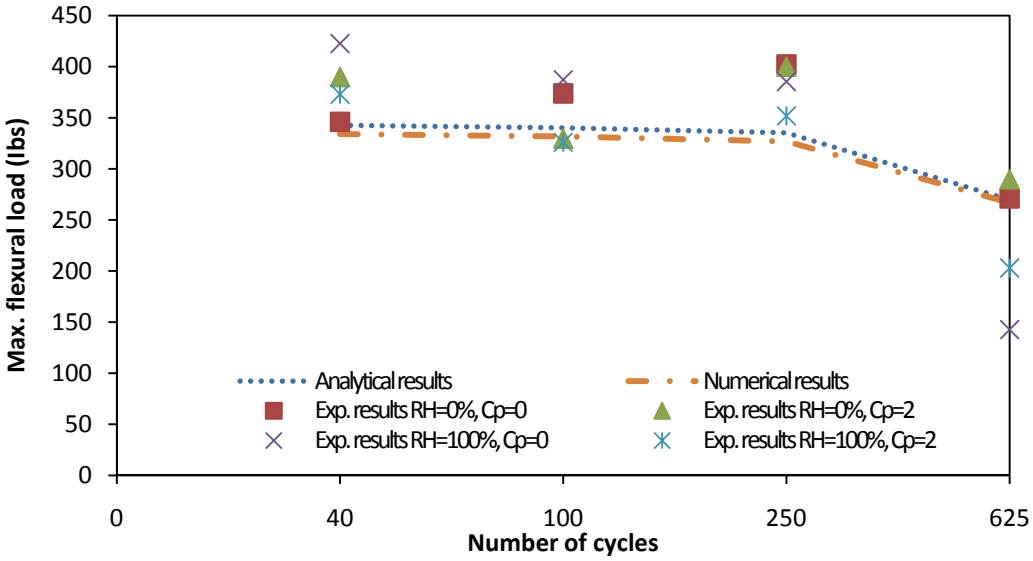

Figure 7.62: Flexural failure load-number of cycle curves for epoxy beams T=100^{o}C

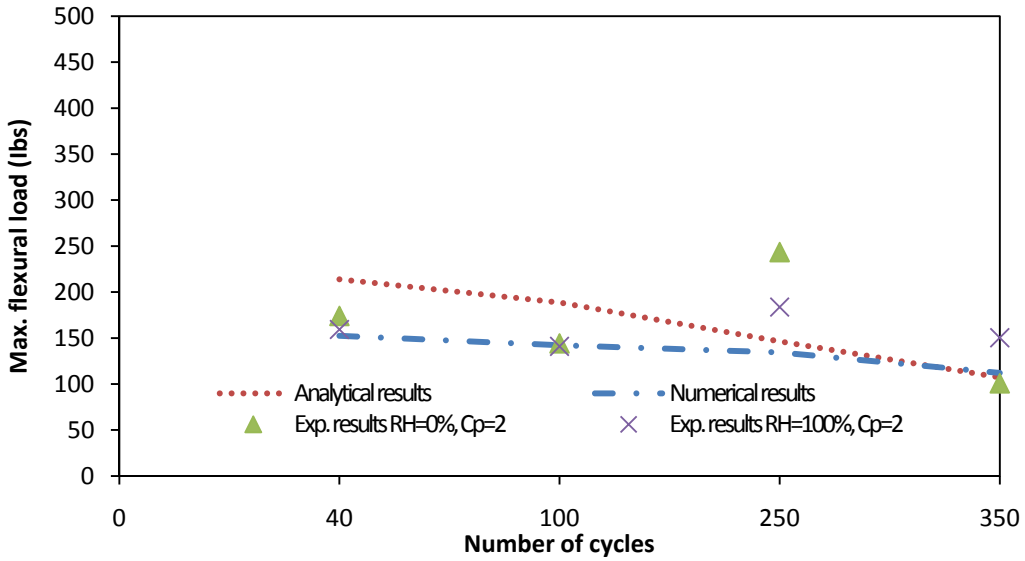

Figure 7.63: Flexural failure load-number of cycle curves for epoxy beams T=180^{o}C

7.5.4 FRP Strengthened Concrete Beams

Table 7.17: Comparison of failure flexural loads among analytical, numerical, and experimental results for strengthened concrete beams

Temp °C	# 0f cycles	$P_{(Analy.)}$ lbs	$P_{(Num.)}$ lbs	Pe lbs	$\frac{P_e}{P_{(Analy)}}$	$\frac{P_e}{P_{(Num)}}$
RT	0	2905.8	3761.20	3849.35	1.32	1.02
	40	2923.3	4018.30	4110.00	1.41	1.02
	100	2947.8	4061.17	4170.00	1.41	1.03
	250	2993.3	4313.08	4445.00	1.48	1.03
	625	3052.7	4318.40	4538.00	1.49	1.05
100	40	3057.7	4191.80	4215.50	1.38	1.01
	100	3054	4190.40	4632.25	1.52	1.11
	250	3046.6	4185.35	4679.75	1.54	1.12
	625	2950	3956.21	4725.00	1.60	1.19
180	40	2868.1	3859.03	3885.25	1.35	1.01
	100	2831	3358.12	3399.75	1.20	1.01
	250	2768	3027.58	3058.75	1.11	1.01

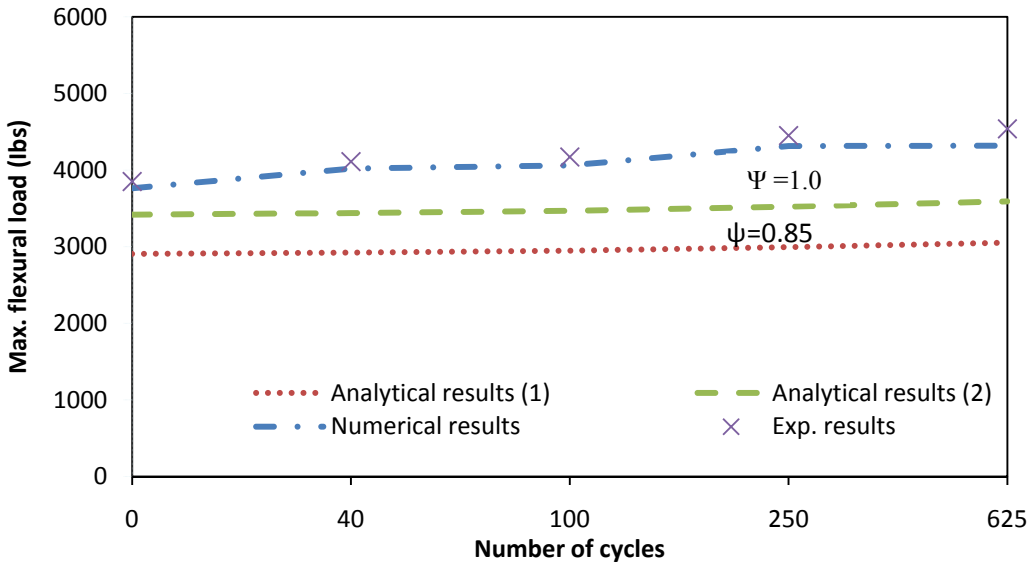

Figure 7.64: Flexural failure load-number of cycle curves for strengthened concrete beams at RT

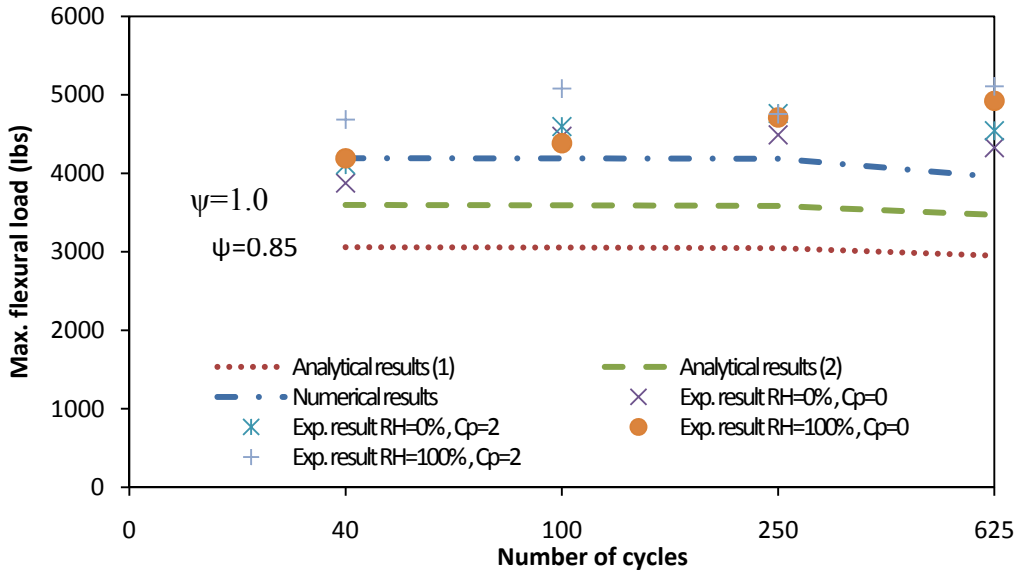

Figure 7.65: Flexural failure load-number of cycle curves for strengthened concrete beams, T=100°C

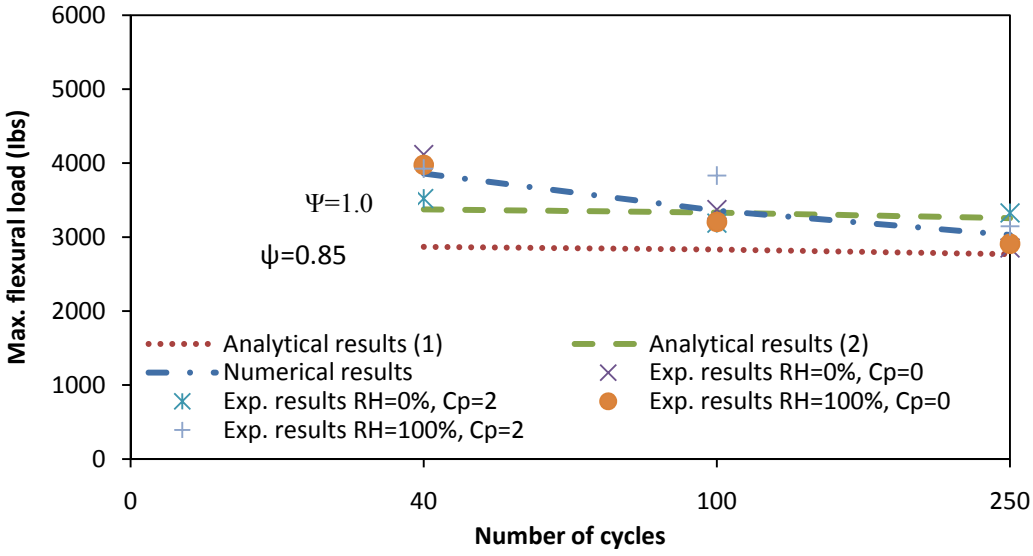

Figure 7.66: Flexural failure load-number of cycle curves for strengthened concrete beams, T=180°C

7.5.5 FRP strengthened concrete columns

Table 7.18: Comparison of failure Compressive loads among analytical, numerical, and experimental results for strengthened concrete columns

Temp.	Cy	$P_{(Analy.)}$[a] lbs	$P_{(Analy.)}$[b] lbs	$P_{(Num.)}$[c] lbs	Pe[d] lbs	$\frac{P_e}{P_{(Analy)}}$	$\frac{P_e}{P_{(Num)}}$
RT	0	70568.00	74282.1	85371.19	96101.00	1.36	1.13
	40	70623.00	7434.0	86238.58	92304.75	1.31	1.07
	100	70700.00	74421.0	87994.97	95877.00	1.36	1.09
	250	70844.00	74572.6	90020.95	102970.00	1.45	1.14
	625	71032.00	74770.5	93224.12	105759.00	1.49	1.13
100	40	71021.00	74758.9	98310.54	108187.00	1.52	1.10
	100	92054.00	96898.9	97794.45	-	-	-
	250	90898.00	95682.1	91592.37	-	-	-
	625	84919.00	89388.4	84958.67	91664.10	1.08	1.08
180	40	81251.00	85527.3	80027.91	83159.60	1.02	1.04
	100	79429.00	83609.4	77326.76	77003.10	0.97	1.00
	250	74114.00	78014.7	74485.37	70029.80	0.94	0.94

[a]=analytical ultimate load using ACI318-code ϕ=0.85
[b] =analytical ultimate load using ACI318-code ϕ=1.0
[c] = Numerical failure load
[d]= Experimental failure load

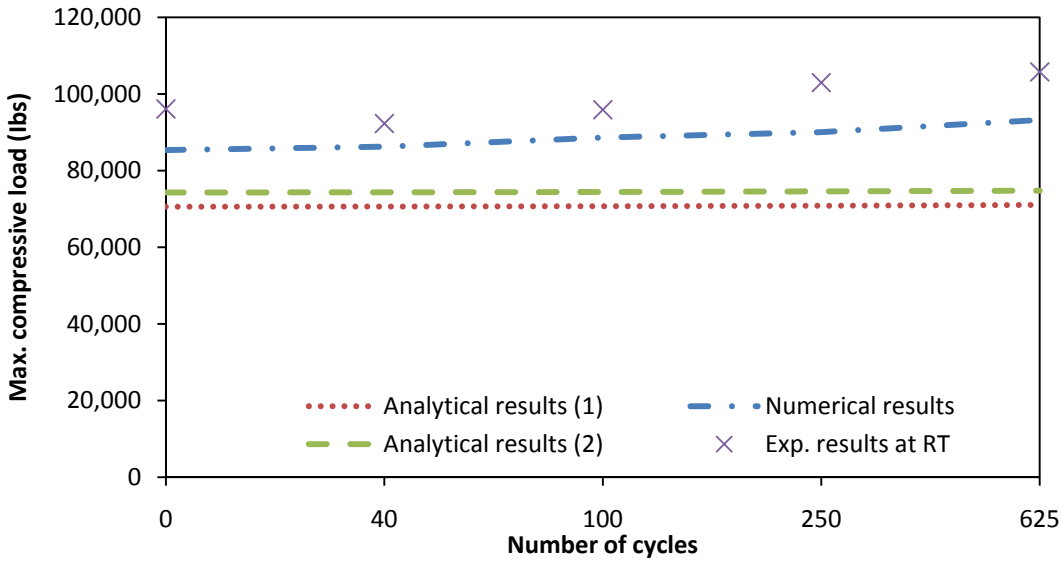

Figure 7.67: Compressive failure load-number of cycle curves for strengthened concrete columns at RT

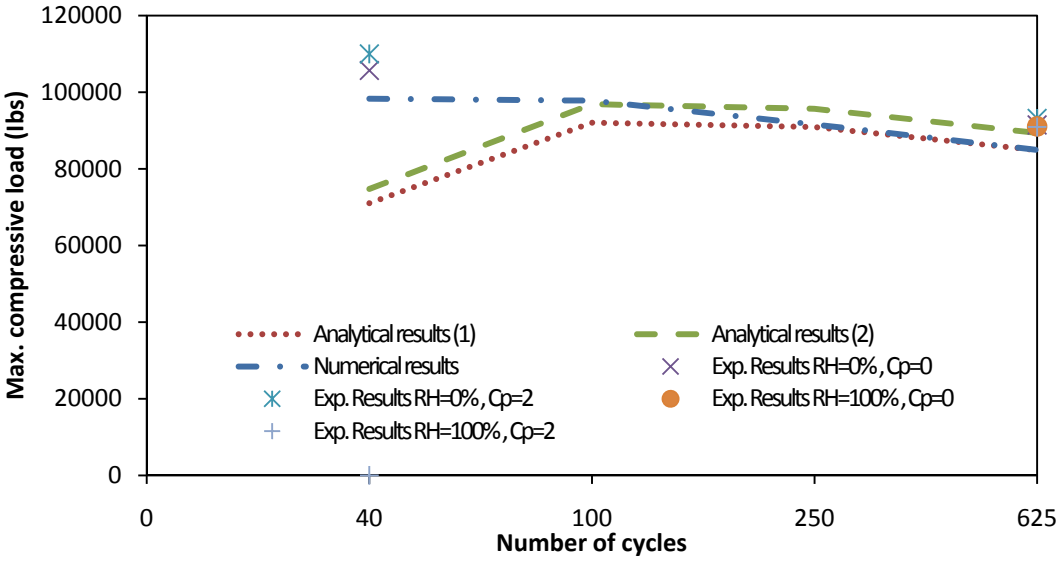

Figure 7.68: Compressive failure load-number of cycle curves for strengthened concrete columns, T=100°C

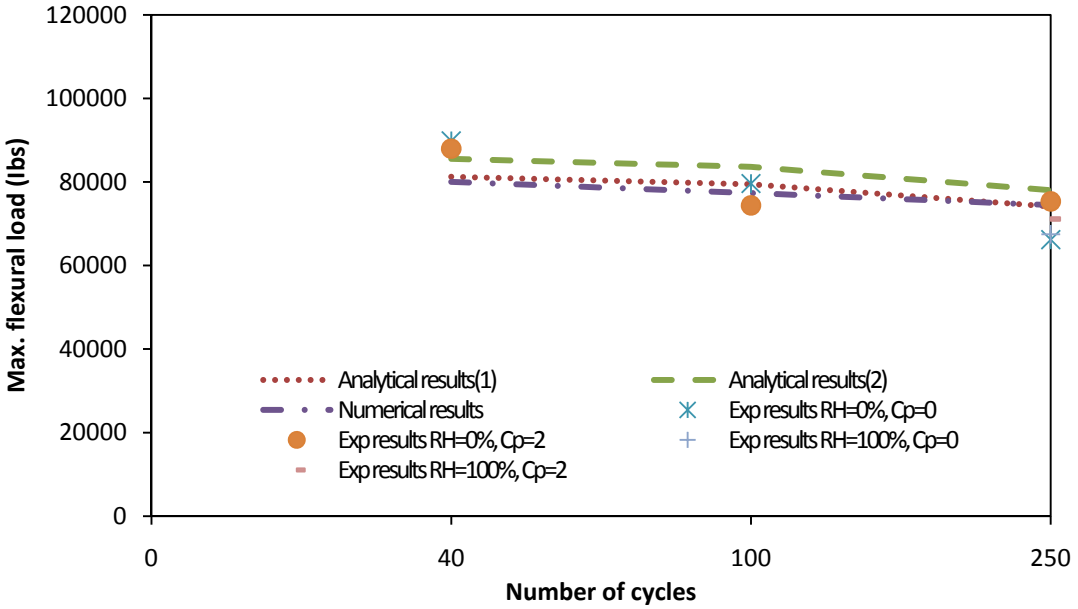

Figure 7.69: Compressive failure load-number of cycle curves for strengthened concrete columns, T=180°C

CHAPTER 8 FRP SURFACE PROTECTION

8.1 Introduction

Fiber Reinforced Plastic (FRP) "composite" material presents numerous advantages over steel or aluminum materials. Benefits include better surface aesthetics, lack of corrosion, lower superstructure weight leading to greater payload or speed potential and good environmental properties. Unlike for steel or aluminum, there are no standard guidelines for how to protect the FRPs composite materials against fire. FRP strengthening is critically dependent upon the bonding adhesive. Therefore in such cases as fire or extreme temperature, it is logical to specify a suitable protection system that provides thermal insulation and prevents the glass transition temperature of the adhesive being reached.

Barnes and Fidell (2006) reported tests that used a proprietary cementitious fire protection of between 15 and 20mm thickness, and supplemental bolted fastenings. They concluded that this thickness of fire protection was insufficient to keep the adhesive temperature below its glass transition and hence preserve strengthening of the beams. Other proprietary systems have been developed specifically to protect bonded FRP strengthening and these have been tested on beams, columns and slabs (Bisby *et al*. 2005, Williams *et al.* 2006). These tests confirmed that it is difficult to keep the temperature of the adhesive below glass transition, and focused upon the strength of the concrete structure.

In this research two different cement mortars were used as protection material against environmental conditions. The protected specimens were exposed to 180^{o}C temperature and 100% relative humidity, the number of cycles were 80 and 150 cycles, while the cycles period was 2 hours.

8.2 Selection of Protection Materials

Two different components of cement mortar were selected and used to protect the FRP strengthening sheet against moderate temperature. The first selection of these cement mortar components was called mix ”A” that consists of type I Portland cement, sand, and water by mixing ratio of 1: 3: 0.4 by weight respectively. Cement and sand were mixed on dry for 1.0 minute, and then water added and mixed for 2.0 minutes. While the second mix “B” consists of type I Portland cement, gravel, sand, and water, the mixing ratio by weight was 1: 2: 1: 0.45 respectively. The size of gravel passed on sieve # 8 (2.36 mm or 0.469″) and remained on sieve #16 (1.18mm or 0.937″), while the grains of sand was 300μm. The same procedures of mixing and time of mixing were followed for both mixes. Figure 8.1 shows the cement mortar mix “B”

Figure 8.1: Cement mortar mix “B”

8.3 Protection Procedures

The procedure of protection was consistent for both types of mixing, as a 10 mm thickness of cement mortar was applied on the FRP sheet surface of the aim specimens. Four strengthened beam specimens and four strengthened column specimens were also protected by

utilizing mix “A”. Another four strengthened beam specimens and four strengthened column specimens were protected by using mix “B”. The Cement mortar was applied carefully on the surface of the FRP strengthening sheets as shown in figure (8.2).

Figure 8.2: Protection of FRP sheets with cement mortar

In order to make the specimen surface as level as possible for the test, after applying the cement mortar, the surface was leveled by using suitable scoop (troweling) as shown in figure (8.3).

Figure 8.3: Make the surface balanced

To insure that the entire target surface is covered and achieved a good protection, the cement mortar mix was extended 1.0″ over the four edges, (see figure 8.4)

Figure 8.4: Protect the specimen aspects

The same procedures were done to protect the target column specimens, where they were coated by 10 mm thickness of cement mortar. The mortar was applied on the FRP strengthening sheet through the entire external perimeter of the specimens, (Figure 8.5).

Figure 8.5: Protection procedures for column specimen

Figure 8.6: Strengthened columns protected by cement mortar

The cement mortar was cured for 7 days by using wetted plastic sheet method as shown in figures (8.7and 8.8).

Figure 8.7: Wet plastic curing for beam specimens

Figure 8.8: Plastic sheets curing for column specimens

8.4 Protection Results and Discussion

After completing the curing period, eight beam specimens and eight column specimens were exposed to different environmental conditions. 50% of these specimens were protected by utilizing mix "A" and the other half was by using mix "B".

8.4.1 Protected Beam Specimens

B128, B129, B130, and B131 were protected by using mix "A", whereas the first two specimens were exposed to 180^{o}C temperature, 100% relative humidity, and subjected to 80 cycles (160 hrs). While the second two specimens were exposed to the same temperature and humidity, but the number of cycles was 150 cycles (300 hrs). The cycle period was constant (2 hrs) for all specimens. All specimens were subjected to the center point flexural load test until failed (see figure 8.9).

Figure 8.9: Center-point flexural load test, B128

Table 8.1 shows the maximum flexural load, flexural strength results, and the mode of failure as well for 80 cycle specimens. Comparing with unprotected specimens, no change occurred in the mode of failure whereas, all these specimens failed due to FRP delamination figures (8.10 and 8.11), but an improvement in the flexural strength results was observed comparing with the control specimens and unprotected specimens as well. This increase in the results of flexural strength indicates that some improvement occurred in the bond surface between concrete and FRP strengthening sheet as a result of the protection. For instance, after 80 cycles of exposing, the flexural strength was 42% above the control specimen results. While for an unprotected specimen with the same temperature and humidity, but the number of cycles was only 40 cycles, (table 6.40 chapter six), the flexural strength was just 28% above the control specimen results.

Table 8.1: Flexural strength test results for protected beams subjected to different environmental conditions.- Mix “A”

Beam no.	Temp °C	RH %	Cy	Max. load lbs	Mean lbs	Flex. strength (psi)	Difference - %	Failure mode
B128	180	100	80	4287.9	4372	1206.0	42.8	Delamination
B129				4455.9		1253.2		Delamination
B130			150	3954.7	4023	1112.3	31.4	Delamination
B131				4092.2		1151.0		Delamination

-Percentage difference of max. load increasing or decreasing compared with control result.
*Lab temperature,
+Lab humidity,
!Cycle period,

Figure 8.10: Concrete flexural crack and FRP delamination, B128

Figure 8.11: FRP delamination of B129, no rupture on the FRP surface

By using cement mortar mix ”B”, as shown in table 8.2, the flexural strength after 80 cycles increased 50.3% comparing with the flexural strength results of control specimens, and after 150 cycles the increase was 33.2%. While for the unprotected specimen after 40 cycles, the flexural strength increased only 28% on the result of control specimens, and 25% after 100. Although the time of exposing to environmental condition for the protected specimens was more than those unprotected specimens, the flexural strength results of protected specimens were higher than unprotected ones, which confirm that the protection material added some improvement on the bond strength between concrete surface and FRP strengthening sheet. The flexural load vs. mid-span deflection curves are shown in figure 8.12.

Table 8.2: Flexural strength test results for protected beams subjected to different environmental conditions.- Mix “B”

Beam no.	Temp °C	RH %	Cy	Max. load Ibs	Mean Ibs	Flex. strength (psi)	Difference - %	Failure mode
B132	180	100	80	4611.9	4603	1297.1	50.3	Delamination
B133				4593.8		1292.0		Delamination
B134			150	4337.8	4078	1220.0	33.2	Delamination
B135				3817.5		1073.7		Delamination

-Percentage difference of max. load increasing or decreasing compared with control result.
*Lab temperature,
+Lab humidity,
!Cycle period

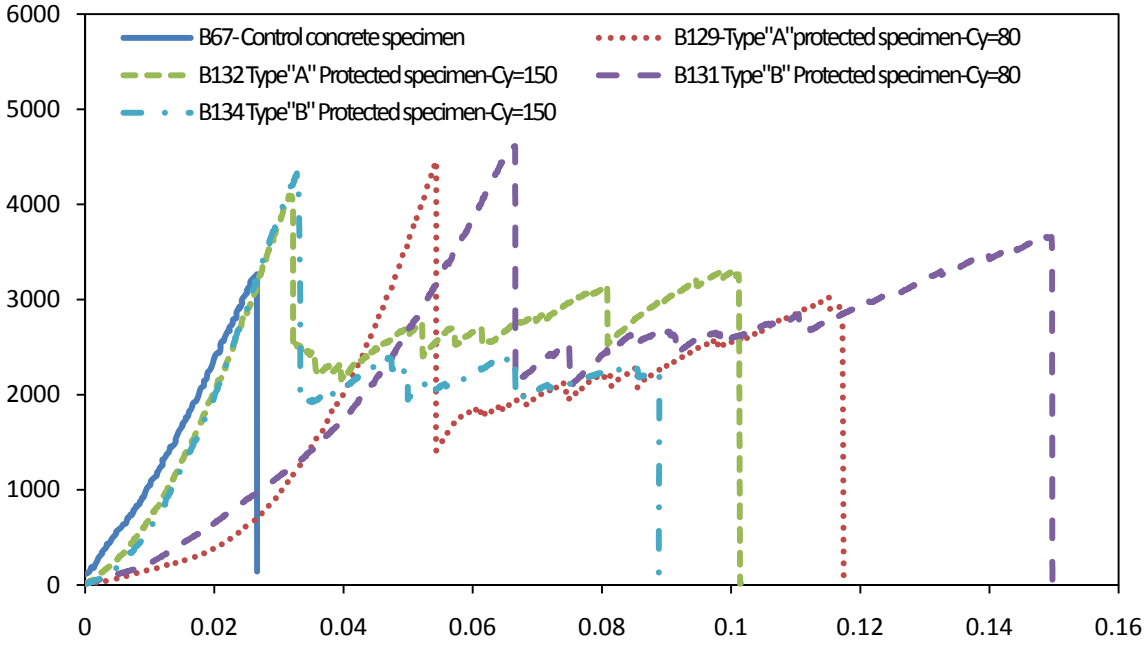

Figure 8.12: Flexural load vs. mid-span deflection curves for protected beam specimens (Cy = 80 and 150)

8.4.2 Protected Column Specimens

Four strengthened column specimens C108 to C111 were protected by using mix “A” and subjected to different environmental conditions after they had been cured for 7 days, and then subjected to compressive strength test, (Figure 8.13).

Figure 8.13: Compressive strength test, protected column

The compressive load, compressive strength, and mode of failure results are showing in table 8.3. The modes of failure were FRP rupture for all specimens (see figure 8.14). The protection cover separated on the specimen and fell down before the specimen fail.

Figure 8.14: FRP rupture of protected column specimen

Comparing to the control specimen results, while the compressive strength for unprotected specimens exposed to 180°C for 40 cycles was 5.4% above the control results, the protected specimen results after 80 cycles showed increase of 19.2% above the control specimen results for the specimens protected by mix "A" and 21.4% for those were protected by mix "B", see table (8.4).

Table 8.3: Compressive strength test results for protected beams subjected to different environmental conditions- Mix "A"

Col. no.	Temp °C	RH %	Cy!	Max. Load (lbs)	Mean lbs	Comp. strength (psi)	Difference - %	Failure mode
C108	180	100	80	83210.7	82404.8	6621.7	19.2	FRP Rupture
C109				81598.9		6493.4		FRP Rupture
C110			150	72321.2	74897.7	5755.1	8.3	FRP Rupture
C111				77474.2		6165.2		FRP Rupture

By increasing the time of exposing to 150 cycles (300 hrs), the compressive strength results for mix "A" specimens were 8.3 % over the control results and 11.4% for mix "B" specimens. Whilst the compressive strength result for unprotected specimens after 100 cycles was 5.4% above than the control specimen results, whereas the reduction was ?% after 150 cycles. Figure 8.15 explains the relationship between the compressive load and deflection of these column specimens.

Table 8.4: Compressive strength test results for protected beams subjected to different environmental conditions.- Mix "B"

Col. no.	Temp °C	RH %	Cy!	Max. load (lbs)	Mean lbs	Comp. strength (psi)	**Difference** - %	Failure mode
C112	180	100	80	81926.5	83925.1	6519.5	21.4	FRP Rupture
C113				85923.7		6837.6		FRP Rupture
C114			150	74349.9	77019.3	5916.6	11.4	FRP Rupture
C115				79688.6		6341.4		FRP Rupture

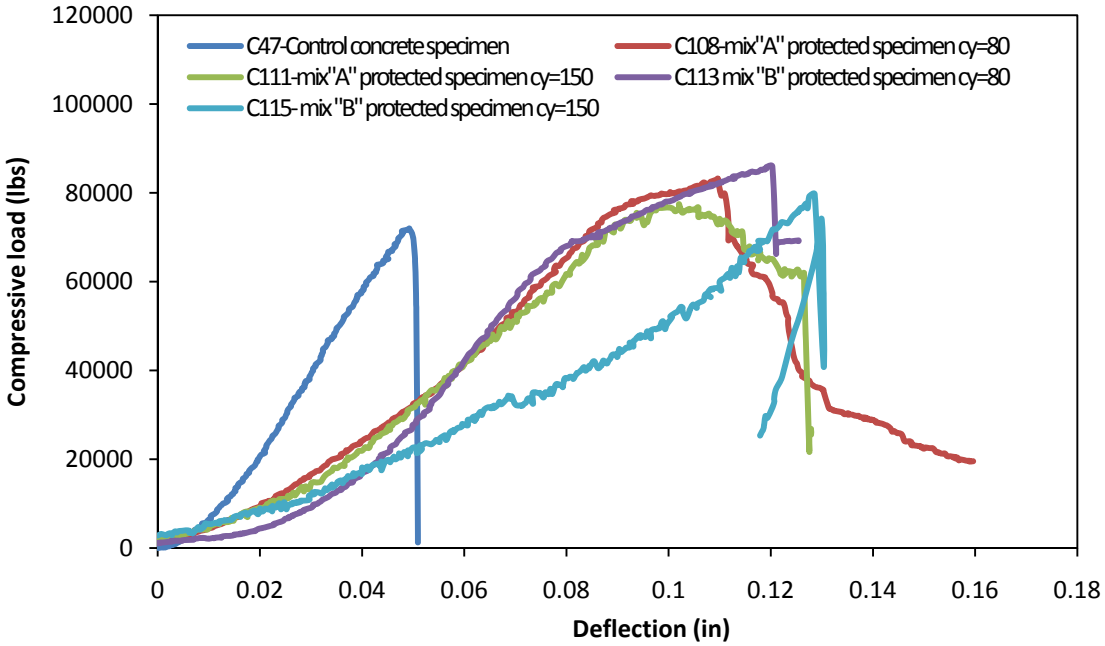

Figure 8.15: Compressive load vs. deflection curves for protected column specimens

CHAPTER 9 CONCLUSIONS AND FUTURE WORK

9.1 Conclusions

The intent of this research was to develop a durability performance of FRP strengthened beams and columns that are exposed to different environments. Extensive laboratory tests have been implemented for unstrengthened and FRP strengthened concrete beams and columns. In addition, several epoxy beams were casted and exposed to different environmental conditions and then subjected to the flexural load test.

The results that have been obtained experimentally, evaluated and compared to the analytical solutions and numerical results. These results concluded to the following:

***Effect of temperature*:** the flexural strength of concrete beams increased due to subjecting to 100^{o}C of temperature, the magnitudes of flexural strength increases varied with the number of cycles. The strength was the highest after 250 cycles, comparing to 100 cycles, then the strength was reduced after 625 cycles. By exposing to 180^{o}C of temperature, the maximum flexural load showed an increase about 18% after 100 cycles and only 1% after 625 cycles comparing to the control specimen.

The compressive strength for concrete column specimens that were exposed to 100^{o}C of temperature, improved about 50% after 250 cycles, and about 25% after 625 cycles compared to the control specimen. The high temperature (180^{o}C) has an adversely influence on the compressive strength of the specimens.

The epoxy beam specimens showed good improvements in flexural strength. An increase of 65% over the control specimen was obtained after being exposed to 100^{o}C of temperature and 250 cycles, but the stiffness of the specimens decreased because the material became much more ductile. The specimens that were exposed to 180^{o}C of temperature showed continuing decreases

in flexural strength with increasing the times of exposure, while the stiffness increased (becoming stiffer with time). This concludes that the flexural strength of Tyfo-S epoxy material improves under the 100^{o}C temperature environment until 250 cycles and decreases under the 180^{o}C temperature environment. All the epoxy beam specimens exposed to 100^{o}C of temperature ruptured.

The flexural strength of strengthened concrete beams after subjected to100^{o}C of temperature and 40 cycles, showed improvement, ranging from 46% to about 55% over the control specimens (plain concrete control specimen).

In summary, compared to the standard laboratory condition results, 100^{o}C of temperature showed that an improvement in the strength of both unstrengthened and FRP strengthened concrete beams/columns, and epoxy beams until 250 cycles. No degradation occurred for any specimen that was strengthened by SikaWrap Hex 113C CFRP and exposed to 100^{o}C, the mode of failure was FRP rupture for all specimens. By exposing to 180^{o}C of temperature, both the flexural and compressive strength decreased and the FRP delamination was the dominant mode of failure for all beam specimens that were exposed to 180^{o}C of temperature.

Effect of relative humidity: Two different relative humidities (0% and 100%) were utilized in this research. The experimental test results indicate that humidity has some influence on the strength of concrete beams and columns especially at 180^{o}C. For instance, the flexural strengths of the samples conditioned at 100% relative humidity were less than those results of 0% relative humidity at the same numbers of cycle.

The level of relative humidity has an important influence on the maximum deflection of epoxy beam specimens. For example, after 625 cycles, the deflection of the 0% humidity specimens was 2-4 times higher than that of the 100% humidity specimens.

Effect of Number of cycles*:* the number of cycles played an essential influence on the materials strength for both concrete and FRP composites. The concrete results recorded an improvement in the strength by about 35% after 100^{o}C of exposure and 100 cycles, 40% after 250 cycles, and 26% after 625 cycles; while due to exposure to 180^{o}C of temperature, the strength decreased compared to 100^{o}C of temperature. At standard laboratory conditions, the resin material showed an improvement of flexural strength about of 9%, 12%, 37%, and 38% compared to the control specimens after 40, 100, 250, and 625 cycles respectively. After 100^{o}C of temperature, the average strengths were improved by 57%, 46%, 58%, after 40, 100, and 250 cycles respectively. 180^{o}C temperature results recorded a noticeable decreases by -31%, after -40 cycles, -41% due to 100 cycles, and -12% after 250 cycles; while by -48% after 350 cycles.

In conclusion, the strength of materials improves by aging of exposure (number of cycle) under the standard laboratory conditions. Such strength increases continue up to 250 cycles when being exposed to 100^{o}C of temperature, but the strength recorded noticeable decreases after 625 cycles,. By exposing to 180^{o}C of temperature the strength decreased compared to the control specimens.

Cycle periods: With 100^{o}C of temperature, no strong effect of the cycle period (2hr vs. constant temperature) on the deflection has been noticed, especially when the number of cycles was 250 cycles or less. By increasing the temperature to 180^{o}C, the effect of cycle period (2 hours vs. constant temperature at 180^{o}C) diminished more.

9.2 Future Work

In this research, the durability performance of the bonding behavior between concrete and FRP surfaces has been studied by subjecting the beam and column specimens to mechanical loads and different environmental conditions. Although, this work is close to the real conditions

of the structures, future research can be done by considering only the effect of different environmental conditions without mechanical loads that can be made by subjecting the specimens to another distractive test such as pull-out test, or through using non-destructive tests. These tests may indicate if the debonding between concrete and FRP strengthening sheets that may happen due to hygrothermal effects only.

Most of the concrete elements are encased by cement mortar (plastering) after being constructed to improve irregular concrete surfaces that may happen due to form works, to give better aesthetic shape to the element and the building in general, to protect the element from harsh environments, and to make the element ready to receive paint. In this research, preliminary beams and columns have been protected against temperature and humidity by utilizing two different cement mortar coatings of thickness of 10 mm. Some improvements in strength were observed. Therefore, a future work can be done by increasing the thickness of the mortar or different mixes and thoroughly examine how such coatings may improve the strength and protect the bond between concrete and FRP strengthening materials.

REFERENCES

1. Gibson, R.F. ‘ Principles of Composite Material Mechanics’ ,second edition, Taylor & Francis Group,LLC,2007.
2. Ritchie, P. A., Thomas, D. A., Lu, L. W., and Connelly, G. M. _1991_.“External strengthening of concrete beams using fiber-reinforced plastics.” ACI Struct. J., 88, 490–500.
3. Saadatmanesh, H., and Ehsani, M. R. _1991_. “RC beams strengthened with GFRP plates. I: Experimental study.” J. Struct. Eng., 117_11_,3417–3433.
4. Meier, U., Deuring, M., Meier, H., and Schwegler, G. _1992_. “Strengthening of structures with CFRP laminates: Research and applications in Switzerland.” Advanced composite materials in bridges and structures, Canadian Society for Civil Engineering, Sherbrooke, Quebec, Canada, 243–251.
5. Pan, J. ;Leung, C. K. Y. ‘Effect of Concrete Composition on FRP/Concrete Bond Capacity’ Journal of composites for construction, /December. 2007,p611-618.
6. Choi. H.T.; West, J.S.; Soudki,K.A.’ Analysis of the Flexural Behavior of Partially Bonded FRP Strengthened Concrete Beams’ Journal of composites for construction, /July/August. 2008 ,P375-286.
7. Park, S. “ Durability of adhesive joints between concrete and FRP reinforcement in aggressive environments”, PhD Dissertation, The University of Texas at Austin, August 2005.
8. Atadero, R. A. ‘Development of loading resistance factor design for strengthening of reinforced concrete structural’ PhD Dissertation in structural engineering, University of xCalifornia, San Diego ,2006.
9. Duthinh, D. ; and Starnes, M. “Strength and Ductility of Concrete Beams Reinforced with Carbon FRP and Steel” ,U.S. DEPARTMENT OF COMMERCE Techno logy Administration

Building and Fire Research Laboratory National Institute of Standards Gaithersburg, MD 20899, November 2001.

10. Oh, H., Sim, J. ; Ju, M. ; Lee, Y.T. ; Lee, K.H. 'Flexural capacity of concrete beam strengthened with near surface mounted carbon fiber reinforced polymer', The 3rd ACF International Conference ACF/VCA 2008.
11. Taljsten, B. 'FRP Strengthening of Existing Concrete Structures' Design Guidelines: Lulea University Printing Office: Lulea, Sweden, 2002.
12. Bank, L., (2006). Composite for construction: 'Structural design with FRP materials' Wiley, New York.
13. Matthews, F.L.; Davies, G.A.O. ; Hitchings, D. ; and Soutis, C.' Finite element modeling of composite materials and structures' , Woodhead Publishing Ltd, 2000.
14. Deo, R.B. ; Saff, C.R."Composite Materials Testing and Design", American society for testing and materials1996.
15. Malvar, L. J.; Joshi, N. R. ; Beran, J. A. ; and Novinson,T. 'Environmental effects on the short-term bond of carbon fiber-reinforced polymer .CFRP. composites'. Journal of composites for construction, / February. 2008.
16. Class notes of "Mechanics and Design of Structures Using Advanced Composites" course, University of Ottawa,CA
17. Dussek I.J. "Strengthening of bridge beams and similar structures by means of epoxy resin bonded external reinforcement, Transport research record, National Research Council, 1974, No. 785,1974,pp21-24.

18. International Federation for Structural Concrete. Externally Bonded FRP Reinforcement for RC Structures; International Federation for Structural Concrete, Lausanna, Switzerland, 2001.

19. Alkhrdaji, T. and A. Nanni, "Surface Bonded FRP Reinforcement for Strengthening/Repair of Structural Reinforced Concrete,"Proc., ICRI-NRCC Workshop, Baltimore, MD, Oct. 30, 1999, 19 ppA.

20. Yunping Xi, Y. ; Chang, S. ; and Li, A. Y. “Long-term durability of fiber- reinforced polymers (FRPS) and in-situ monitoring of FRP bridge decks at O’ Fallon Park Brifge”, Final Report, Report No. CDOT-DTD-R-2004-03.

21. Naval Facilities Engineering Service Center, “Navy Advanced Composite Technology in Waterfront Infrastructure,” Special Publication SP-2046-SHR, Port Hueneme, 1998.

22. Supaviriyakit, T.; and Pornpongsaroj, P. “Finite element analysis of FRP-strengthened RC beams”, Songklanakarin J. Sci. Technol. Vol. 26 No. 4 Jul.-Aug. 2004

23. Yalim, B.; Kalayci, A. S.; and Mirmiran, A. ‘Performance of FRP-strengthening RC beams with different concrete surface profiles’. Journal of composites for construction, Nov, Dec. 2008.

24. Watson, R. J. ~1998!. ‘‘Case histories of structural rehabilitation utilizing composites in industrial and marine environments.’’ Fiber Composites in Infrastructure, ICCI’98, 2nd Int. Conf. on Composites in Infrastructure, H. Saadatmanesh and M. R. Ehsani, eds., Univ. of Arizona, Tucson, Ariz., 113–125.

25. Karbhari, V. M. and Zhao, L. (1998). Issues Related to Composite Plating and environmental Exposure Effects on Composite-concrete Interface in External Strengthening, Composite Structures, 40(3-4): 293–304.

26. Malvar, L. J. ~1998a!. ‘‘Durability of composites in concrete.’’ CDCC’98,First International Conference on Durability of Composites for Construction, R. Benmokrane and H. Rahman ~eds.!, Univ. of Sherbrooke, Quebec, Canada, 361–372.

27. American Concrete Institute (ACI). (2000). “Guide for the design and construction of externally bonded FRP system for the strengthening concrete structures.” Report by ACU Committee 440 “ACI-440.2R-2000.

28. Busel, J. P. (1995) ‘FRP composites in construction application-a profile in progress’. SPI composite institute.

29. Meiarashi, S., Kishima, T., Nishizaki, I., and Sasaki, I. ~1998!. ‘‘Application of fiber reinforced plastics to construction structural materials. Volume 1: Examples of application of FRP as a primary structural material.’’ Cooperative Research Report No. 252, Public Works Research Institute, Ministry of Construction, Tsukuba, Japan.

30. Haque, A., Mahmood, S., Walker, L., and Jeelani, S., “Moisture and Temperature Induced Degradation in Tensile Properties of Kevlar-Graphite/Epoxy Hybrid Composites,” Journal of Reinforced Plastics and Composites, Vol. 10, No. 3, pp. 132-145, 1991.

31. Birger, S., Moshonov, A., and Kenig, S., “The Effects of thermal and Hygrothermal Ageing on the Failure Mechanisms of Graphite-Fabric Epoxy Composites Subjected to Flexural Loading,” Composites, Vol. 20, pp. 341-348, July 1989.

32. Foster, S. K., and Bisby, L. A. ‘Fire survivability of external bonded FRP strengthening systems’ Journal of composites for construction, Vol.12, No. 5, October 1,2008.

33. Vpgel, H. ; and Svecova, D., “ Thermal compatibility and bond strength of FRP reinforcement in prestressed concrete applications”, Journal of composites for construction, Sep/ Oct.. 2007,459-468.

34. Gheorghiu, C.; Labossiere, P. ; and Raiche, A."Environmental fatigue static behavior of RC beams with carbon-fiber-reinforced polymer", Journal of composites for construction,

35. Masmoudi, R.; Zaidi, A. ; and Gerard, P. ' Transverse thermal expansion of FRP bars embedded' Journal of composites for construction ASCE/September/October 2005.

36. Tadeu, A.J.B. and Branco, F.J.F.G., "Shear tests of steel plates epoxy-bonded to concrete under temperature", Journal of Materials in Civil Engineering, 12, 1, 2000, pp. 74-80.

37. Di Tommaso, A., U. Neubauer, A. Pantuso and F. S. Rostásy (2001) 'Behavior of adhesively bonded concrete-CFRP joints at low and high temperatures' in Mechanics of Composite Materials Vol. 37, Nr. 4, pp. 327-338.

38. Klamer, E. L., D. A. Hordijk and C. S. Kleinman (2006) 'Debonding of CFRP laminates externally bonded to concrete specimens at low and high temperatures' in Mirmiran, A. and Nanni, A. (Eds.) Third International Conference on FRP Composites in Civil Engineering (CICE 2006), pp. 35-38.

39. Leung, H., Balendran, R. and Lim, C. (2001). Flexural Capacity of Strengthened Concrete Beam Exposed to Different Environmental Conditions, Proceedings of the International Conference of FRP Composites in Civil Engineering: Hong Kong, China, pp. 1597–1606.

40. Grace, N. F. and Singh, S. B. (2005). Durability Evaluation of Carbon Fiber-reinforced Polymer Strengthened Concrete Beams: Experimental Study and Design, ACI Structural Journal, 102(1): 40–51.

41. Ouyang, Z.; and Wan, B. ' Modeling of moisture in FRP strengthened concrete specimens'. Journal of composites for construction, July/ August. 2008.

42. Ouyang Z. and Wan. B. (2006). Deterioration Mechanism of Bond Between CFRP Plate and Concrete in Moisture Environment, Third International Conference on FRP Composites in Civil Engineering (CICE 2006), Miami, Florida, USA, pp. 263–266.

43. Lin, M. W., Berman, J. B., Khoshbakht, M., Feickert, C. A., and Abatan, A. O. _2006_. "Modeling of moisture migration in an FRP reinforced masonry structure." Build. Environ., 41, 646–656.

44. Nishizaki, L. ; and Meiarashi, S. ' Long-term deterioration of GFRP in water and moist environment'. Journal of composites for construction, /February. 2002.

45. Minnetyan, L., Murthy, P. L.N., and Chamis,C.C.' Progressive fracture in composite subjected to hygrothermal environemnt'.

46. Chajes, M. J., Thomson Jr, T. A. and Farschman, C. A. (1995). Durability of Concrete Beams Externally Reinforced with Composite Fabrics, Construction and Building Materials, 9(3): 141–148.

47. Petal, S. R., and Case, S. W.' Durability of hygrothermally aged graphite/epoxy woven composite under combined hygrothermal conditions' International journal of fatigue 24 (2002) 1295-1301.

48. Mostofinejad, D.; Talaeitaba ,S.B.," Finite Element Modeling of RC Connections Strengthened with FRP Laminates" Iranian Journal of Science & Technology, Transaction B, Engineering, "Vol. 30, No. B1 Printed in The Islamic Republic of Iran, 2006 © Shiraz University.

49. Gorji, M.S., "Analysis of FRP Strengthened Reinforced Concrete Beams Using Energy Variation Method",World Applied Sciences Journal 6 (1): 105-111, 2009.

50. Kishi, N. ; Zhang, G. ; Mikami, H. “Numerical Cracking and Debonding Analysis of RC Beams Reinforced with FRP Sheet”, Journal of composites construction Nov./Dec. 2005. 507-514

51. Lu, X.Z. ; Teng, J.G. ; Ye, L. P. ; and Jiang, J. J., “Intermediate Crack Debonding in FRP-Strengthened RC Beams: FE Analysis and Strength Model”, Journal of composites construction March/April 2007. 161-174.

52. Kotynia, R., and Kaminska, M. E. _2003_. “Ductility and failure mode of RC beams strengthened for flexure with CFRP.” Rep. No. 13, Dept. of Concrete Structures, Technical Univ. of Lodz, Poland.

53. Kotynia, H. ; Baky, A. ; Neale, K. W. ; and Ebead, U.A., “Flexural Strengthening of RC Beams with Externally Bond CFRP Systems: Test Results and 3D Nonlinear FE Analysis”, Journal of composites construction March/April 2008. 190-201.

54. Padavet, P. “nfluence of Temperature on Concrete and its Modulus of Elasticity”, 40th International Conference Experimental Stress Analysis., 3. – 6. VI. 2002, PRAHA/PRAGUE, CZECH REPUBLIC.

55. Toutanji, H. A. and Gomez, W. (1997). Durability Characteristics of Concrete Beams Externally Bonded with FRP Composite Sheets, Cement and Concrete Composites, 19(4): 351–358.

56. White, G. R.; and Jones, F.R., in Proceeding conference’ ICCM9’, Madrid, Spain, 5, 601-608,July 1993.

57. Davalos, J. F., Kodkani, S. S., Ray, I. and Boyajian, D. M. (2005). A Fracture Mechanics Approach for Interface Durability of Bonded FRP to Concrete, 7th International Symposium

on Fiber-reinforced (FRP) Polymer Reinforcement for Concrete Structures, SP230, Kansas City, Kansas, USA, pp.1465–1480.

58. (ACI-318-05) " Building code requirements for structural concrete (ACI 318-05) and Commentary (ACI 318R-05)

59. Bathe, K. J., Finite Element Procedures, Prentice-Hall, Inc., Upper Saddle River, New Jersey, 1996.

60. Adams, V. and Askenazi, A., Building Better Products with Finite Element Analysis, OnWord Press, Santa Fe, New Mexico, 1998.

61. Fib (2001) fib Bulletin 14. Externally bonded FRP reinforcement for RC structures, Lausanne: fédération internationale du béton.

62. Klamer, E. L. , Hordijk, D. A., and Hermes, M. C.J. 'The influence of temperature on RC beams strengthened with externally bonded CFRP reinforcement'. HERON Vol. 53(2008) No.3.

63. Pan, J.; and Leung, C.K.Y. " Effect of multiple secondary cracks on FRP debonding from the substrate of reinforced concrete beams".

64. Teng, JG.; Chen, Jf. ; Smith, ST.; and Lam, L. "FRP-strengthened RC structures". John Wiley $Sons, ltd,2002.

65. Warren, G. E. ''Waterfront repair and upgrade, advanced technology demonstration site No. 2: Pier 12, NAVSTA San Diego.'' Site Specific Rep. SSR-2419-SHR, Naval Facilities Engineering Service Center, Port Hueneme, Calif,1998

66. Mostofinejad, D.; and Talaeitaba, S. B. "Finite Element Modeling of RC Connections Strengthened with FRP Laminates", Iranian Journal of Science & Technology, Transaction B, Engineering, Vol. 30, No. B1 Printed in The Islamic Republic of Iran, 2006.

67. ASTM C33-07, “Standard Specification for Concrete Aggregates”, 2008

68. ASTM E11-04, “Standard Specification for Wire Cloth and Sieves for Testing Purpose”, 2008

69. ASTM C143/C143 M-08, “Standard Test Method for Slump of Hydraulic-Cement Concrete”, 2008

70. ASTM C293-08, “Standard Test Method for Flexural Strength of Concrete (Using Simple Beam with Center-Point Loading)”, 2008

71. C39/C 39/M-05 “Standard Test Method for Compressive Strength of Cylindrical Concrete Specimens”, 2008.

72. ASTM D 790-07, “Standard Test Methods for Flexural Properties of Unreinforced and Reinforced Plastic and Electrical Insulation Materials”, 2008.

73. Thomsen, H., Spacone, E., Limkatanyu, S. and Camata, G. (2004) “Failure Mode Analyses of Reinforced Concrete Beams Strengthened in Flexure with Externally Bonded Fiber-Reinforced Polymers.” Journal of Composites for Construction, 8: 123–131.

74. ACI Committee 440 (2002) “Guide for the Design and Construction of Externally Bonded FRP Systems for Strengthening Concrete Structures” (440.2R-02), American Concrete Institute, Farmington Hills, Michigan.

75. James G. MacGregor , James K. Wight (reinforced concrete Mechanics and Dseign) (fourth edition) Pearson Prentice Hall, Upper Saddle River, New Jersey 07458 (William J. Hall, Editor) 2005.

76. (ACI-318-08) “ Building code requirements for structural concrete (ACI 318-08) and Commentary (ACI 318R-08)

77. Lara M. Vigneron, Jacques G. Verly, and Simon K. Warfield “On Extended Finite Element Method (XFEM) for Modelling of Organ Deformations Associated with Surgical Cuts” Boston, USA

78. N. Moës, N. Sukumar, B. Moran and T. Belytschko (2000), "An Extended Finite Element Method (X-FEM) for Two- and Three-Dimensional Crack Modeling," in ECCOMAS 2000**,** Barcelona, Spain, September 11–14, 2000

79. E. Giner, N. Sukumar, J. E. Tarancón and F. J. Fuenmayor (2009), "An Abaqus Implementation of the Extended Finite Element Method," Engineering Fracture Mechanics, Vol. 76, Number 3, pp. 347–368.

80. Babuska I, Melenk JM. The partition of unity method. International Journal for Numerical Methods in Engineering 1998; 40(4):727-758.

81. Matthew J. P., Nam-Ho Kim; and Timothy Davis “Reanalysis of the Extended Finite Element Method for Crack Initiation and Propagation” 2010 AIAA SDM Student Symposium.

82. Jensen, E., Grace, N., Eamon, C.D., Shi, X., and Matsagar, V. (2009). “Life cycle cost analysis of CFRP reinforced concrete bridges,” Transportation Research Board 88th Annual Meeting, Washington, D.C., January 2009.

83. Lu, F., Ayoub, A. “ Effect of Bond Properties on the Behavior of FRP-Strengthened RC Girders Subjected to Monotonic and Cyclic Loads” SP-258—8

84. Wu, H.C., “Mechanical Interaction between Concrete and FRP,” Journal of Composites for Construction, Vol.4, No.2, pp.96-98, 2000.

ABSTRACT

DURABILITY PERFORMANCE OF FRP STRENGHTENED CONCRETE BEAMS AND COLUMNS EXPOSED TO HYGROTHERMAL ENVIRONMENT

by

ABULGASEM M. ELARBI

August 2011

Advisor: Dr. Hwai-Chaung Wu

Major: Civil and Environmental Engineering (Structural Engineering)

Degree: Doctor of Philosophy

Concrete structures deteriorate over time due to exposure to various environments, including hot and humid weather. High temperature, wind, and air humidity in many hot climates can all have a negative impact on the performance of concrete structures. The most important factors are temperature and humidity – often times these effects are not immediately evident and develop years later – making determination of responsibility difficult and repair expensive.

Fiber reinforced polymer (FRP) composites have been recognized as a viable material for strengthening/retrofitting deficient structures, due to their superior performance. FRP sheets/fabrics are usually bonded to existing reinforced concrete structures. Due to their high specific strength/stiffness and lightweight, these materials can offer significant advantages over more traditional materials such as concrete and steel.

The present investigation intends to study the effects of changing hygrothermal conditioning cycles (either by changing relative humidity and temperature is kept constant, or by changing temperature but relative humidity is maintained same) on the durability performance of FRP strengthened concrete beams and columns. The study include the long term influence of moisture, high temperature, and combined hygrothermal conditions on the mechanical properties

of FRPs composites and the effect of deteriorated composites on the structural behavior of concrete beams and columns when subjected to realistic environmental conditions. This study includes also the study of the fracture behavior between concrete and external FRP strips in hygrothermal condition. The overall approach consists of experiments, analysis, and computations.

An extensive experimental research has been done throughout implement and test several sets of specimens include epoxy beams, concrete beams and columns, and FRP strengthened concrete beams and columns exposed to different environmental conditions. Carbon and glass fiber reinforcement polymer with resin material were provided from two different resources have been utilized in this study.

Also, two and three-dimensional extended finite element method (X-FEM) is developed and implemented in the ABAQUS-CAE package to predict the bond strength at the interface between concrete and FRP strengthening fabric.

In addition, analytical calculations for epoxy beams, non-strengthened concrete beams, and columns, FRP strengthened beams and columns were developed based on the ACI 318 and ACI 440.2R-02 including the environmental effects based on the temperature dependent factor.

To confirm the validity of the analysis process and the solution obtained, the flexural load and compressive load were acquired using the analytical calculations compared to experimental results and FE analysis

Finally, conclusions and suggestions for future study research are presented, including development of the protection of FRP strengthening materials.

AUTOBIOGRAPHICAL STATEMENT

ABULGASEM ELARBI

Abulgasem received his B.Sc. in Civil Engineering in 1991 and his master degree in Civil Engineering “Structural Engineering” in 2001. Both his Bachelor and master degrees were from Al-Fateh University, Tripoli-Libya. Since 2007, he has been studying towards his doctoral degree in Civil Engineering at Wayne State University since 2007. His research interests are durability performance of FRP strengthened concrete structures exposed to different environmental conditions, finite element modeling of composites, concrete technology, and structures and materials testing.

Abulgasem has been in many professional and student organizations as well. He is a member of The Scientific Engineers Society-Libya, Civil Engineering Honor Society (Chi Epsilon)-USA, and The National Engineering Honor Society (Tau Beta Pi), USA. Furthermore, he received the Best Teaching Assistant Award from the Wayne State University College of Engineering in 2011.